Using iron sulphide as a marker to decipher taphonomic signals in fossil marine successions

Christopher Reedman

School of Earth and Environmental Sciences

Cardiff University

This thesis is being submitted in partial fulfilment of the requirements for the degree of *Doctor of Philosophy*

July 2021

ABSTRACT

Iron sulphide is established as a marker to decipher taphonomic signals in the Early Jurassic of Dorset and East Devon. The extent to which pyrite replacement contributes to the representation of ecological skeletal diversity is evaluated. Variations in the preservation and composition of the shelly fossil record are analysed in relation to taphonomic processes associated with the Missing Molluscs effect.

The replacement context for syn-sedimentary pyritisation broadly functioned as a taphonomic window in two scenarios: within the TAZ where aerobic decay of retained organic matter established localised reducing conditions inside ammonoid shells and enabled pyrite precipitation, or where the TAZ was elevated to within the water column such that molluscan spat and ammonoids were pyritised. Local buffering effects were imposed during bacterial sulphate reduction and pyrite precipitation.

The fossil record was influenced by faunal recovery and anoxia at the T-J boundary interval; changing palaeoenvironmental conditions, notably fluctuations in the redox state; and taphonomic biases. Taphonomic distortion was significant in oxic environments where skeletal diversity was high, and moot within dysaerobic/anoxic environments where diversity was low. In open marine settings with a diverse biota, primary biomineralogical shell composition is significant in distortion; the type of bias affects different trophic levels whose presence is in part ecologically controlled.

The application of iron palaeoredox proxies, specifically Fe_{HR}/Fe_T and Fe_{Py}/Fe_{HR} ratios, to characterise changes in bottom water redox conditions within the local strata requires further work. Infrequent Fe_{HR}/Fe_T ratios reflect inferred oxygen conditions, but the range of lithology specific values shows extensive overlap and most inferred non-anoxic samples plot spuriously above the anoxic threshold. Masking of depositional redox signals relates to the validity of Fe_{HR}/Fe_T ratios in oxic carbonate-rich sediments, bioturbation that altered original Fe_{HR}/Fe_T ratios via physical mixing, and sampling resolution. Most data should be considered a time-averaged representation of palaeoenvironmental redox conditions.

ACKNOWLEDGEMENTS

Throughout the duration of my PhD I have felt the kindness and support of mentors, friends, and family. The hard truth of my journey is that without the compassion shown to me by others, I would not have made it to this point. My family, particularly my parents, have supported me tirelessly throughout the entirety of my life; I am grateful to you for providing me every opportunity to succeed and I can only hope to make you proud.

During my PhD, Lesley Cherns and Paul Wright have taught me the value of scientific rigour and encouraged my passion for palaeontology through their enthusiasm, dedication, and gentle encouragement. I also owe a great deal to the talented scientists and researchers who have helped me throughout my studies; special thanks go to Ernest Chi Fru and Tony Oldroyd for teaching me so much and helping to develop the content of my thesis. I am also grateful to Robert Raiswell for his willingness to address queries and provide insight when I was struggling with the complexities of the topic.

The work in this thesis was made possible by a Cardiff University Sir Charles Wright Match-Funded Endowment Studentship; I would also like to thank the Jurassic Coast Trust and Dinosaurland Fossil Museum who provided funding at different times.

To my mentor and friend David Sole, I am thankful for the guidance you have provided me throughout the duration of my PhD and continue to provide in my career. Your wisdom, fairness, and character inspire me. Thank you to my friends Rob Moore and James Carroll who have always shown patience, compassion, and a willingness to help in all endeavours. A special mention extends to the fossil hunters and geologists on the Jurassic Coast who helped to foster my excitement for the subject, especially Phil D, Mike H, and Sam S.

Whilst I am sure it was a contributing factor to me taking an excruciating amount of time to finish my PhD, I would like to thank all of the folks in Cardiff that have shared this journey with me. Special thanks go to Aidan S, Josh A, Harry L, James W, James P, Jamie G, Jamie P, Joanna B, Matt H, Max J, Niall G, Nick W, Sam B, and Sarah G. Finally I want to thank Ioana, who has been my rock throughout the hardest times. The support and encouragement you have provided throughout the last 3 years are a testament to your character. Thank you for being patient with me & for Simon the rabbit.

For Mum and Dad.

CONTENTS

List of Tables

List of Figures

CHAPTER 1

1. INTRODUCTION AND GEOLOGICAL SETTING

1.1. Preservation and the fossil record

The fossil record is rarely a true representation of original palaeoecology and is subject to taphonomic processes that distort the relative abundance and diversity of all major groups. The selective removal of soft tissues and soft-bodied biota from the fossil record is common in most sedimentary successions (Seilacher et al., 1985, Allison, 1988, Allison and Briggs, 1991, Allison and Bottjer, 2010) and their survival requires lagerstätten preservation such as the Beecher's Trilobite Bed (e.g. Briggs et al., 1991, Briggs and Edgecombe, 1993, Raiswell et al., 2008) or the Burgess Shale-type (e.g. Butterfield, 1990, Butterfield, 2003, Gaines, 2014). Whilst the poor preservation potential of soft tissues and soft-bodied organisms is widely accepted, selective dissolution of vulnerable shelly groups is not fully appreciated and results in a poorly recognised, albeit semi-quantifiable, distortion of the molluscan fossil record (e.g. Cherns and Wright, 2000, Wright et al., 2003, Cherns et al., 2008). The underrepresentation of a group that has generally been considered survivable implies that previous ecological and taphonomic studies should be reconsidered with respect to the 'Missing Molluscs effect' (Wright et al., 2003).

1.1.1. Taphonomy

Taphonomy was defined by Efremov (1940) and generally represents the process of fossilisation from death to burial. It describes the physical, chemical, and biological processes that control the preservation or eradication of different fossil groups (e.g. Allison and Briggs, 1991, Allison and Bottjer, 2010).

Taphonomy is a non-uniform process that influences replacement, preservation, and distortion of the fossil assemblage as a function of the depositional environment (Allison and Bottjer, 2010). The concept of 'taphofacies' was introduced by Brett and Baird (1986) who suggested that specific taphonomic trends could be attributed to different sedimentary facies. Principal taphofacies vary over a range of geological and geographical settings, but local and lateral inconsistencies can occur within a single environment or formation.

Wright et al. (2003) showed that dissimilar depositional conditions in a near-shore and off-shore carbonate ramp setting within the Early Jurassic of Wales controlled local acidic conditions via the supply of sediment and winnowing of organic matter. The extent of this taphonomic influence is also closely linked to the nature of fossil concentrations (Wright et al., 2003, Cherns et al., 2008) which Kidwell et al. (1986) ascribe to three main contexts: a. allochthonous – inconsistent with the original life habit owing to transportation and thus representative of the accumulation horizon, b. autochthonous – in life position with no evidence for post-mortem transportation, and c. parautochthonous – minor evidence for re-working or transportation but still moderately representative of the original setting.

1.1.2. The Taphonomically Active Zone

The taphonomic signature of fossil marine shelly communities is influenced by processes in the Taphonomically Active Zone or TAZ (e.g. Aller, 1982, Davies et al., 1989, Wright et al., 2003, Cherns et al., 2008, Cherns and Wright, 2009, Cherns et al., 2011; fig. 1.1). This variable realm of unspecified thickness and elevation is defined by environmental and geochemical conditions that promote carbonate dissolution (*sensu* Aller, 1982); it is positioned near to the sediment/sea water interface (e.g. Davies et al., 1989) and/or within the bio-irrigated, oxygenated upper sediment column (Aller, 1982). Within the TAZ, distortion of the molluscan assemblage is achieved via selective aragonite dissolution (Cherns and Wright, 2000, Nelson et al., 2003, Wright et al., 2003, Bush and Bambach, 2004, James et al., 2005, Knoerich and Mutti, 2006, Cherns et al., 2008, Jordan et al., 2015, Wright and Cherns, 2016) and referred to as the Missing Molluscs effect (Cherns et al., 2000, Wright et al., 2003).

Dissolution of shell aragonite is achieved via microbially induced acidity – a product of the aerobic decay of organic matter (e.g. Canfield and Raiswell, 1991a) and strengthened through bioturbational oxidation of hydrogen sulphide produced in the sulphate reduction zone (SRZ) (e.g. Aller, 1982, Canfield and Raiswell, 1991a, Sanders, 2003, Sanders, 2004) (see review by Cherns et al., 2008). Environmental conditions which affect residency time control the extent to which taphonomic processes distort the molluscan assemblage (Cherns et al., 2008). Within oxygenated bottom waters, dissolution is extensive since molluscan fauna are exposed to acidity in the TAZ during accumulation and early burial (Wright et al., 2003). Conversely, in anoxic conditions, dissolution is limited as the TAZ is elevated to within the water column enabling accumulation to occur below of its influence (Cherns et al., 2008).

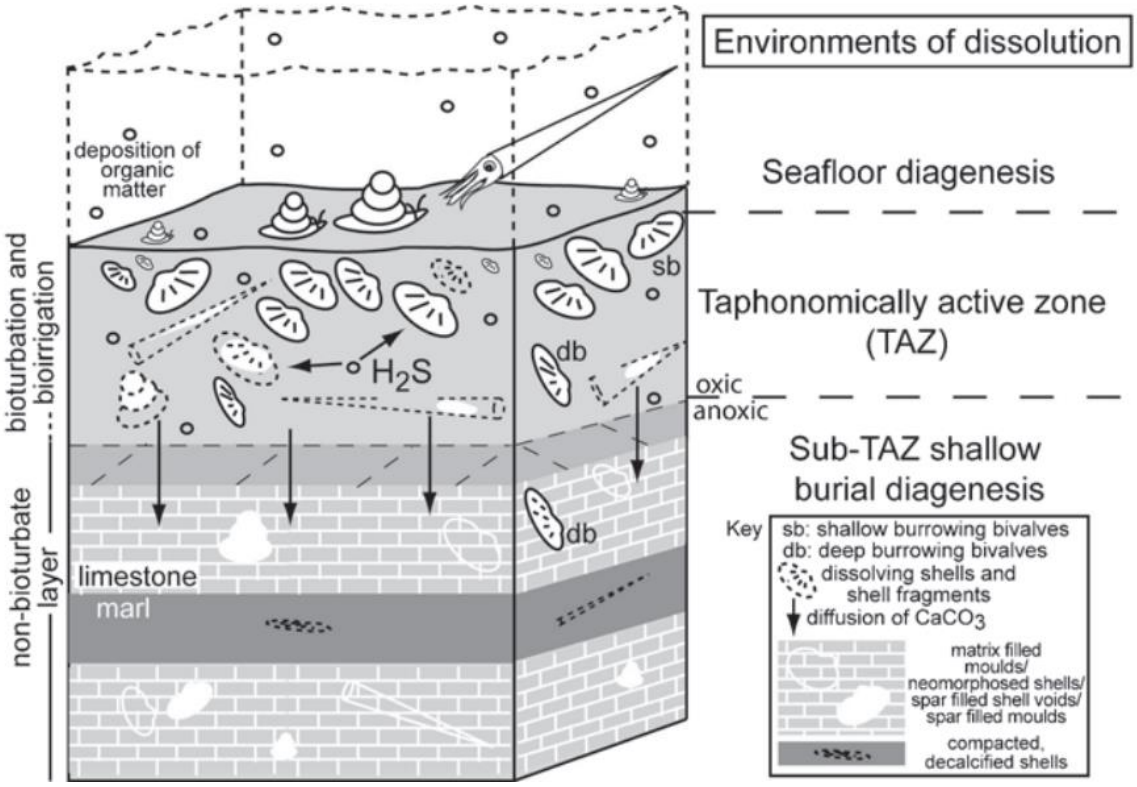

Figure 1.1 – An illustration by Cherns et al. (2011) of the Taphonomically Active Zone. Within the aerated upper sediment column, microbially induced acidity produced via the aerobic decomposition of organic matter and oxidation of H2S is responsible for dissolution of most of the aragonitic molluscan assemblage.

Selective dissolution of molluscan groups with an aragonitic shell mineral composition is a consequence of the varying solubility of different calcium carbonate polymorphs (Wright et al., 2003). Biogenic $CaCO_3$ has three natural polymorphs which, in order of decreasing solubility, include high-Mg calcite, aragonite, and low-Mg calcite (Canfield and Raiswell, 1991a, Foote et al., 2015). Distortion of the trophic structure is then enhanced through the consistency with which biomineralisation of specific groups is achieved; for example, gastropods are predisposed to aragonite secretion and therefore more vulnerable to dissolution than calcitic forms (e.g. Wright et al., 2003).

Cherns and Wright (2011) recognised that taphonomic distortion is also closely linked to the size of the shell; the authors suggest that small forms and micromolluscs, irrespective of biomineralisation, are vulnerable to dissolution in the TAZ (Cherns and Wright, 2011). Poorer representation of small individuals as a consequence of collecting bias may also contribute to their underrepresentation in many assemblages (Cherns and Wright, 2011). Taphonomic bias imposed by poor preservation potential and loss of micromolluscs was discussed in other settings by Cooper et al. (2006) and Foote et al. (2015).

1.1.3. Quantifying the Missing Molluscs effect

Selective dissolution of vulnerable shelly groups is evident in various geological and geographical settings (e.g. Walter and Burton, 1990, Brachert and Dullo, 2000, Cherns and Wright, 2000, Nelson and James, 2000, Wright et al., 2003, Bush and Bambach, 2004, James et al., 2005, Knoerich and Mutti, 2006, Cherns et al., 2008, Caron and Nelson, 2009, Cherns and Wright, 2009, Cherns et al., 2011, Hendy, 2011, Foote et al., 2015). Measuring the extent of this taphonomic influence is difficult and can only be achieved where comparison is possible with similar settings in which true ecological diversity is preserved by unique syn-sedimentary conditions or skeletal lagerstätte preservation (Cherns et al., 2008).

Initial description of the Missing Molluscs effect by Cherns and Wright (2000) was based on contrasting fossil assemblages in two comparable Wenlock (Lower Silurian) successions. In the typical calcitic fauna of Vattenfallet, the fossil assemblage was dominated by brachiopods (pedically-attached or recumbent epifauna) over bivalves and other molluscs (Cherns and Wright, 2000). In contrast, the silicified fauna of Möllbos preserved a more complete, diverse bivalve component (relative to the brachiopod groups) which accounts for 70 % of the total fossil assemblage (Cherns and Wright, 2000); more than 98 % of the preserved bivalves had a formerly aragonitic shell composition (Cherns and Wright, 2000). Given the environmental and sedimentological similarities between the two units, Cherns and Wright (2000) attributed differences in the respective Gotland fossil assemblages to selective dissolution of aragonitic groups within the TAZ.

Similar trends were observed in the Early Jurassic of South Wales, UK where rapid replacement by silica pre-dated selective dissolution within the TAZ (Wright et al., 2003). In the typical Liassic Porthkerry Formation, calcitic and bimineralic epifaunal bivalves (*Pinna, Plagiostoma,* and *Gryphaea*) were the dominant fauna (Wright et al., 2003). Examination of a similar assemblage excavated at the Ford Motor Company in Bridgend (Hodges, 1986, Hodges, 1991, Hodges, 2000) showed that silicification of the marine shelly palaeocommunity was responsible for a significant increase in the relative abundance and diversity of originally aragonitic molluscs (Wright et al., 2003); in this setting, formerly aragonitic groups account for 84 % of the total fossil assemblage (Wright et al., 2003). Calcitic and bimineralic molluscan fauna were evidently unaffected by selective dissolution and were similarly abundant in both successions (Wright et al., 2003).

Despite recognition of a widespread taphonomic process responsible for selective dissolution of originally aragonitic biota (e.g. Cherns and Wright, 2000, Wright et al., 2003), Kidwell (2005) showed that shell composition and consequent taphonomic biases had no effect on bivalve macroevolutionary biodiversity. This observation necessitates the survival of true ecological diversity throughout the Phanerozoic in settings termed 'taphonomic windows' (Cherns et al., 2008). Cherns et al. (2008) summarise this concept as the geochemical and sedimentological processes or conditions capable of preserving formerly aragonitic shells; they include storm beds, dysaerobic/anoxic environments, and early cementation/lithification.

According to Cherns et al. (2008), the storm bed taphonomic window is characterised by concentrations of epifauna and shallow infauna that have been transported within, and then deposited from, a suspended sediment package during high energy conditions (e.g. Kidwell and Brenchley, 1994, Li and Droser, 1999; fig. 1.2). The prolonged survival of vulnerable shelly groups is achieved via the winnowing of digestible organic matter which limits microbially induced acidity (Wright et al., 2003) and rapid burial that restricts residency time within the TAZ and enables alkalinity to develop in the SRZ (e.g. Canfield and Raiswell, 1991b) (see review by Cherns et al., 2008). Storm concentrations further inhibit selective dissolution by mediating acidity through the consumption of fragmented shells (e.g. Sanders, 2003, Sanders, 2004) (Cherns et al., 2008).

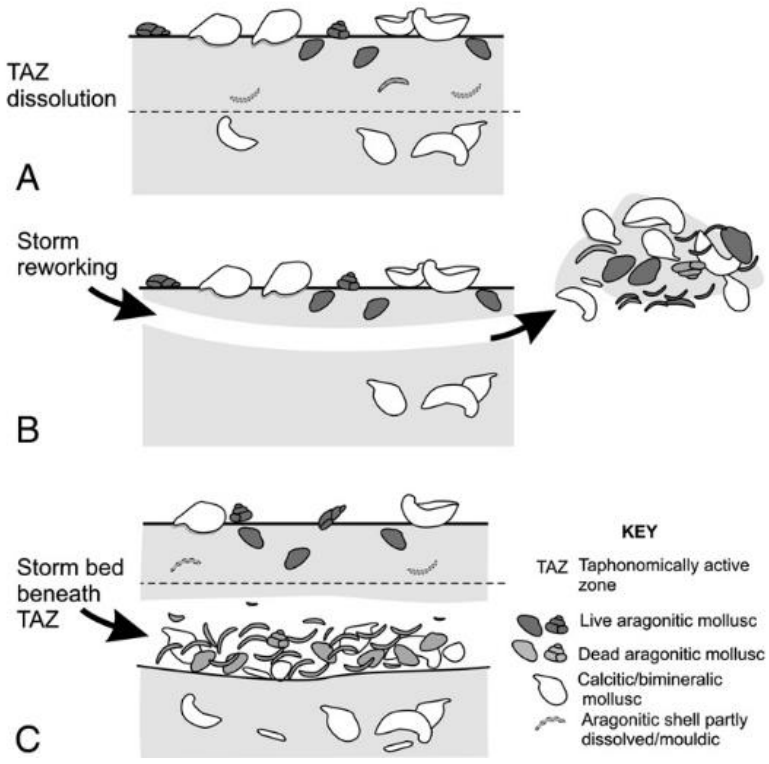

Figure 1.2 – An illustration by Cherns et al. (2008) of the mechanisms by which originally aragonitic fauna are preferntially preserved in the storm bed taphonomic window; A. typical conditions resulting in the selective dissolution of aragonitic shells within the TAZ, B. turbulent bottom waters remove organic matter and scour infauna and epifauna, and C. deposition beneath the acidic TAZ (Cherns et al., 2008).

The authors attributed shell beds in dysaerobic/anoxic environments to a number of potential causal factors including seasonal anoxia (e.g. Oschmann, 1988, Oschmann, 1991) and algal bloom events (e.g. Oschmann, 1991) (see review by Cherns et al., 2008). The survival of originally aragonitic fauna in this taphonomic window was the result of a limited residency time within the acidic TAZ following elevation of the redox boundary above the sediment surface (Cherns et al., 2008). In widespread reducing conditions, the lack of organic matter decay and bioturbation allows for the development of local alkalinity during bacterial sulphate reduction (BSR) (Canfield and Raiswell, 1991b, Sanders, 2003, Sanders, 2004, Hendry et al., 2006). Hudson (1982) also describes the potential for reducing micro-environments to develop within the organic-rich internal voids of mollusc shells beneath restricted bottom waters; this process may contribute to improved preservation potential of vulnerable groups through processes associated with syn-sedimentary pyritisation.

Based on predictions by James et al. (2005), Cherns et al. (2008) also discussed the potential for originally aragonitic fauna to be well represented where early cementation locked vulnerable shells into the sediment prior to dissolution. This model has been connected with the preservation of deep-burrowing aragonitic bivalves (e.g. Cherns and Wright, 2009, Cherns et al., 2011) and there is evidence to suggest it can protect from destructive processes in bioturbated sediments (Cherns et al., 2008). Originally aragonitic shelly groups are typically preserved as moulds or replaced shells (e.g. Palmer and Wilson, 2004, Palmer et al., 1988, Cherns et al., 2008).

1.1.4. Missing Molluscs in the Early Jurassic of Dorset and East Devon, UK

Based on previous studies of similar Early Jurassic offshore carbonate ramp settings in Wright et al. (2003) and Cherns and Wright (2009), taphonomic distortion associated with the Missing Molluscs effect is expected in the marine successions of Dorset and East Devon. However, contrary to predicted widespread selective dissolution of shell aragonite, formerly aragonitic groups occur at numerous horizons throughout the Blue Lias Formation (BLF) and basal Charmouth Mudstone Formation (CMF) (e.g. Cope and Sole,

2000, Curtis et al., 2000, Paul et al., 2008, Andrew et al., 2010, Lord et al., 2010, Pugh et al., 2014, Jordan et al., 2015, Weedon et al., 2018, Atkinson and Wignall, 2019).

Jordan et al. (2015) and Jordan (2016) tested the Missing Molluscs effect in Bed 29 (*sensu* Lang, 1924) of the BLF – a concentration lagerstätte containing abundant ammonoid fossils; the atypically high number of individuals was attributed to sedimentary condensation (Jordan et al., 2015, Jordan, 2016). According to the authors, selective dissolution of originally aragonitic shells was prevented via accumulation during anoxic intervals when acidic conditions within the TAZ were restricted (Jordan et al., 2015, Jordan, 2016); similar dysaerobic/anoxic environments were recognised for their potential to act as taphonomic windows by Cherns et al. (2008). Ammonoid preservation then required that burial and early carbonate cementation occurred prior to the re-establishment of oxygenated bottom waters in order to facilitate three-dimensional replacement by calcite spar (Jordan et al., 2015, Jordan, 2016); the return of oxic depositional conditions, coincident with acidity in the TAZ, resulted in the partial dissolution or un-roofing of ammonoid moulds (Jordan et al., 2015, Jordan, 2016). The potential for survival or loss of aragonitic groups dependant on fluctuating and/or unstable local oxygen conditions is an important consideration for taphonomic biases throughout the Early Jurassic of Dorset and East Devon. An alternative model for ammonoid preservation in the BLF was recently proposed by Weedon et al. (2018) in which rapid burial followed by storm-related non-deposition promoted early cementation and limestone formation prior to shell aragonite dissolution.

1.1.5. Summary

Taphonomic distortion of the fossil marine shelly community by processes associated with the Missing Molluscs effect must be examined prior to considering palaeoecological, sedimentological, and palaeoenvironmental interpretations throughout geological time. As a result, there is a real need to review biases associated with the fossilisation of molluscan fauna and of assemblages which were previously assumed to be representative. Cherns et al. (2008) emphasise the use of taphonomic windows as a means to recognise distortion via the selective dissolution of vulnerable (aragonitic and high-Mg calcitic) groups.

1.2. Sedimentary pyritisation and fossil preservation

Pyritisation of fossils is recorded throughout the Phanerozoic in a range of different geological and geographical settings (e.g. Cooper, 1977, Hudson, 1982, Fisher, 1986, Babcock and Speyer, 1987, Briggs et al., 1991, Briggs and Edgecombe, 1993, Grimes et al., 2002, Bölücek and Ilhan, 2006). It is a particularly common phenomenon within Jurassic marine mudrocks associated with the fossilisation of molluscan fauna (e.g. Hudson, 1982, Fisher and Hudson, 1985, Fisher, 1986, Andrew et al., 2011, Paul, 2011).

1.2.1. Sedimentary pyrite formation

Reactions. The formation of pyrite requires BSR (Berner, 1970, Berner, 1984, Berner, 1985). This process, the biological reduction of sulphate by bacteria utilising organic matter as an energy source (Berner, 1970, Berner, 1984), is expressed by equation 1 (Coleman and Raiswell, 1995). Alternatively, sulphate reduction may be considered with regards to its main metabolic products (eq. 2; Fisher, 1986).

$$1.\ 2CH_2O + SO_4^{2-} = 2HCO_3^- + H_2S$$

$$2.\ 2CH_2O + SO_4^{2-} = S^{2-} + 2CO_2 + 2H_2O$$

In reducing conditions, hydrogen sulphide (H_2S) reacts with ferrous iron or iron-bearing mineral phases to produce an iron monosulphide (Berner, 1970), the precursor to pyrite (Berner, 1970, Berner, 1984, Fisher and Hudson, 1987). In Fisher and Hudson (1987), this reaction is modelled with the oxidised iron compound goethite (eq. 3).

$$3.\ 3H_2S + 2FeO.OH = 2FeS + S^0 + 4H_2O$$

A final reaction between iron monosulphides (e.g. mackinawite) and elemental sulphur results in the formation of pyrite (eq. 4; Berner, 1970, Fisher and Hudson, 1987).

$$4.\ FeS + S^0 = FeS_2$$

Components. The formation of sedimentary pyrite requires several key components, these are: sulphate reducing bacteria, organic matter, sulphate, and iron (e.g. Berner, 1970, Fisher and Hudson, 1987). Previous studies have identified the nature and source of each component within the marine setting (e.g. Berner, 1970, Berner, 1985, Fisher and Hudson, 1987).

- *sulphate reducing bacteria* – bacterial reduction of sulphate to hydrogen sulphide is achieved by anaerobic microbes that occupy the SRZ or reducing micro-

environments within closed voids and at concentrations of organic matter (e.g. Hudson, 1982, Fisher and Hudson, 1987).

- *digestible organic matter* – organic matter is the main source of energy and a reducing agent for BSR (Berner, 1970).
- *sulphate* – the process of BSR requires sulphate supplied from the overlying water column (Berner, 1970, Fisher and Hudson, 1987). Previous studies have identified that in anoxic conditions, sulphate is sourced by direct contact with seawater (Fisher and Hudson, 1987); in oxic conditions, it is sourced by diffusion, sediment mixing, and bioturbation (Fisher and Hudson, 1987).
- *iron* – the formation of pyrite requires H_2S to react with iron; the latter is sourced from oxidised iron compounds or iron-bearing mineral phases delivered via sediment transport (Fisher and Hudson, 1987).

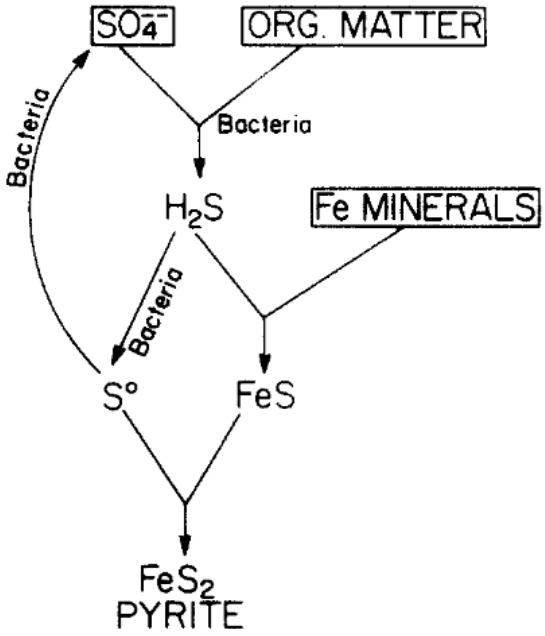

Figure 1.3 – Illustration of the sedimentary pyrite formation process by Berner (1985) including the main reactants (after Berner, 1972).

BSR and pyrite precipitation cease as either organic matter, sulphate, or iron becomes a limiting factor (Raiswell et al., 1988, Raiswell et al., 2018). Widespread bottom water anoxia is not a pre-requisite for sedimentary pyritisation (Kaplan et al., 1963, Hudson and Palframan, 1968, Hudson, 1982, Fisher, 1986, Fisher and Hudson, 1987) since local reducing micro-environments can facilitate pyrite precipitation in closed voids – important for fossilisation – or associated with organic matter such as faecal pellets (Hudson, 1982,

Fisher and Hudson, 1987). Pyrite fossil replacement is known from sediments that contain trace fossils and benthic fauna (Hudson, 1982); modern environments near the coast of Southern California (e.g. Kaplan et al., 1963, Goldhaber and Kaplan, 1974) also contain pyrite in various oxygen conditions (Hudson, 1982).

Previous authors have identified the limiting factors for pyrite formation in different sedimentary settings (e.g. Berner, 1970, Berner, 1984, Berner, 1985, Raiswell et al., 1988, Raiswell et al., 2018). Beneath oxygenated bottom waters, pyrite formation in the anoxic sediment column is limited by the availability of organic matter (Berner, 1970, Berner, 1984, Berner, 1985, Raiswell et al., 1988, Raiswell et al., 2018), in part as a consequence of aerobic consumption at the bioturbated sediment surface (Berner, 1985, Fisher and Hudson, 1987). In contrast, beneath euxinic bottom waters, pyritisation is driven by the widespread availability of sulphate from the overlying seawater as well as the improved potential for organic matter to survive into the SRZ so iron is the limiting factor (Berner, 1970, Berner, 1984, Berner, 1985, Raiswell and Berner, 1985, Raiswell et al., 1988, Raiswell et al., 2018). For the purposes of this study, sulphate is not considered a potential limiting factor due to its availability in the water column; sulphate does however limit pyrite formation beneath freshwater (Berner, 1984, Berner, 1985, Raiswell et al., 2018).

Sedimentary pyrite formation has the potential to influence precipitation or dissolution of carbonate when considered with respect to relative iron availability or limitation (Coleman, 1985, Fisher, 1986, Coleman and Raiswell, 1995). Fisher (1986) states that iron limitation during BSR can result in the loss of H_2S or HS^- via diffusion, following hydrolysation of S^{2-} and liberation of hydroxyl ions, thus facilitating the precipitation of calcium carbonate (eqs. 5, 6, and 7; Fisher, 1986).

$$5.\ S^{2-} + H_2O = HS^- + OH^-$$

$$6.\ HS^- + H_2O = H_2S + OH^-$$

$$7.\ CO_2 + 2OH^- + Ca^{2+} = CaCO_3 + H_2O$$

In contrast, where iron is available during BSR, dissolution of calcium carbonate is achieved (eqs. 8 and 9; Fisher, 1986).

$$8.\ Fe^{2+} + SO_4^{2-} + 2CH_2O = FeS + 2HCO_3^- + 2H^+$$

$$9.\ 2H^+ + 2CaCO_3 = 2Ca^{2+} + 2HCO_3^-$$

The consequences of differential iron availability, specifically the resultant precipitation or dissolution of calcium carbonate, is an important taphonomic control when considering the pyritic replacement of molluscan fauna (see review by Fisher, 1986).

1.2.2. Iron Palaeoredox Proxies

Many geochemical techniques exist to reconstruct redox conditions within ancient marine environments and explore its effect on fossil preservation; these are typically contrasted with modern, analogous sediments in order to establish parameters for predicted conditions (see review by Raiswell et al., 2018). Previous studies have advised that analyses are used in association with palaeoecological, geochemical, and sedimentological data as a means to corroborate interpretations (Raiswell et al., 2018).

Degree of Pyritisation. The Degree of Pyritisation (DOP), defined by Berner (1970), was the foundation for several subsequent iron palaeoredox proxies. It was introduced as a means to investigate iron limitation associated with the formation of sedimentary pyrite (Berner, 1970, see review by Raiswell et al., 2018). Berner (1970) determined DOP as:

$$\text{DOP} = \text{Pyrite Fe}/(\text{Pyrite Fe} + \text{HCl soluble Fe}$$

In early studies (e.g. Berner, 1970, Raiswell et al., 1988), HCl soluble iron was taken to represent the iron-bearing mineral phases that could react with hydrogen sulphide, on a diagenetic time-scale, to form pyrite (Raiswell et al., 2018); it was measured using the HCl extraction method of Berner (1970). Raiswell et al. (1988) expanded the use of DOP on the basis that if iron was the constant limiting factor for pyrite formation beneath euxinic bottom waters, and other factors became limiting before iron in normal marine settings, then iron limitation could be applied as a proxy for euxinia and the extent to which HCl soluble iron has been converted to pyrite (i.e. DOP) used thereafter to determine the degree of bottom water oxygenation (Raiswell et al., 1988, see review by Raiswell et al., 2018). Higher DOP values were regarded as the product of a more complete conversion of iron to pyrite where exposure to hydrogen sulphide was greatest i.e. beneath euxinic bottom waters (Raiswell et al., 1988, Raiswell et al., 2018). Parameters for the use of DOP to identify aerobic, restricted, and inhospitable bottom waters were given by Raiswell et al. (1988).

It was later shown that not all iron-bearing mineral phases are equally reactive to sulphide (e.g. Canfield, 1989, Canfield et al., 1992, Raiswell and Canfield, 1996). The HCl extraction method had the capacity to dissolve poorly-reactive or unreactive iron minerals

such as sheet silicates (Canfield et al., 1992, Raiswell et al., 1994, Canfield et al., 1996, Raiswell and Canfield, 1996) and was therefore an unreliable account of the true reactive iron pool (see review by Raiswell et al., 2018). Moreover, because these poorly-reactive or unreactive iron-bearing mineral phases were unlikely to form pyrite (e.g. Canfield et al., 1992), it was concluded that the high DOP values recorded in euxinic conditions were inconsistent with the original mechanism proposed by Raiswell et al. (1988) and were actually the product of an enriched highly reactive iron pool (Canfield et al., 1996) (see review by Raiswell et al., 2018). Despite revisions to the method and its interpretation, Raiswell et al. (2018) still regard DOP as an effective way of investigating bottom water oxygen conditions in their comprehensive review of the iron palaeoredox proxies.

Iron speciation. The Indicator of Anoxicity (IoA) (*sensu* Raiswell et al., 2001), or the ratio of highly reactive iron (Fe_{HR}) to total iron (Fe_T) (Fe_{HR}/Fe_T), is used to reconstruct bottom water redox conditions in modern and ancient marine settings (Raiswell and Canfield, 1998, Raiswell et al., 2001, Poulton and Raiswell, 2002, Lyons and Severmann, 2006, Poulton and Canfield, 2011, Clarkson et al., 2014, Raiswell et al., 2018). The method's development followed previous advancements in the quantification of Fe_{HR} that addressed the non-uniform reactivity of different iron-bearing mineral phases (e.g. Canfield, 1989, Canfield et al., 1992, Raiswell and Canfield, 1996) and established that high DOP values were the product of Fe_{HR} enrichment beneath anoxic/euxinic bottom waters (e.g. Canfield et al., 1996, Raiswell and Canfield, 1998) (see review by Raiswell et al., 2018).

Detrital iron-bearing minerals can be separated depending on their relative reactivity with hydrogen sulphide (Fe_{HR}, $Fe_{Unreactive}$ or Fe_U, and $Fe_{PoorlyReactive}$ or Fe_{PR}) (Canfield et al., 1992, Raiswell and Canfield, 1996, Raiswell and Canfield, 1998, Raiswell et al., 2001, Poulton and Raiswell, 2002, Poulton and Canfield, 2005, Lyons and Severmann, 2006, Raiswell et al., 2018); accurate quantification of the different iron pools was furthered by the development of a sequential extraction procedure by Poulton and Canfield (2005). Raiswell and Canfield (1998) demonstrated that a finite fraction of reactive iron, within the total iron pool (Fe_T), can form pyrite in anoxic sediments beneath oxic or poorly-oxygenated bottom waters (Fe_{HR}/Fe_T = 0.4 *sensu* Raiswell et al., 2001; 0.38 *sensu* Raiswell and Canfield, 1998). In anoxic/euxinic conditions, Fe_{HR}/Fe_T ratios are greater than this threshold and indicate disassociation of the reactive iron pool from the lithogenous supply (Canfield et al., 1996, Raiswell and Canfield, 1998, Raiswell et al., 2001). High Fe_{HR}/Fe_T ratios, factoring in the poorly-reactive or unreactive nature of different iron-bearing

mineral phases such as sheet silicates (e.g. Canfield et al., 1992, Raiswell and Canfield, 1996), requires the enrichment of Fe_{HR} (Canfield et al., 1996, Raiswell and Canfield, 1998, Raiswell et al., 2001). Within these parameters, the extent of anoxic Fe_{HR} enrichment (Fe_{HR}/Fe_T) can be used to determine the degree of bottom water oxygenation (e.g. Raiswell and Canfield, 1998, Raiswell et al., 2001, Poulton and Raiswell, 2002, Canfield et al., 2008, Clarkson et al., 2014, see review by Raiswell et al., 2018).

Previous studies indicate that a principal source of Fe_{HR} enrichment is via intra-basinal mobilisation of reduced iron from the oxic shelf (e.g. Wijsman et al., 2001, Anderson and Raiswell, 2004, Lyons and Severmann, 2006, Severmann et al., 2008, Clarkson et al., 2014, Raiswell et al., 2018). In euxinic conditions, mobilised iron reacts with dissolved sulphide and forms pyrite (within the water column) that settles in the sediment and enriches the Fe_{HR} pool (Raiswell and Canfield, 1998, Wijsman et al., 2001, Lyons and Severmann, 2006, Severmann et al., 2008, Raiswell et al., 2018); in non-sulphidic (ferruginous) conditions, mobilised iron is precipitated as unsulphidised minerals such as $Fe_{Oxyhydroxides}$ or $Fe_{Carbonates}$ (Poulton and Canfield, 2011). The Fe_{HR}/Fe_T ratio is unable to differentiate between ferruginous or euxinic anoxic conditions (FeII-rich and sulphide-rich respectively) but the sulphidic state can be determined using the Fe_{Pyrite}/Fe_{HR} ratio (*sensu* Poulton et al., 2004); this method measures the extent to which highly reactive iron-bearing mineral phases have been converted to pyrite (Poulton et al., 2004, Canfield et al., 2008, Poulton and Canfield, 2011, Raiswell et al., 2018).

1.2.3. Summary

Exploring the origin of pyrite replacement and its role in the survival of vulnerable shelly fauna has the potential to enhance our understanding of palaeoecological, palaeoenvironmental, and taphonomic controls associated with the Missing Molluscs effect (*sensu* Cherns and Wright, 2000). Moreover, syn-sedimentary pyritisation could have acted as a taphonomic window (*sensu* Cherns et al., 2008), and may preserve a truer representation of ecological skeletal diversity and abundance.

Iron speciation provides an accessible method to reconstruct specific palaeoenvironmental conditions associated with the pyritic replacement of fossils. In a broader sense, it could be used to measure the degree of bottom water oxygenation for different (pre-diagenetic) lithologies in limestone-marl alternations, which could then be correlated with palaeoecological and taphonomic trends. There is a practical benefit in applying the

technique to a fossiliferous succession in that iron palaeoredox proxies can be contrasted with palaeontological data to test their validity.

1.3. Geological setting and stratigraphy

Famed for the quality and quantity of fossils they continue to yield, the classic British Jurassic marine successions include the Blue Lias and Kimmeridge Clay of Dorset, the Jet Rock of Yorkshire, and the Blue Lias of the Glamorgan Coast. These strata show major variation in primary depositional process, sedimentology, and lithology as well as secondary, diagenetic history. This study concentrates on the Early Jurassic successions of Dorset and East Devon, part of the Jurassic Coast World Heritage Site.

1.3.1. The Late Triassic-Early Jurassic strata of Dorset and East Devon, UK

The Late Triassic-Early Jurassic marine strata exposed on the Dorset and East Devon coastline are a part of the larger Wessex Basin (*sensu* Kent, 1949). This sedimentary depocentre is comprised of a near-complete succession of Late Palaeozoic – Cenozoic strata (Lake and Karner, 1987) (fig. 1.4). The Late Triassic-Early Jurassic lithostratigraphy in this study follows Hesselbo et al. (2004), based on Warrington et al. (1980) (fig. 1.5). The exact position of the Triassic-Jurassic boundary was, up until recently, undefined (Hesselbo et al., 2004, Barras and Twitchett, 2007); some of the different positions inferred by previous studies across SW Britain (e.g. George et al., 1969, Orbell, 1973, Poole, 1979, Cope et al., 1980, Poole, 1980, Hallam, 1990, Poole and Cope, 1991, Warrington et al., 1994, Hesselbo et al., 2002) were summarised by Hesselbo et al. (2004) (fig. 1.5). Recent definition of the T-J boundary (Hillebrandt et al., 2007, Hillebrandt et al., 2013) has allowed for correlation of its position in SW Britain above the base of the BLF (e.g. Clémence et al., 2010, Mander et al., 2013) (fig. 1.5).

A key palaeontological and palaeoenvironmental control on the Early Jurassic strata of the Wessex Basin was the Triassic-Jurassic extinction event; again, its exact timing is debated (see review by Hesselbo et al., 2004) but it is generally thought to have occurred within the Cotham Member of the Lilstock Formation (Hesselbo et al., 2004, Wignall and Bond, 2008, Atkinson and Wignall, 2019) (fig. 1.5). Hallam (2002) suggests that this would have manifested as a prolonged Late Triassic extinction as opposed to a single catastrophic event. It has been inferred by previous studies that the T-J extinction was likely associated with flood-basalt volcanism in the Central Atlantic Magmatic Province (fig. 1.6) that

produced major environmental changes (Marzoli et al., 1999, Hames et al., 2000, Pálfy et al., 2001, Wignall, 2001a, Hesselbo et al., 2002, Pálfy et al., 2002, Pálfy, 2003, Hesselbo et al., 2004, Marzoli et al., 2004, Pugh et al., 2014). The consequences of volcanism potentially included major sea-level fluctuations (e.g. Hallam and Wignall, 1999, Hallam, 2002, Hesselbo et al., 2004), the release of volcanic gases (McElwain et al., 1999, Hames et al., 2000, Hesselbo et al., 2002, Hesselbo et al., 2004, Pugh et al., 2014), liberation of methane gas hydrates (Marzoli et al., 1999, Hesselbo et al., 2002, Hesselbo et al., 2004), and bottom water anoxia, all of which could contribute to a negative ecological impact.

In SW Britain, the earliest Jurassic strata occur within the basal part of the BLF (Clémence et al., 2010, Mander et al., 2013, Pugh et al., 2014, Weedon et al., 2018, Weedon et al., 2019) (fig. 1.5); however, since this study is based on a lithostratigraphic account that coincides with the limestone-marl alternations of the BLF, the base of the sampled section does not correlate with the T-J extinction event nor the T-J boundary. The base of the BLF is shared with the Langport Member or White Lias Formation (*sensu* Gallois, 2008b) (fig. 1.5) and is taken at the top surface of a local, coarse conglomerate in Pinhay Bay, Devon (Wignall, 2001b, Hesselbo et al., 2004, Gallois, 2008b, Atkinson and Wignall, 2019) or, more generally, at the erosive upper surface of the Sun Bed which contains common *Diplocraterion* burrows (Wignall, 2001b, Hesselbo et al., 2004, Gallois, 2008b); the nature of this boundary is laterally variable and described in detail by Wignall (2001b).

The BLF is an exclusively marine succession; the organic-rich paper shales at its base have been attributed to initial deposition beneath anoxic bottom waters (Wignall, 2001b, Barras and Twitchett, 2007) but this lithology was replaced over a short vertical distance by regular limestone-marl repetitions (e.g. Lang, 1924). Previous studies have inferred that lithological alternations represent cyclic changes in the degree of bottom water oxygenation; carbonate-rich lithologies (light marls and bioturbated limestones) represent well-oxygenated bottom waters whilst laminated, organic-rich lithologies (paper shales, shales, and laminated limestones) represent dysaerobic/anoxic conditions (Weedon, 1986, Bottrell and Raiswell, 1989, Moghadam and Paul, 2000, Hesselbo et al., 2004, Mander et al., 2008, Paul et al., 2008, Weedon et al., 2018). Numerous authors have inferred this trend to be the product of Milankovitch cyclicity (e.g. House, 1985, Weedon, 1986, Waterhouse, 1999, Weedon et al., 1999, Moghadam and Paul, 2000, Paul et al., 2008, Ruhl et al., 2010, Weedon et al., 2019). The alternating nature of the BLF is consistent throughout the succession although the relative proportion of limestone beds decreases in

the *Liassicus* Chronozone (Weedon et al., 2018) and towards the top of the section; Weedon et al. (2018) state that, in the former, this phenomenon is the result of temporary sea level rise. The upper boundary of the BLF is taken at the erosive upper surface of the laterally persistent bioturbated limestone bed, Grey Ledge (Hallam and Lang, 1960, Gallois, 2008a).

The CMF is another exclusively marine succession; the boundary between the BLF and overlying CMF is marked by a significant decrease in the relative proportion of limestone beds (Gallois, 2008a) and a lack of regular limestone-marl alternations (Paul et al., 2008). This study focuses on the basal CMF, specifically the SWB and BVM. The SWB and BVM are without extensive lithological variation and are generally dominated by argillaceous marine mudrocks with rare diagenetic limestone beds (e.g. Lang et al., 1923, Lang and Spath, 1926); previous studies have inferred a depositional environment within increasingly restricted oxygen conditions and/or temporary anoxia (Rukin, 1990), probably associated with deeper waters as evidenced by the paucity of bioturbated limestone beds.

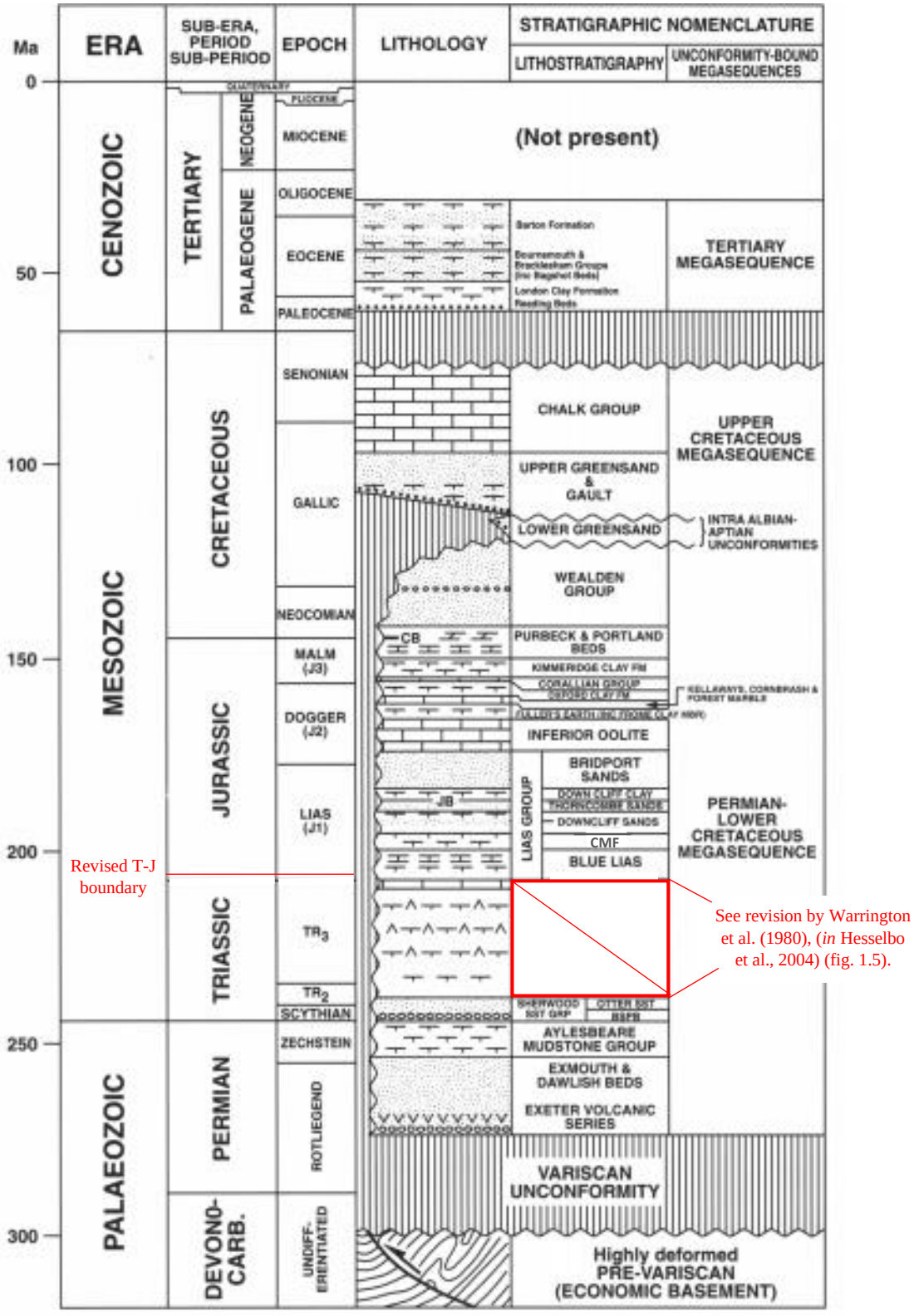

Figure 1.4 – Stratigraphy of the Wessex Basin edited from Underhill and Stoneley (1998). The Late Triassic-Early Jurassic lithostratigraphy has since been revised and now follows Warrington et al. (1980), (*in* Hesselbo et al., 2004) (fig. 1.5). Placement of the T-J boundary has been correlated to the lower part of the BLF (e.g. Clémence et al., 2010, Mander et al., 2013, Pugh et al., 2014, Weedon et al., 2018, Weedon et al., 2019) (fig. 1.5).

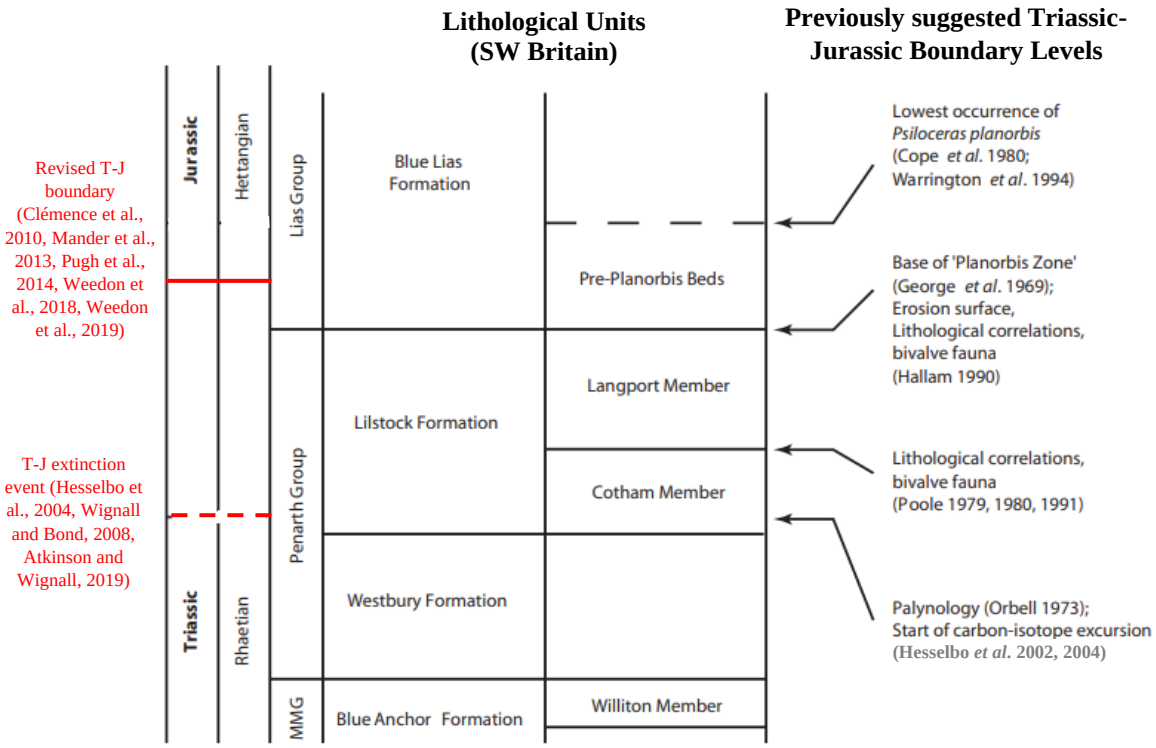

Figure 1.5 – Stratigraphy of the Late Triassic-Early Jurassic section in SW Britain from Hesselbo et al. (2004), based on Warrington et al. (1980). Hesselbo et al. (2004) summarised the T-J boundaries suggested by previous studies on the right. Definition of the T-J boundary has since been correlated to the lower part of the BLF (Clémence et al., 2010, Mander et al., 2013); the T-J extinction event is positioned within the Cotham Member (Hesselbo et al., 2004, Wignall and Bond, 2008, Atkinson and Wignall, 2019).

1.3.2. Palaeogeography of Britain in the Early Jurassic

In the Early Jurassic, Britain was an epi-continental marine realm located in the Tethys Sea approximately 30 – 35 degrees north of the equator (Lord et al., 2010, Jordan et al., 2015) (fig. 1.6). Warm shallow seas meant that life flourished, evidenced by an abundant marine fossil record preserved in both the BLF and CMF (e.g. Duffin, 1981, McGowan, 1993, Donovan, 2006, Paul et al., 2008, Andrew et al., 2011, Bennett et al., 2012).

Small archipelagic island chains populated the Tethys and were likely positioned at the Cornubian Massif and Mendip Hill areas (Rukin, 1990). These islands were subject to episodic storm and/or flood events (Lord et al., 2010) so whilst the Lower Lias is exclusively marine, it does contain a rich and diverse terrestrial biota. The most common land-based fossils are fragments of lignite or plant remains, specifically conifers with rare cycads and horsetails (Lord et al., 2010). Occasional insect fossils (e.g. Soszyńska-Maj et al., 2016, Kelly et al., 2017, Tihelka, 2019) were likely transported via woody detritus (Soszyńska-Maj et al., 2016). Dinosaur remains, specifically *Scelidosaurus harrisonii* (e.g.

Newman, 1968, Martill et al., 2000, Norman, 2001), are rare but these too indicate the proximity of diverse terrestrial ecosystems.

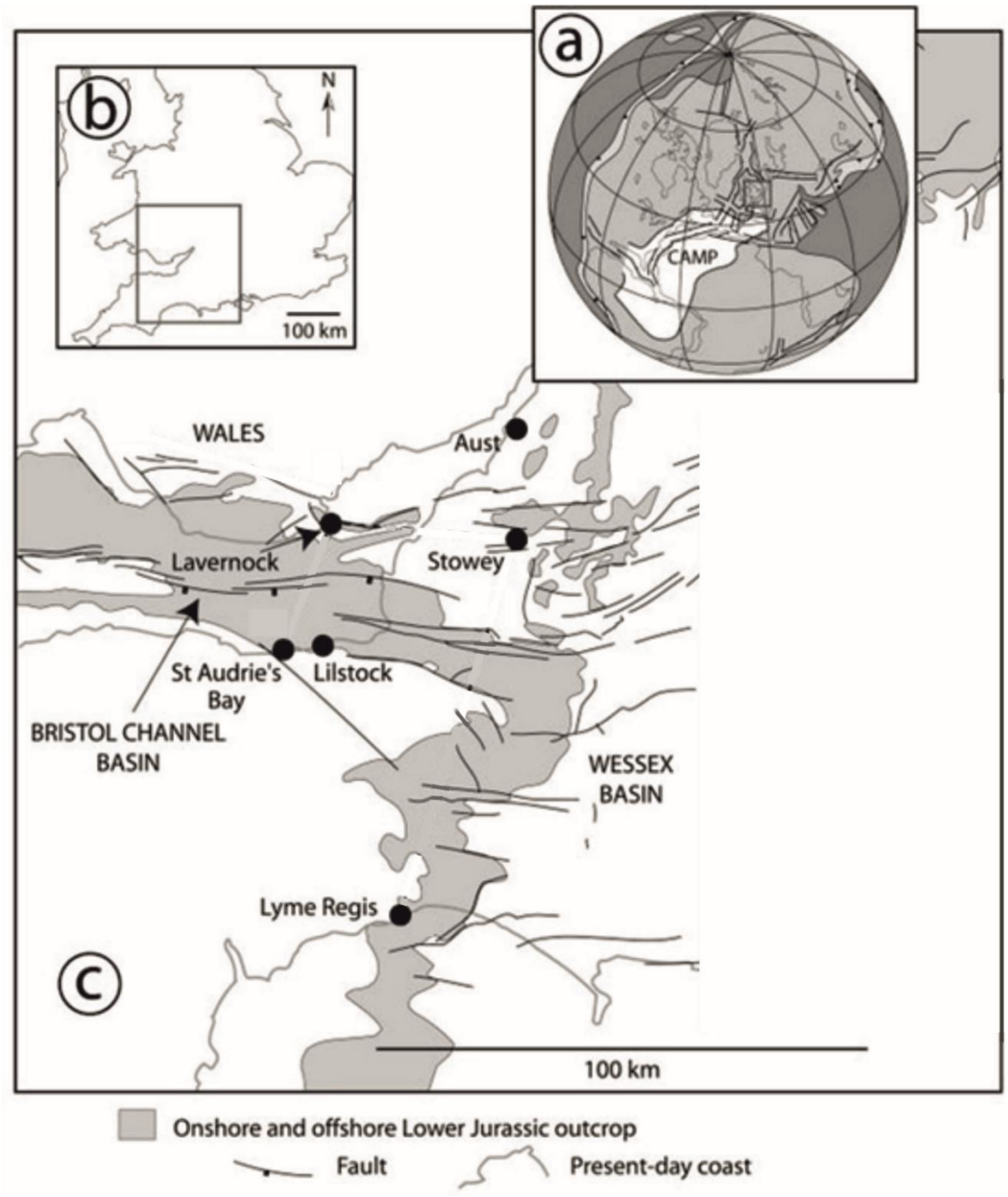

Figure 1.6 – Figure edited from Hesselbo et al. (2004) and references therein. a. Palaeogeography of the Triassic-Jurassic boundary (from Hesselbo et al., 2004; after Ziegler, 1990; position of CAMP after McHone, 2000), b. geographical position of exposures in SW Britain, c. position of Triassic-Jurassic exposures in SW Britain.

1.4. Main research questions

1. To what extent does syn-sedimentary pyritisation contribute to the preservation of true ecological molluscan abundance and diversity, and can this be considered a taphonomic window?

In order to understand the preservation potential of processes associated with syn-sedimentary pyritisation, the replacement pathway will be reconstructed and used to infer the relative timing of pyrite precipitation, local and widespread oxygen conditions, the origin of reactants, and position relative to the SRZ. This study will then investigate how each of these factors can promote or prevent known taphonomic biases associated with the Missing Molluscs effect. The potential for syn-sedimentary pyritisation to preserve true ecological abundance and diversity will be explored by contrasting the pyritic assemblage with the typical, lithology-specific fossil assemblage as well as other taphonomic window fauna from similar settings.

2. To what extent are marked variations in the preservation and composition of the shelly fossil assemblage a consequence of taphonomic processes associated with the Missing Molluscs effect and how is this influenced by environmental and diagenetic factors?

Using data collected from the BLF, variations in the preservation and composition of the shelly fossil assemblage will be quantified for each lithology in the Early Jurassic of Dorset and East Devon. By qualifying the difference between a predicted faunal assemblage – based on observations of an early silicified fauna in Wright et al. (2003) – and the typical fossil assemblage, taphonomic distortion can be estimated as a function of lithology as well as for the principal states of bottom water oxygenation. Comparison with taphonomic windows from similar settings – including syn-sedimentary pyritisation – will help to test the unique preservation potential of such features and examine whether this factor varies in different sedimentary settings.

3. To what extent can iron palaeoredox proxies be used to reconstruct palaeoenvironmental conditions in the Early Jurassic of Dorset and East Devon?

Using complimentary palaeontological and sedimentological data, this study will explore whether Fe_{HR}/Fe_T and Fe_{Py}/Fe_{HR} ratios can be used to determine bottom water redox conditions in the BLF of Dorset and East Devon. Based on these results, it will be possible

to assess the use of iron palaeoredox proxies to reconstruct palaeoenvironmental conditions in such settings and identify small-scale fluctuations, on a bed-by-bed basis, in lithologically variable successions. This investigation will subsequently help to interpret how palaeoenvironmental conditions, particularly the bottom water redox state, influenced palaeoecological and taphonomic controls on the fossil marine shelly community.

1.5. Thesis outline

Chapter 2 is a revised lithostratigraphic account of the BLF and basal CMF (Early Jurassic) in Dorset and East Devon. This work will be used to co-ordinate geochemical, palaeontological, and taphonomic investigations later in the thesis. Re-evaluation of historic accounts (e.g. Lang et al., 1923, Lang, 1924, Lang and Spath, 1926, Weedon, 1987) is necessary to provide an accurate representation of the current exposure and ensure consistency with the sampling programme used throughout. The section is subdivided to group lithologically similar units and capture general trends without many minor bed divisions. This chapter introduces key fossiliferous horizons that will be discussed later in the thesis including particular reference to their origin, sedimentology, and inter-sectional variability.

Chapter 3 provides a high-resolution palaeoecological study of the BLF in Dorset and East Devon. The main component of this work is a field-based examination and quantification of the macrofaunal fossil assemblage for the majority of individual beds identified in the revised lithostratigraphic log. Using supplementary data regarding the abundance and diversity of ichnotaxa in Barras and Twitchett (2007) and Jordan (2016), this chapter explores the use of shelly fauna as a means to reconstruct the response of macrobenthos to palaeoenvironmental conditions in the Early Jurassic and investigates the impact of small-scale fluctuations in the dominant redox state on the shelly palaeocommunity. The influence of taphonomic controls associated with the Missing Molluscs effect will be introduced within this chapter before further examination later in the thesis.

Chapter 4 explores the potential for iron palaeoredox proxies, specifically the Fe_{HR}/Fe_T and Fe_{Py}/Fe_{HR} ratios, to characterise bottom water redox conditions in the Early Jurassic of Dorset and East Devon. Iron speciation focuses on the BLF and a regular sampling protocol will be used to identify small-scale fluctuations that correlate with lithological alternations as well as large-scale temporal changes in the dominant redox state. By

grouping Fe_{HR}/Fe_T data into revised lithological classifications, the relationship between lithology and depositional environment can be tested.

Following investigations to establish palaeoecological and palaeoenvironmental trends throughout the Early Jurassic of Dorset and East Devon, Chapter 5 reviews the nature of pyrite fossil replacement in the marine mudrocks of the CMF. A diverse assemblage of pyritised ammonoid moulds is used to reconstruct the pyrite replacement pathway and identify how specific processes associated with BSR and pyrite precipitation contribute to the preservation of originally aragonitic fauna by preventing selective dissolution within the TAZ. The potential for syn-sedimentary pyritisation to act as a taphonomic window is discussed later in the thesis.

Chapter 6 addresses the atypical survival of unaltered shell aragonite approximating soft tissue attachment areas in ammonoid moulds from the CMF of Dorset. The distribution and morphology of these veneers is examined across multiple genera in order to ascertain their structural origin and identify specific muscle scar groups with respect to existing classifications. This chapter reconstructs the unique syn-sedimentary conditions required to preserve original aragonite and considers the wider implications of this phenomenon for taphonomic biases associated with the Missing Molluscs effect.

Chapter 7 explores the influence of taphonomic biases associated with the Missing Molluscs effect in lithology-specific fossil assemblages from the Early Jurassic of Dorset and East Devon. The chapter combines palaeoenvironmental and palaeoecological data from the BLF to qualify taphonomic distortion – measured as the difference between the predicted faunal assemblage and the typical fossil assemblage – as a function of different states of bottom water oxygenation. The differential preservation potential of taphonomic windows is also considered. This study provides the basis for a developmental model to estimate the extent of taphonomic distortion associated with the Missing Molluscs effect in global Jurassic marine mudrocks, either as a function of lithology or based on the inferred depositional environment.

Chapter 8 integrates the individual elements of the thesis in order to address the main research questions outlined in Section 1.4. The implications of this investigation for our understanding of taphonomic processes in the Early Jurassic of Dorset and East Devon are summarised. A final consideration is given to the direction of future research.

CHAPTER 2

2. LITHOSTRATIGRAPHY OF THE EARLY JURASSIC SUCCESSIONS IN DORSET AND EAST DEVON (BLUE LIAS AND BASAL CHARMOUTH MUDSTONE FORMATIONS), UK

2.1. Introduction

Initial examination of the Early Jurassic stratigraphy around Dorset and East Devon in South England was undertaken by eminent early geologists (e.g. De la Beche, 1822, De la Beche, 1826, Wright, 1860, Woodward, 1893, Woodward and Ussher, 1911). Formative review of the lithostratigraphy of the BLF was later completed by Lang (1924) and subsequently revised by Weedon (1987) and Jordan (2016). The overlying CMF was subdivided by Cox et al. (1999), in ascending stratigraphic order, to the SWB, BVM, BM, and GA members. An additional subdivision of the BVM was recommended by Page (2004), referred to as the Stonebarrow Pyritic Member (SPM), to separate the pyritiferous marls at the top of the section although it was not applied herein. This study is concerned only with the basal CMF, specifically the SWB and BVM (including the SPM), in order to examine those strata with the greatest lithological contrast when compared to the underlying BLF. The stratigraphy of the basal SWB (previously the topmost BLF) was described by Lang (1924), but the main section was examined by Lang et al. (1923); these accounts were followed more recently by a revised lithostratigraphy and bed-numbering system in Gallois (2008a). The stratigraphy of the BVM (including the SPM) was described by Lang and Spath (1926).

The subdivided, bed-by-bed approach of Lang et al. (1923), Lang (1924), and Lang and Spath (1926) has resulted in the widespread adoption of these bed-numbering systems in modern literature (e.g. Hallam and Lang, 1960, Page, 1994, Curtis et al., 2000, Simms, 2004, Donovan, 2006, Andrew et al., 2010, Lord et al., 2010, Andrew et al., 2011, Jenkyns and Weedon, 2013, Pugh et al., 2014). Previous studies have provided detailed sedimentological, palaeontological, and geochemical analysis of key units within the Early Jurassic successions of Dorset and East Devon and specific interests include Bed 29 (*sensu* Lang, 1924) in the BLF (e.g. Paul et al., 2008, Jordan et al., 2015, Jordan, 2016), the *Birchi* tabular and nodular beds of the SWB (e.g. Raiswell, 1971, Marshall, 1982, Rukin, 1990, Wolff et al., 1992) and the Coinstone hiatus of the BVM (Lang, 1945, Hallam, 1969, Sellwood, 1972, Hesselbo and Palmer, 1992, Hallam, 1999).

The aim of this chapter is to provide a detailed, consistent lithostratigraphic account of the Early Jurassic successions in Dorset and East Devon that will then be applied to palaeontological, sedimentological, and geochemical analysis throughout the thesis. It was necessary to revise previous accounts in order to correct for potential differences following erosion of the vertical cliff profile since its last description, to correlate the

lithostratigraphy with the sampling programme used, and also because many of the original measured outcrops are now difficult or impractical to access. The study area is part of an actively eroding coastline which, when one considers the moderate potential lateral variability in both sedimentology and thickness, could produce inconsistencies between previous and future accounts of the strata. In order to ensure consistency across the entire section, in anticipation of comparative analysis between the different formations, the revised lithostratigraphic logs follow a modified version of the lithological classification presented by Weedon (1986). This chapter addresses the following:

Blue Lias Formation. The lithostratigraphy of the BLF in Dorset and East Devon is revised in full. The succession is subdivided in order to group sedimentologically/lithologically similar sections and investigate palaeoecological and geochemical trends (see chapters 3 and 4) without minor bed divisions. Fossil content in the BLF is discussed in Chapter 3. Bed numbers used throughout the thesis follow Lang (1924).

Shales-with-Beef Member. Some revisions were made to the lithostratigraphy of the SWB (*sensu* Gallois, 2008a); this chapter also considers lateral variability in the lithology and thicknesses of different sections by comparing a number of separate lithostratigraphic logs from across the length of the exposure. Key fossiliferous horizons discussed later in the thesis are reviewed in detail, particularly referencing their individual origin, sedimentology, and fossil content. Revised section numbers follow Gallois (2008a) whereas individual bed numbers follow Lang et al. (1923) and Lang (1924).

Black Ven Marl Member (including the Stonebarrow Pyritic Member). A revised lithostratigraphy of the BVM is presented in order to address considerable inconsistencies – specifically on the Black Ven exposure – between the modern cliff profile and previous lithostratigraphic accounts. Lateral variability in the lithology and thicknesses of different sections is also considered (as above). Key fossiliferous horizons discussed later in the thesis are described in detail (as above), many of which were not recognised by Lang and Spath (1926). Bed numbers follow Lang and Spath (1926).

2.2. Material and methods

Blue Lias Formation Study Area. The BLF was examined in coastal cliff outcrops between Lyme Regis, Dorset (approx. SY 33566 91565) and Pinhay Bay, Devon (approx. SY

31806 90779) (figs. 2.1, 2.2, and 2.3). The repetition of measured lithostratigraphic logs along the length of the exposure was not possible; the eastward dipping bedding of the non-terraced cliff profile meant only a limited vertical fraction was accessible at any one position (figs. 2.1 and 2.2). As a result, the lithostratigraphic account is a composite that was recorded along the length of the outcrop at the base of the cliff and on foreshore reefs beneath mean low water.

Figure 2.1 – A representative section of the lower-mid BLF exposed in coastal cliff outcrops in Pinhay Bay, Devon (approx. SY 32414 90833) (fig. 2.3). Note the basal limestone ledge is H54; for a full revised lithostratigraphy see Section 2.3.2. Scale = 1 m.

Figure 2.2 – A representative section of the upper BLF and lowermost SWB exposed in coastal cliff outcrops and on the foreshore ledges at Monmouth Beach, Dorset (approx. SY 32920 91144) (fig. 2.3). As a result of the eastward dipping bedding, progressively higher strata are encountered at beach level as one traverses eastward across the study area. Note the basal limestone ledge is Top Tape; for a full revised lithostratigraphy see Section 2.3.2. Scale = 1 m.

Charmouth Mudstone Formation Study Area. The SWB and BVM of the CMF were examined in coastal cliff outcrops between Lyme Regis (approx. SY 34355 92134) and Charmouth, Dorset (approx. SY 36452 93041) (figs. 2.4 and 2.5). Due to the limited height of the terraced cliff profiles and obscuration by landslide debris, it was not possible to compile a complete lithostratigraphic log for each member at all measured sections; moreover, measured logs required compositing from multiple nearby outcrops and therefore some deviation from and/or overlap between published geographic positions is to be expected. Lithostratigraphy of the SWB was examined at four approximate sections on the Black Ven exposure: 2008 Landslide, Spittles Landslide, Pinnacle Landslide, and Charmouth Heritage Centre sections (figs. 2.4 and 2.5); Lang et al. (1923) measured the succession near to the Charmouth Heritage Centre Section (figs. 2.4 and 2.5) and the Gallois (2008a) account was measured near to the Spittles Landslide Section (fig. 2.4). The SWB is not present east of the River Char although it has been recorded at the mouth of the river (fig. 2.5) in the fault zone at mean low water (Gallois, 2008a). The lithostratigraphy of the BVM was examined at the same four sections (figs. 2.4 and 2.5) and compared with the original Lang and Spath (1926) account from Stonebarrow Beach/East Beach (fig. 2.5).

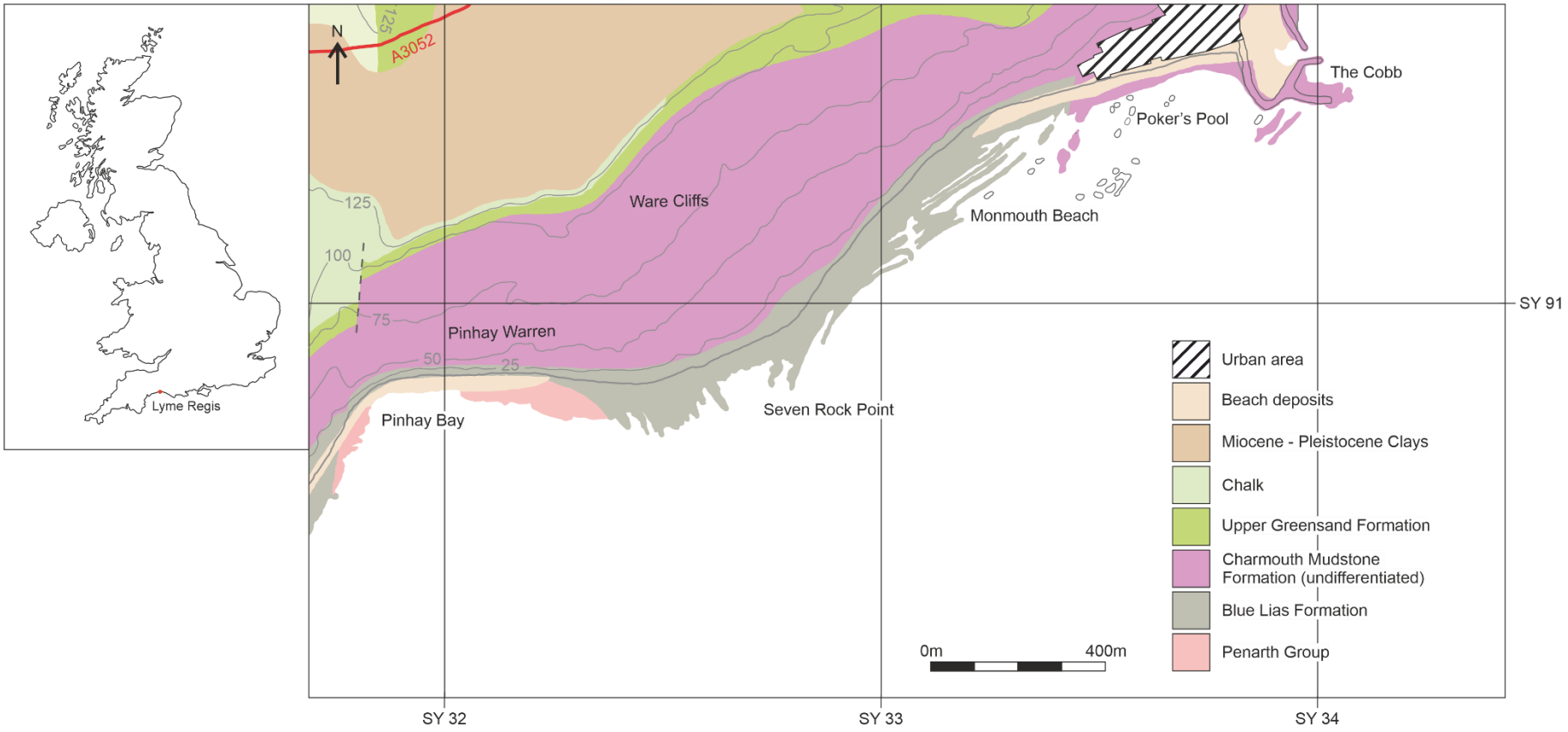

Figure 2.3 – Left: Outline map of the UK highlighting the study area. Right: Map sketch of the study area between Lyme Regis, Dorset (approx. SY 33566 91565) and Pinhay Bay, Devon (approx. SY 31806 90779). Data amended from EDINA Geology Digimap Service < https://digimap.edina.ac.uk >.

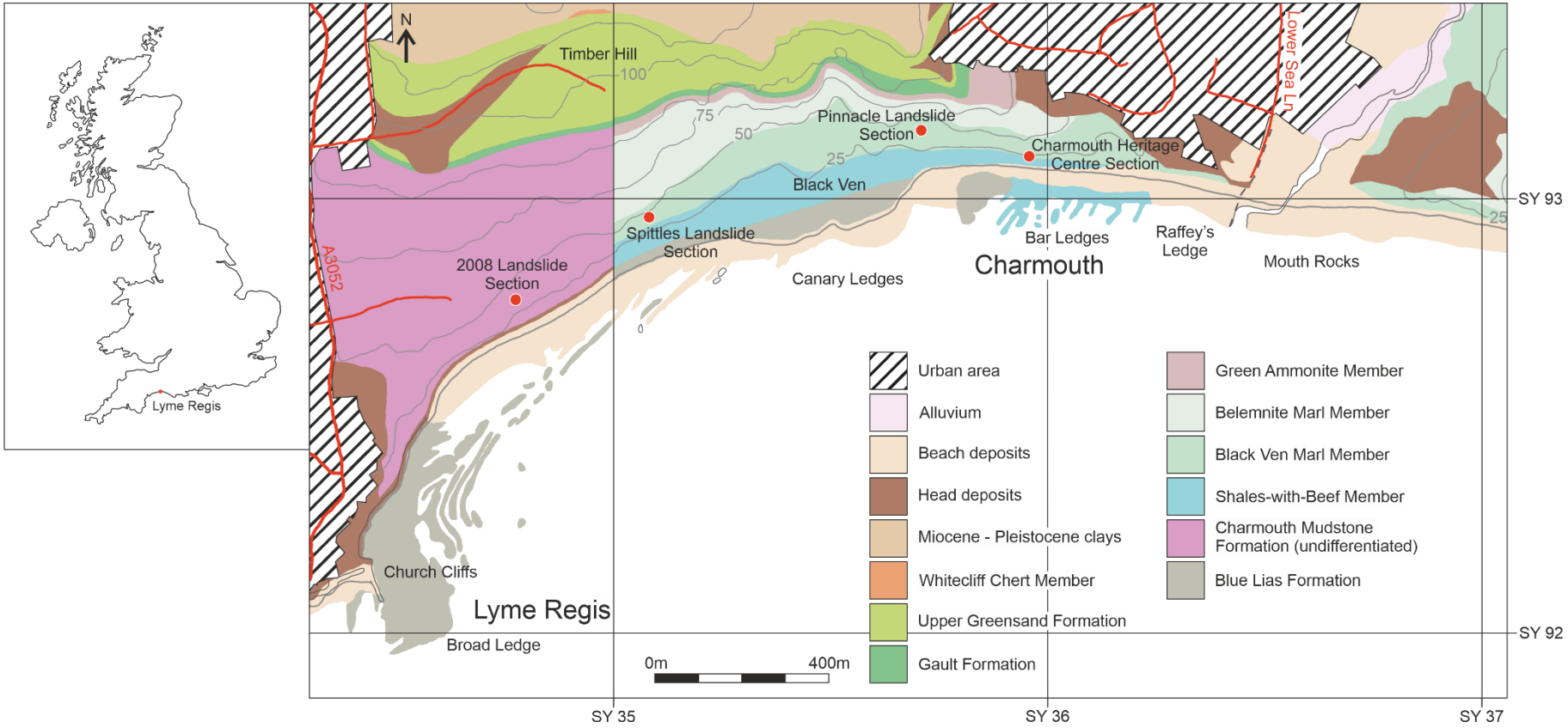

Figure 2.4 – Left: Outline map of the UK highlighting the study area. Right: Map sketch of the Black Ven exposure between Lyme Regis (approx. SY 34355 92134) and Charmouth, Dorset (approx. SY 36452 93041) showing the geographical position of the following measured sections; 2008 Landslide Section, Spittles Landslide Section, Pinnacle Landslide Section, and Charmouth Heritage Centre Section. Data amended from EDINA Geology Digimap Service < https://digimap.edina.ac.uk >.

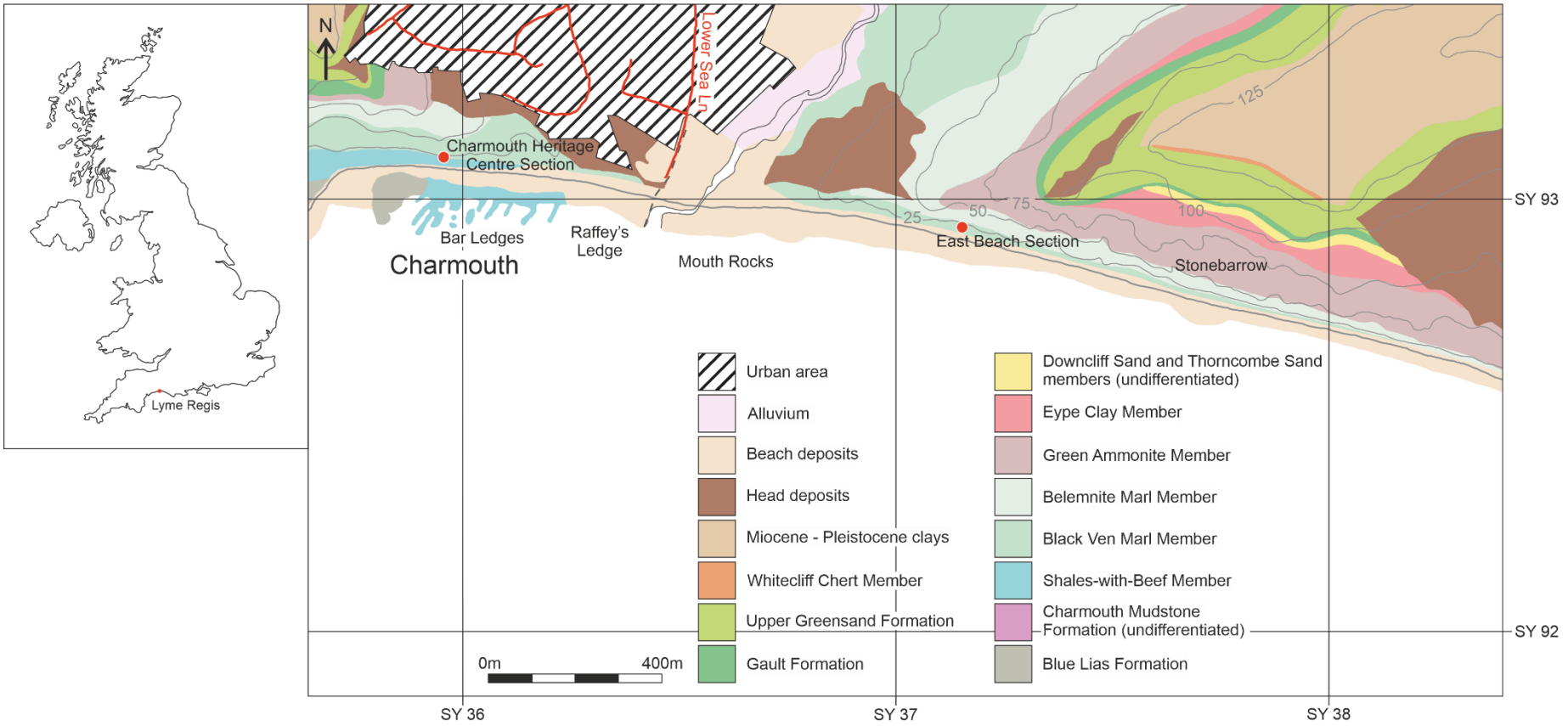

Figure 2.5 – Left: Outline map of the UK highlighting the study area. Right: Map sketch of the Stonebarrow exposure to the east of Charmouth, Dorset (approx. SY 37178 92944) showing the geographical position of the following measured sections; Charmouth Heritage Centre Section and East Beach Section. Data amended from EDINA Geology Digimap Service < https://digimap.edina.ac.uk >.

The sections examined (in eastward progression) were as follows:

2008 Landslide Section (2008LS) (fig. 2.4). This most westward exposure lies immediately east of Lyme Regis (approx. SY 34789 92772) and above the famous Church Cliffs (fig. 2.4). The coastal cliff outcrop exposes an approximately 17.6 m thick section of the SWB, between SB 7 (part) and the SWB/BVM boundary at the base of the *Birchi* Tabular Bed. The lower part of the SWB is incompletely exposed following the 2008 landslide movement. Above this, exposed on an upper terraced feature, is a central fraction of the BVM (approximately 5.4 m thick) between BVM 9 (part) and BVM 11 (part). The remainder of the member is obscured by landslide debris.

Spittles Landslide Section (SLS) (fig. 2.4). Positioned above Spittles Beach in the centre of Black Ven (approx. SY 35042 92917), the SWB is exposed between SB 6 and SB 15; the section measures approximately 24.4 m in thickness. The basal BVM, between BVM 1 and BVM 2 (part), is exposed directly above the SWB and measures approximately 2 m in thickness. In addition, an approximately 27.7 m thick section of the BVM, between BVM 2 (part) and BVM 11 (part), is present on the middle cliff terrace; the two sections of BVM 2 are unconnected. The upper part of the member is obscured by landslide debris from the overlying BM.

Pinnacle Landslide Section (PLS) (fig. 2.4). This coastal cliff outcrop is positioned above the prominent Pinnacle Landslide (approx. SY 35703 93151) on the foreshore of Charmouth's West Beach (fig. 2.4). The SWB is an incomplete section between SB 7 (part) and SB 15 that measures approximately 22.3 m in thickness. The BVM is also incomplete, measuring approximately 21.5 m between BVM 2 (part) and BVM 14.

Charmouth Heritage Centre Section (CHCS) (figs. 2.4 and 2.5). This is the most eastward measured section (approx. SY 35942 93116) at the Black Ven exposure (figs. 2.4 and 2.5). The SWB is incomplete and spans SB 7 (part) to SB 15, measuring approximately 18.2 m in thickness. The BVM is exposed in its entirety and measures approximately 47.4 m in thickness.

East Beach Section (EBS) (fig. 2.5). This is the only lithostratigraphic log discussed east of the River Char (fig. 2.5). The section was not measured by CR owing to safety considerations; instead, the original lithostratigraphic account of Lang and Spath (1926) has been used for reference. The position marked on the map approximates the main outcrop (approx. SY 37178 92944; fig. 2.5) but it is likely that the authors produced a

composite log, measured along the length of the exposure, in accordance with the eastward dipping bedding bringing progressively higher strata to beach level as the cliff profile is traversed (fig. 2.6). Fault movement and displacement places the entire SWB and the lowest BVM, specifically BVM 1 to BVM 2 (part), below beach level (Lang and Spath, 1926). The remainder of the member, between BVM 2 (part) and BVM 17, measures approximately 34 m in thickness (Lang and Spath, 1926).

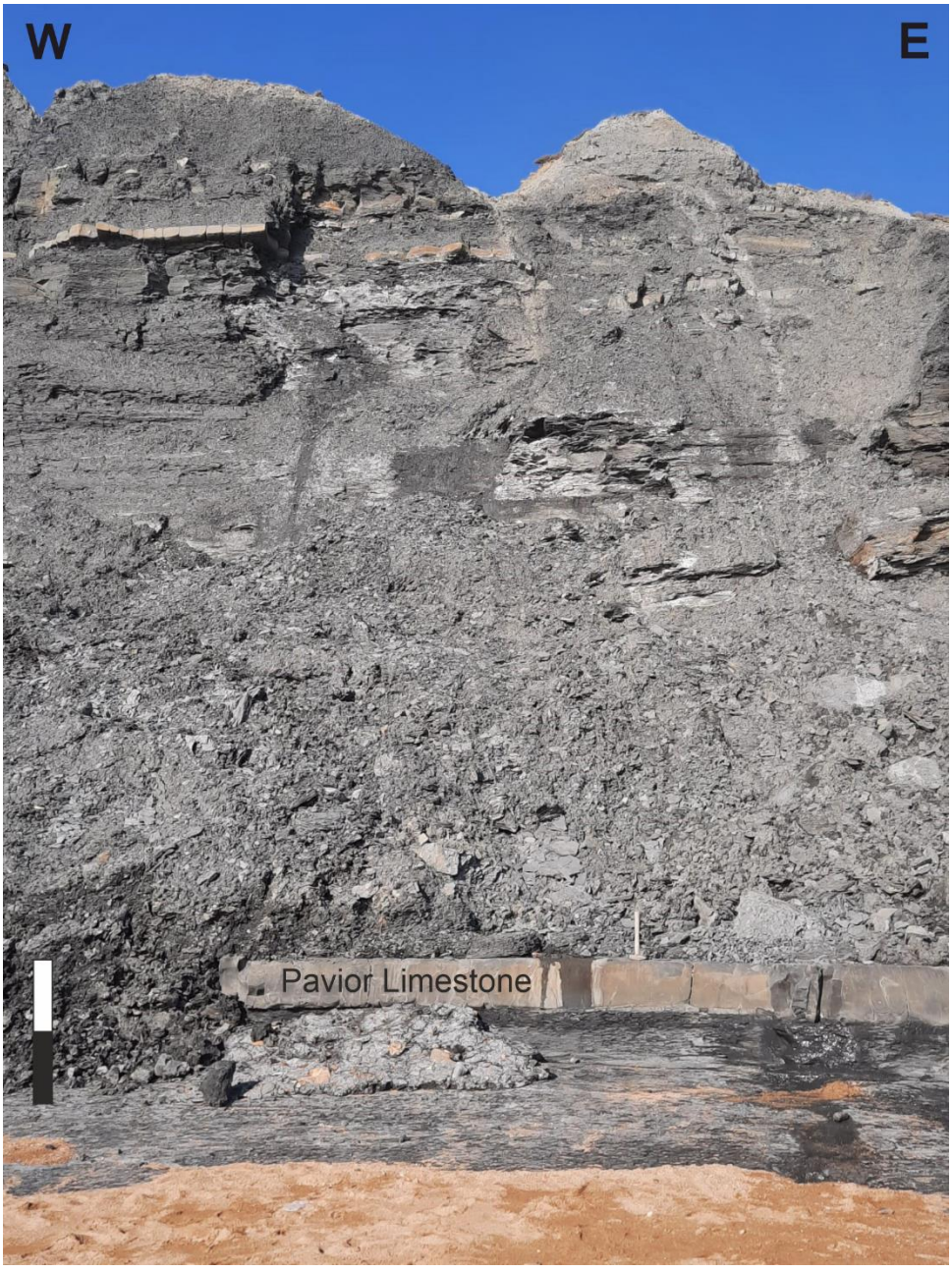

Figure 2.6 – A representative section of the middle BVM exposed in coastal cliff outcrops at Stonebarrow/East Beach, Dorset (fig. 2.5). Note the basal limestone is likely the Pavior Limestone or BVM 4; for a full revised lithostratigraphy see Section 2.3.4. The EBS was not measured by CR owing to safety concerns. Scale = 1 m.

2.3. Results

2.3.1. Lithological classification for the Early Jurassic of Dorset and East Devon

Weedon (1986) proposed five different rock types to describe and categorise the various lithologies of the BLF; this classification has been widely adopted (e.g. Weedon, 1987, Bottrell and Raiswell, 1989, Arzani, 2004, Arzani, 2006, Weedon et al., 2018) and includes: limestones, light and dark marls, paper shales and laminated limestones (Weedon, 1986, Weedon, 1987). Only minor revisions have been made to the Weedon (1986) classification scheme herein, specifically the introduction of a shale category to act as an intermediate stage between dark marls and paper shales. Whilst distinction between the different argillaceous lithologies is clear at a fresh exposure, the categories are sometimes difficult to distinguish following prolonged weathering; as a result, the revised classification scheme is considered a qualitative rather than quantitative approach. The lithological classifications of Lang et al. (1923), Lang (1924), and Lang and Spath (1926) have been revised, as best as possible, to fit the lithological classifications used herein for comparative purposes. Where individual beds are described in detail throughout the thesis, estimates are given for the proportion of key sedimentological components. Photomicrographs were taken using a Leica DM750P microscope with reflected light module attachment and Leica LAS (Leica Application Suite) Imaging Software; the variable use of plane-polarised, cross-polarised, and reflected light microscopy is indicated in individual figures.

Limestones (bioturbated). Limestones in the BLF show a range of morphologies and sedimentological compositions (e.g. Lang, 1924, Hallam and Lang, 1960, Paul et al., 2008, Weedon et al., 2018) that range from mudstones to wackestones with a variable bioclastic component and limited detrital minerals (e.g. Hallam and Lang, 1960). In the CMF, this lithology is less common, and beds of this type are replaced locally by ferroan dolomites or dolomitic limestones; for the purposes of this study, these are not classified separately since the lithotype is not referenced later in the thesis. Limestones often have a poorly-cemented, argillaceous margin (Hallam and Lang, 1960). Two distinct forms of bioturbated limestone have been recognised by previous authors (e.g. Arzani, 2006, Paul et al., 2008):

> *Nodular bioturbated limestones*. Pale grey, bioturbated mudstones to wackestones, characterised by lenticular concretions that measure up to approximately 2 m in length and 50 – 250 mm in thickness; these limestones are typically hosted within calcareous light marls (Weedon et al., 2018). Although concretions are sometimes

isolated, it is common for them to coalesce horizontally (Arzani, 2006, Weedon et al., 2018). This form also includes laterally persistent limestones with an irregular or hummocky upper surface. Nodular limestones generally lack internal structure/laminations (Hallam and Lang, 1960, Paul et al., 2008) and contain a diverse fossil assemblage preserved *in situ* or randomly oriented (e.g. Paul et al., 2008, Jordan, 2016; see chapters 3 and 7).

Planar bioturbated limestones. Laterally persistent along the length of the exposure, this form includes bioturbated limestones with a planar upper and lower surface (e.g. Arzani, 2006, Paul et al., 2008). Pale grey mudstones to wackestones are typically thicker than their nodular counterparts (approximately 50 – 400 mm), although both have similar fossil assemblages (see chapters 3 and 7) and lack internal structure/laminations (Paul et al., 2008).

Previous studies have inferred that limestones were deposited beneath oxygenated bottom waters (e.g. Weedon, 1986, Moghadam and Paul, 2000) and both forms show evidence for bioturbation and sediment mixing through the destruction of original internal laminae (e.g. Hallam and Lang, 1960, Paul et al., 2008). Limestones are the product of early cementation (Hallam, 1964, Weedon, 1987, Arzani, 2006, Paul et al., 2008, Weedon et al., 2018); pre-diagenetic sediments were consistent with the light marl lithology (Weedon, 1987, Weedon et al., 2018). Weedon et al. (2018) state that formation followed turbulent bottom waters and a period of non-deposition via the winnowing of organic matter and fine sediment; non-deposition initiates cementation as it promotes anaerobic methane oxidation within the SRZ which generates carbonate as per the Raiswell (1988) model (Raiswell, 1988, Bottrell and Raiswell, 1989, Weedon et al., 2018). According to Weedon et al. (2018), although early cementation occurred within the SRZ (*sensu* Raiswell, 1988), complete cementation of the limestone was achieved during late diagenesis (*sensu* Curtis et al., 2000, Raiswell and Fisher, 2000). The complete process is described in the model proposed by Weedon et al. (2018). Cementation of limestones by $CaCO_3$ was likely aided by the dissolution of originally aragonitic and presumably high-Mg calcitic molluscan fauna (e.g. Bottrell and Raiswell, 1989, Arzani, 2004, Arzani, 2006, Weedon et al., 2018); as a result, limestones are generally considered poorly representative of original ecological diversity (Cherns and Wright, 2000, Wright et al., 2003).

Light (conchoidal) marls. Pale grey light marls are homogeneous, exhibit a conchoidal surface when weathered, and lack original laminae; previous studies have inferred that this was the result of extensive bioturbation and sediment mixing beneath well-oxygenated bottom waters (e.g. Weedon, 1986, Weedon et al., 2018). In this classification, the light marl lithology of Weedon (1986) has been taken to represent the palest calcareous sediments from the succession in exclusivity. Light marls typically occur as thin beds (approximately 10 – 50 mm in thickness) that share a gradational contact with adjacent bioturbated limestones or occupying the spaces between limestone nodules. Thicker, isolated beds of the light marl lithology are also present throughout the succession, but these are generally rare.

Dark (conchoidal) marls. In this classification, the dark marl lithology of Weedon (1986) has been taken to exclusively represent medium-dark grey sediments that exhibit a conchoidal surface when weathered and show little bedding-parallel fissility. Dark marls are texturally similar to light marls (Weedon et al., 2018) although microspar and organic/clay-rich laminae are evident (Weedon, 1986, Weedon, 1987, Arzani, 2006, Weedon et al., 2018). In the BLF, dark marls vary in thickness (approximately 50 – 500 mm) and are often interbedded with bioturbated limestones and other argillaceous lithologies; dark marls in the overlying CMF are significantly thicker (up to approximately 9.5 m) and generally uniform. The fossil assemblage typically contains ammonoids and moderately diverse macrobenthos (see chapters 3 and 7).

Shales. The introduction of a shale category to the revised classification scheme allows for a more precise distinction to be made between the different argillaceous lithologies. In previous accounts (e.g. Weedon, 1986) there was no intermediate stage between dark marls and paper shales. Dark grey shales show moderate bedding-parallel fissility – owing to microspar and organic/clay-rich laminae – that is transitional between the conchoidal dark marls and fissile paper shales. Once weathered, laminae separate along regular planar surfaces to form thin sheets approximately 5 – 30 mm in thickness. Laterally impersistent, thin (5 – 30 mm) beef bands are often associated with these sediments in the basal CMF.

Paper shales. This lithology correlates with the end-member of the Weedon (1986) classification and accounts for dark grey/black paper shales that are finely fissile owing to a texture comprised predominantly of organic and clay-rich laminae with associated carbonate-rich laminae (e.g. Hallam and Lang, 1960, Weedon, 1986, Weedon, 1987,

Arzani, 2004, Arzani, 2006, Weedon et al., 2018); the latter has been attributed to neomorphosed zooplankton faecal pellets (Weedon, 1986, Weedon, 1987, Weedon et al., 2018). The molluscan fossil assemblage is generally limited to nektonic and planktonic groups such as ammonoids (see chapters 3 and 7). Paper shales are less common in the BLF and range between approximately 50 – 300 mm in thickness; within the overlying CMF, individual beds are thicker (approximately 50 mm – 1.6 m), pyritiferous, and contain thin (5 – 20 mm) beef bands. Previous studies have inferred that deposition of these sediments was beneath variable dysaerobic/anoxic conditions (e.g. Weedon, 1986, Ebukanson and Kinghorn, 1990, Wignall and Hallam, 1991, Moghadam and Paul, 2000, Wignall, 2001b, Arzani, 2004).

Limestones (laminated). Two distinct forms of laminated limestone are present in the Early Jurassic of Dorset and East Devon, these are planar laminated limestones and concretionary laminated limestones. In the CMF only, laminated limestones are often locally replaced by ferroan dolomites or dolomitic limestones; for the purposes of this study, no distinction is made between these sediments owing to their close association, localised nature, and because the dolomitic lithotype is not referenced later in the thesis.

Planar laminated limestones. This form is consistent with the laminated limestone classification of previous studies (e.g. Hallam and Lang, 1960, Weedon, 1986, Weedon, 1987, Arzani, 2004, Arzani, 2006, Weedon et al., 2018). Individual beds are often laterally persistent and characterised by parallel, planar upper and lower surfaces although a less common lenticular morphology is also known to occur (Weedon 1986). Planar laminated limestones are contained within organic-rich paper shales or similar sediments (e.g. Arzani, 2004). The internal texture is predominantly comprised of microspar and organic/clay-rich laminae (Weedon, 1987, Arzani, 2004, Arzani, 2006). In the BLF, planar laminated limestones are restricted to the *Tilmanni* or *Planorbis* chronozones and generally occur in lithology-specific bundles (e.g. BL 5 and BL 7). There were few examples recorded in the CMF.

Concretionary laminated limestones. This form of laminated limestone accounts for the notable fossiliferous concretions from Lyme Regis and Charmouth, Dorset (e.g. Cope and Sole, 2000, Curtis et al., 2000, Andrew et al., 2010). Concretionary laminated limestones do not occur in the BLF and those within the CMF show

extensive sedimentological and palaeontological variability (for individual descriptions refer to sections 2.3.3 and 2.3.4). Concretions exhibit a range of different morphologies but are predominately sub-spheroidal or cylindrical and measure approximately 0.1 – 1.5 m in diameter and 0.01 – 0.3 m in thickness; the morphology of concretions within a single bed can vary significantly along the length of the exposure. Less common tabular beds can reach up to approximately 0.3 m thick. The majority of concretions are contained within laminated paper shales or similar sediments and have a thin argillaceous margin. The sedimentological composition of concretions varies extensively, but is typically comprised of microsparitic, peloidal, and organic/clay-rich laminae that are sometimes arranged in upward-fining sequences (e.g. Curtis et al., 2000); horizontal layers of fragmented and disarticulated shells (0.5 – 2 mm thick) are also common (e.g. Curtis et al., 2000).

Weedon et al. (2018) assert that the formation of planar laminated limestones, as with bioturbated limestones, follows a period of non-deposition associated with storm activity; the low frequency of this lithology is a consequence of the rarity/weakness of storm events in the corresponding sedimentary setting (Weedon et al., 2018). In contrast, Curtis et al. (2000) have inferred that concretionary laminated limestone formation follows deposition of a suspended sediment package and burial of organic matter that initiates diagenetic cementation at depth and does not require a pause in sedimentation.

2.3.2. Revised lithostratigraphy of the Blue Lias Formation in Dorset and East Devon

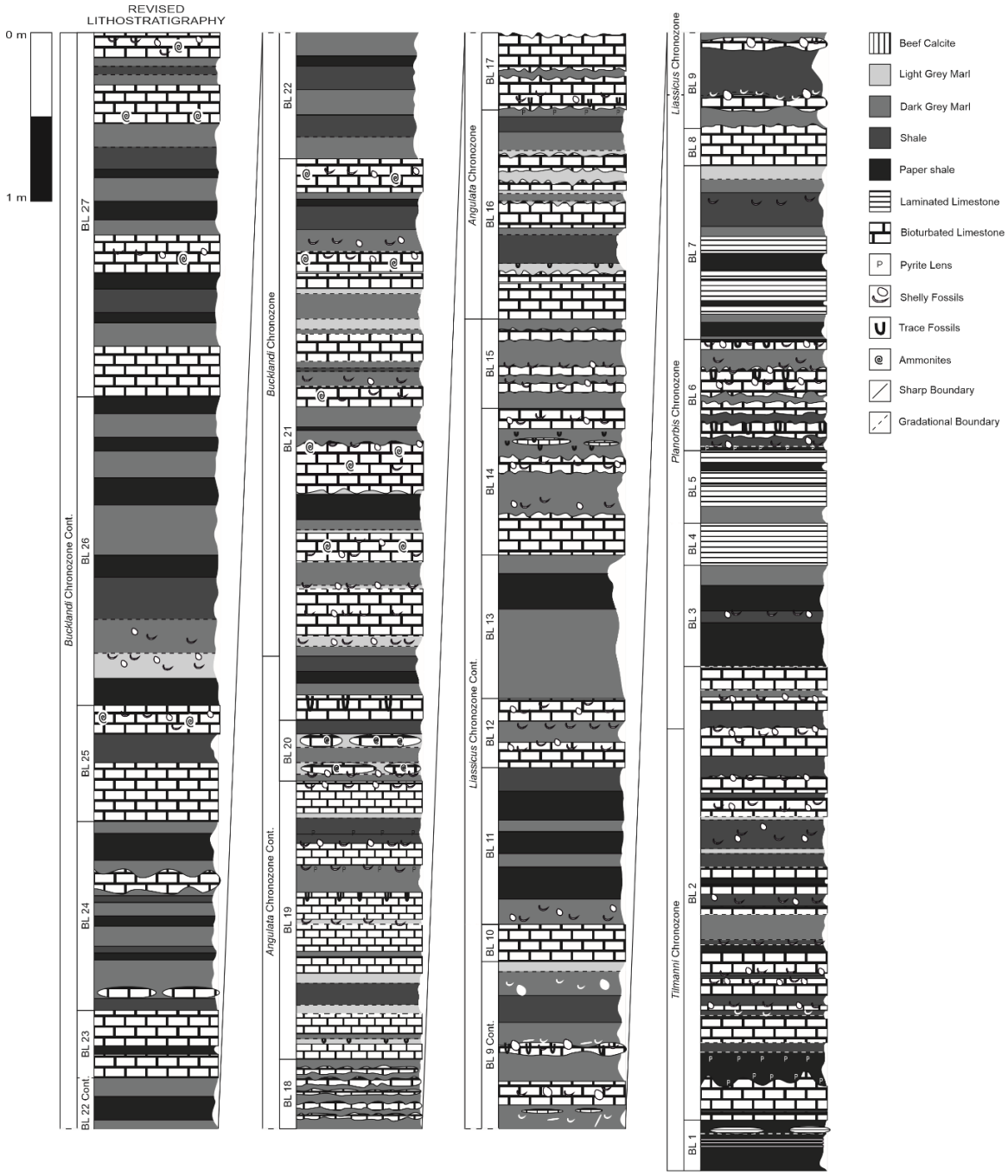

Figure 2.7 – The revised lithostratigraphic log for the BLF in Dorset and East Devon, measured between Lyme Regis and Pinhay Bay (fig. 2.3). Key in figure. Scale = 1 m.

BL 1 (0.3 m) = the basal section of the BLF is dominated by mostly unfossiliferous, laminated paper shales (e.g. Wignall, 2001b) (fig. 2.10). According to Wignall (2001b), extensive cementation of the upper fraction (locally) grades into the base of BL 2 at H2. A thin (40 mm) bed of impersistent, planar laminated limestones is present in the upper part

of the section (figs. 2.8 and 2.10); lenticles are enclosed by paper shales that share a gradational boundary with the lower limestone surface (fig. 2.10). Wignall (2001b) records a local, fossiliferous bedding surface within the centre of the paper shales that is dominated by disarticulated *Modiolus minimus* and echinoid spines. The laminated limestones are poorly fossiliferous and contain a low number of intact bivalve spat (see Chapter 3).

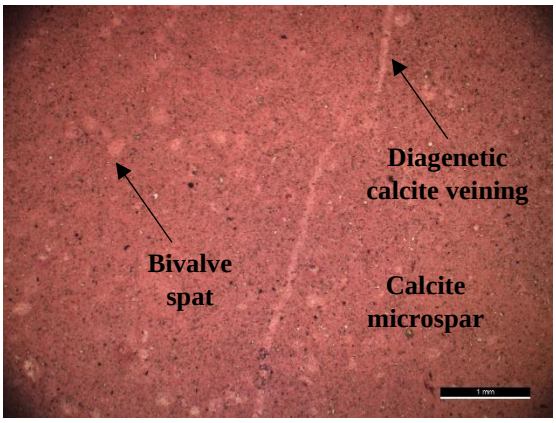

Figure 2.8 – Stained carbonate peel, viewed under plane-polarised light, of a planar laminated limestone from BL 1; the sediment composition is dominated by uniform microspar. Bivalve spat are rare and replaced by medium/coarse (10 – 100 μm) calcite spar (see Chapter 3). Minor diagenetic calcite veining is evident. Scale = 1 mm.

BL 2 (2.69 m) = the lower boundary of the section is taken at the base of the first persistent bioturbated limestone (H2) in the BLF and the upper boundary is positioned at the top surface of the youngest bioturbated limestone (H28) preceding replacement of the dominant carbonate lithology with laminated limestones in BL 4 (fig. 2.10). At the base of the section there are large (50 – 200 mm) hummocks on the upper surface of H4 (H2 in Wignall, 2001b) (see also Hallam and Lang, 1960; fig. 2.10).

Shales are the dominant non-limestone lithology and occupy (partially or in full) 11 of the 13 interbeds (fig. 2.10); the other argillaceous lithologies are uncommon and, in order of decreasing relative abundance, include paper shales (n = 5), dark marls (n = 2), and light marls (n = 1) (fig. 2.10). The section contains a high number (n = 14) of thin (30 – 160 mm), pale grey bioturbated limestones (fig. 2.10) that generally lack internal structure; the exception is a pair of basal limestones (H2 and H4) which, according to Wignall (2001b), show well-preserved laminations at the top and bottom of the bed. Limestone-shale contacts are typically sharp, unlike the gradational boundaries that separate bioturbated limestones from light and dark marls (fig. 2.10); each bed is laterally persistent and can be traced along the length of the exposure. Limestones contain an abundant macrofaunal fossil assemblage dominated by *Liostrea* and *Plagiostoma* (see Chapter 3).

When viewed under magnification as stained carbonate peels, bioturbated limestones have an abundant microfaunal fossil component (average = 34 % of total sediment composition; see Chapter 3). Bioclasts are replaced by coarse (10 – 200 μm) calcite spar that does not preserve the original shell microstructure (fig. 2.9); replacement and/or recrystallisation, particularly of bivalve spat, is poor in several of the central limestone beds (e.g. H12 and H16) (fig. 2.9). There is no original sediment structure/lamination and well-defined circular burrows, without bioclasts, are present in H8 (fig. 2.9).

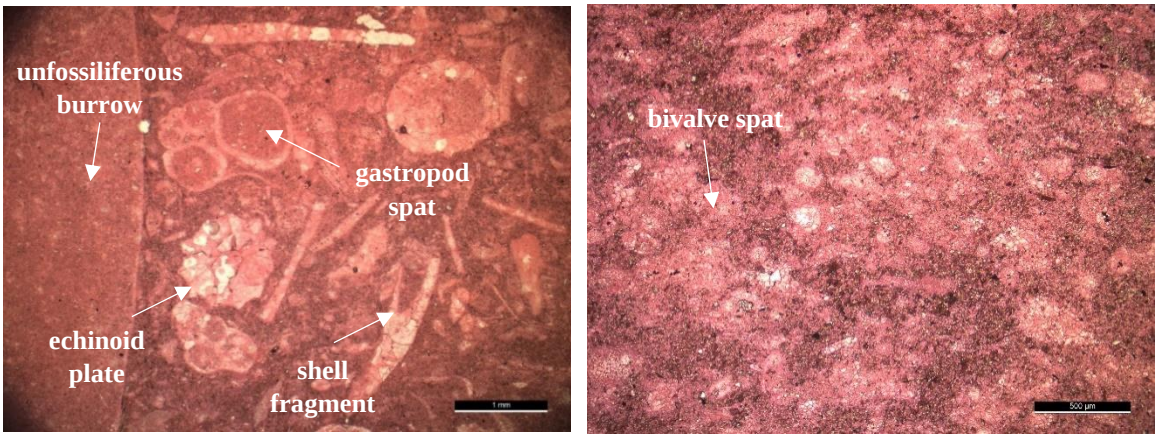

Figure 2.9 – Stained carbonate peels, viewed under plane-polarised light, showing the variable sediment composition of bioturbated limestones in BL 2. Left (H8): coarse bioclastic wackestone with abundant fossils including bivalve and gastropod spat as well as echinoid plates; note the unfossiliferous circular burrow. Right (H16): bioclastic wackestone with poorly distinguishable bivalve spat. Scales = 1 mm and 500 μm respectively.

BL 3 (0.6 m) = this section is an argillaceous lithology bundle that can be subdivided to a paper shale/shale/paper shale repetition in its lower part and a topmost bed of conchoidal dark marls (fig. 2.10). The two paper shale beds are significantly thicker (average = 0.21 m) than the shale interbed (0.07 m) and dark marls (0.12 m) (fig. 2.10). A thin (10 – 20 mm), fossiliferous shell layer in the centre of the section has randomly oriented, disarticulated, and fragmentary *Liostrea*, *Plagiostoma*, and echinoid spines (fig. 2.10).

BL 4 (0.25 m) = this planar laminated limestone is present along the length of the exposure. BL 4 is atypically thick for this lithology (0.25 m) and both the upper and lower surfaces have a sharp contact with the dark marls above and below (figs. 2.10 and 2.11). An unfossiliferous composition is dominated by uniform calcite microspar (> 95 %).

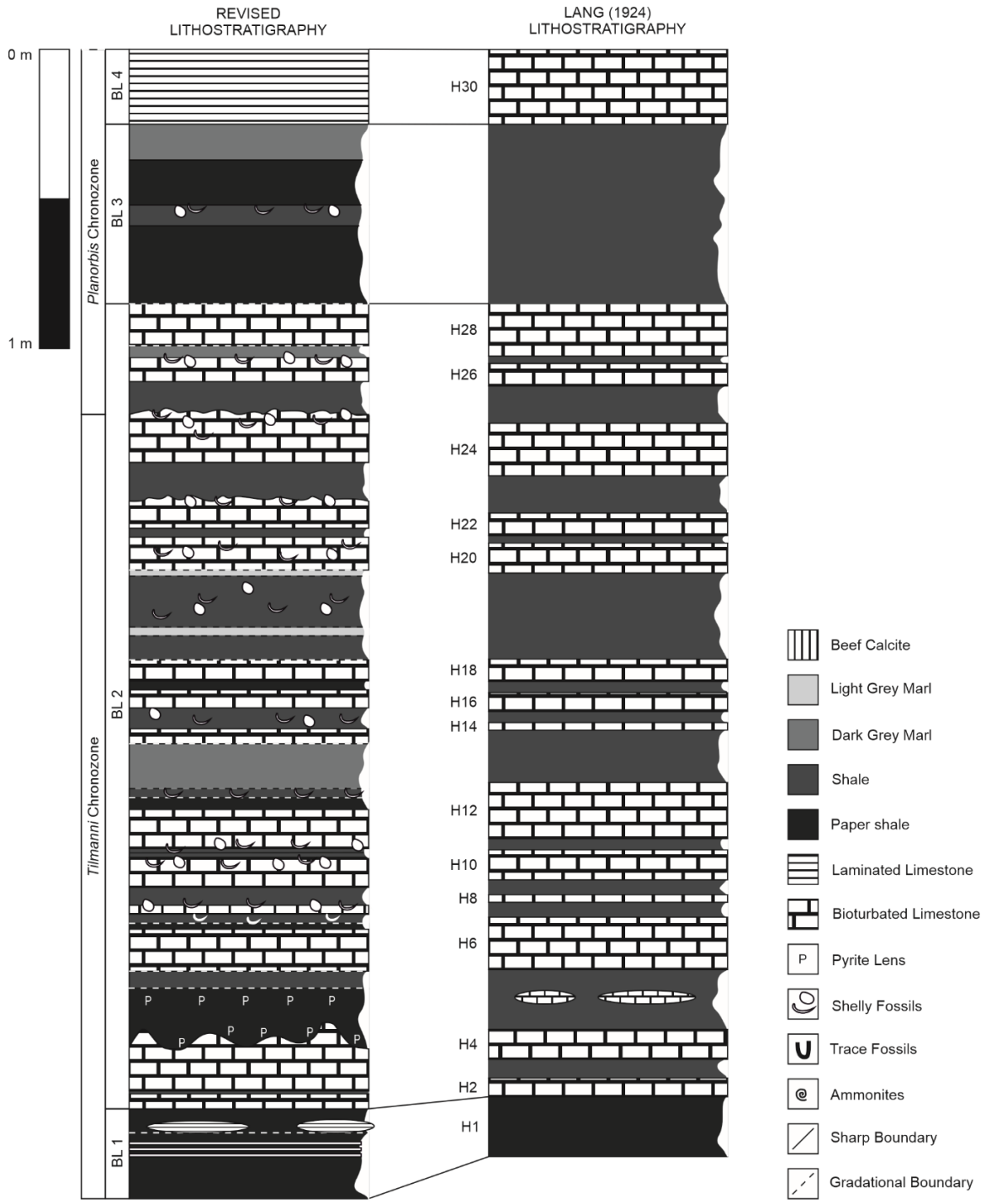

Figure 2.10 – Revised lithostratigraphy of BL 1 – BL 4. Comparison is offered to the lithostratigraphic log of Lang (1924). Key in figure. Scale = 1 m.

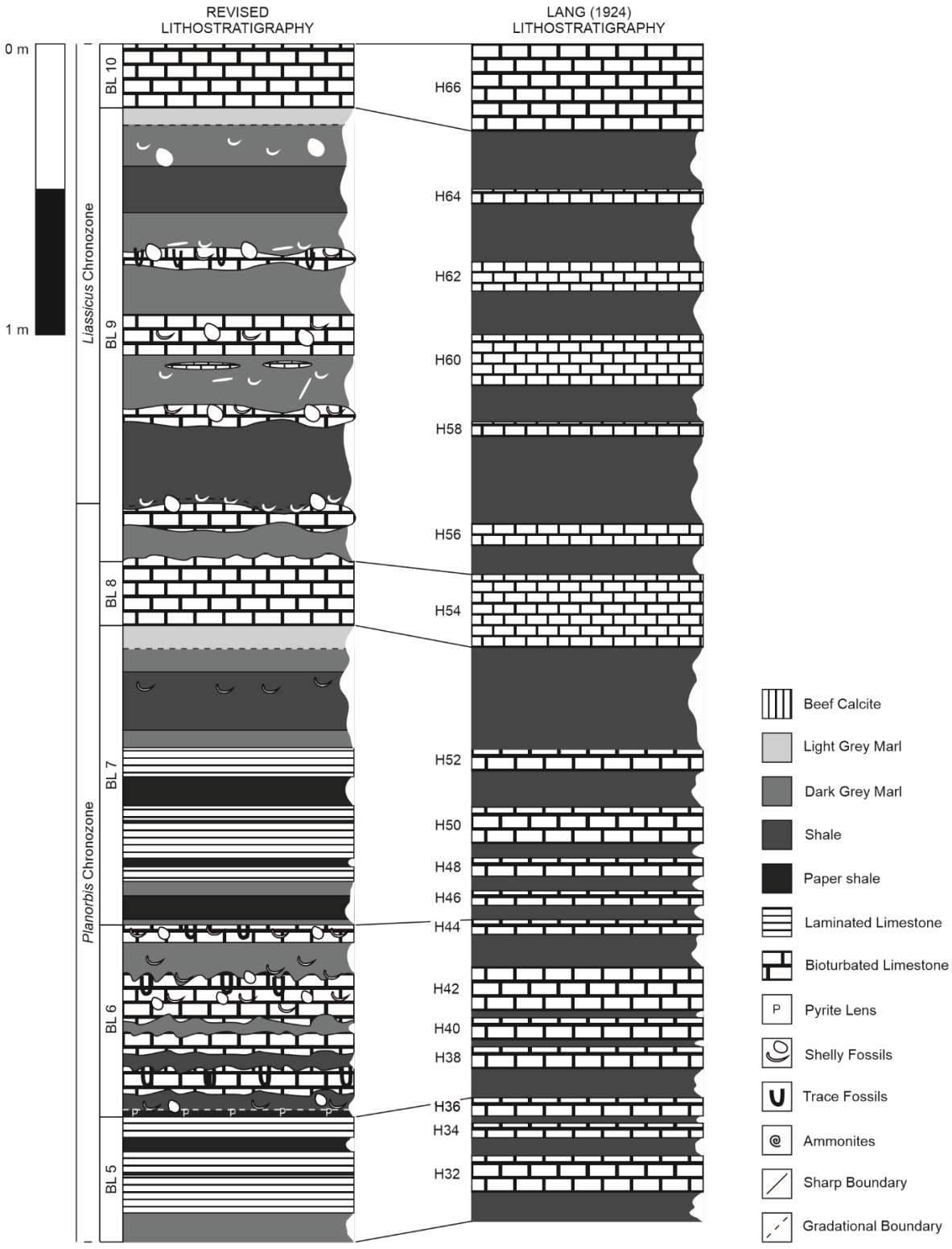

Figure 2.11 – Revised lithostratigraphy of BL 5 – BL 10. Comparison is offered to the lithostratigraphic log of Lang (1924). Key in figure. Scale = 1 m.

BL 5 (0.43 m) = three laminated limestone beds are separated via sharp and planar contacts by argillaceous paper shales (figs. 2.11 and 2.12). Laminated limestones are consistently thicker (70 – 130 mm) than their paper shale interbeds (10 – 50 mm) (fig.

2.11). At the base of the section is a single bed of uniform conchoidal dark marls (100 mm; fig. 2.11). Irregular pyrite concretions, up to 20 mm in diameter, are present on the upper surface of the topmost limestone (H36) and cover approximately 1 % of its surface area.

Figure 2.12 – A photograph of BL 5 (part) and BL 6 (part) in Pinhay Bay, Devon (fig. 2.3) to illustrate the contrast between planar laminated limestones and irregular bioturbated limestones. Note the various argillaceous interbeds which include paper shales, shales, and dark marls. There is an additional lenticular laminated limestone highlighted in blue that was laterally limited and therefore not included within the revised lithostratigraphic log (fig. 2.11). Moderate lateral variability in the thicknesses of different beds and the perspective of the image mean that the section shown here may vary from the revised lithostratigraphic log (fig. 2.11). Size of hammer = 350 mm.

BL 6 (0.66 m) = this section marks the return of bioturbated limestones as the dominant carbonate lithology for a limited period, before once again being replaced by laminated limestones in BL 7 (fig. 2.11). A simple argillaceous lithology bundle comprised of a thin layer of paper shales (25 mm) overlain by shales (55 mm) occupies the space between the youngest laminated limestone of BL 5 and the oldest bioturbated limestone of BL 6 (figs.

2.11 and 2.12). In the main body of the section, four limestone beds (60 – 180 mm thick) are separated by shale (n = 1; 40 mm thick) and dark marl (n = 2; 30 – 100 mm thick) interbeds (fig. 2.11); sharp contacts divide the different alternations at irregular upper and lower surfaces (fig. 2.11). The sediment composition of different limestones shows extensive variability (fig. 2.13). Poor cementation of the basal bed H38 is coincident with large crystals of calcite spar (up to 50 μm) and abundant, imbricated bioclasts occasionally replaced by pyrite (fig. 2.13); in other beds, shell fragments and spat are generally replaced by coarse calcite spar (10 – 200 μm; fig. 2.13).

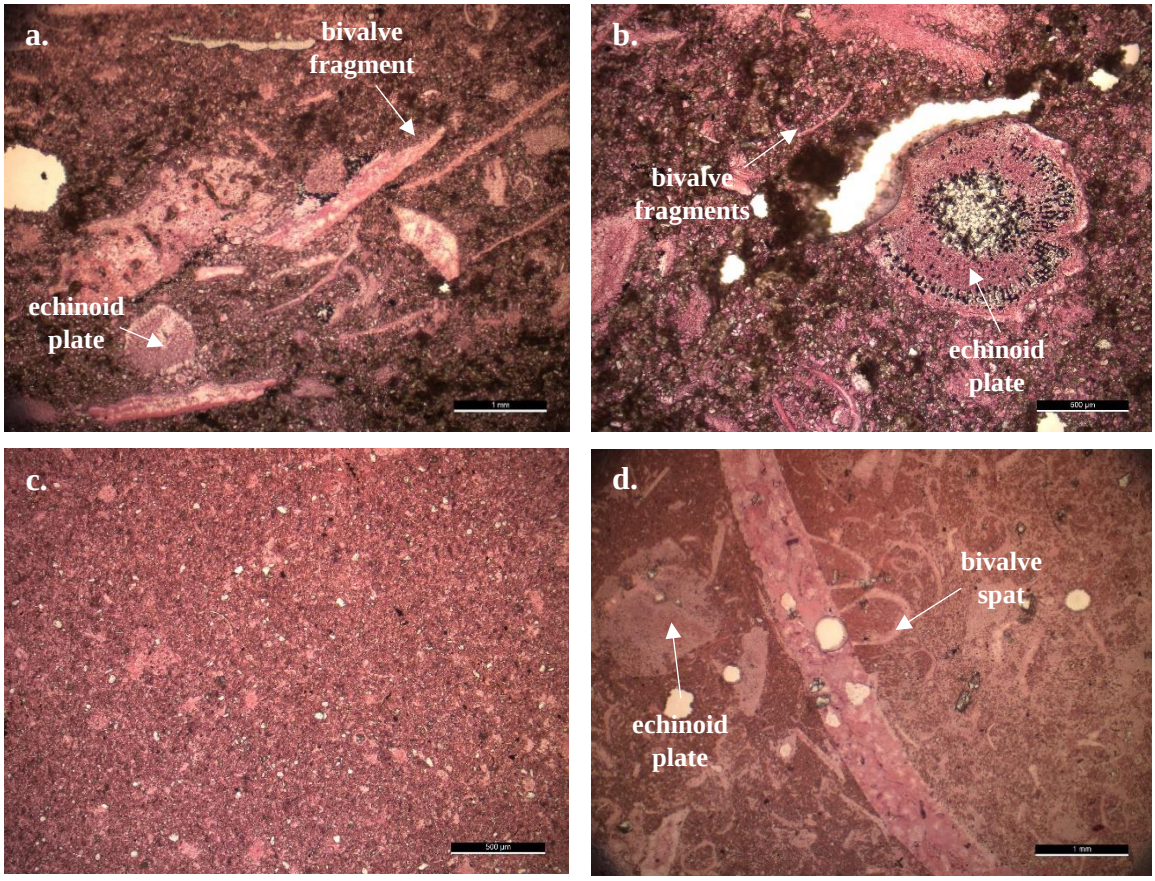

Figure 2.13 – Stained carbonate peels, viewed under plane-polarised light, showing the sedimentology of limestones in BL 6. a. (H38): poorly-cemented wackestone with imbricated shell fragments (scale = 1 mm); b. (H38): partial pyritisation of an echinoid plate (scale = 500 μm); c. (H42): unfossiliferous sediment (scale = 500 μm); and d. (H44): shell lens within a well-cemented limestone (scale = 1 mm).

BL 7 (1.03 m) = in the main body of the section, four planar laminated limestones (50 – 120 mm thick) are separated by thin (10 – 100 mm) paper shale interbeds (fig. 2.11). At its base is a relatively thin (0.15 m) argillaceous lithology bundle that has a single dark marl/paper shale/dark marl repetition (fig. 2.11). The topmost bundle is thicker (0.42 m) and contains a dark marl/shale/dark marl repetition in the lower part and a single bed of

light marl, which measures 80 mm thick, directly below H54 (figs. 2.11 and 2.14). In H50, microfaunal bioclasts are arranged in horizontal layers up to 3 mm in thickness (fig. 2.15).

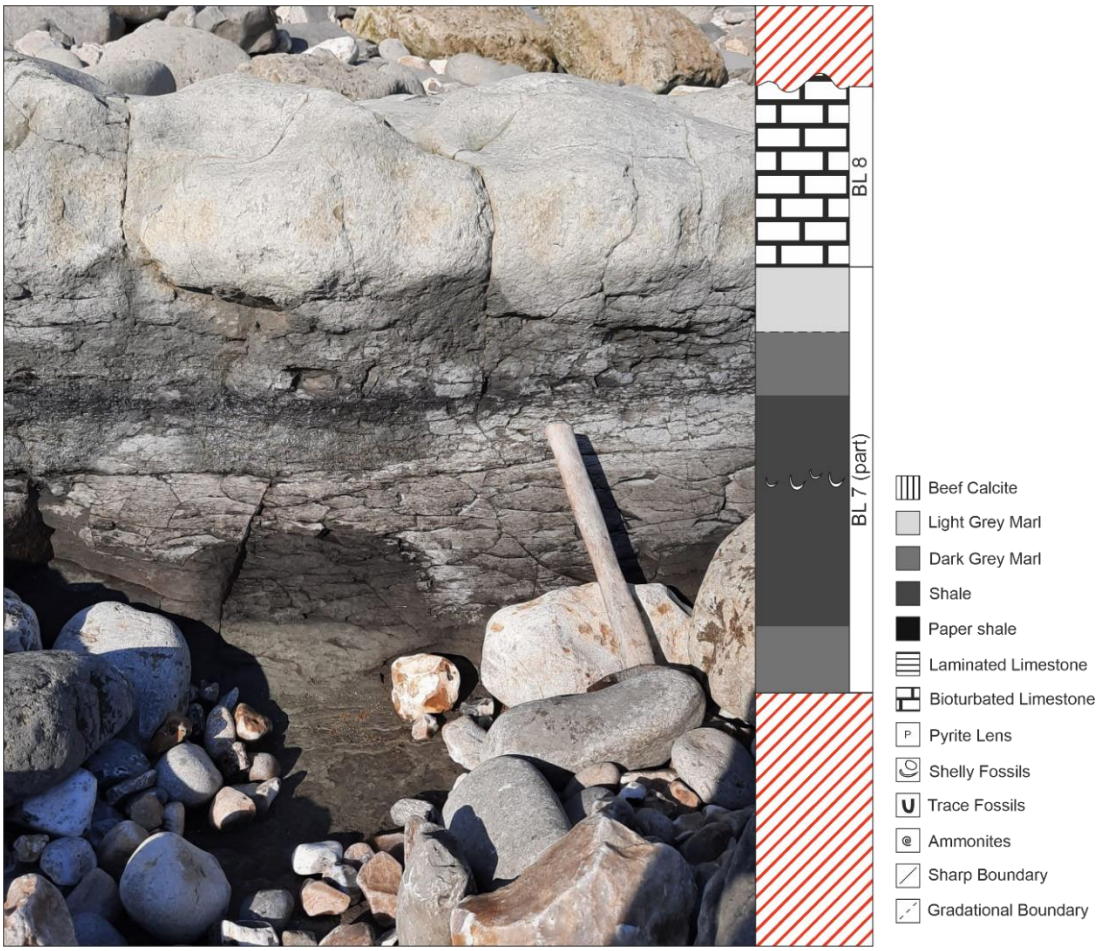

Figure 2.14 – A photograph of BL 7 (part) and BL 8 in Pinhay Bay, Devon (fig. 2.3) to illustrate an argillaceous lithology bundle that features (in ascending vertical order) a dark marl/shale/dark marl repetition capped by light marls. Moderate lateral variability in the thicknesses of different beds, undulating or irregular surface contacts, and the perspective of the image mean that the section shown here may vary from the revised lithostratigraphic log (fig. 2.11). Note that classification of the different argillaceous lithologies is qualitative and difficult on a weathered profile. Size of hammer = 350 mm.

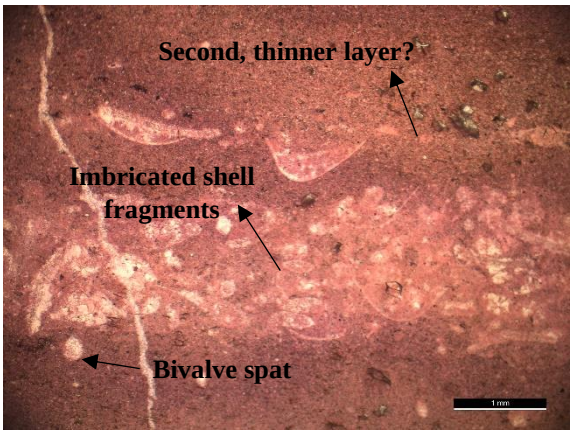

Figure 2.15 – Stained carbonate peel, viewed under plane-polarised light, of H50 – a planar laminated limestone in BL 7. Note the thin (3 mm) shell layer dominated by bivalve spat and imbricated shell fragments as well as a possible second layer above. Scale = 1 mm.

BL 8 (0.22 m) = this section is comprised of a single bioturbated limestone bed that has a well-cemented, homogeneous internal structure. BL 8 forms a persistent foreshore reef at Pinhay Bay, Devon (fig. 2.3) and is recognised in the field by its hummocky upper surface.

BL 9 (1.56 m) = the section has three laterally persistent, irregular bioturbated limestone beds (H56, H58, and H62) that are formed of nodules which completely or partially coalesce across the horizontal axis (figs. 2.11 and 2.16). The upper limestone surfaces are covered in abundant disarticulated and/or fragmented bioclasts (see Chapter 3). There is a single layer of widely spaced, non-coalescing bioturbated limestone nodules below H60 that measure approximately 0.4 m in diameter and up to 30 mm in thickness (fig. 2.11). In the centre of BL 9 is a thick (0.14 m) tabular bioturbated limestone (figs. 2.11 and 2.16). The topmost argillaceous lithology bundle is comprised of a dark marl/shale (although lateral transitions/non-weathered parts are frequently more appropriately classified as paper shales)/dark marl repetition capped by a thin bed (60 mm) of light marls (figs. 2.11 and 2.16); other argillaceous interbeds in the section are restricted to an atypical type of greenish shales? that transition to dark marls (n = 1) and dark marls (n = 3) (figs. 2.11 and 2.16). Weedon et al. (2018) have inferred a possible hiatus at H58 citing field data, including encrusting organisms on ammonoids and abundant echinoid fragments in the marls above, as evidence for increased turbulence resulting in non-deposition.

Figure 2.16 – A photograph of BL 9 and BL 10 in Pinhay Bay, Devon (fig. 2.3) to illustrate the difference between nodular bioturbated limestones and tabular bioturbated limestones (see in text description). Moderate lateral variability in the thicknesses of different beds, undulating or irregular surface contacts, and the perspective of the image mean that the section shown here may vary from the revised lithostratigraphic log (fig. 2.11). Note that classification of the different argillaceous lithologies is qualitative, can vary laterally, and is difficult on a weathered profile. Size of hammer = 350 mm.

BL 10 (0.22 m) = the section is comprised of a fossil-poor, tabular bioturbated limestone (figs. 2.11 and 2.16) that forms a persistent foreshore reef at Pinhay Bay, Devon (fig. 2.3).

BL 11 (0.93 m) = dark marl-paper shale alternations constitute the majority of an entirely argillaceous section that is capped by a single shale bed (figs. 2.17 and 2.18). The paper shale and shale layers are thick (0.13 – 0.19 m and 0.14 m respectively), laterally persistent, and fissile when weathered whereas dark marls are generally thinner (0.07 – 0.15 m) and show little to no bedding-parallel fissility (figs. 2.17 and 2.18). The contact between the different lithologies is sharp and planar (fig. 2.18). BL 11 is the thickest section without limestone alternations below BL 22 in the *Bucklandi* Chronozone (fig. 2.7). A reduction in the number of limestones within the *Liassicus* Chronozone was attributed to sea level rise by Weedon et al. (2018).

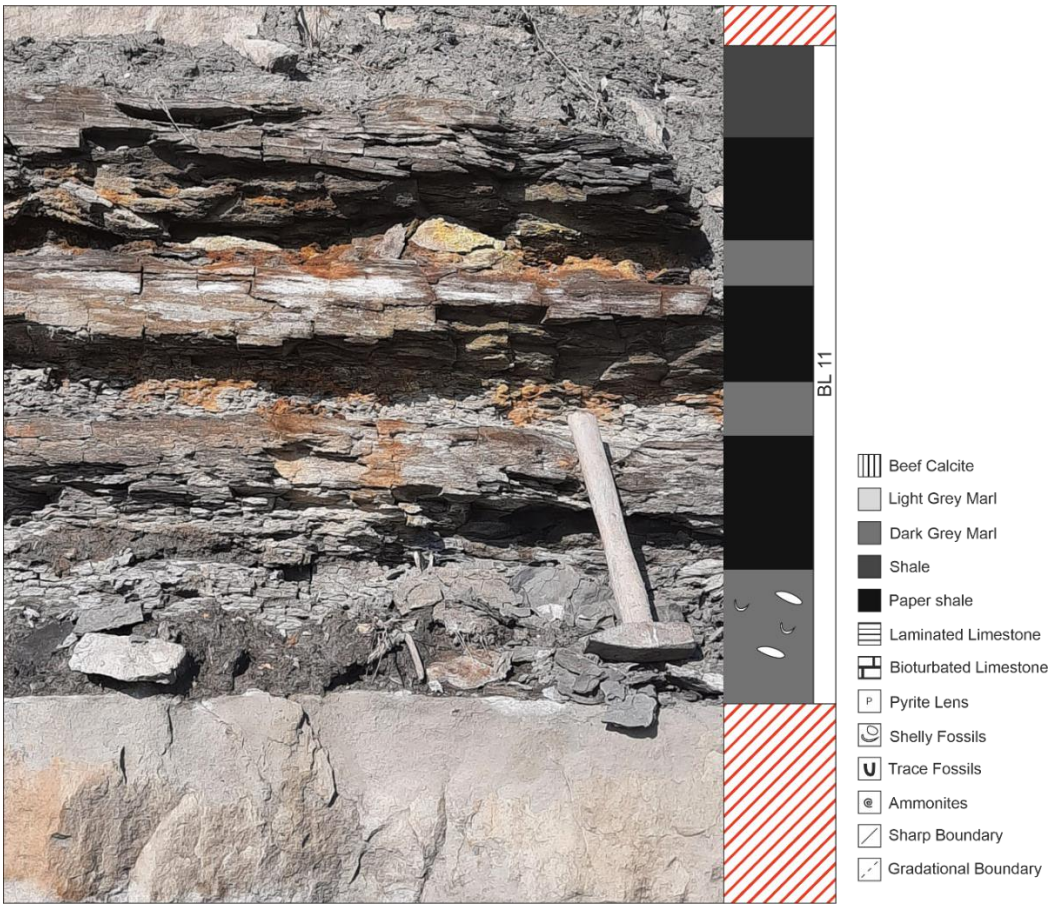

Figure 2.17 – A photograph of BL 11 in Pinhay Bay, Devon (fig. 2.3) to illustrate the paper shale-dark marl alternations in this entirely argillaceous section. Moderate lateral variability in the thicknesses of different beds and the perspective of the image mean that the section shown here may vary from the revised lithostratigraphic log (fig. 2.18). Note that classification of the different argillaceous lithologies is qualitative, can vary laterally, and is difficult on a weathered profile. Size of hammer = 350 mm.

BL 12 (0.41 m) = poorly-cemented, tabular bioturbated limestones of uniform thicknesses (average = 0.15 m) are present at the top and bottom of the section (fig. 2.18); these are separated by a similarly thick (0.12 m) dark marl interbed (fig. 2.18). Weedon et al. (2018) have inferred a possible depositional hiatus at H68 that approximates the position of the BL 11/BL 12 boundary in this study.

BL 13 (0.85 m) = BL 13 is a simple argillaceous lithology bundle comprised of two dark marl beds, at the top and bottom of the section, separated by a single paper shale interbed (0.21 m thick) in the upper-central part (fig. 2.18). The basal dark marls are atypically thick (0.53 m) for an individual, homogeneous argillaceous bed in the lower BLF. Dark marls have a sparse, poorly diverse fossil assemblage that is dominated by *Liostrea*, *Plagiostoma*, and echinoids whereas the paper shale lithology is without fossils (see Chapter 3).

BL 14 (0.87 m) = in this section, the three main bioturbated limestone beds are separated by dark marls (fig. 2.18); the thickness of these limestones is irregular (90 – 240 mm) and the upper and lower surfaces vary from a hummocky to planar morphology (fig. 2.18). Below H76 is a single layer of widely spaced, nodular bioturbated limestones that measure up to 1 m in diameter and 40 mm in thickness (fig. 2.18).

BL 15 (0.53 m) = this section has a total of three bioturbated limestone beds (average = 70 mm thick), with hummocky upper and lower surfaces, separated by uniform dark marl interbeds of different thicknesses (30 – 150 mm) (fig. 2.18). Both lithologies have a sparse fossil assemblage dominated by *Liostrea*, *Plagiostoma*, and echinoids (see Chapter 3).

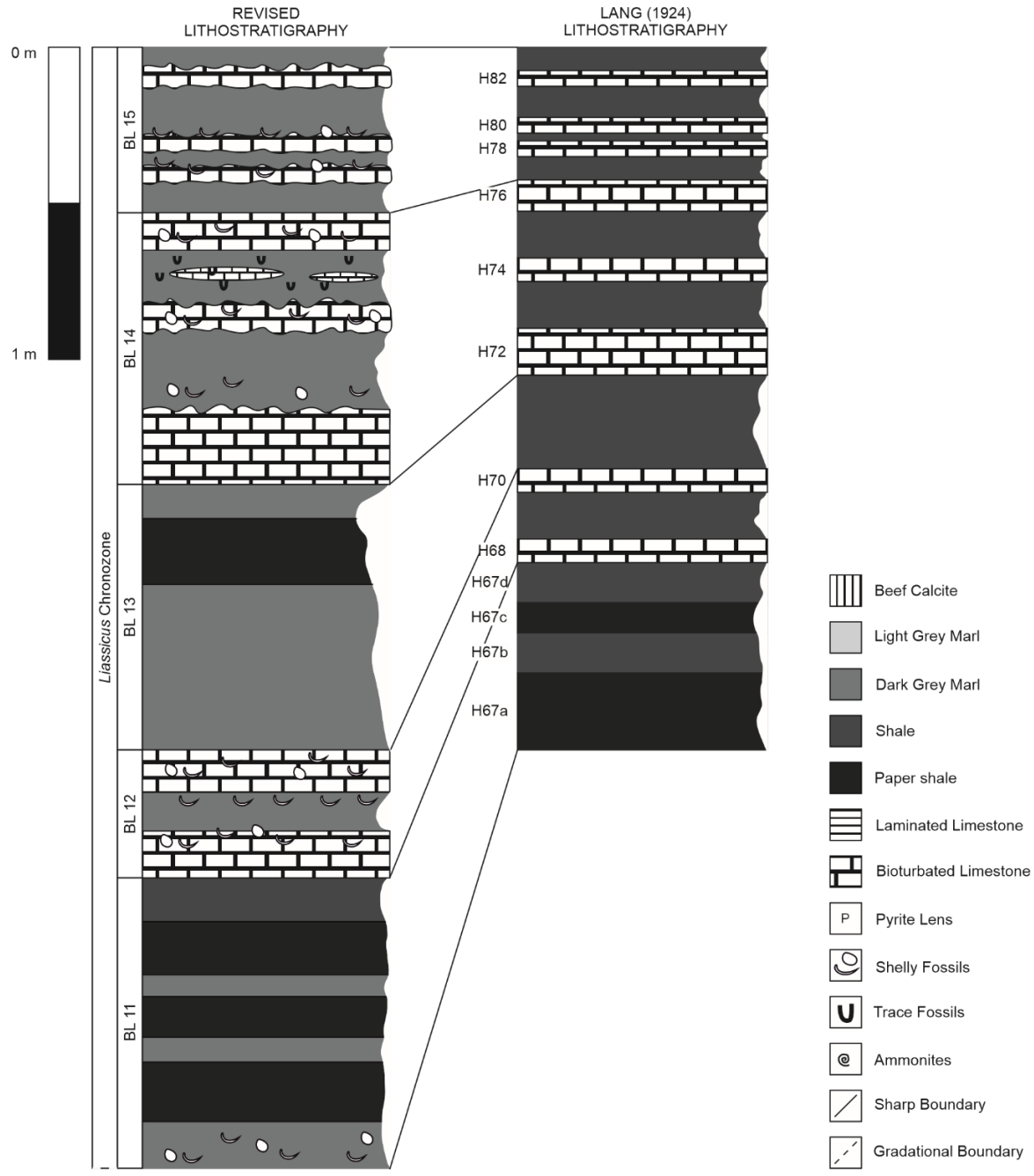

Figure 2.18 – Revised lithostratigraphy of BL 11 – BL 15. Comparison is offered to the lithostratigraphic log of Lang (1924). Key in figure. Scale = 1 m.

BL 16 (1.24 m) = bioturbated limestones of different thicknesses (60 – 290 mm) are separated by variable argillaceous lithology bundles (fig. 2.19). Each limestone has a hummocky upper surface and well-cemented, homogeneous internal texture. H84 is locally divided by an impersistent light marl lens (fig. 2.19). A thin (20 – 50 mm) layer of light marl overlays each of the limestone beds, but the two lithologies share an atypically sharp contact (fig. 2.19); in contrast, light marl-dark marl/shale boundaries are gradational (fig.

2.19). The topmost argillaceous lithology bundle (0.26 m thick) has a basal light marl bed overlain by a dark marl/shale/dark marl repetition (fig. 2.19).

BL 17 (0.47 m) = a pair of thick (average = 0.22 m) bioturbated limestones with hummocky upper and lower surfaces are separated by a thin (30 mm) interbed of dark marls (fig. 2.19). The basal limestone has abundant, irregular pyrite spheroids (10 – 30 mm in diameter) that cover approximately 2 % of its lower surface.

BL 18 (0.4 m) = the four/five closely spaced, irregular bioturbated limestone beds in BL 18 are of a uniform thickness (30 – 50 mm) and present along the length of the exposure (fig. 2.19). Their unique morphology is formed of small lenticular nodules, approximately 50 – 300 mm in diameter, that partially or fully coalesce across the horizontal axis. Limestones are separated by dark marl interbeds of similar thicknesses (20 – 40 mm; fig. 2.19). Weedon et al. (2018) position a depositional hiatus at Bed 1c and suggest that closely spaced limestones within this part of the *Angulata* Chronozone reflect non-deposition and condensation.

BL 19 (1.65 m) = a total of 7 tabular bioturbated limestone beds are separated by variable argillaceous lithologies or lithology bundles (fig. 2.19). Each of the limestones is of a similar thickness (90 – 190 mm) and has planar upper and lower surfaces (fig. 2.19). Argillaceous sediments at the base of the section (below Third Tape) are predominately comprised of light marls (n = 4) with infrequent dark marls (n = 2) and shales (n = 1) (fig. 2.19); in the upper part of the section there is an equal number of light marl, dark marl and shale layers although thicknesses vary significantly (fig. 2.19). The contacts between non-limestone lithologies are gradational (fig. 2.19). Thin (1 – 5 mm) layers of pyritic sediment/inorganic concretionary pyrite are present in the topmost dark marls and shales (fig. 2.19). The macrofaunal fossil assemblage is highly irregular and discussed later in the thesis (see Chapter 3).

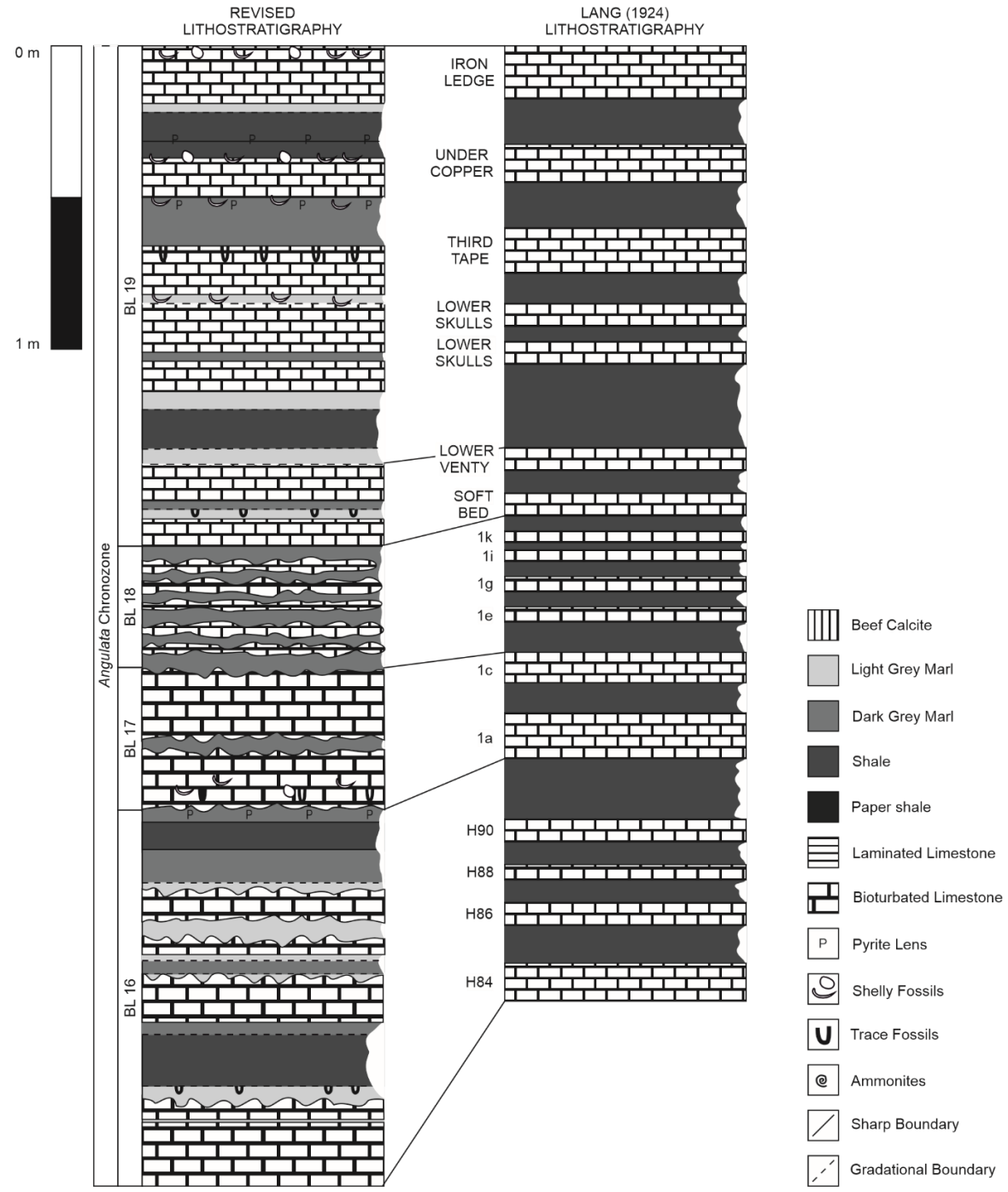

Figure 2.19 – Revised lithostratigraphy of BL 16 – BL 19. Comparison is offered to the lithostratigraphic log of Lang (1924). Key in figure. Scale = 1 m.

BL 20 (0.36 m) = the pair of nodular bioturbated limestone beds in BL 20, measuring 70 mm and 80 mm in thickness respectively, contain lenticular concretions up to 1 m in diameter (fig. 2.20). Nodules have an isolated or coalescent morphology and the space between them is occupied by light marls (fig. 2.20); there is a thin (10 – 30 mm), argillaceous margin around the limestones that creates a gradational contact with the

surrounding sediment. Argillaceous interbeds are comprised of dark marls (40 mm and 90 mm thick) at the base of the section and shales (80 mm thick) in the upper part (fig. 2.20).

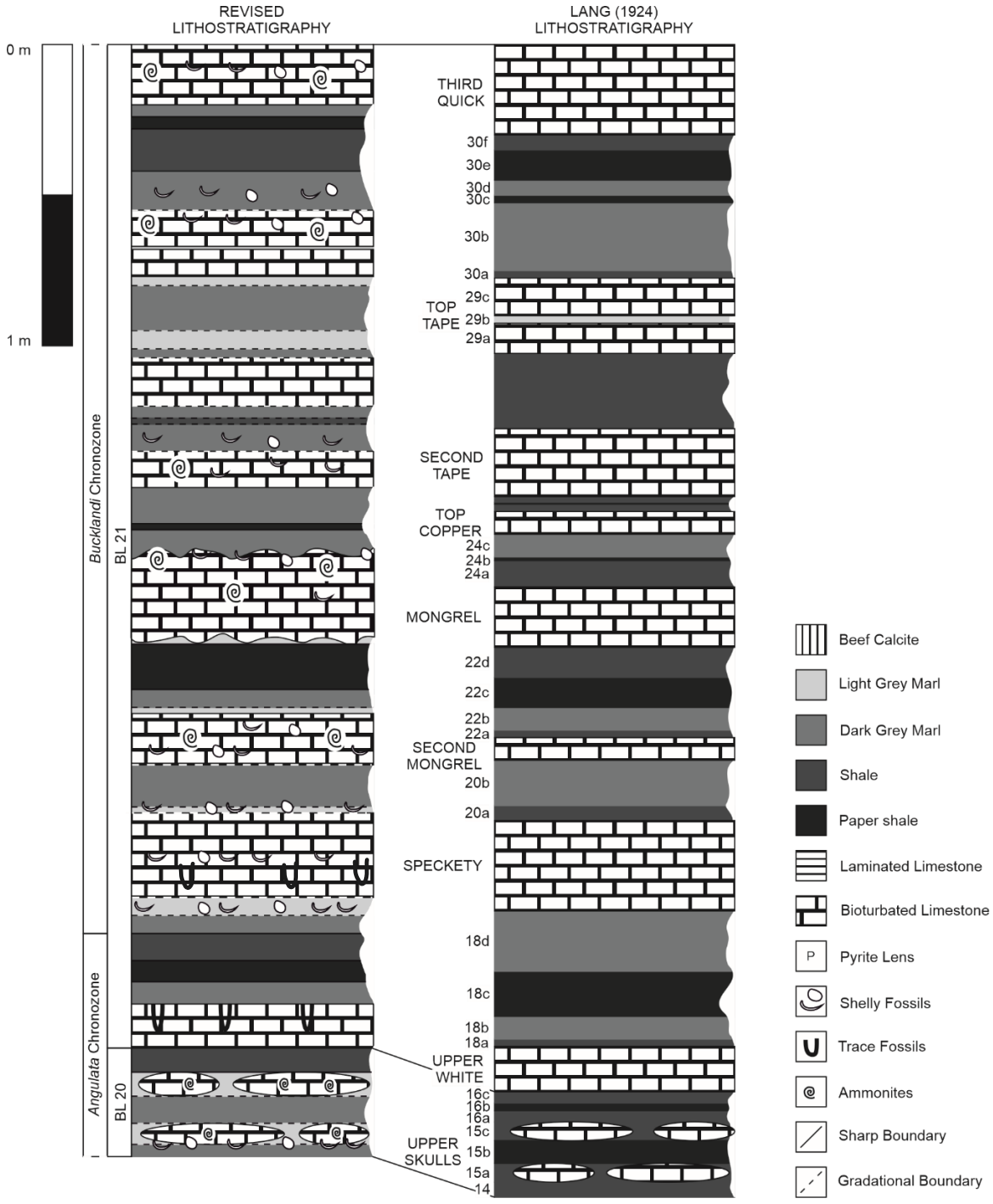

Figure 2.20 – Revised lithostratigraphy of BL 20 and BL 21. Comparison is offered to the lithostratigraphic log of Lang (1924). Key in figure. Scale = 1 m.

BL 21 (3.33 m) = a total of 8 tabular bioturbated limestones of different thicknesses (0.12 – 0.3 m) are separated by variable argillaceous lithology bundles that lack a clear trend regarding the order of different lithologies (fig. 2.20). Thin (20 – 60 mm) layers of light

marl are adjacent to the upper and/or lower surfaces of several of these limestones (n = 4) (fig. 2.20). All of the limestones are fossiliferous, but key individuals include the Speckety – a thick (0.28 m) bioturbated limestone with a central (40 mm) argillaceous layer containing well-defined ichnotaxa, and Top Tape – a concentration lagerstätte known as the Ammonite Graveyard and noteworthy for the high number of large (50 – 300 mm) ammonoids preserved on its upper surface (e.g. Jordan et al., 2015) (see Chapter 3). Previous studies have described evidence for seafloor erosion associated with several of the limestones, including Speckety, Mongrel, and Top Copper (e.g. Weedon, 1986, Weedon, 1987, Weedon et al., 2018).

BL 22 (1.05 m) = BL 22 is a single argillaceous lithology bundle that can be subdivided in to two distinct components (fig. 2.21). At the base of the section there is a pair of dark marl-shale repetitions containing individual beds of similar thicknesses (0.13 – 0.15 m) (fig. 2.21); the upper part is comprised of two paper shale-dark marl repetitions that show significant variation in the thicknesses of different beds (0.06 – 0.19 m) (fig. 2.21).

BL 23 (0.4 m) = a pair of laterally persistent, tabular bioturbated limestones are separated by a thin layer of paper shales (50 mm) (fig. 2.21). The thickness of the lower limestone bed (Gumption) varies along the length of the exposure; at the measured section it was 0.14 m thick but is known to thin locally to approximately 50 mm.

BL 24 (1.12 m) = the main section is a complex, primarily argillaceous lithology bundle that contains dark marls, shales, and paper shales (fig. 2.21). There is a laterally persistent, irregular limestone in the upper part of the section (0.14 m thick) and an impersistent nodular limestone bed (70 mm thick), with isolated lenticles that measure up to 3 m in diameter, at its base (fig. 2.21). Paper shale and shale beds below the Rattle limestone are thinner (40 – 70 mm) than their dark marl counterparts (up to 0.16 m) (fig. 2.21); above this the dominant lithology is reversed, and paper shales are thicker (0.16 m) than dark marls (up to 100 mm) (fig. 2.21). The contact between different argillaceous lithologies is sharp and planar (fig. 2.21).

BL 25 (0.69 m) = two laterally persistent tabular limestones of different thicknesses (0.35 and 0.17 m) are separated by a single shale interbed (fig. 2.21). The succession is difficult to access above this point at Monmouth Beach, Dorset (fig. 2.3) and therefore the reliability of any measurements/observations should reflect this situation.

Figure 2.21 – Revised lithostratigraphy of BL 22 – BL 25. Comparison is offered to the lithostratigraphic log of Lang (1924). Key in figure. Scale = 1 m.

BL 26 (1.83 m) = another exclusively argillaceous lithology bundle, BL 26 can be subdivided in to two overlapping trends (fig. 2.22). At the base of the section is a relatively thick (0.16 m) bed of paper shales overlain by a complete sequence of argillaceous lithologies i.e. light marls-dark marls-shales-paper shales (fig. 2.22). The upper part of the section contains alternating paper shales (n = 4) and dark marls (n = 3) (fig. 2.22); paper

shales are consistently the thinner of the two lithologies (80 – 160 mm and 140 – 300 mm respectively; fig. 2.22).

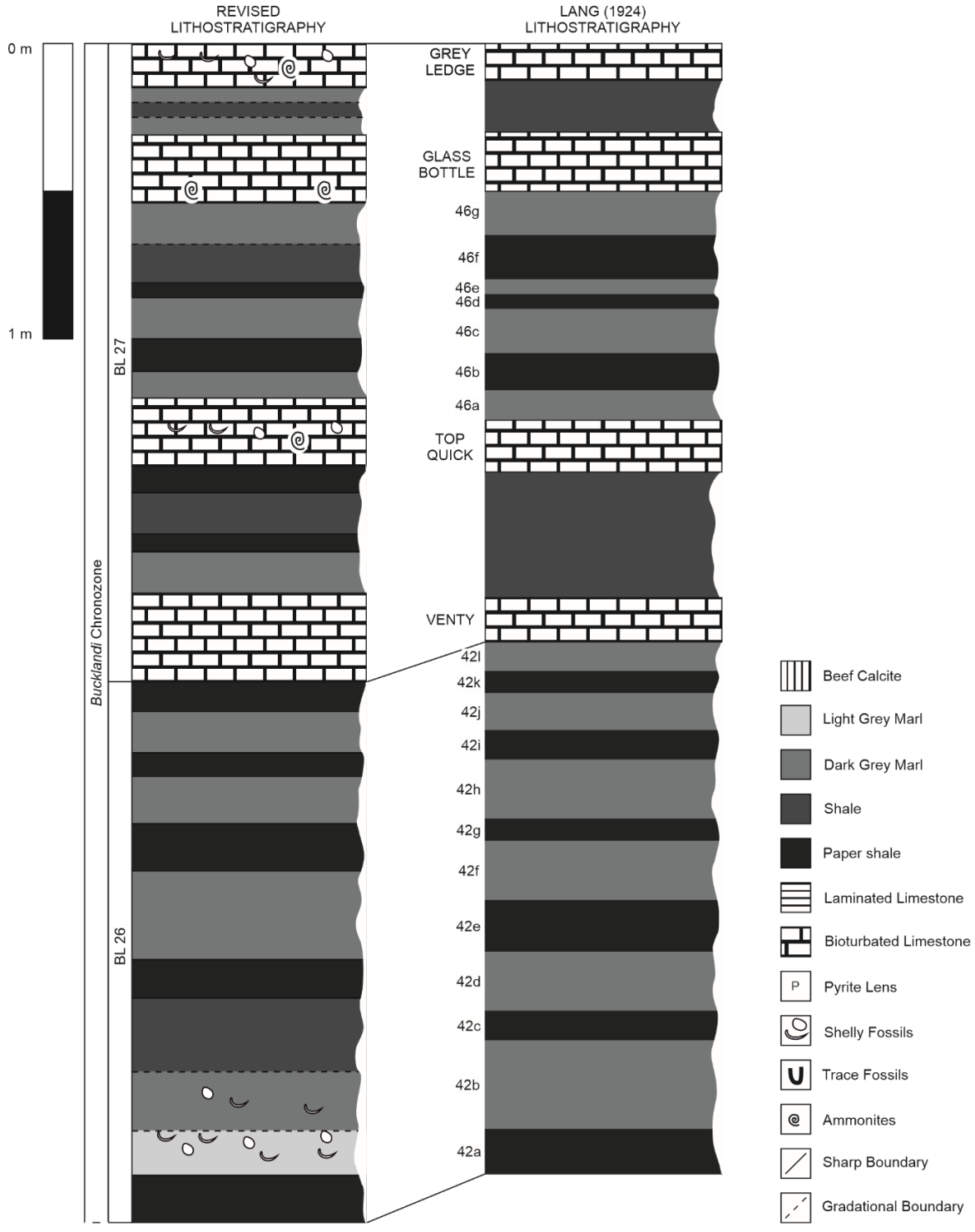

Figure 2.22 – Revised lithostratigraphy of BL 26 and BL 27. Comparison is offered to the lithostratigraphic log of Lang (1924). Key in figure. Scale = 1 m.

BL 27 (2.16 m) = a series of four tabular bioturbated limestones, separated by variable argillaceous lithology bundles, cap the BLF (fig. 2.22). The limestones are of varying

thicknesses (0.15 – 0.3 m) and generally have sharp upper and lower contacts (fig. 2.22). Thin (50 – 90 mm) paper shale beds are common in the lower part of the section (below Glass Bottle; n = 4) whereas dark marls (n = 6) and shales (n = 3) are persistent throughout (fig. 2.22). The top surface of Grey Ledge has abundant ichnotaxa (*Arenicolites* and *Diplocraterion*) and *Arietites* ammonoids (Gallois and Paul, 2009); previous studies have inferred that there was an erosive surface at this position (e.g. Hallam and Lang, 1960, Gallois, 2008a, Gallois and Paul, 2009). The top of Grey Ledge marks the BLF-CMF boundary (Hallam and Lang, 1960, Gallois, 2008a, Gallois and Paul, 2009).

2.3.3. Revised lithostratigraphy of the Shales-with-Beef Member in Dorset

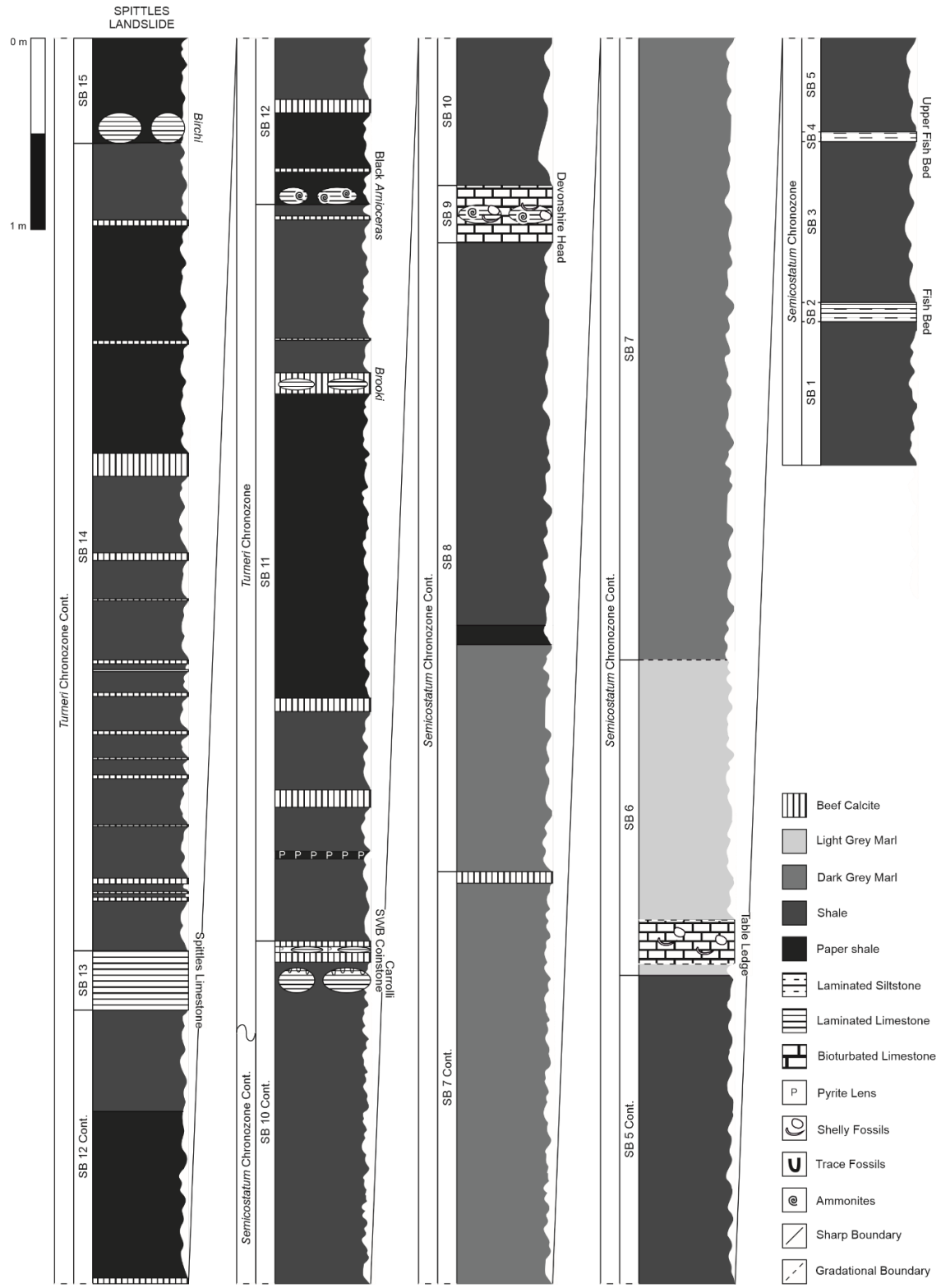

Figure 2.23 – The revised lithostratigraphic log for the SWB (SB 6 – SB 15) at the SLS, Dorset (fig. 2.4). The basal section (SB 1 – SB 5) was based on measurements from Lang (1924) and included for reference purposes only. Revised section numbers follow Gallois (2008a) whereas individual bed numbers follow Lang et al. (1923) and Lang (1924). Key in figure. Scale = 1 m.

The following lithostratigraphic account of the SWB uses the section numbering system of Gallois (2008a) and offers comparison with the lithostratigraphic log of Lang et al. (1923). The basal SWB (SB 1 – SB 5) is present at the SLS on Black Ven (fig. 2.4), but the outcrop is impossible to examine following recent obscuration by landslide debris. A reference section for the aforementioned strata is included in this study (fig. 2.23), based on measurements from Lang (1924), but is intended for comparative purposes only. As it is not referenced later in the thesis, no attempt was made to describe the lithology, sedimentology and/or fossil content of the basal section between SB 1 – SB 5.

SB 6 (1.65 m) = the section is primarily comprised of pale grey, calcareous light marls (fig. 2.24) that are conchoidal on a weathered surface and show no recognisable bedding-parallel fissility. At the base of the section is a thick (0.23 m), tabular bioturbated limestone bed (fig. 2.24) with a poorly-cemented, muddy sediment composition; the lithology shows moderate lateral variation and is locally replaced by a dolomitic limestone. An argillaceous upper and lower margin results in a gradational contact with the sediments above and below (fig. 2.24). The light marl fossil assemblage is limited to compressed *Arnioceras* ammonoid moulds, whereas Table Ledge has a limited epifaunal assemblage (*Calcirhynchia* and *Liostrea*) and compressed *Arnioceras*.

SB 7 (5.4 m) = obscuration by landslide debris at the 2008LS and SLS meant that detailed description of the lithostratigraphy was difficult. At the PLS and CHCS, varying proportions of the section are beneath beach level (fig. 2.24). In the western part of Black Ven, specifically the 2008LS and SLS, those parts of the section that were accessible are made up of conchoidal dark marls (fig. 2.24). At the PLS, dark marls alternate with thick shale beds and the two lithologies are separated by multiple laterally impersistent beef bands (10 – 100 mm thick) (fig. 2.24). Light marls were only found at the eastern end of Black Ven, specifically the PLS and CHCS (fig. 2.24). The upper boundary of SB 7 is taken at the top surface of a fibrous beef calcite band (60 mm thick) that is laterally persistent across the 2008LS, SLS, and PLS but replaced at the CHCS by a thick (0.24 m), tabular muddy limestone bed underlain by thin (40 mm), widely spaced septarian limestone nodules measuring up to 0.3 m in diameter (fig. 2.24). Both limestone beds contain poorly-preserved *Arnioceras* ammonoids.

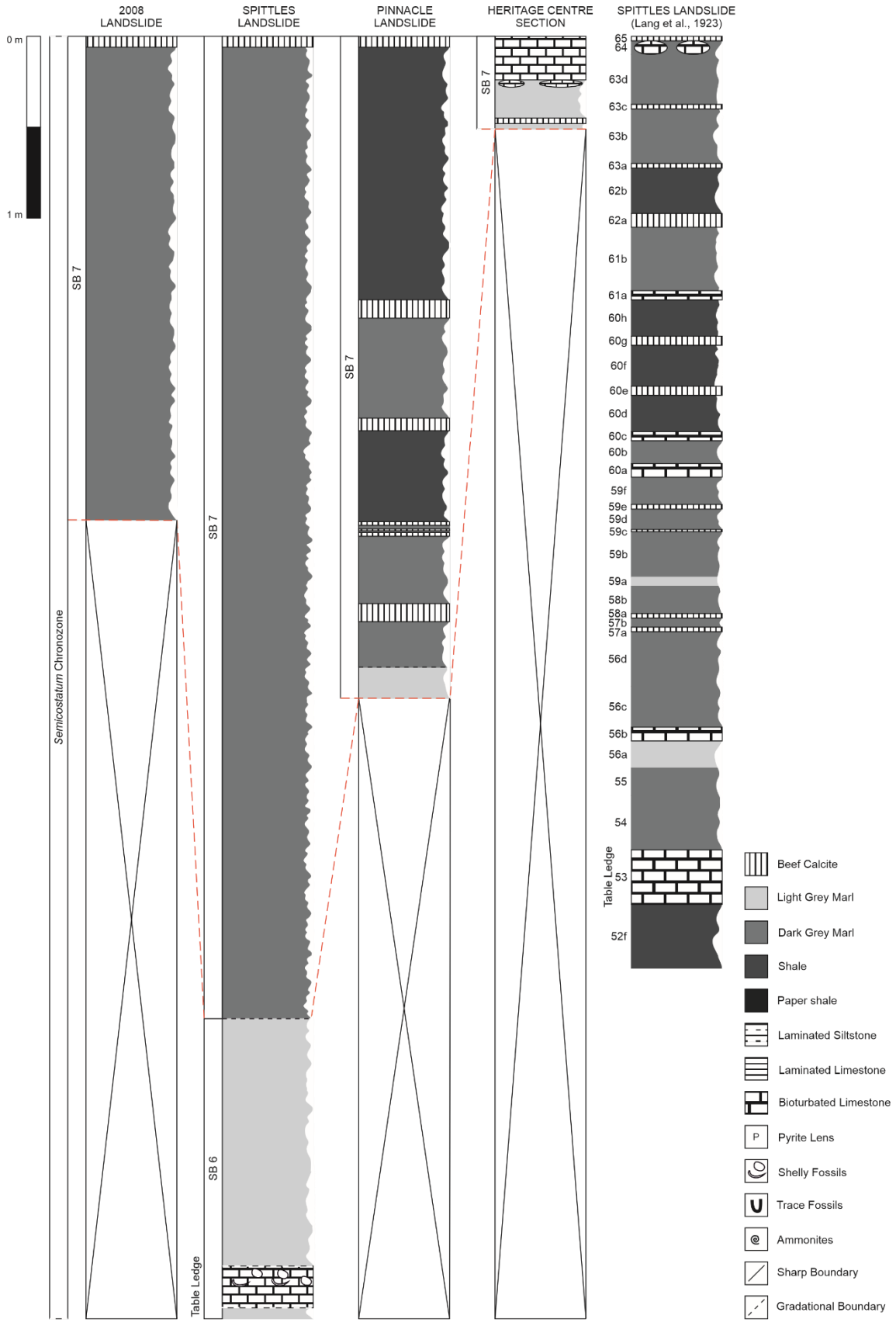

Figure 2.24 – Lithostratigraphy, including lateral variability in the lithology and thicknesses, of SB 6 – SB 7 across the measured sections on Black Ven, Dorset (fig. 2.4). Revised section numbers follow Gallois (2008a). Comparison is offered to the lithostratigraphy of Lang et al. (1923). Key in figure. Scale = 1 m.

SB 8 (1.4 – 3.55 m) = the section is comprised of variable argillaceous lithologies or lithology bundles (fig. 2.26). At the 2008LS, SB 8 is made up entirely of dark grey shales (fig. 2.26). At the SLS and PLS, there are variable proportions of shales in the upper part of the section and conchoidal dark marls in the lower part (fig. 2.26). The CHCS has a pair of dark marl beds (0.4 m thick), separated by a thick (1 m) shale interbed, at the base of the section (fig. 2.26); this lithology bundle is capped by a single, relatively thin (0.2 m) layer of light marl that shares a (local) gradational contact with the base of the Devonshire Head limestone (fig. 2.26). Previous studies (e.g. Lang et al., 1923, Gallois, 2008a) record a nodular septarian limestone (*Alcinoë* Bed) within SB 8 that has not been identified in this account (fig. 2.26). The thickness of SB 8 varies significantly; minimum and maximum thicknesses were recorded at the 2008LS (1.4 m) and PLS (3.55 m) respectively (fig. 2.26).

SB 9 or Devonshire Head (0.17 – 0.3 m) = SB 9 is a laterally persistent tabular limestone (fig. 2.26) that is difficult to classify owing to significant lithological variability. Its most common form is a dark grey/brown, well-cemented muddy limestone (e.g. Gallois, 2008a) that is replaced locally by a brown ferroan dolomite or dolomitic limestone. At the 2008LS there is a single layer of small pyritic concretions enclosed by beef limestone on its upper surface that measure up to 70 mm in thickness and 100 mm in diameter (fig. 2.26). At the SLS, shell-rich lenses of peloidal laminated limestone are enclosed by the main tabular body (fig. 2.26); these features measure up to 100 mm in thickness and 0.4 m in length (fig. 2.26). The abundant fossil assemblage is dominated by randomly orientated molluscan fauna including bivalve and gastropod spat as well as *Arnioceras* ammonoids (fig. 2.25). Fossils are replaced by coarse calcite spar (100 – 900 μm) and pyritic margins, approximately 50 μm in thickness and comprised of aggregated pyrite crystals, partially coat the external surface of calcitic ammonoid moulds (fig. 2.25).

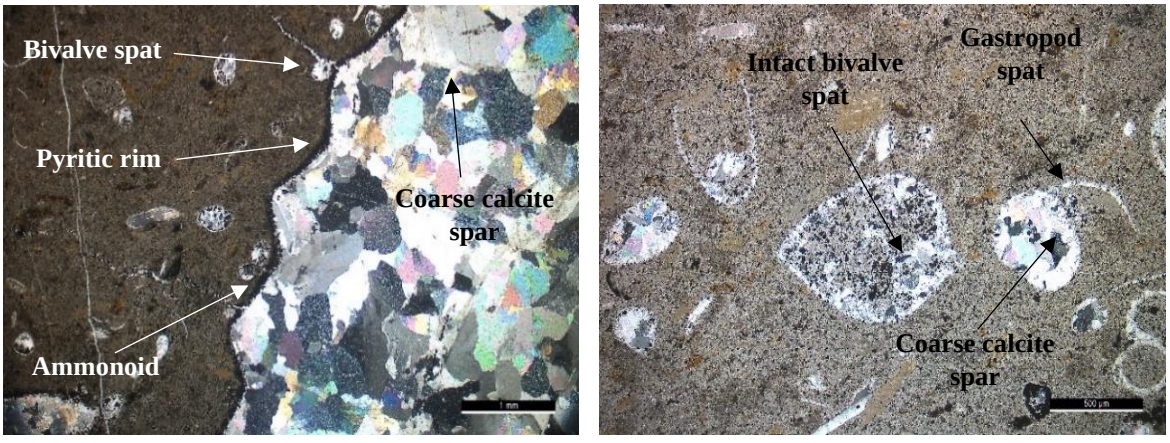

Figure 2.25 – Photomicrographs of the peloidal laminated limestone lenses in SB 9 under cross-polarised light. Left: pyritic rim coating a calcitic ammonoid mould. Right: bivalve and gastropod spat. Scales = 1 mm and 500 μm respectively.

SB 10 (2.02 – 3.52 m) = SB 10 was not identified in its original form (*sensu* Gallois, 2008a) west of the CHCS (fig. 2.26). Therefore, in order to make a clear distinction between SB 10 and SB 11 in this study, the revised boundary is taken as the upper surface of a thick, laterally persistent beef band present at the 2008LS and SLS (0.18 and 0.11 m respectively) that is replaced by a laterally variable limestone/dolomitic limestone at the PLS and CHCS (0.3 and 0.17 m respectively) (fig. 2.26). Grey shales constitute the entirety of the argillaceous lithology component at the 2008LS, SLS, and PLS (fig. 2.26); at the CHCS there is a single additional bed of dark marls (0.6 m thick) at the base of the section (fig. 2.26).

The Carrolli Bed is a layer of concretionary laminated limestones that occur at different heights within SB 10 along the length of the exposure (fig. 2.26). It is positioned in the lower-central part of the 2008LS, at the top of the SLS, and at the base of the CHCS (fig. 2.26); the concretionary component is missing from the PLS, but this may be an artefact of limited exposure (fig. 2.26). These peloidal, organic-rich wackestone concretions are relatively thin (70 – 130 mm), widely spaced (1 – 3 m), and share a gradational contact with the enclosing sediment. The upper surface has *Diplocraterion* trace fossils that penetrate 10 – 30 mm into the nodule. The fossil assemblage is limited to molluscan spat, compressed *Arnioceras* ammonoids, and rare epifaunal bivalves (*Oxytoma*).

The SWB Coinstone is a pyritic concretionary laminated limestone that is exclusive to the SLS and enclosed by a thick (0.11 m) beef band at the top of SB 10 (fig. 2.26). Thin (20 – 30 mm), planar wackestone concretions have a 1 – 5 mm rim of pyrite on the upper and lateral surfaces. Closely spaced circular borings are abundant on the outer pyritic layer (40 % of total area), measure 2 – 3 mm in diameter, and penetrate approximately 0.5 – 2 mm into the nodule. The SWB Coinstone is similar to the Coinstone hiatus of the BVM (see Section 2.3.4) and so it is possible that the two units share a similar origin/diagenetic history; the borings on the outer surfaces are indicative of exhumation and exposure as a hardground prior to reburial (e.g. Hallam, 1969, Hesselbo and Palmer, 1992).

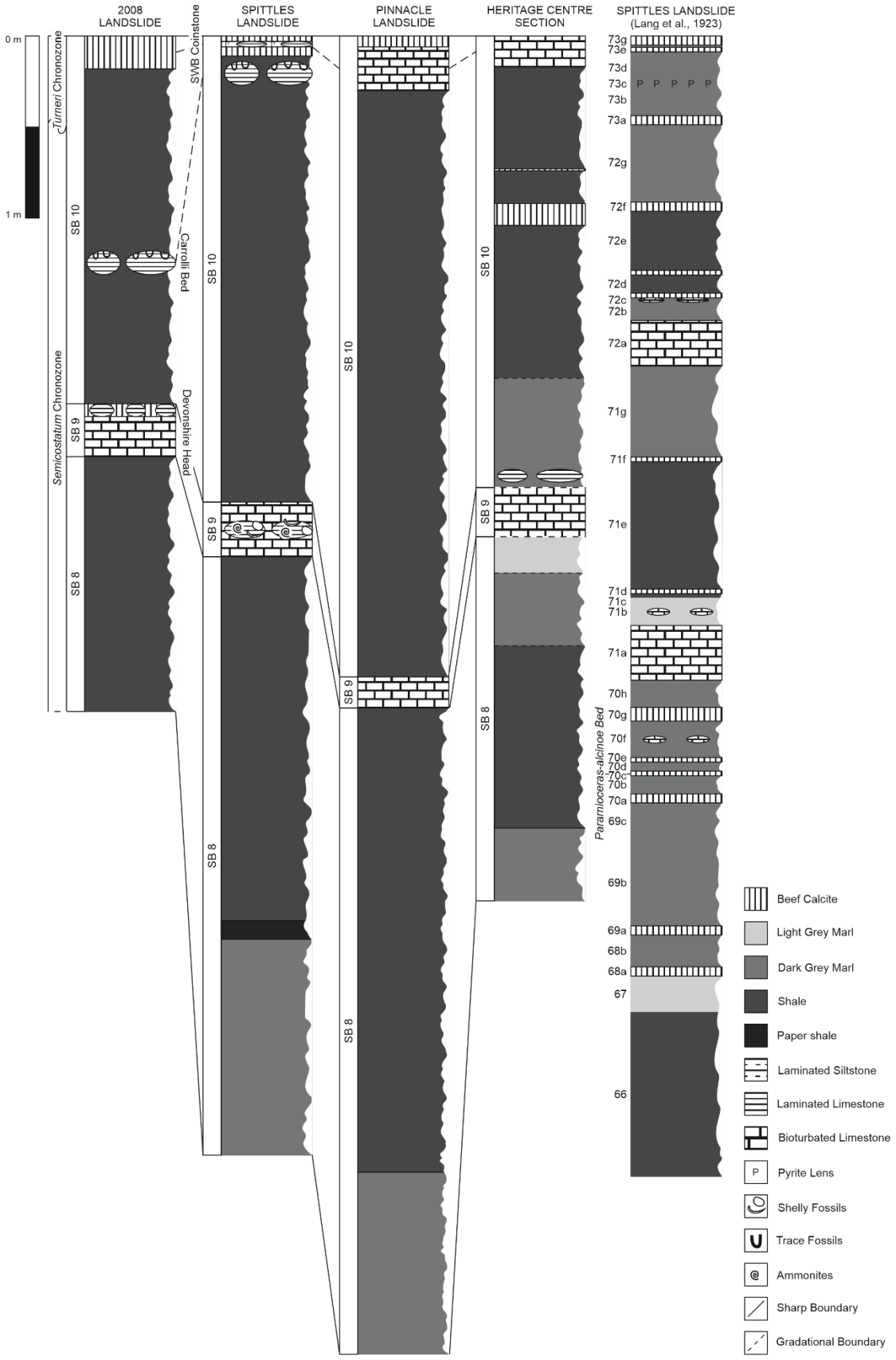

Figure 2.26 – Lithostratigraphy, including lateral variability in the lithology and thicknesses, of SB 8 – SB 10 across the measured sections on Black Ven, Dorset (fig. 2.4). Revised section numbers follow Gallois (2008a). Comparison is offered to the lithostratigraphy of Lang et al. (1923). Key in figure. Scale = 1 m.

SB 11 (3.85 – 4.79 m) = the section is dominated by dark grey shales that are divided by multiple thick beef bands (up to 100 mm in thickness; fig. 2.27) and numerous thin, laterally impersistent beef bands (generally not figured). The SLS has an additional central unit of fissile paper shales (1.6 m thick; fig. 2.27). Both argillaceous lithologies have a limited fossil assemblage that contains marine reptiles and poorly-preserved, compressed ammonoid moulds. The laterally persistent beef band in the upper part of the section measures approximately 0.1 m thick and contains a layer of laminated limestones known locally as the *Brooki* Bed (fig. 2.27). These peloidal wackestone concretions are widely spaced (up to 2 m apart), measure up to 0.5 m in diameter, and contain *Caenisites* ammonoids preserved as calcitic internal moulds.

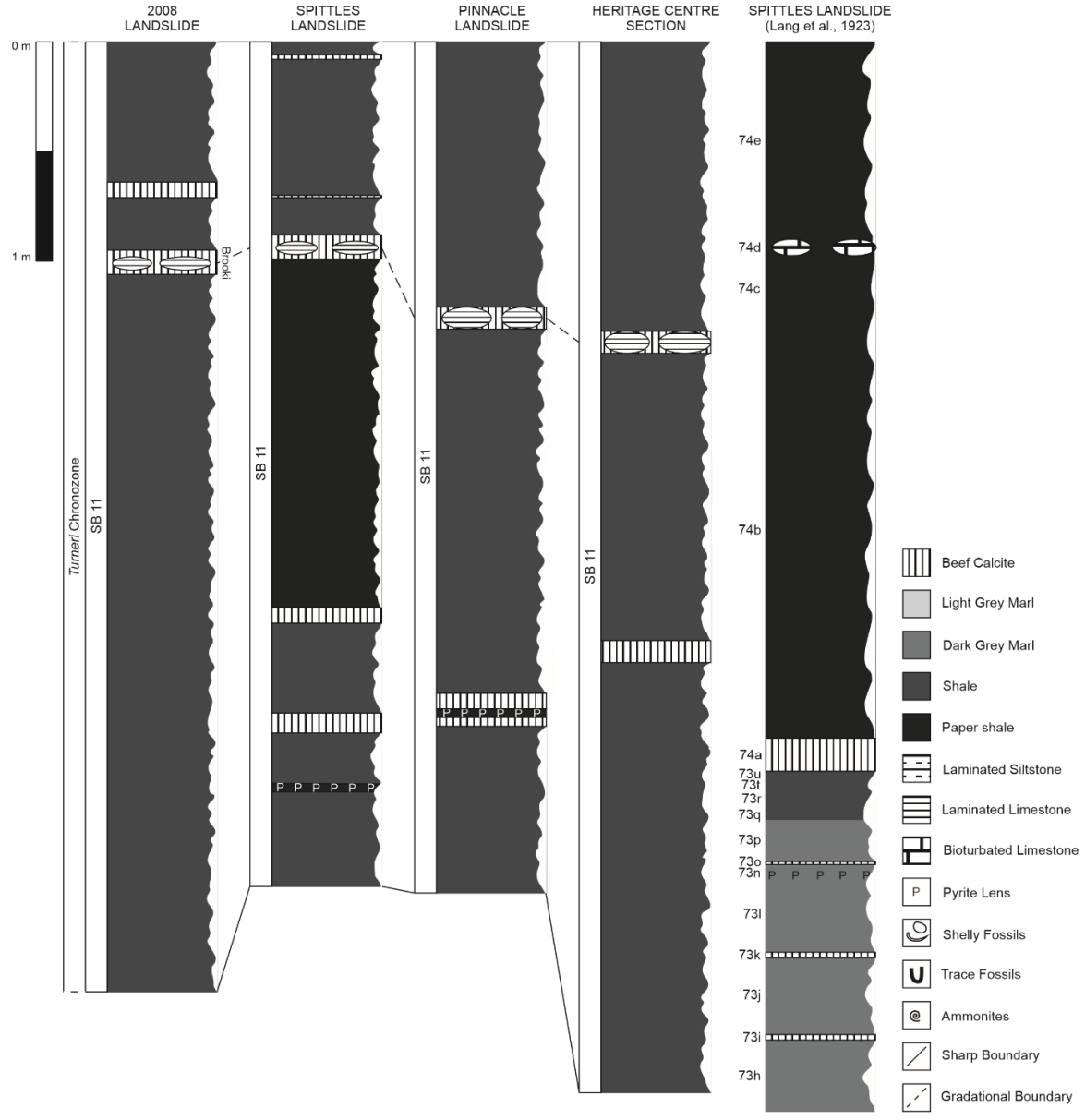

Figure 2.27 – Lithostratigraphy, including lateral variability in the lithology and thicknesses, of SB 11 across the measured sections on Black Ven, Dorset (fig. 2.4). Revised section numbers follow Gallois (2008a). Comparison is offered to the lithostratigraphy of Lang et al. (1923). Key in figure. Scale = 1 m.

SB 12 (2.23 – 4.02 m) = at the western end of Black Ven, specifically the 2008LS and SLS, SB 12 contains a basal limestone-bearing unit of black, fissile paper shales (0.26 and 0.48 m respectively; fig. 2.29); the remainder of the argillaceous lithology component is comprised of paper shales and/or shales (fig. 2.29). The PLS and CHCS are without limestone concretions and the argillaceous component is restricted to shales (fig. 2.29). Multiple beef calcite bands (20 – 180 mm thick) divide the section (fig. 2.29).

The layer of concretionary laminated limestones at the base of SB 12 is known as the Black *Arnioceras* Bed; it is replaced at the PLS and CHCS by a thick (0.18 m) fibrous beef calcite band (fig. 2.29). Widely spaced (0.5 – 2 m), lenticular concretions that measure up to 2 m in length and 90 mm in thickness contain an abundant assemblage of randomly oriented *Arnioceras* ammonoids and molluscan spat (fig. 2.28) (see Chapter 7). The fossil assemblage does not appear to be preserved in the paper shales between concretions, but this may be an artefact of poor exposure in the weathered cliff profile. Bioclasts account for a variable proportion of the overall sediment composition (up to a maximum of 60 %) and are preserved by coarse calcite spar (50 – 500 μm; fig. 2.28); the remaining sediment is comprised of microspar, peloids, and organic matter (fig. 2.28).

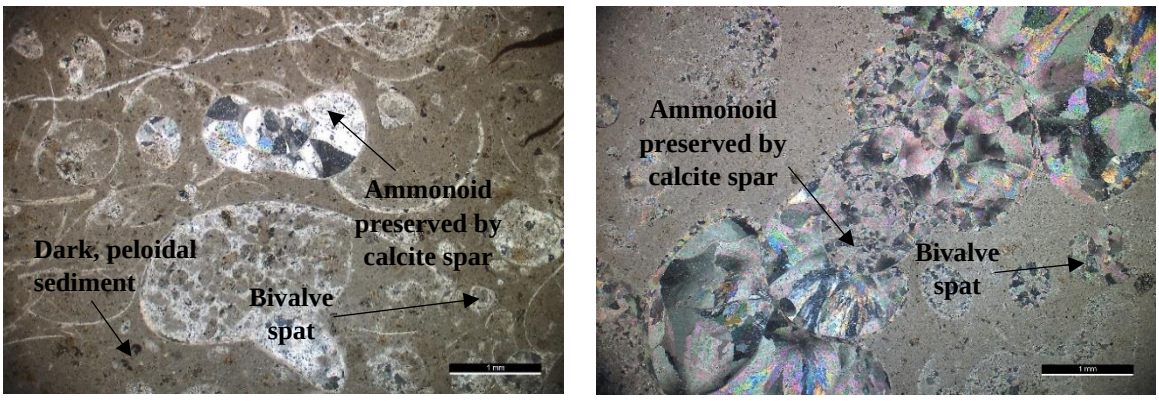

Figure 2.28 – Photomicrographs of the Black *Arnioceras* Bed concretions under cross-polarised light. Ammonoids and spat are abundant, preserved by coarse (50 – 500 μm) calcite spar. The sparite in the right image has undulous extinction which is typically associated with saddle dolomite. Scale = 1 mm.

SB 13 or Spittles Limestone (0.1 – 0.31 m) = the Spittles Limestone shows significant lithological variability along the length of the exposure (e.g. Gallois, 2008a) and is locally replaced by a ferroan dolomite or dolomitic limestone. At the 2008LS and SLS, it is a thick

(approximately 0.3 m), planar laminated limestone bed with a blocky morphology (fig. 2.29). The internal texture is comprised of calcite microspar, clay/organic-rich laminae (10 – 100 μm) and thin (1 – 3 mm), horizontal layers of imbricated shell fragments. SB 13 is replaced by a persistent beef band at the PLS (0.22 m thick) and by a pair of thin (30 mm) beef bands enclosing laminated limestone lenses (40 mm thick) at the CHCS (fig. 2.29).

SB 14 (2.69 – 4.22 m) = at the 2008LS and SLS, the lower-central part of SB 14 is comprised of shales that are subdivided by laterally impersistent beef bands of varying thicknesses (10 – 120 mm) (fig. 2.29); in the upper part of both sections, paper shales are the dominant lithology (fig. 2.29). At the PLS and CHCS, SB 14 is mostly made up of shales except for a thin (110 mm) bed of paper shales at the top of each section (fig. 2.29). It was not possible to examine the lithostratigraphy of the CHCS in detail owing to obscuration by landslide debris. A layer of sub-cylindrical, peloidal laminated limestone concretions at the 2008LS (fig. 2.29), measuring up to 0.4 m in diameter and 0.13 m in thickness, are sedimentologically and morphologically similar to the *Birchi* Bed of SB 15.

SB 15 (0.55 – 0.61 m) = the main section is made up of fissile black paper shales (fig. 2.29). At the base of SB 15 is a layer of concretionary laminated limestones, known locally as the *Birchi* Bed, that show significant lithological and morphological variability along the length of the exposure (see review by Rukin, 1990).

The *Birchi* Bed at the 2008LS and CHCS contains closely spaced, sub-spheroidal, peloidal laminated limestone concretions that share a gradational contact with the enclosing paper shales and measure up to 0.5 m in diameter and 0.16 – 0.22 m in thickness (fig. 2.29). The CHCS has a central beef band, up to 70 mm thick, that (locally) occupies the space between limestone nodules (fig. 2.29). At the PLS, laminated limestone concretions similar to those at the 2008LS and CHCS are enveloped by a thick (up to 0.23 m) bed of laminated ferroan dolomite (e.g. Rukin, 1990) with beef bands (20 – 50 mm thick) on the upper and lower surfaces (fig. 2.29); these complex structures form large blocks up to 2 m in length (see review by Rukin, 1990). At the SLS, the *Birchi* Bed shows considerable lateral variation with limestones similar to both types observed over a short distance. The morphology and lithology of the *Birchi* Bed and *Birchi* Tabular Bed (BVM 1; see section 2.3.4) are closely linked (see review by Rukin, 1990). The *Birchi* concretions are highly fossiliferous, but the assemblage is limited to nektonic and planktonic groups; molluscan fossils are preserved as internal moulds replaced by coarse calcite spar.

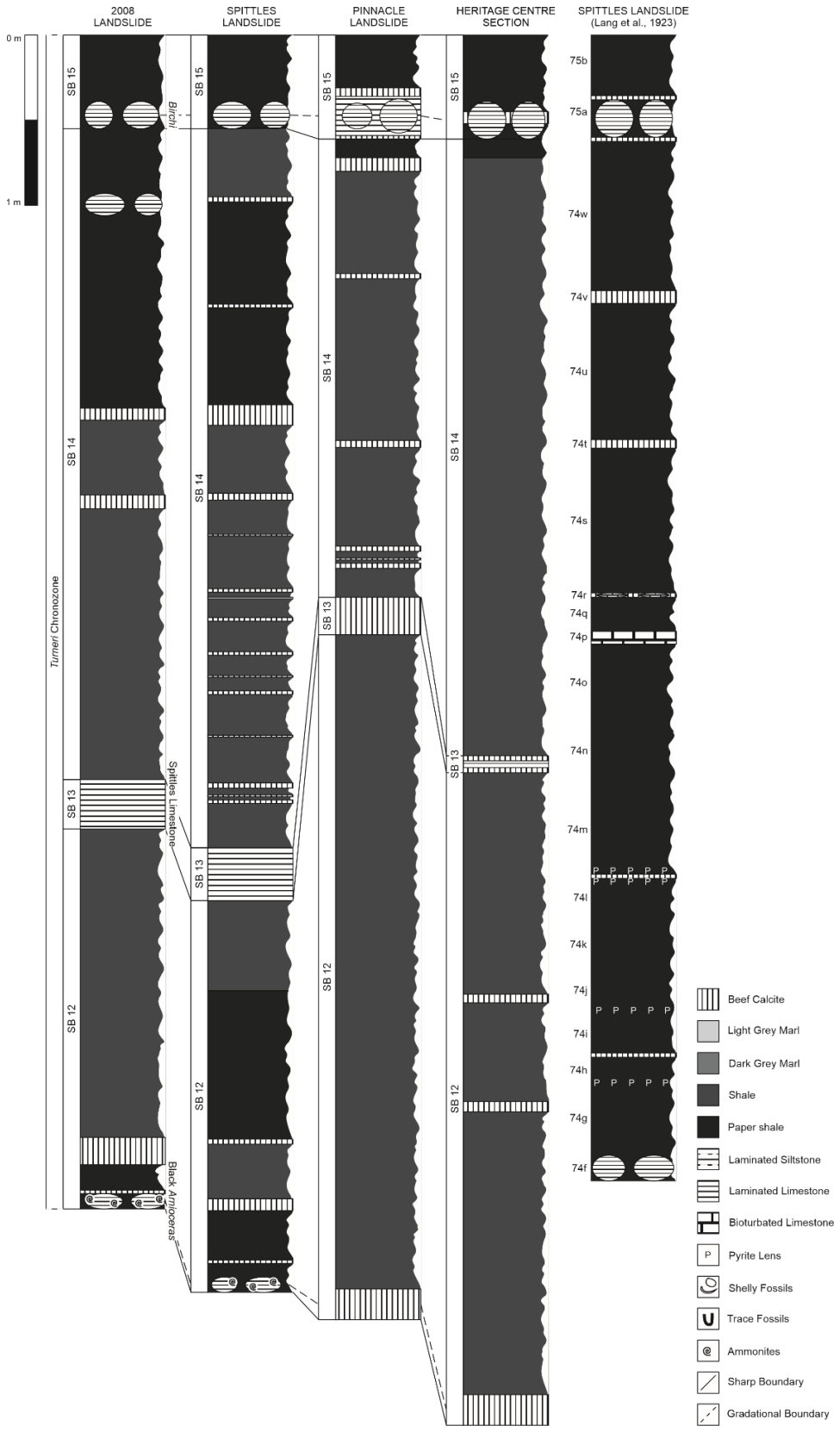

Figure 2.29 – Lithostratigraphy, including lateral variability in the lithology and thicknesses, of SB 12 – SB 15 across the measured sections on Black Ven, Dorset (fig. 2.4). Revised section numbers follow Gallois (2008a). Comparison is offered to the lithostratigraphic log of Lang et al. (1923). Key in figure. Scale = 1 m.

2.3.4. Revised lithostratigraphy of the Black Ven Marl Member in Dorset

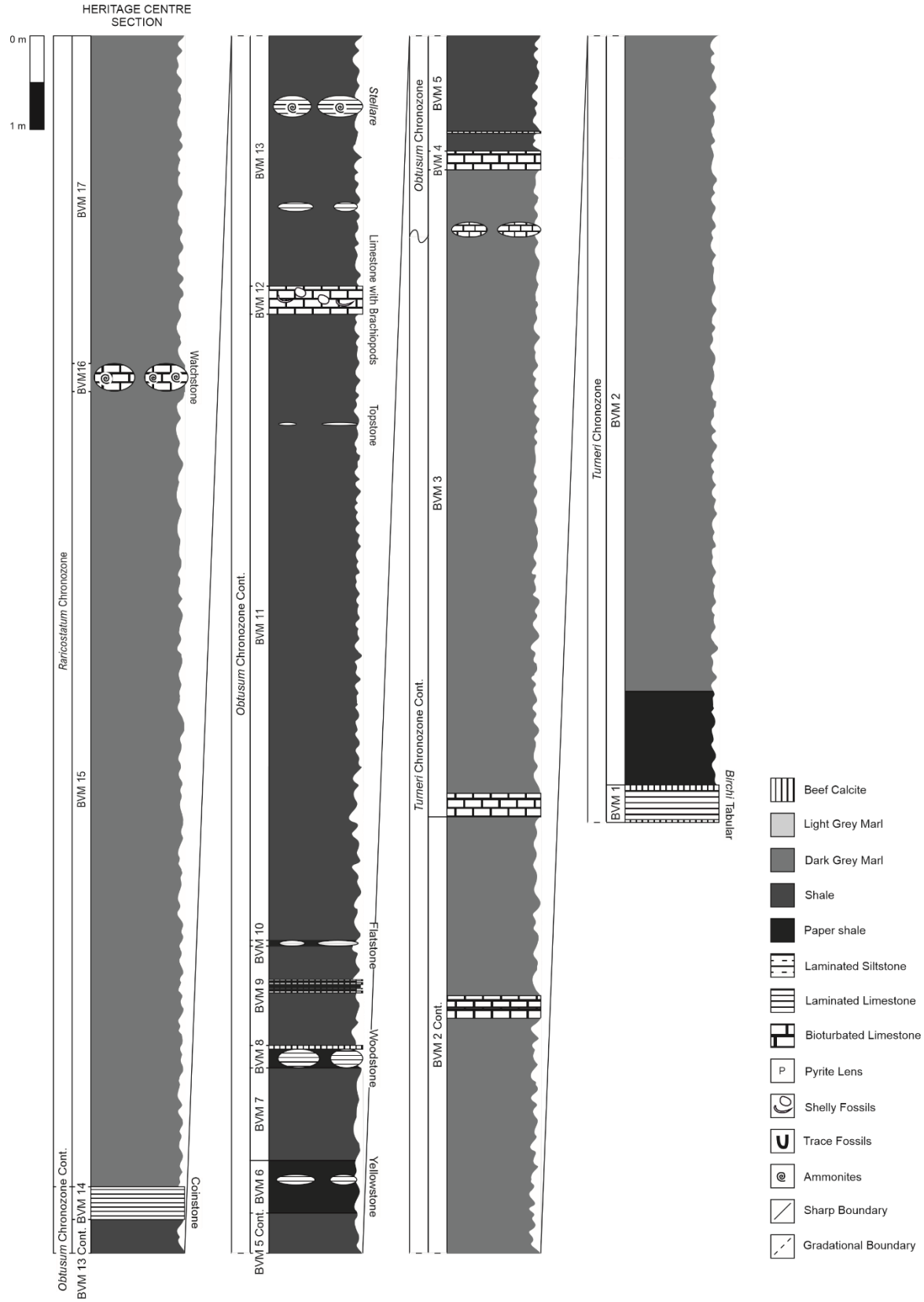

Figure 2.30 – The revised lithostratigraphic log for the BVM at the CHCS, Dorset (fig. 2.4). Key in figure. Scale = 1 m.

BVM 1 or *Birchi* Tabular (0.4 m) = the laterally persistent *Birchi* Tabular Bed has an inconsistent lithology that varies between a ferroan dolomite (*sensu* Rukin, 1990) and a peloid-rich, microsparitic laminated limestone. The typical morphology of both lithotypes is a thick (up to 0.4 m), blocky bed with planar upper and lower surfaces (fig. 2.31); this is replaced locally by large (up to 2 m in length), lenticular concretions that partially coalesce across the horizontal axis. The *Birchi* Tabular Bed has thin layers of beef calcite (15 – 30 mm) on its upper and lower surfaces at the SLS and CHCS (fig. 2.31). Lateral variability in lithology and morphology cannot be correlated to a specific position along the length of the exposure and so, for the purposes of this study, only the laminated limestone is considered. The *Birchi* Tabular Bed was examined in detail by Rukin (1990). BVM 1 is below beach level to the east of the River Char (Lang and Spath, 1926).

BVM 2 (12.66 m) = this section is exposed in full at the CHCS only (fig. 2.31). The lowest part of BVM 2 (below Bed 78) was not examined at the EBS by Lang and Spath (1926) so this account is not discussed. At the SLS and CHCS, BVM 2 has a thick (1.56 m and 1 m respectively) layer of paper shales at its base and conchoidal dark marls throughout the remainder of the section (fig. 2.31). Two nodular limestone beds (80 mm and 100 mm thick) are present in the central part of BVM 2 at the SLS (fig. 2.31); concretions are widely spaced (1 – 3 m) and unfossiliferous. A pair of closely-spaced limestone beds, each approximately 120 mm thick, occur in the upper part of the section at the CHCS (fig. 2.31).

BVM 3 (4.68 – 9.25 m) = the base of BVM 3 is taken at the lower surface of an argillaceous tabular limestone (0.24 – 0.3 m thick) that is present along the length of the exposure, but locally replaced by a dolostone or ferroan dolomite (fig. 2.32). The argillaceous lithological component at the PLS, CHCS, and EBS (after Lang and Spath, 1926) is made up of conchoidal dark marls (fig. 2.32). At the SLS, dark marls occur in the lower-central part of BVM 3 and are overlain by dark grey shales in the upper part of the section (fig. 2.32). There are two nodular limestone beds (0.1 m and 0.15 m thick) at the SLS with widely spaced concretions (1 – 3 m) (fig. 2.32); the lower limestone can be traced to the PLS and EBS (fig. 2.32). An additional argillaceous limestone bed (0.15 – 0.4 m thick) in the upper part of the section is laterally persistent but varies between a tabular and nodular morphology (fig. 2.32). The overall thickness of BVM 3 is expanded at the SLS where it reaches a maximum vertical thickness of 9.25 m (fig. 2.32).

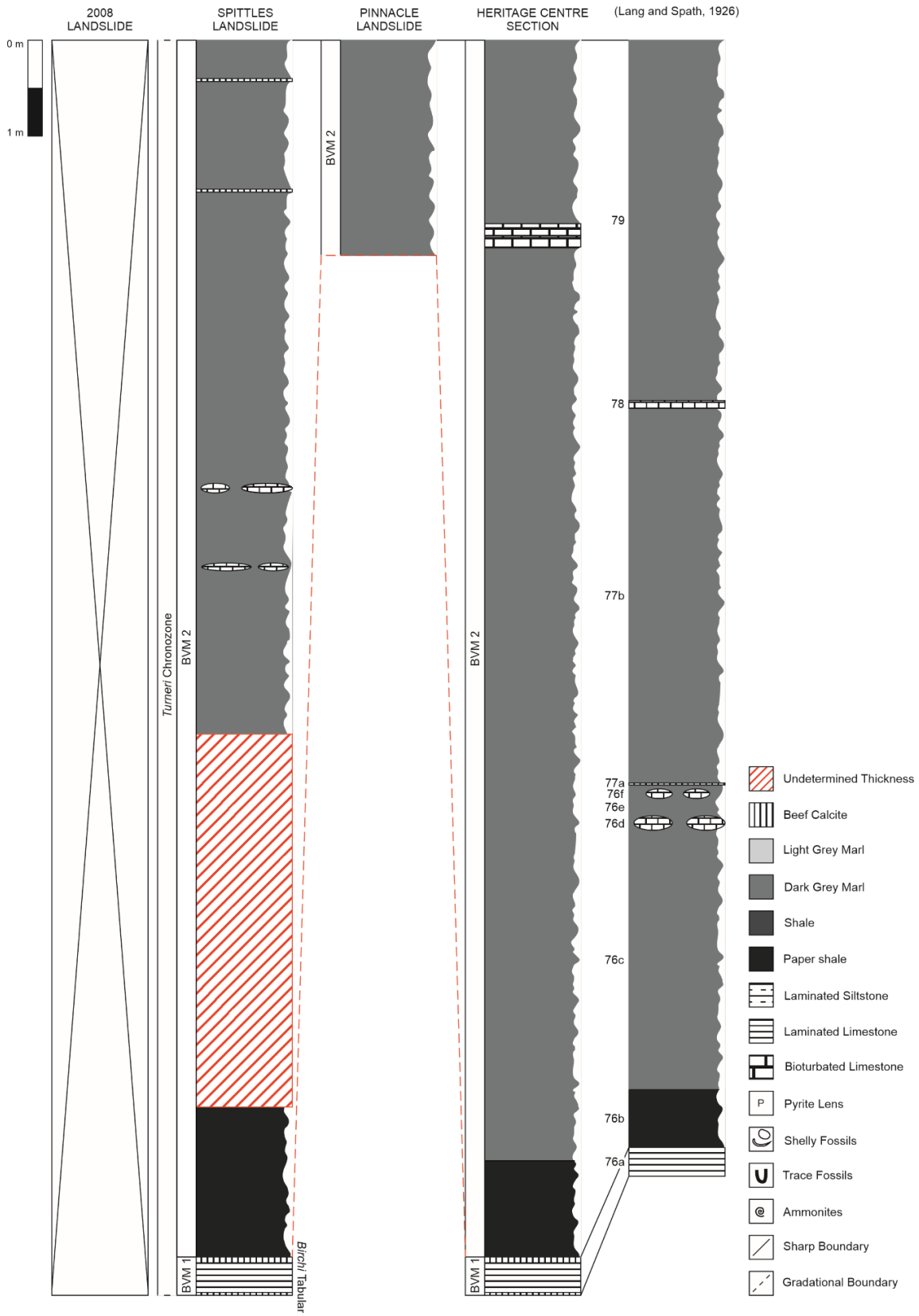

Figure 2.31 – Lithostratigraphy, including lateral variability in the lithology and thicknesses, of BVM 1 – BVM 2 across the measured sections on Black Ven, Dorset (fig. 2.4). Comparison is offered to the lithostratigraphic log of Lang and Spath (1926), although this section was not exclusive to the EBS (fig. 2.5). Key in figure. Scale = 1 m.

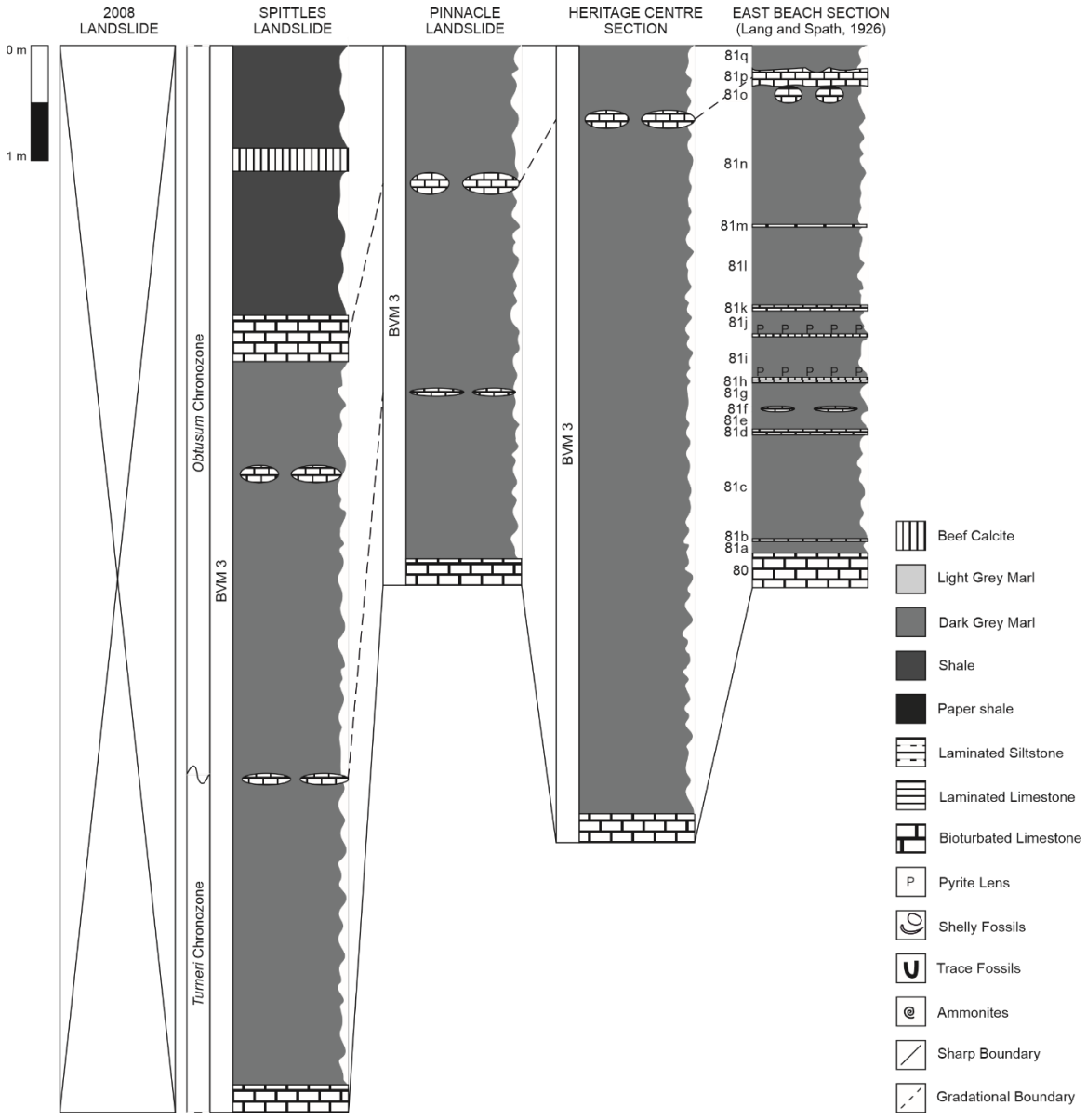

Figure 2.32 – Lithostratigraphy, including lateral variability in the lithology and thickness, of BVM 3 across the measured sections on Black Ven, Dorset (fig. 2.4). The lithostratigraphic log for the EBS (fig. 2.5) follows Lang and Spath (1926). Key in figure. Scale = 1 m.

BVM 4 or Pavior (0.15 – 0.4 m) = BVM 4 is a laterally persistent, homogeneous tabular limestone bed that measures up to 0.4 m in thickness (fig. 2.33); it is replaced locally by a dolomitic limestone of similar morphology. The typical sediment composition is dominated by microspar (95 %) with horizontal, elongate fragments of organic matter that lack coherent concentration into laminae. The upper and lower surfaces are argillaceous but share a moderately sharp contact with the sediments above and below. The unit is poorly fossiliferous and contains infrequent, compressed ammonoid moulds.

BVM 5 (0.8 – 1.88 m) = at the SLS, PLS, and CHCS, BVM 5 is made up of dark grey shales (fig. 2.33). The otherwise uniform sedimentological composition contains a series of 4 – 5 pyritic sediment layers (< 10 mm thick) in the centre of the PLS section (fig. 2.33). The lithostratigraphy of the EBS, between the base of BVM 5 – top of BVM 9, is poorly developed (Lang and Spath, 1926); individual sections cannot be identified nor correlated with the Black Ven exposure (Lang and Spath, 1926) (fig. 2.33).

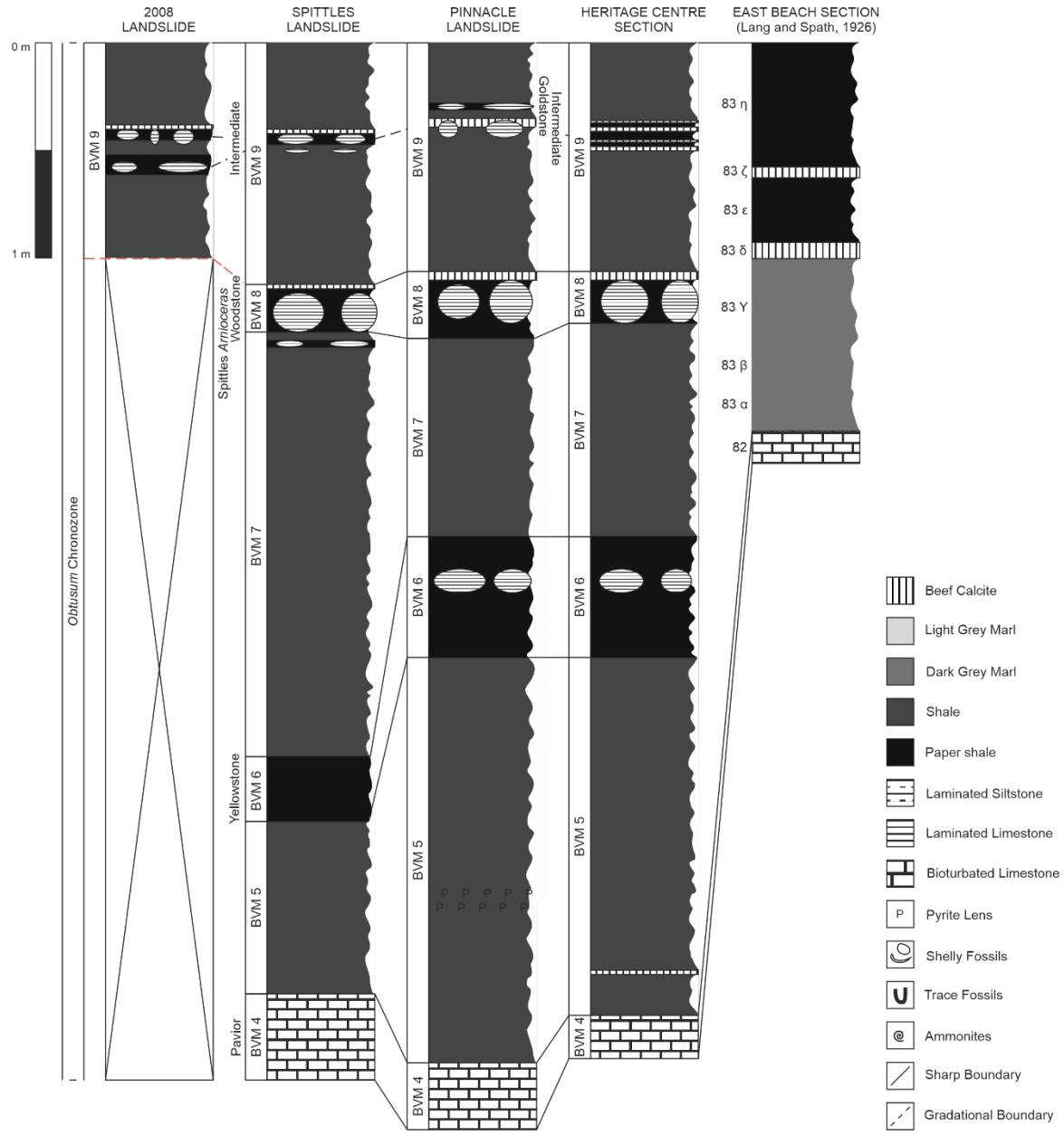

Figure 2.33 – Lithostratigraphy, including lateral variability in the lithology and thicknesses, of BVM 4 – BVM 9 across the measured sections on Black Ven, Dorset (fig. 2.4). The lithostratigraphic log for the EBS (fig. 2.5) follows Lang and Spath (1926). Key in figure. Scale = 1 m.

BVM 6 or Yellowstone (0.3 – 0.56 m) = the section is comprised of a single bed of fissile, dark grey/black paper shales (fig. 2.33) that are recognisable by a semi-resistant profile in the cliff face (Lang and Spath, 1926). BVM 6 contains a central layer of concretionary laminated limestones at the PLS and CHCS (Yellowstones) that measure in excess of 1 m in diameter, have an outer argillaceous margin (10 – 30 mm thick), and share a semi-gradational contact with the surrounding sediment (fig. 2.33). The section is thinner at the SLS (0.3 m) and lacks limestone concretions (fig. 2.33).

Yellowstone concretions are skeletal/peloidal wackestones with a well-preserved, primarily nektonic or planktonic fossil assemblage that includes ammonoids and veliger spat (fig. 2.34). The sedimentological composition is dominated by differentially compacted, irregular peloids (50 – 400 μm) and calcite microspar (fig. 2.34). Organic material (likely plant) is abundant and there are irregular proportions of pyrite, quartz, clay, and bioclasts. The internal laminated texture is the result of horizontal, poorly-developed laminae (0.1 – 1 mm thick); lenses of molluscan spat, up to 2 mm thick, are also common (fig. 2.34).

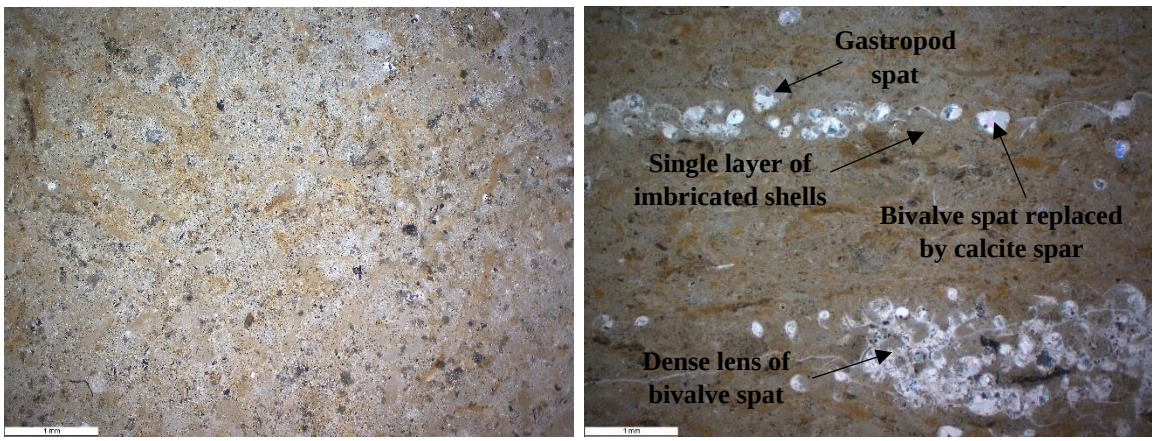

Figure 2.34 – Photomicrographs of a Yellowstone concretion under cross-polarised light. Note that molluscan spat occur in planar lenses up to 2 mm thick; shells are replaced by calcite spar. Scale = 1 mm.

BVM 7 (0.92 – 1.97 m) = BVM 7 is a mostly argillaceous section dominated by shales (fig. 2.33). Near to the upper boundary, 40 mm below BVM 8 and exclusive to the SLS, is the Spittles *Arnioceras* Bed – a layer of thin (30 mm) pyritic concretions within a bed of pyritiferous paper shales (fig. 2.33). These concretions have a fossiliferous laminated limestone core that contains abundant *Arnioceras* ammonoids, surrounded by a thin (1 – 10 mm), uneven layer of pyrite coating the outer surface (fig. 2.35; see Chapter 7).

The core skeletal packstone/peloidal wackestone has a variable sediment composition and contains microspar, peloids, organic matter, detrital minerals, and pyrite aggregates arranged into semi-coherent, sub-millimetre laminae that deflect around the uneven surface of bioclasts (fig. 2.35). These occasionally exhibit upward transitions from pyritic sediment to peloidal, microsparitic, and organic/clay-rich layers (fig. 2.35). The main shell bed has a high proportion of bioclasts that account for up to 60 % of the total sediment composition (fig. 2.35). Separated from the limestone core by a sharp, irregular transition zone, the pyritic margin is made up of pyrite aggregates (30 – 200 μm), abundant shell fragments (0.2 – 5 mm), and small patches of peloidal wackestone (fig. 2.35). The fossil assemblage in both lithologies is dominated by *Arnioceras* ammonoids as well as molluscan spat, and indeterminate shell fragments arranged sub-parallel to bedding (fig. 2.35). For more details regarding fossil preservation in the Spittles *Arnioceras* concretions, refer to Chapter 7.

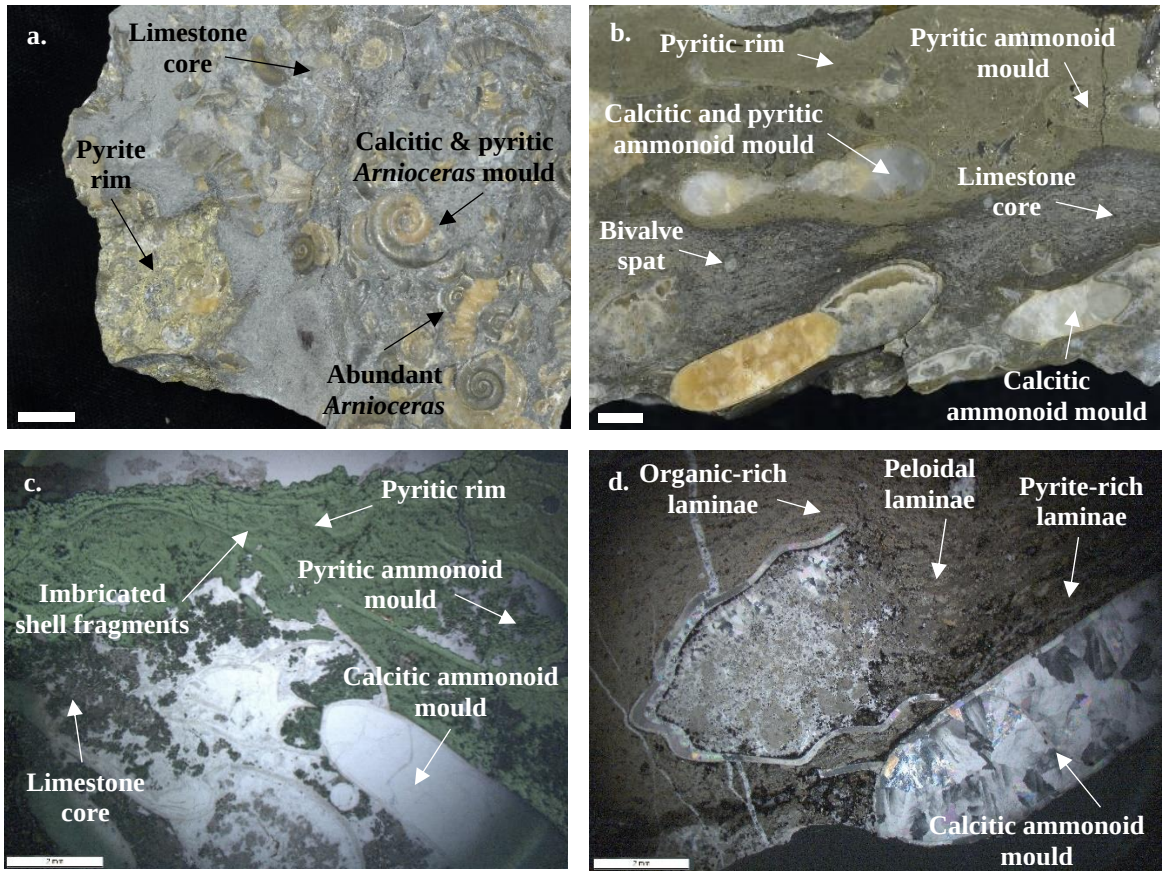

Figure 2.35 – a. hand specimen of a Spittles *Arnioceras* concretion split along the central, fossiliferous bedding plane; b. cross-section through the concretion showing the top pyritic rim and half of the middle limestone core; c. photomicrograph of the concretion under reflected light showing the composition of the pyritic, shell-rich rim; d. photomicrograph of the skeletal packstone under cross-polarised light with deflected laminae. Scale (a.) = 10 mm; scale (b.) = 5 mm; scale (c. and d.) = 2 mm.

BVM 8 or Woodstone (0.22 – 0.31 m) = the section is comprised of a single bed of fissile, dark grey/black paper shales that have been examined at the SLS, PLS, and CHCS (fig. 2.33). In the centre of the section is a layer of thick (0.16 – 0.2 m), spheroidal or cylindrical laminated limestone concretions measuring up to 1 m in diameter (fig. 2.33); most contain a central fragment of fossilised wood and are known locally as Woodstones. The sedimentological composition of these concretions is similar to the Yellowstones (BVM 6; fig. 2.34). BVM 8 is capped by a thin (20 – 40 mm), laterally persistent beef calcite band (fig. 2.33).

BVM 9 (1.06 – 1.12 m) = the section is predominantly made up of dark grey shales that persist along the length of the exposure (fig. 2.33); at the 2008LS, SLS, and PLS, pyritiferous paper shale interbeds occur at most concretionary horizons (fig. 2.33). The central Intermediate Bed has thin (50 – 80 mm), fossiliferous laminated limestone concretions at each exposure except for the CHCS where these are locally replaced by a series of thin beef bands (10 – 20 mm) interbedded with paper shales (fig. 2.33). At the 2008LS and SLS, there is an additional concretionary horizon that is lithologically and morphologically similar to the Intermediate Bed (fig. 2.33).

At the PLS there is a thin (20 mm) bed of paper shales, known locally as the Goldstone Bed, that contains pyritiferous laminated limestone concretions (fig. 2.33); it occurs in this form over a short lateral distance (approximately 20 metres). In the centre of the Goldstone Bed, spanning both the limestone concretions and paper shales, is a thin (0.5 – 2 mm) pyritic lens made up almost entirely of intact veliger spat from the cardiid bivalve genus *Protocardia* (P. Palmer *pers comms with* M. Foster, 1992) (fig. 2.36; see Chapter 7); indeterminate turreted gastropod larvae and ammonoids (e.g. *Asteroceras*, *Promicroceras*, and *Xipheroceras*) are also present (see Chapter 7). The typical limestone sediment composition is a peloidal wackestone with varying proportions of calcite microspar, uncrushed peloids (50 – 200 μm), aggregated sedimentary pyrite, and bioclasts (fig. 2.36); local concentrations of pyrite are associated with clustered molluscan spat (fig. 2.36). The limestone shows sub-millimetre laminations of peloidal, microsparitic, and organic/clay-rich laminae which deform around the uneven upper surface of the shell lens.

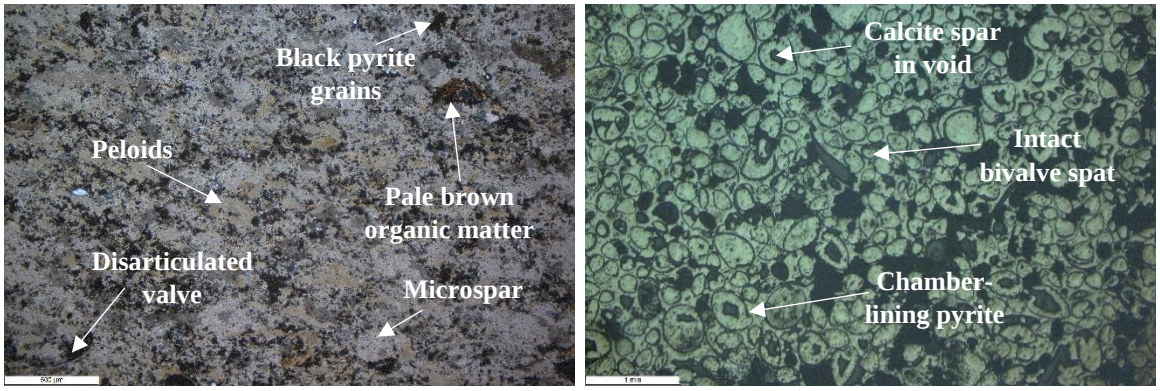

Figure 2.36 – Photomicrographs showing the variable sedimentological composition of the Goldstone concretions. Left: the typical peloidal wackestone/packestone lithology under cross-polarised light. Right: the pyritiferous, fossiliferous shell lens dominated by articulated bivalve spat under reflected light microscopy. Scales = 500 μm and 1 mm respectively.

BVM 10 or Flatstone (60 – 120 mm) = the section is comprised of a single bed of dark grey/black, fissile paper shales that contain laminated limestone concretions measuring in excess of 1 m in length and up to 0.12 m thick (fig. 2.37); Lang and Spath (1926) state that these concretions are poorly developed and laterally variable on the Black Ven exposure when compared to the EBS (fig. 2.37). Flatstones contain a diverse fossil assemblage which includes ammonoids (e.g. *Promicroceras*, *Asteroceras*, *Xipheroceras* etc), marine reptiles, and rare terrestrial biota such as insects.

BVM 11 (6.69 – 7.2 m) = along the length of the Black Ven exposure, specifically the 2008LS, SLS, PLS, and CHCS, BVM 11 is dominated by dark grey shales with laterally impersistent beef bands (figs. 2.37 and 2.38); there is a single bed of light marls (0.3 m thick) at the top of the section that is exclusive to the PLS (fig. 2.38). At the EBS, Lang and Spath (1926) recorded greater variation in the types of argillaceous lithology present (figs. 2.37 and 2.38); interbedded paper shales and shales of different thicknesses at the base of the section are overlain by conchoidal dark marls in the upper part (Lang and Spath, 1926; figs. 2.37 and 2.38). A thin (30 – 100 mm), concretionary laminated limestone bed (Topstone) in the upper part of BVM 11 is present along the length of the exposure (fig. 2.38). Topstones are fossiliferous lenticular wackestones that contain a well-preserved fossil assemblage dominated by ammonoids. At the PLS, there is a second layer of laminated limestone concretions, 0.2 m above the Topstones, which are morphologically and lithologically similar to the former (fig. 2.38).

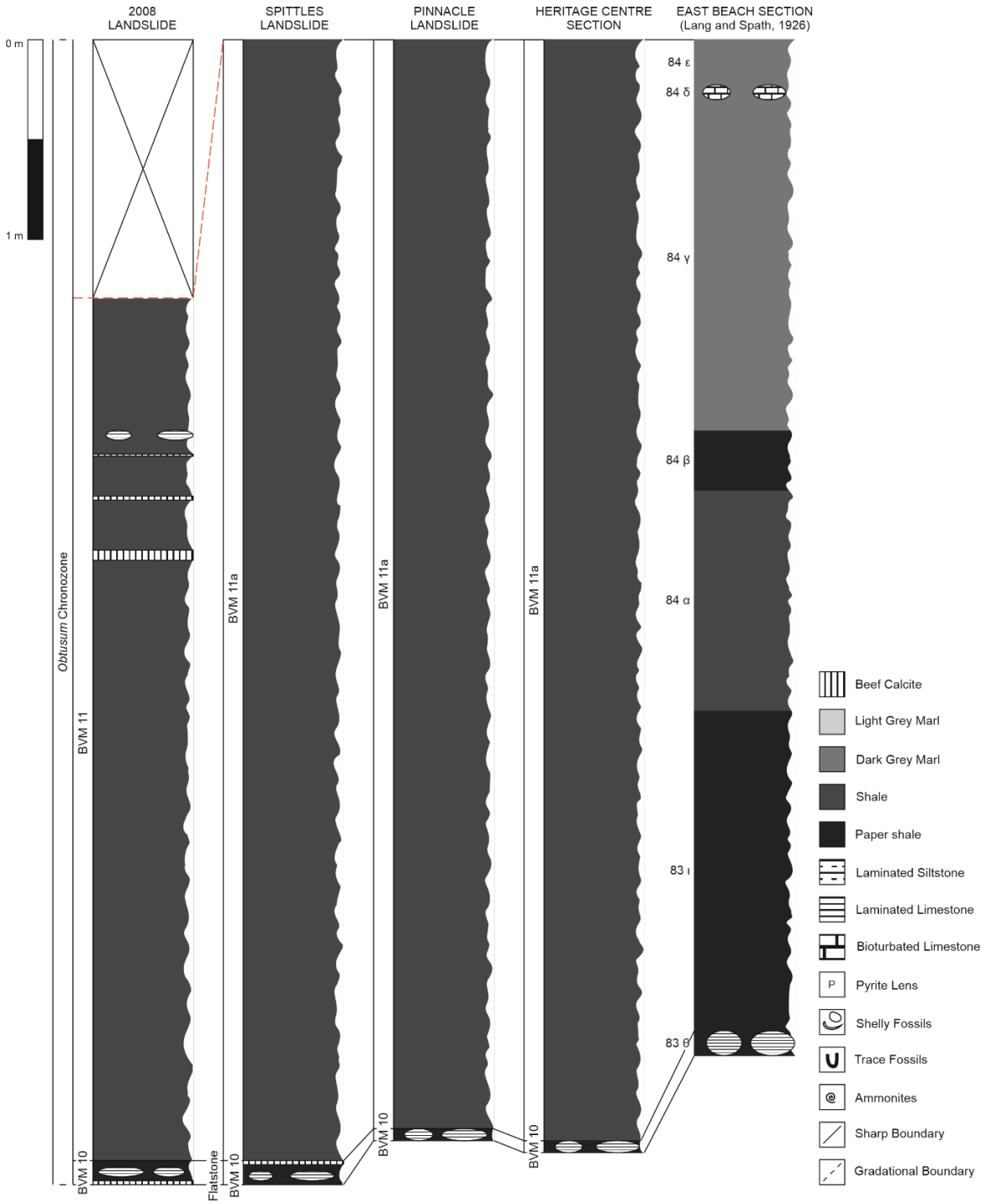

Figure 2.37 – Lithostratigraphy, including lateral variability in the lithology and thicknesses, of BVM 10 – BVM 11a across the measured sections on Black Ven, Dorset (fig. 2.4). The lithostratigraphic log for the EBS (fig. 2.5) follows Lang and Spath (1926). Key in figure. Scale = 1 m.

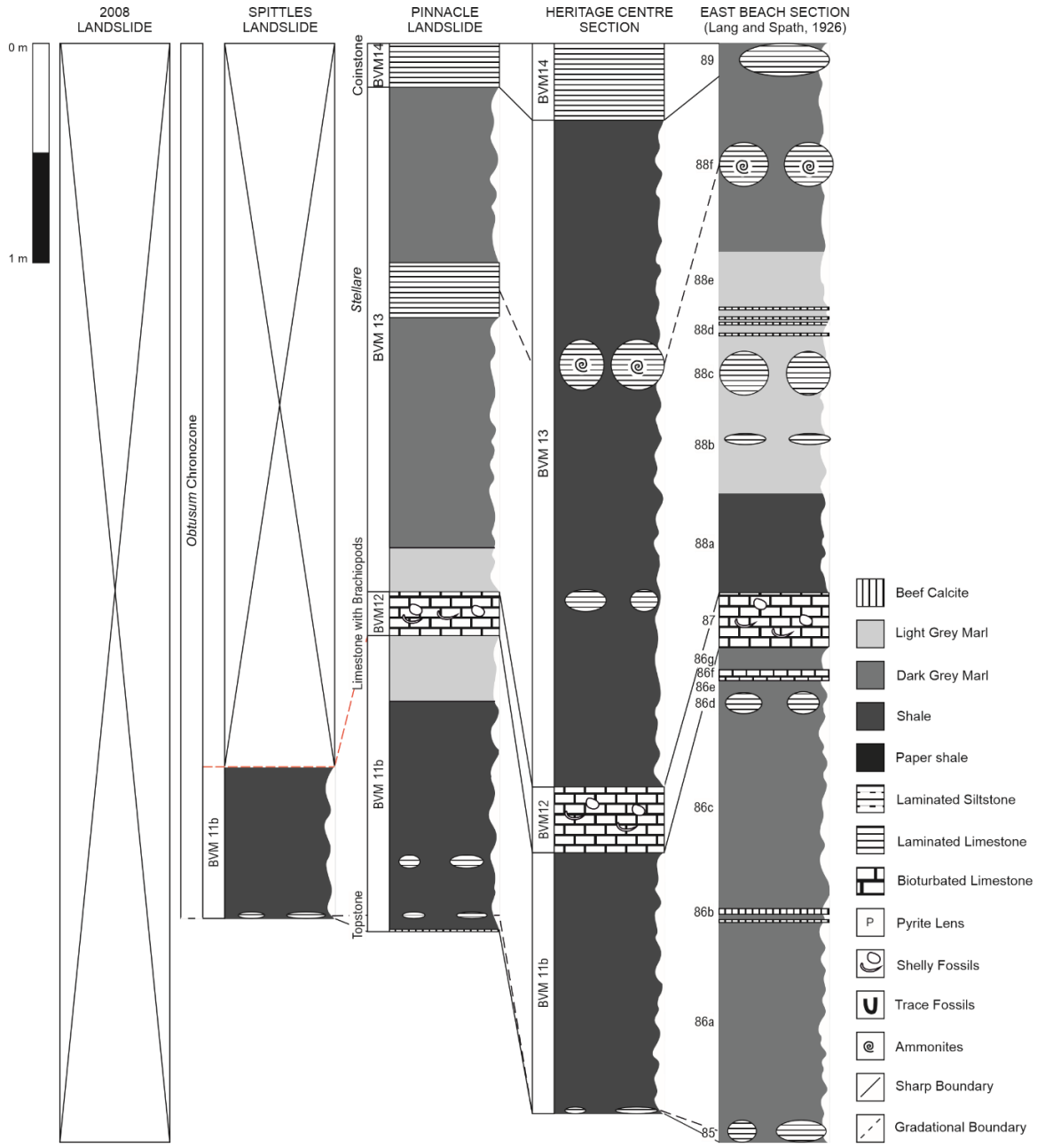

Figure 2.38 – Lithostratigraphy, including lateral variability in the lithology and thicknesses, of BVM 11b – BVM 14 across the measured sections on Black Ven, Dorset (fig. 2.4). The lithostratigraphic log for the EBS (fig. 2.5) follows Lang and Spath (1926). Key in figure. Scale = 1 m.

BVM 12 or Limestone with Brachiopods (0.2 – 0.3 m) = the Limestone with Brachiopods is a pale brown, laterally persistent tabular limestone bed (fig. 2.38); it contains an abundant assemblage of *Calcirhynchia* brachiopods.

BVM 13 (2.34 – 3.03 m) = BVM 13 is an irregular, lithologically variable section that is difficult to correlate along the length of the exposure (fig. 2.38). The most distinctive feature is a layer of large, septarian laminated limestone concretions (*Stellare*) that

measure up to 1.5 m in diameter and approximately 0.2 m thick (fig. 2.38); this form is locally replaced by a septarian limestone, of similar thickness and bulk sediment composition, at the PLS (fig. 2.38). *Stellare* concretions are notable for the semi-compacted *Asteroceras stellare* ammonoids they contain. The section cannot be examined *in situ* to the west of Black Ven, specifically at the 2008LS and SLS, due to obscuration by landslide debris; the presence of the *Stellare* Bed has been inferred from *ex situ Stellare* concretions found at beach level below both outcrops. Argillaceous lithologies at the eastern end of the Black Ven exposure, specifically the PLS and CHCS, are dominated by dark marls and shales respectively, with a single bed of light marls (0.2 m thick) above BVM 12 at the PLS (fig. 2.38). At the EBS, the section was originally divided into different types of marl by Lang and Spath (1926); when revised in accordance with the lithological classification herein, BVM 13 is comprised of basal grey shales (bedded marl *sensu* Lang and Spath, 1926) that are overlain by a central unit (1.1 m thick) approximating the light marl lithology (pale marls *sensu* Lang and Spath, 1926), and a topmost bed of conchoidal dark marls (0.8 m thick) that contain the *Stellare* concretions (fig. 2.38). Additional concretionary limestones are present in the lower part of section at the CHCS and EBS (fig. 2.38), but these are generally unfossiliferous.

BVM 14 or Coinstone (0.15 – 0.35 m) = the Coinstone Bed is a unique horizon in the CMF of Dorset; its main interest, a pyritic hardground that marks a hiatus between the top of the *Stellare* Subzone (*Obtusum* Zone) to the base of the *Densinodulum* Subzone (*Raricostatum* Zone) (Hallam, 1969), is exclusive to the EBS (Hesselbo and Palmer, 1992). The hiatus concretions have a variable lithology and morphology (e.g. Hesselbo and Palmer, 1992), but are generally represented by large (up to approximately 0.8 m in length and 0.15 m in thickness), planar septarian laminated limestones (fig. 2.38). The upper and lateral concretionary surfaces have abundant cylindrical borings (approximately 5 – 30 % total surface area) that measure up to 5 mm in diameter and 30 mm in length (Hallam, 1969). There is a thin (1 – 10 mm) pyritic margin coating the outer surface of most concretions (e.g. Hallam, 1969, Hesselbo and Palmer, 1992). Correlation with the Black Ven exposure is difficult as the lithology of the Coinstone Bed differs significantly either side of the River Char. At the PLS and CHCS, the Coinstone is a laterally variable, blocky laminated limestone (0.2 – 0.35 m thick) that is locally replaced by septarian concretions (fig. 2.38). It lacks the pyritic margin and extensive boring seen at the EBS; previous studies have also indicated that there is no evidence for erosion at this horizon on the Black

Ven exposure (e.g. Hallam, 1969). The origin, lithology, palaeontology, and diagenetic history of the Coinstone Bed have been described in detail by previous studies (e.g. Lang, 1945, Hallam, 1969, Sellwood, 1972, Hesselbo and Palmer, 1992, Hallam, 1999).

Above BVM 14, the remainder of the BVM was difficult to access *in situ* along the length of the Black Ven exposure and can only be examined at the CHCS where it overlaps two offset cliff terraces. Accurate quantification of true vertical thickness was difficult and so the CHCS should be considered a semi-quantitative account from BVM 15 – BVM 17 (fig. 2.39). The aforementioned strata are most accessible at the EBS, as per Lang and Spath (1926), where they can be accessed at beach level.

BVM 15 (8.49 – 9.35 m) = BVM 15 is dominated by fossiliferous dark grey marls (fig. 2.39) that contain a well-preserved, pyritic ammonoid assemblage distributed throughout the section (see chapters 5 and 7). Ammonoid moulds are significantly more abundant at the EBS, but it is unclear whether this is because fossiliferous horizons are less well developed on Black Ven at the CHCS or simply because *ex situ* material is more available east of the River Char where the section is positioned nearer to beach level.

BVM 16 or Watchstone (0.15 m) = the Watchstone Bed is a complex unit that contains fossiliferous, septarian limestone lenticles (fig. 2.39). Watchstones have a diverse fossil assemblage that is dominated by calcitic *Echioceras* ammonoid moulds; the majority of fossils were distorted by diagenetic calcite veins (1 – 5 mm thick) and preserved sub-parallel to bedding. The irregular, argillaceous upper surface has poorly-preserved *Echioceras* ammonoid impressions and/or mud-filled moulds. The origin, lithology, and palaeontology of the Watchstones was described in detail by Sellwood (1972).

BVM 17 (3.5 – 3.9 m) = lithologically similar to BVM 15, BVM 17 is made up of conchoidal dark marls (fig. 2.39). It also contains a similar pyritised ammonoid assemblage but there are fewer fossiliferous horizons, a lower relative abundance of fossils, and specimens are often poorly preserved by comparison. The position of the boundary between the top of the BVM and the base of the overlying BM, which also correlates to the Sinemurian-Pliensbachian boundary in Dorset, is taken as the erosive discontinuity at the base of Bed 103/Hummocky Limestone (*sensu* Lang and Spath, 1926; not figured) after Hesselbo and Jenkyns (1995).

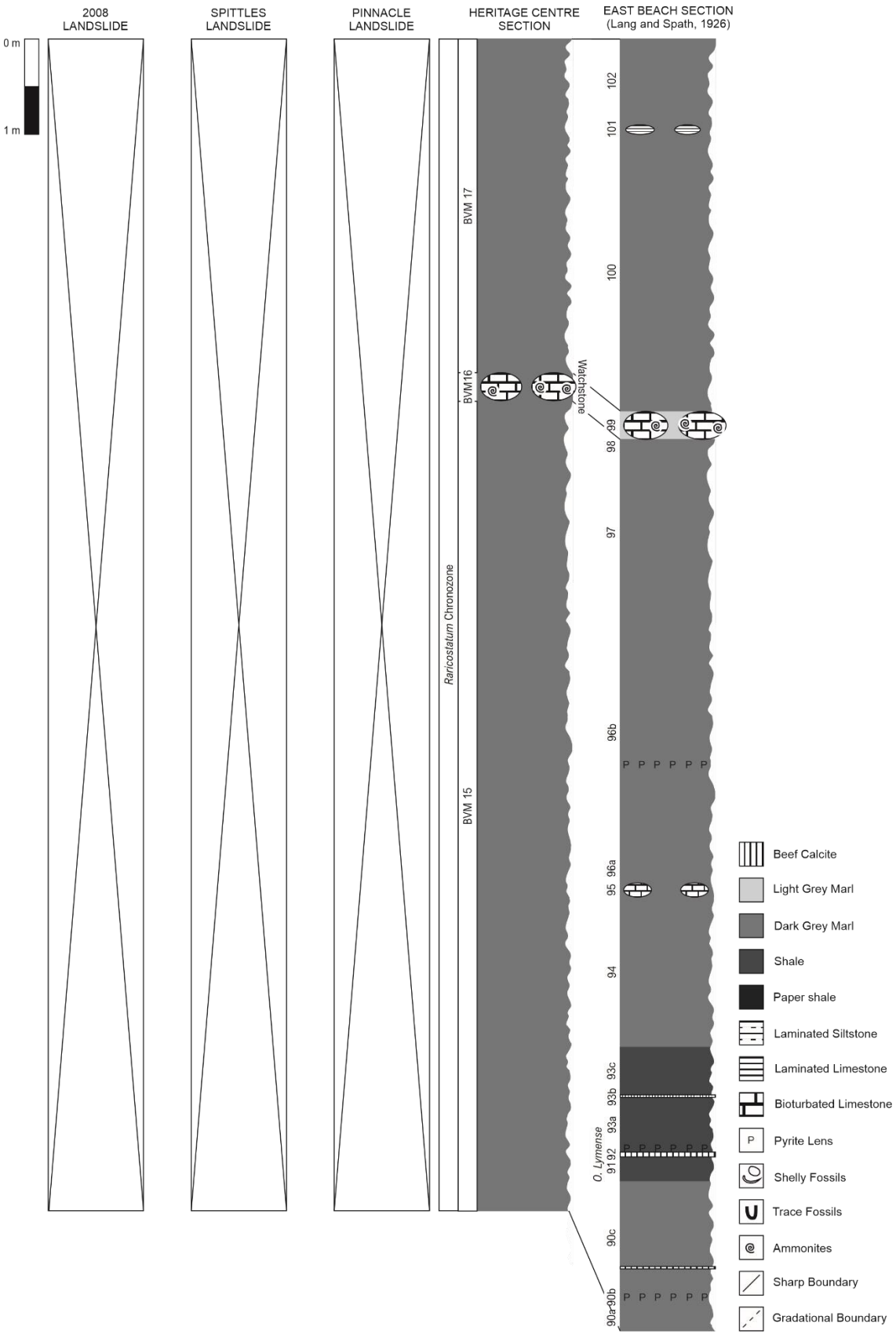

Figure 2.39 – Lithostratigraphy, including lateral variability in the lithology and thicknesses, of BVM 15 – BVM 17 across the measured sections on Black Ven, Dorset (fig. 2.4). The lithostratigraphic log for the EBS (fig. 2.5) follows Lang and Spath (1926). Key in figure. Scale = 1 m.

2.4. Summary

The Early Jurassic successions of Dorset and East Devon in South England, specifically the BLF and basal CMF (SWB and BVM), show significant lithological variation that can nonetheless be categorised with respect to a revised lithological classification scheme amended after Weedon (1986). This method of division – namely, bioturbated limestones (nodular and planar), light marls, dark marls, shales, paper shales, and laminated limestones (planar and concretionary) – has enabled the grouping of lithologically similar units in order to explore large-scale palaeoenvironmental, palaeoecological, and taphonomic controls on fossil marine shelly communities later in the thesis. It also allows for the constraint and correlation of lithology-specific trends in order to advance the potential to model such factors in global Jurassic marine successions.

3. AN ACCOUNT OF THE MACROFAUNA AND PALAEOECOLOGY OF THE BLUE LIAS FORMATION (EARLY JURASSIC) IN DORSET AND EAST DEVON, UK

3.1. Introduction

The fossiliferous limestones and mudrocks of the BLF in Dorset and East Devon have been subject to extensive palaeontological investigation. Many previous studies have described the abundant and exceptionally well-preserved vertebrate fossils (e.g. Cruickshank, 1994, Benton and Spencer, 1995, Lord et al., 2010, Vincent and Taquet, 2010, Massare and Lomax, 2018) as well as the ammonoid biota (e.g. Paul et al., 2008, Lord et al., 2010, Jordan et al., 2015, Jordan, 2016, Weedon et al., 2018). The trace fossils and ichnotaxa of the succession have also been examined (e.g. Hallam and Lang, 1960, Moghadam and Paul, 2000, Martin, 2004, Twitchett and Barras, 2004, Barras and Twitchett, 2007, Lord et al., 2010, Jordan, 2016) as have other molluscan groups (e.g. Hallam and Lang, 1960, Lord et al., 2010, Pugh et al., 2014, Jordan, 2016, Atkinson and Wignall, 2019).

The fossil record of the BLF is not uniform throughout the succession; it was affected by a number of different factors that influenced either the original (predicted) faunal assemblage or the representation of different groups within the fossil assemblage. Palaeoenvironmental conditions such as the degree of bottom water oxygenation exerted a significant palaeoecological control and can be correlated approximately with lithological alternations (e.g. Weedon, 1986, Moghadam and Paul, 2000, Wignall, 2001b, Hesselbo et al., 2004, Martin, 2004, Paul et al., 2008). Varying bottom water redox states – oxic, restricted, and dysaerobic/anoxic – coincided with different faunal and/or ichnofaunal assemblages (Moghadam and Paul, 2000, Martin, 2004, Barras and Twitchett, 2007, Paul et al., 2008). The influence of palaeoenvironmental conditions is particularly evident in the basal BLF above the T-J boundary interval (Hallam, 1996, Barras and Twitchett, 2007, Mander et al., 2008, Pugh et al., 2014) where anoxia, evidenced by the deposition of black shales and supporting geochemical proxies (see Chapter 4; Wignall, 2001b), has been cited by a number of authors as the cause of a negative palaeoecological impact on the benthic assemblage that led to a prolonged or staged biotic recovery (e.g. Barras and Twitchett, 2007, Mander et al., 2008). The succession is also influenced by a taphonomic control that concerns the potential for selective dissolution of originally aragonitic fauna within the TAZ to distort the fossil assemblage (*sensu* Cherns and Wright, 2000, Wright et al., 2003). In similar Jurassic offshore carbonate ramp settings, this process was responsible for an approximately 80 % loss in original ecological skeletal diversity (Wright et al., 2003). Taphonomy is linked to the prevailing palaeoenvironmental conditions and so all of these factors should be considered in unison.

This chapter provides a high-resolution palaeoecological study of the microfaunal and macrofaunal fossil components of the BLF in Dorset and East Devon. By increasing the sampling resolution and incorporating data from argillaceous lithologies, this account expands on previous work by Pugh et al. (2014) who used palaeoecological trends in limestone beds from the same succession to explore the response of benthic macrofauna to palaeoenvironmental conditions following the T-J extinction event. This study also provides an opportunity to investigate the impact of small-scale, lithology-specific fluctuations in the dominant redox state on marine benthos. These observations, coupled with existing ichnotaxomic data (e.g. Barras and Twitchett, 2007, Jordan, 2016), will be used to infer the degree of bottom water oxygenation in order to corroborate iron palaeoredox proxies (Fe_{HR}/Fe_T and Fe_{Py}/Fe_{HR} ratios) later in the thesis and test the validity of their application for assessing redox conditions in the BLF (see Chapter 4). The data will also be used to explore variable taphonomic controls on the abundance and diversity of different shelly groups in the Early Jurassic mudrocks of Dorset and East Devon (see Chapter 7).

3.2. Material and methods

The BLF was examined in coastal cliff outcrops and foreshore reefs between Lyme Regis, Dorset (approx. SY 33566 91565) and Pinhay Bay, Devon (approx. SY 31806 90779) (fig. 2.3; see Chapter 2). Bed-numbering follows Lang (1924).

3.2.1. Macrofaunal counts

Macrofaunal counts were conducted on the upper surfaces of individual beds identified in the revised lithostratigraphic log (see Chapter 2). Counts were not taken for the entirety of the BLF owing to the occasional lack of exposure at different heights throughout the formation; the upper part of the BLF between BL 22 and BL 27 was not examined since it is only exposed in the vertical cliff face and bedding surfaces were not accessible. The total number of sampled horizons was as follows: limestones = 57, light marls = 10, dark marls = 28, shales = 14, paper shales = 17, and laminated limestones = 7. There was negative sampling bias towards non-carbonate lithologies as these were often obscured by resistant capping limestones and, following infrequent exposure, quickly destroyed by erosion.

The macrofaunal fossil component was quantified within a 0.5 x 0.5 m quadrat and counts were repeated at two separate locations to resolve the spatial heterogeneity of the

assemblage (methodology after Pugh et al., 2014). The methodology required that the quadrat covered half of the fossil's surface area for it to be counted (Pugh et al., 2014). Where exposure was limited, particularly in the basal formation, the sample area was composited from nearby outcrops. Despite how the data is figured, it is important to note that macrofaunal counts were taken on eroded wave cut platforms and therefore represent an undefined position at depth within the bed; this is an important constraint since the fossil content of many sampled horizons was not constant throughout their vertical thickness. The nature of the exposure and resolution of the study meant that it was not possible to quantify how the macrofaunal fossil component changed within a single bed. Areas of the bedding surface that showed evidence for process-driven alteration of the fossil assemblage (via storm events, winnowing, or scour filling) were avoided where possible. Owing to the potential for post-mortem transport (e.g. Hallam and Lang, 1960, Paul et al., 2008, Jordan, 2016), macrofaunal counts were contrasted with supporting ichnological data in Barras and Twitchett (2007) and Jordan (2016).

Most bivalve and brachiopod fossils have been identified to a genus- or species-specific level (fig. 3.1). The deep-burrowing anomalodesmatan bivalves *Pleuromya* and *Pholadomya* were sometimes difficult to distinguish owing to mouldic preservation and diagenetic dissolution of the aragonitic shell as well as associated characteristic surface features; as a result, their classification was based on simple morphological observations only and should therefore be considered speculative, particularly since their shape is often disproportionately affected by erosion across inequilateral valves held in life position. This was considered an acceptable supposition since both genera are identical in terms of ecological niche and taphonomic survival rate. Bivalves that could not be classified were grouped into a single, indeterminate category (edited after Pugh et al., 2014). Ammonoids, crinoids, gastropods, and echinoids were not subdivided by genus since the mode of life was consistent within each class.


a.
b.
c.
d.
e.
f.

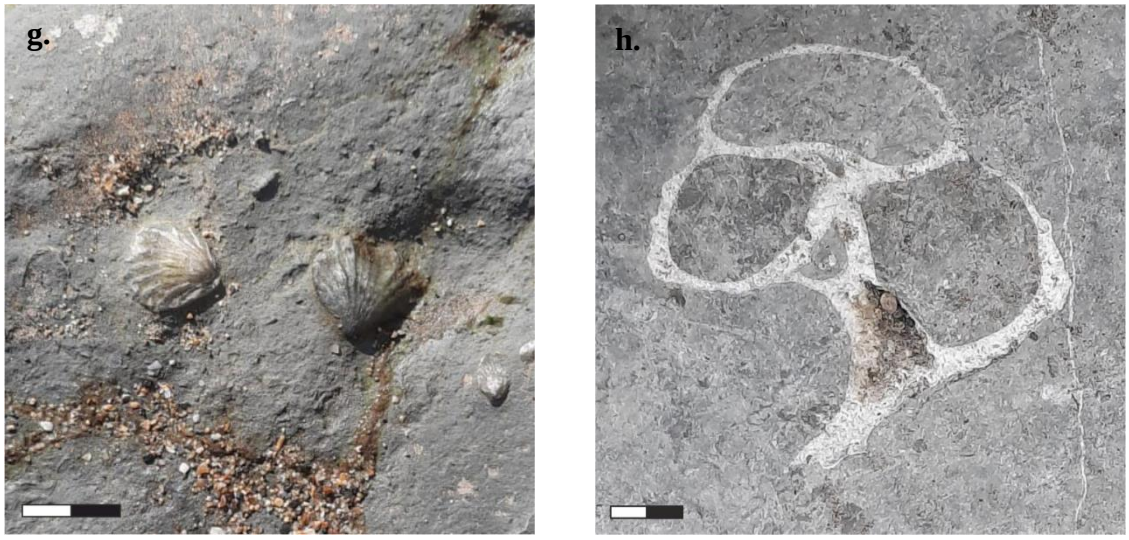

Figure 3.1 – Examples of fossils found in the BLF of Dorset and East Devon. a. a single *Liostrea* valve found *ex situ* on the surface of a shelly bioturbated limestone; b. a typical *Gryphaea* found *ex situ* in a thin marly lens on the surface of a bioturbated limestone; c. a large *Plagiostoma* valve found *ex situ* in a shelly bioturbated limestone; d. a *Pseudolimea* found *ex situ* on the surface of a shelly bioturbated limestone; e. a large *Antiquilima* showing erosive damage to the shell margin preserved in H58 (fig. 2.11); f. an articulated *Pleuromya*? preserved on the upper surface of H38 at the limestone-shale transition (fig. 2.11); g. *Calcirhynchia calcaria* in the dark marls above the Mongrel limestone bed (fig. 2.20); h. cross-section of a gastropod exposed in the Second Tape limestone bed (fig. 2.20). Scale = 10 mm.

Numerical counts were used to quantify the number of bioclasts within the sample area, including recognisable shell fragments that measured over 5 mm in length; these data were subsequently recalculated to reflect the minimum number of individuals (MNI) and compensate for broken and/or disarticulated fossils. Pugh et al. (2014) established the framework for MNI on local strata although it was edited in this account; complete shells, single disarticulated valves, paired articulated valves, up to 10 echinoderm fragments (crinoid ossicles or echinoid spines), and up to 10 identifiable shell fragments of the same type were all taken to represent one individual. It is important to note that whilst including shell fragments improves the overall completeness of the study by ensuring better representation from different shelly groups, it likely results in an overestimation of the number of individuals within the assemblage and is not representative of the extent of original occupation within the quadrat's area. For all of the sampled horizons, MNI counts were used to determine the proportion of each taxon as a percentage of the overall fossil assemblage. Each of the four palaeoecological metrics discussed by Pugh et al. (2014) were calculated and figured using data from this study. Based on the author's original account, abundance was taken as the MNI per bed and species richness as the number of

different taxa; statistical analysis in PAST was used to determine evenness and diversity (for full details see Pugh et al., 2014). An estimated coverage of the bedding surface by macrofauna was also given.

3.2.2. Microfaunal counts

The microfaunal fossil component was quantified for the majority of laminated and bioturbated limestone beds within the lower-central BLF (BL 1 – BL 19); a total of 44 bioturbated limestones and 7 laminated limestones were examined. Samples were taken from random heights within each bed to gauge the approximate relative abundance and constitution of the microfaunal fossil assemblage, but these data do not represent the overall limestone composition since the sedimentology and fossil content within a single bed, particularly at this scale, varies extensively. The resolution of the study meant that it was not possible to quantify how the fossil content changed within individual limestones. Non-carbonate alternations were not examined for this part of the investigation.

Point counts were conducted on stained carbonate peels taken from polished surfaces cut oblique to the original bedding in order to better represent the average sediment composition; stained carbonate peels were produced using the methodology of Katz and Friedman (1965). A 16 x 98 point grid, spaced at 28 μm horizontally and 139 μm vertically, was superimposed over a graphically-rendered photomicrograph of the slide and shells/shell fragments at the intersection between grid lines were counted. Photomicrographs were taken using a Leica DM750P microscope and Leica LAS (Leica Application Suite) Imaging Software under plane-polarised light microscopy. Fossils were identified to class level where possible. The amount of microfauna in each sample was given as a percentage of the total sediment composition and the proportion of each bioclast was calculated as a percentage of the overall microfaunal fossil assemblage.

3.2.3. Supplementary data

Previous accounts of trace fossil distribution in the BLF by Barras and Twitchett (2007) and Jordan (2016) were superficially modified and included for comparative discussion. Since different lithostratigraphic accounts were used in each of the three studies (including this work), there were moderate inconsistencies in the measured thickness and lithological classification assigned to individual beds. As a result, in order to prepare the data for comparison with macrofaunal distribution in this chapter, the position and depth of

ichnotaxa were approximated from the original accounts; for quantitative descriptions refer to Barras and Twitchett (2007) and Jordan (2016) respectively.

3.3. Results

BL 1 = the basal paper shales are without macrofauna (fig. 3.2; table 3.1). The single laminated limestone bed contains a minor microfaunal component (3 % of total sediment composition) comprised of intact bivalve spat (fig. 3.2). Wignall (2001b) recorded a thin, central lens (unquantified) of disarticulated *Modiolus minimus* and echinoid spines. There are no ichnotaxa (Barras and Twitchett, 2007, Jordan, 2016; fig. 3.2).

BL 2 = the bioturbated limestones in BL 2 contain an abundant microfaunal component (average = 34 % of total sediment composition; fig. 3.2). Up to and including H18, microfauna account for an average of 37 % of the total sediment composition (fig. 3.2); intact bivalve spat represent an average of 26 % of this assemblage whilst echinoid plates/spines are a relatively minor component (average = 5 %) (fig. 3.2). Microfauna account for less of the total sediment composition above H18 (average = 29 %), but there is a moderate shift in the constitution of the microfaunal assemblage that is expressed as an increase in the proportion of echinoid fragments (average = 12 %) and a decrease in the amount of intact bivalve spat (average = 6 %) (fig. 3.2).

Between H4 and H18, the exposed bedding surfaces of the bioturbated limestones have poor macrofaunal coverage (average = 2 %; fig. 3.2) and low species richness (average number of different taxa = 3; fig. 3.3; table 3.1). The composition of the assemblage is dominated by *Liostrea* (average = 80 %) with sparse *Plagiostoma*, *Pseudolimea*, and an indeterminate bivalve genus (average = 2 %, 1 %, and 15 % respectively) (fig. 3.2; table 3.1). H10 and H16 are unique in that they contain the semi-infaunal bivalve *Modiolus minimus* (fig. 3.2; table 3.1). Limestones in the upper part of the section (H22 – H28) have greater macrofaunal coverage (average = 7 %; fig. 3.2) and high species richness (average number of different taxa = 6; fig. 3.3; table 3.1). *Liostrea* remains a dominant component of the fossil assemblage (average = 58 %), but there is a greater proportion of *Plagiostoma* (average = 23 %) in association with other epifaunal (*Antiquilima*, *Pseudolimea* and *Pseudopecten*), semi-infaunal (*Pinna* and *Modiolus*), and infaunal (*Pleuromya*) bivalve genera (fig. 3.2; table 3.1). Shell material within these upper limestones is fragmented and randomly-oriented. Echinoid spines were observed in the majority of limestones above and

including H22 (fig. 3.2; table 3.1) although Jordan (2016) identified complete tests in H4 and H6 as well as disarticulated spines in a number of additional beds; crinoid ossicles are present in H26 and H28 (fig. 3.2; table 3.1). Macrofaunal diversity at the base of the section (H4 – H10) increases with vertical progression and is approximately inversely proportional to the evenness of the assemblage (fig. 3.3); palaeoecological metrics in the remainder of BL 2 lack a coherent trend (fig. 3.3). According to Barras and Twitchett (2007), limestones in the section are without ichnotaxa (fig. 3.2); conversely, trace fossils were recognised in H24 by Jordan (2016) (fig. 3.2).

Few of the argillaceous interbeds within BL 2 were accessible for study (fig. 3.2). The paper shales of H5a were without macrofauna except for a single *Liostrea* valve, and the same lithology in H13a is unfossiliferous (fig. 3.2; table 3.1). In the shales of H13b, there is moderate species richness (number of different taxa = 4; fig. 3.3; table 3.1) characterised by taxa observed elsewhere in the section (*Liostrea*, *Modiolus*, an indeterminate bivalve genus, and echinoid spines; fig. 3.2; table 3.1). In this account, the first occurrence of echinoids was in H13b, although disarticulated spines were recorded at the base of BL 1 by Hallam and Lang (1960) and Wignall (2001b). H23 has a moderate fossil content (MNI = 33; fig. 3.3) comprised of epifaunal bivalves (*Liostrea*, *Plagiostoma*, and *Pseudopecten*), whereas H25 is without macrofauna (fig. 3.2; table 3.1). Ichnotaxa have been recorded by previous authors in a number of the non-sampled argillaceous interbeds including at the approximate positions of H7, H15 (Jordan, 2016) and H19d (Barras and Twitchett, 2007, Jordan, 2016) (fig. 3.2).

BL 3 = the two paper shale beds within the argillaceous lithology bundle of BL 3 (H29a and H29c) are without macrofauna (fig. 3.2; table 3.1). By contrast, the shales of H29b have limited macrofaunal coverage (3 %) and contain an exclusively epifaunal fossil assemblage of *Liostrea*, *Plagiostoma*, echinoids, and crinoids (fig. 3.2; table 3.1). The occurrence of macrofauna coincides with trace fossils recorded by Jordan (2016) (fig. 3.2).

BL 4 = there is no recorded microfaunal nor macrofaunal fossil component in BL 4 (fig. 3.2; table 3.1). However, trace fossils were identified at the top of H30 by Barras and Twitchett (2007) as well as Jordan (2016) (fig. 3.2).

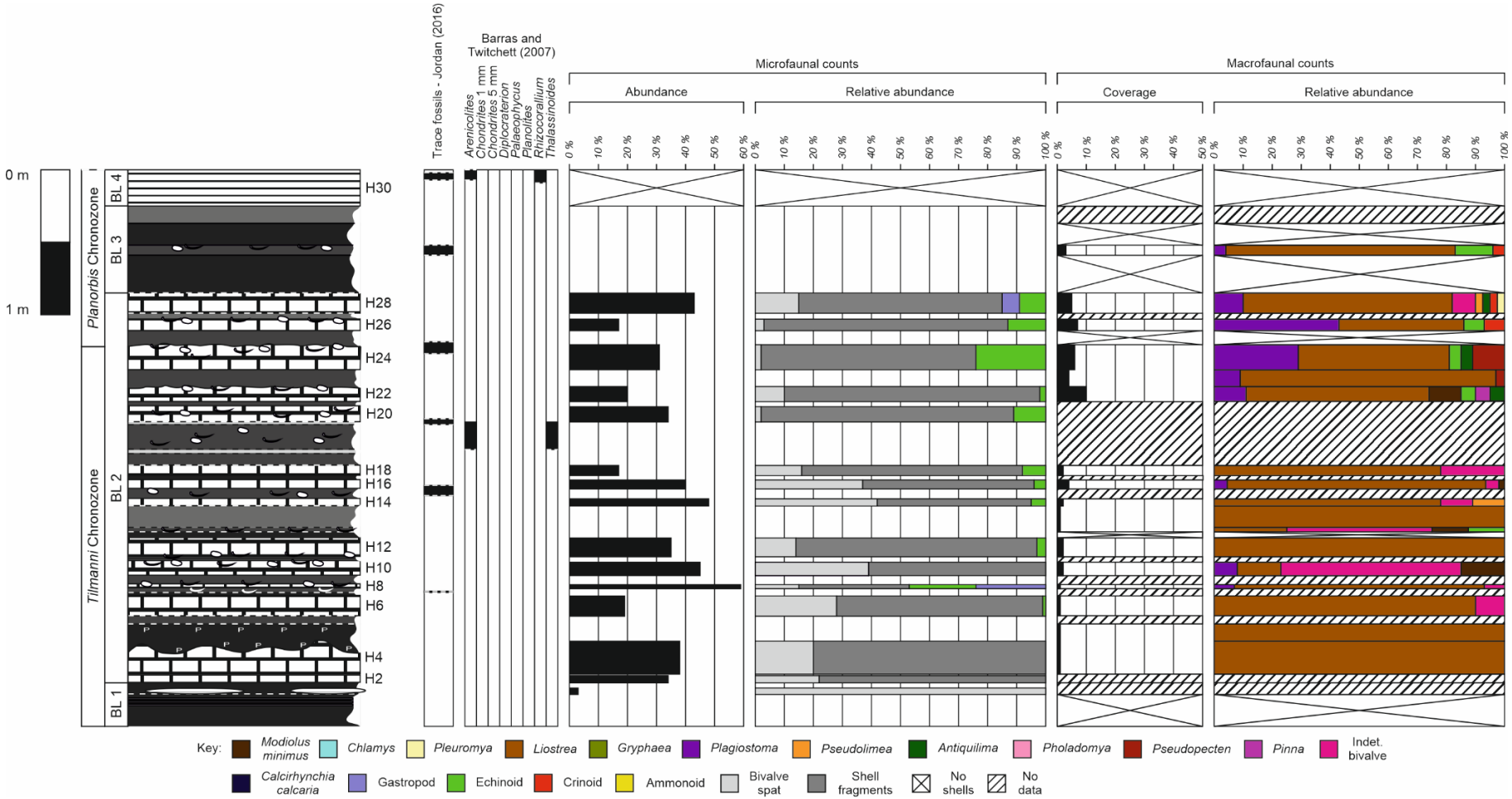

Figure 3.2 – Microfaunal data (proportion of sediment composition/abundance and relative abundance of different bioclasts respectively) and macrofaunal data (percent coverage and relative abundance of different bioclasts from MNI counts respectively) for BL 1 – BL 4. Stratigraphy after the revised lithostratigraphy in Chapter 2. Ichnotaxonomic data after Barras and Twitchett (2007) and Jordan (2016). Components of the micro and macrofaunal counts are shown in the key.

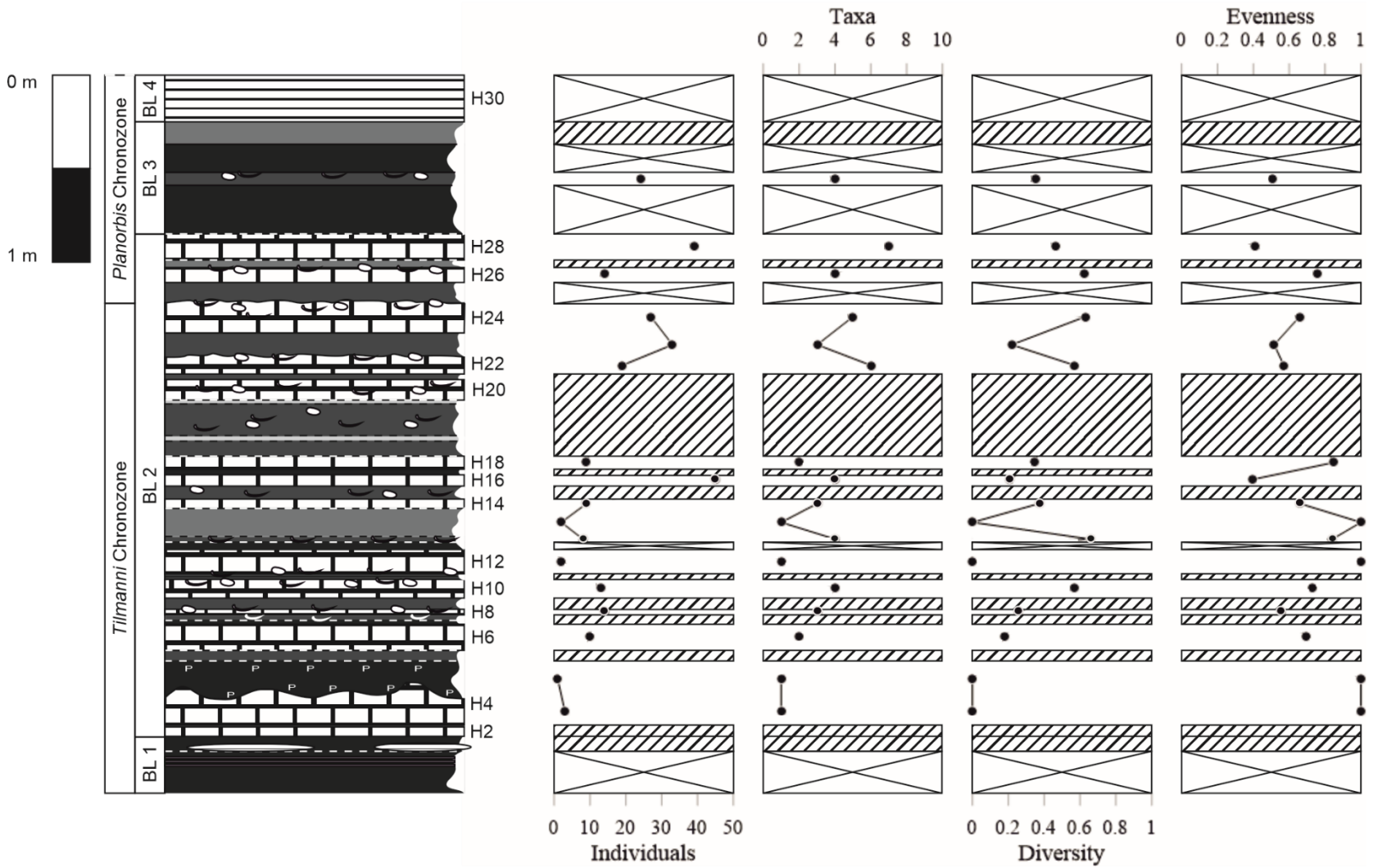

Figure 3.3 – Graphic logs showing the minimum number of individuals, species richness or number of different taxa, diversity, and evenness of the macrofaunal fossil assemblage in BL 1 – BL 4. Stratigraphy after the revised lithostratigraphy in Chapter 2.

BL 4										
Sample	**Lithology**	*Modiolus minimus*	*Chlamys*	*Liostrea*	*Gryphaea*	*Plagiostoma*	*Pseudolimea*	*Antiquilima*	*Pholadomya*	*Pseudopecten*
H30	L.LST	0	0	0	0	0	0	0	0	0
		Pinna	*Pleuromya*	Indeterminate bivalve	*Calcirhynchia calcaria*	Gastropod	Echinoid	Crinoid	Ammonoid	
		0	0	0	0	0	0	0	0	

BL 3										
Sample	**Lithology**	*Modiolus minimus*	*Chlamys*	*Liostrea*	*Gryphaea*	*Plagiostoma*	*Pseudolimea*	*Antiquilima*	*Pholadomya*	*Pseudopecten*
H29 d	D.M	N/A	N/A	N/A	N/A	N/A	N/A	N/A	N/A	N/A
H29 c	P.S	0	0	0	0	0	0	0	0	0
H29 b	SHA	0	0	19	0	1	0	0	0	0
H29 a	P.S	0	0	0	0	0	0	0	0	0
		Pinna	*Pleuromya*	Indeterminate bivalve	*Calcirhynchia calcaria*	Gastropod	Echinoid	Crinoid	Ammonoid	
H29 d	D.M	N/A	N/A	N/A	N/A	N/A	N/A	N/A	N/A	
H29 c	P.S	0	0	0	0	0	0	0	0	
H29 b	SHA	0	0	0	0	0	3	1	0	
H29 a	P.S	0	0	0	0	0	0	0	0	

BL 2										
Sample	**Lithology**	*Modiolus minimus*	*Chlamys*	*Liostrea*	*Gryphaea*	*Plagiostoma*	*Pseudolimea*	*Antiquilima*	*Pholadomya*	*Pseudopecten*
H28	LST	0	0	28	0	4	1	1	0	0
H27	D.M	N/A	N/A	N/A	N/A	N/A	N/A	N/A	N/A	N/A
H26	LST	0	0	6	0	6	0	0	0	0
H25	SHA	0	0	0	0	0	0	0	0	0
H24	LST	0	0	14	0	8	0	1	0	3
H23	SHA	0	0	29	0	3	0	0	0	1
H22	LST	2	0	12	0	2	0	1	0	0
H21	SHA	N/A	N/A	N/A	N/A	N/A	N/A	N/A	N/A	N/A
H20	LST	N/A	N/A	N/A	N/A	N/A	N/A	N/A	N/A	N/A
H19 d	L.M	N/A	N/A	N/A	N/A	N/A	N/A	N/A	N/A	N/A
H19 c	SHA	N/A	N/A	N/A	N/A	N/A	N/A	N/A	N/A	N/A
H19 b	L.M	N/A	N/A	N/A	N/A	N/A	N/A	N/A	N/A	N/A

H19 a	SHA	N/A	N/A	N/A	N/A	N/A	N/A	N/A	N/A	N/A
H18	LST	0	0	7	0	0	0	0	0	0
H17	P.S	N/A	N/A	N/A	N/A	N/A	N/A	N/A	N/A	N/A
H16	LST	1	0	40	0	2	0	0	0	0
H15	SHA	N/A	N/A	N/A	N/A	N/A	N/A	N/A	N/A	N/A
H14	LST	0	0	7	0	0	1	0	0	0
H13 c	D.M	0	0	2	0	0	0	0	0	0
H13 b	SHA	1	0	2	0	0	0	0	0	0
H13 a	P.S	0	0	0	0	0	0	0	0	0
H12	LST	0	0	2	0	0	0	0	0	0
H11	SHA	N/A	N/A	N/A	N/A	N/A	N/A	N/A	N/A	N/A
H10	LST	2	0	2	0	1	0	0	0	0
H9	SHA	N/A	N/A	N/A	N/A	N/A	N/A	N/A	N/A	N/A
H8	LST	0	0	12	0	1	0	0	0	0
H7 b	SHA	N/A	N/A	N/A	N/A	N/A	N/A	N/A	N/A	N/A
H7 a	P.S	N/A	N/A	N/A	N/A	N/A	N/A	N/A	N/A	N/A
H6	LST	0	0	9	0	0	0	0	0	0
H5 b	SHA	N/A	N/A	N/A	N/A	N/A	N/A	N/A	N/A	N/A
H5 a	P.S	0	0	1	0	0	0	0	0	0
H4	LST	0	0	3	0	0	0	0	0	0
H3	SHA	N/A	N/A	N/A	N/A	N/A	N/A	N/A	N/A	N/A
H2	LST	N/A	N/A	N/A	N/A	N/A	N/A	N/A	N/A	N/A
		Pinna	*Pleuromya*	Indeterminate bivalve	*Calcirhynchia calcaria*	Gastropod	Echinoid	Crinoid	Ammonoid	
H28	LST	0	1	3	0	0	0	1	0	
H27	D.M	N/A	N/A	N/A	N/A	N/A	N/A	N/A	N/A	
H26	LST	0	0	0	0	0	1	1	0	
H25	SHA	0	0	0	0	0	0	0	0	
H24	LST	0	0	0	0	0	1	0	0	
H23	SHA	0	0	0	0	0	0	0	0	
H22	LST	1	0	0	0	0	1	0	0	
H21	SHA	N/A	N/A	N/A	N/A	N/A	N/A	N/A	N/A	
H20	LST	N/A	N/A	N/A	N/A	N/A	N/A	N/A	N/A	
H19 d	L.M	N/A	N/A	N/A	N/A	N/A	N/A	N/A	N/A	
H19 c	SHA	N/A	N/A	N/A	N/A	N/A	N/A	N/A	N/A	
H19 b	L.M	N/A	N/A	N/A	N/A	N/A	N/A	N/A	N/A	
H19 a	SHA	N/A	N/A	N/A	N/A	N/A	N/A	N/A	N/A	

H18	LST	0	0	2	0	0	0	0	0	
H17	P.S	N/A	N/A	N/A	N/A	N/A	N/A	N/A	N/A	
H16	LST	0	0	2	0	0	0	0	0	
H15	SHA	N/A	N/A	N/A	N/A	N/A	N/A	N/A	N/A	
H14	LST	0	0	1	0	0	0	0	0	
H13 c	D.M	0	0	0	0	0	0	0	0	
H13 b	SHA	0	0	4	0	0	1	0	0	
H13 a	P.S	0	0	0	0	0	0	0	0	
H12	LST	0	0	0	0	0	0	0	0	
H11	SHA	N/A	N/A	N/A	N/A	N/A	N/A	N/A	N/A	
H10	LST	0	0	8	0	0	0	0	0	
H9	SHA	N/A	N/A	N/A	N/A	N/A	N/A	N/A	N/A	
H8	LST	0	0	1	0	0	0	0	0	
H7 b	SHA	N/A	N/A	N/A	N/A	N/A	N/A	N/A	N/A	
H7 a	P.S	N/A	N/A	N/A	N/A	N/A	N/A	N/A	N/A	
H6	LST	0	0	1	0	0	0	0	0	
H5 b	SHA	N/A	N/A	N/A	N/A	N/A	N/A	N/A	N/A	
H5 a	P.S	0	0	0	0	0	0	0	0	
H4	LST	0	0	0	0	0	0	0	0	
H3	SHA	N/A	N/A	N/A	N/A	N/A	N/A	N/A	N/A	
H2	LST	N/A	N/A	N/A	N/A	N/A	N/A	N/A	N/A	

BL 1										
Sample	**Lithology**	*Modiolus minimus*	*Chlamys*	*Liostrea*	*Gryphaea*	*Plagiostoma*	*Pseudolimea*	*Antiquilima*	*Pholadomya*	*Pseudopecten*
H1 c	P.S	N/A	N/A	N/A	N/A	N/A	N/A	N/A	N/A	N/A
H1 b	L.LST	N/A	N/A	N/A	N/A	N/A	N/A	N/A	N/A	N/A
H1 a	P.S	0	0	0	0	0	0	0	0	0
		Pinna	*Pleuromya*	Indeterminate bivalve	*Calcirhynchia calcaria*	Gastropod	Echinoid	Crinoid	Ammonoid	
H1 c	P.S	N/A	N/A	N/A	N/A	N/A	N/A	N/A	N/A	
H1 b	L.LST	N/A	N/A	N/A	N/A	N/A	N/A	N/A	N/A	
H1 a	P.S	0	0	0	0	0	0	0	0	

Table 3.1 – Macrofaunal data based on the minimum number of individuals for BL 1 – BL 4. Stratigraphy after the revised lithostratigraphy in Chapter 2. LST = limestone, L.M = light marl, D.M = dark marl, SHA = shale, P.S = paper shale, L.LST = laminated limestone. N/A = no sample.

BL 5 = the laminated limestones of BL 5 contain a restricted microfaunal assemblage comprised of bivalve spat and other fragmented shells, that accounts for an average of 1 % of the total sediment composition (fig. 3.4). Whilst H32 and H34 are without macrobenthos, H36 contains sparse epifaunal bivalves and ammonoids (macrofaunal coverage = 1 %) (fig. 3.4; table 3.2). The paper shale interbeds were also without macrofauna except for a single intact *Liostrea* in H33 (fig. 3.4; table 3.2). Barras and Twitchett (2007) recorded no ichnotaxa in the section (fig. 3.4) and trace fossils were not observed whilst conducting field observations; however, Jordan (2016) identified trace fossils in H32 and H36 (fig. 3.4).

BL 6 = in the bioturbated limestones of BL 6, the relative abundance of the microfaunal fossil component is inconsistent (6 – 42 % of the total sediment composition; fig. 3.4). The macrofaunal fossil assemblage, which contains a relatively high proportion of intact shells, has a strong correlation with lithology-specific inferred oxygen conditions (fig. 3.4). Macrofaunal abundance is greatest in the bioturbated limestones (average MNI = 20), and the number of individuals decreases progressively in the various argillaceous interbeds (dark marls = 12 > shales = 6 > paper shales = 3) (fig. 3.5; table 3.2). A similar trend is observed concerning species richness (fig. 3.5); the number of different taxa is greater in the bioturbated limestones (average = 6) than the dark marls (n = 3), shales (n = 3), and paper shales (n = 1) (fig. 3.5; table 3.2). At its maximum, a total of 8 different taxa are present in H44 which includes epifaunal bivalves (*Plagiostoma*, *Liostrea*, *Pseudolimea*, and *Antiquilima*), semi-infaunal bivalves (*Pinna*), echinoids, crinoids, and ammonoids (fig. 3.4; table 3.2). Infaunal bivalves (*Pleuromya*) were exclusive to H38 (fig. 3.4; table 3.2) and had been preserved in life position (fig. 3.1). It is important to note that the macrofaunal content of these beds, particularly fragmentary shell material, is not always evenly distributed e.g. shell fragments in H40 are concentrated in depressions upon the limestone's irregular upper surface. The macrofaunal assemblage within the various argillaceous interbeds is limited to low diversity epifauna (*Plagiostoma*, *Liostrea*, echinoids, and crinoids; fig. 3.4; table 3.2). Barras and Twitchett (2007) record a range of different ichnotaxa from the section including *Palaeophycus*, *Planolites*, *Rhizocorallium*, and *Thalassinoides* (fig. 3.4). In Jordan (2016), the author identified a dissimilar trace fossil assemblage that lacked *Palaeophycus* and *Planolites*, but contained the first occurrence of *Kulindrichnus* in H41. Jordan (2016) also indicates that the majority of beds within BL 6, including argillaceous interbeds, contain trace fossils (fig. 3.4).

BL 7 = the limited microfaunal fossil component in H46 and H50 (average = 2 % of total sediment composition) is dominated by intact bivalve spat (fig. 3.4); the topmost laminated limestone (H52) is without microfauna (fig. 3.4). All laminated limestones lack macrofauna and are without ichnotaxa according to Barras and Twitchett (2007) and Jordan (2016) (fig. 3.4). The basal paper shales (H45b) and topmost shales (H53b) were unfossiliferous, but H51 contained clusters of individual echinoid plates without spines (fig. 3.4; table 3.2). Thin (approximately 10 mm) shell lenses that contain a typical, low diversity epifaunal assemblage (i.e. *Liostrea*, *Plagiostoma*, and echinoids) were identified at non-sampled depths within H53b, H53c (see also Jordan, 2016), and at the base of H45. Argillaceous interbeds lack ichnotaxa (Barras and Twitchett, 2007, Jordan, 2016; fig. 3.4).

BL 8 = a limited microfaunal component in H54 (3 % of total sediment composition) is made up of fragmented shells (79 %) and echinoids (21 %) (fig. 3.4). Macrofaunal coverage is also sparse (2 %), and the restricted fossil assemblage is comprised of *Plagiostoma* (67 %) and echinoid spines (33 %) (fig. 3.4; table 3.2). H54 generally lacks evidence for post-mortem transport, but Jordan (2016) identifies *Kulindrichnus* within the limestone bed which the author suggests have preferentially concentrated crinoid ossicles and echinoid fragments.

BL 9 = the proportion of microfauna in the different bioturbated limestones of BL 9 is irregular (1 – 27 %; fig. 3.4). The percentage of macrofaunal coverage in different lithologies is consistent with inferred oxygen conditions such that it is greatest in the bioturbated limestones (average = 6 %) and progressively less extensive in the light marls (4 %), dark marls (average = 2 %), and shales (average = 1 %) (fig. 3.4). Species richness is also greatest in the bioturbated limestones (average number of different taxa = 7) and a maximum of 9 different taxa were identified in H56 (fig. 3.5; table 3.2). The bivalve assemblage in these bioturbated limestones is dominated by suspension-feeding epifauna, specifically *Plagiostoma* and *Liostrea* (average = 30 % and 26 % respectively; fig. 3.4); additional epifaunal genera (*Pseudopecten*, *Antiquilima*, and *Pseudolimea*) and the infaunal genus *Pholadomya* are also present (fig. 3.4; table 3.2). All of the limestone beds contain echinoid spines, but their relative abundance varies (4 – 55 %; fig. 3.4; table 3.2). Ammonoids are exclusive to H56 and crinoids to H58 (fig. 3.4; table 3.2). By comparison, the fossil assemblages of the argillaceous interbeds, irrespective of lithology, have poor species richness (average number of different taxa = 3; fig. 3.5); these are generally limited to low diversity epifauna (*Plagiostoma*, *Liostrea*, *Pseudolimea*, and echinoids) (fig. 3.4;

table 3.2). A single *Pinna* valve was identified in H61 (fig. 3.4; table 3.2). For most palaeoecological metrics, the range of values between lithological alternations is highest in the lower part of the section (below H60) and increasingly constant above this position (fig. 3.5). Barras and Twitchett (2007) record *Chondrites*, *Planolites*, and *Rhizocorallium* in H60 and H62 (fig. 3.4); Jordan (2016) identified trace fossils, including ichnogenera such as *Thalassinoides* and *Kulindrichnus*, in the majority of beds irrespective of lithology (fig. 3.4). In both accounts, the space between H62 and H66 is without ichnotaxa (Barras and Twitchett, 2007, Jordan, 2016; fig. 3.4).

BL 10 = H66 has a minor microfaunal fossil component (11 % of total sediment composition) and limited macrofaunal coverage (3 %) (fig. 3.4). The typical, low diversity fossil assemblage contains *Plagiostoma* (58 %), *Liostrea* (14 %), an indeterminate bivalve genus (14 %), and echinoids (14 %) (fig. 3.4; table 3.2). Barras and Twitchett (2007) and Jordan (2016) identified ichnotaxa in the upper part of the limestone bed (fig. 3.4).

BL 11 = most palaeoecological metrics in BL 11 (MNI, species richness, and diversity) correlate well with inferred oxygen conditions between adjacent lithologies (fig. 3.7). Paper shales are without macrofauna except for a single *Liostrea* valve in H67d (fig. 3.6; table 3.3). The dark marl alternations have the greatest macrofaunal coverage (average = 4 %) and the most diverse fossil assemblage which includes *Plagiostoma*, *Liostrea*, *Pseudopecten*, an indeterminate bivalve genus, echinoids, and ammonoids (fig. 3.6; table 3.3). Barras and Twitchett (2007) record a lack of ichnotaxa within BL 11, but Jordan (2016) identified burrow mottled bed transitions and trace fossils that were emplaced within the non-paper shale alternations (fig. 3.6).

BL 12 = bioturbated limestones contain a minor microfaunal component (average = 10 % of the total sediment composition; fig. 3.6); in H68, the microfaunal assemblage is dominated by echinoid fragments (52 %) that were missing from H70 (fig. 3.6). The extent of macrofaunal coverage is greater in H68 than H70 (12 % and 2 % respectively; fig. 3.6), but species richness is comparable (average number of different taxa = 6; fig. 3.7; table 3.3). Both limestones have a typical epifaunal assemblage (*Plagiostoma*, *Liostrea*, an indeterminate bivalve genus, crinoids, and echinoids) although H68 also contains the semi-infaunal bivalve genus *Pinna* (fig. 3.6; table 3.3). The dark marl interbed was not examined for macrofauna.

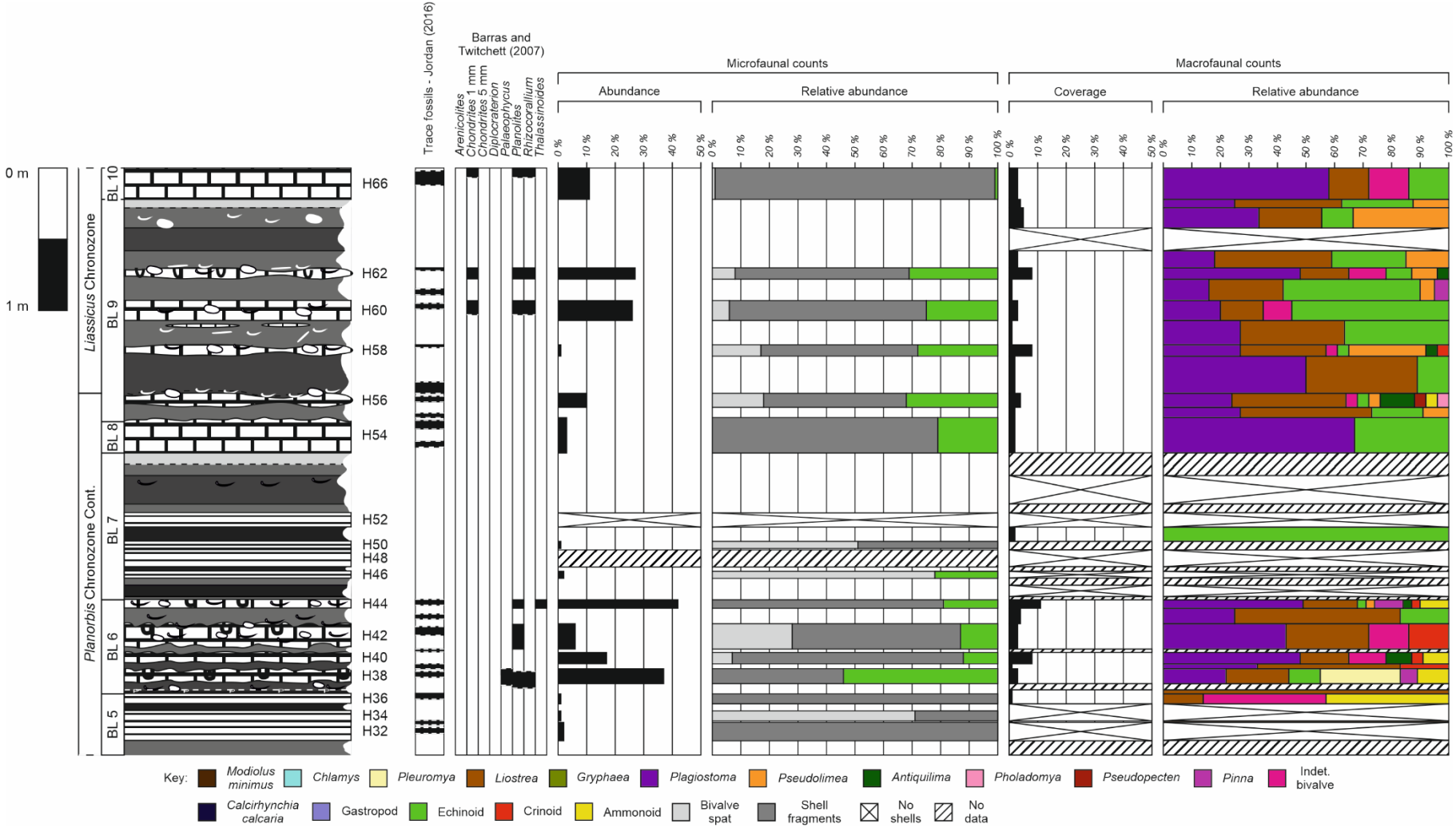

Figure 3.4 – Microfaunal data (proportion of sediment composition/abundance and relative abundance of different bioclasts respectively) and macrofaunal data (percent coverage and relative abundance of different bioclasts from MNI counts respectively) for BL 5 – BL 10. Stratigraphy after the revised lithostratigraphy in Chapter 2. Ichnotaxonomic data after Barras and Twitchett (2007) and Jordan (2016). Components of the micro and macrofaunal counts are shown in the key.

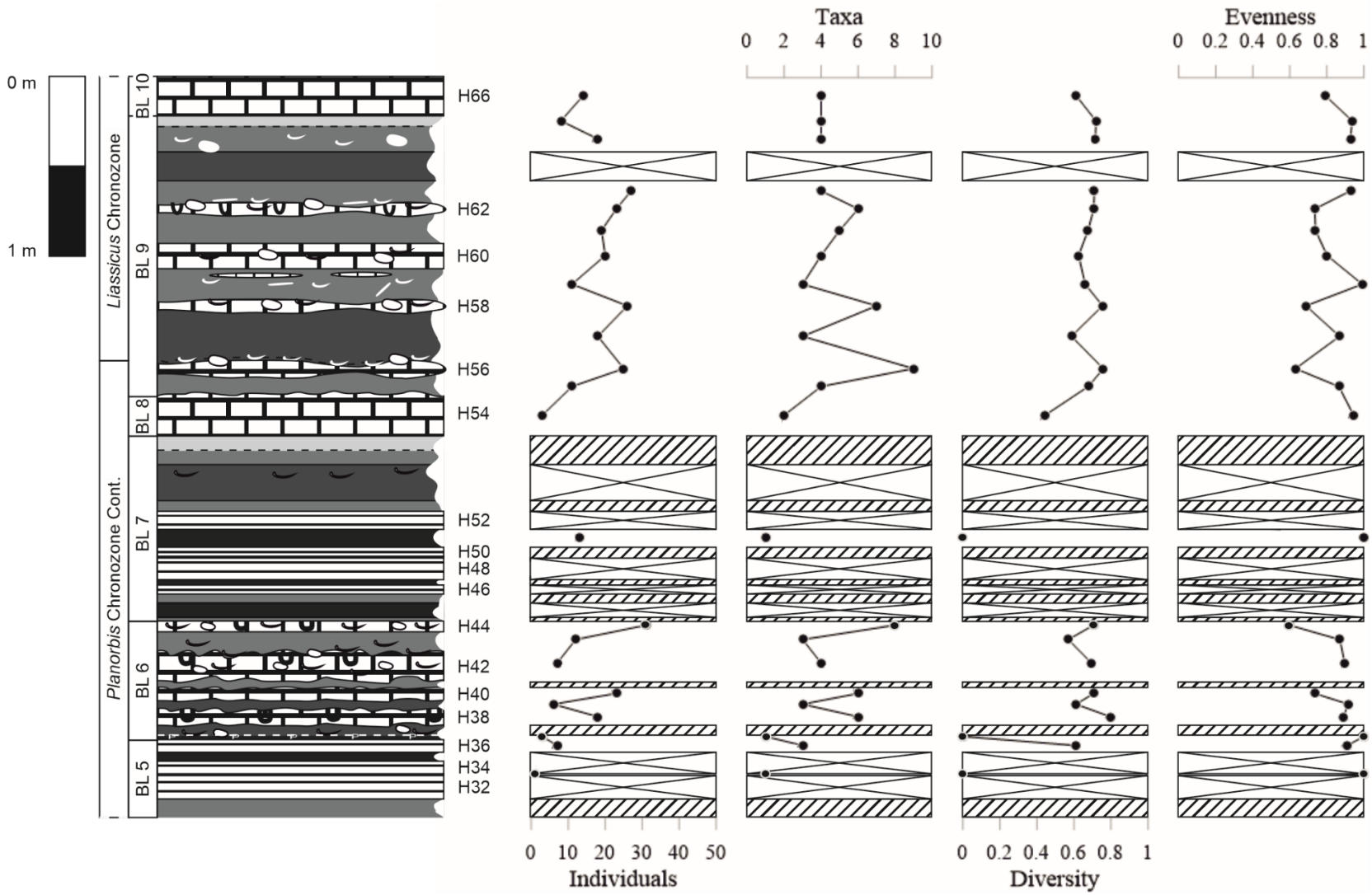

Figure 3.5 – Graphic logs showing the minimum number of individuals, species richness or number of different taxa, diversity, and evenness of the macrofaunal fossil assemblage in BL 5 – BL 10. Stratigraphy after the revised lithostratigraphy in Chapter 2.

BL 10										
Sample	**Lithology**	*Modiolus minimus*	*Chlamys*	*Liostrea*	*Gryphaea*	*Plagiostoma*	*Pseudolimea*	*Antiquilima*	*Pholadomya*	*Pseudopecten*
H66	LST	0	0	2	0	8	0	0	0	0
		Pinna	*Pleuromya*	Indeterminate bivalve	*Calcirhynchia calcaria*	Gastropod	Echinoid	Crinoid	Ammonoid	
		0	0	2	0	0	2	0	0	

BL 9										
Sample	**Lithology**	*Modiolus minimus*	*Chlamys*	*Liostrea*	*Gryphaea*	*Plagiostoma*	*Pseudolimea*	*Antiquilima*	*Pholadomya*	*Pseudopecten*
H63 d	L.M	0	0	3	0	2	1	0	0	0
H63 c	D.M	0	0	4	0	6	6	0	0	0
H63 b	SHA	0	0	0	0	0	0	0	0	0
H63 a	D.M	0	0	11	0	5	4	0	0	0
H62	LST	0	0	4	0	11	2	1	0	0
H61	D.M	0	0	5	0	3	1	0	0	0
H60	LST	0	0	3	0	4	0	0	0	0
H59	D.M	0	0	4	0	3	0	0	0	0
H58	LST	0	0	8	0	7	7	1	0	0
H57	SHA	0	0	7	0	9	0	0	0	0
H56	LST	0	0	10	0	6	1	3	1	1
H55	D.M	0	0	5	0	3	1	0	0	0
		Pinna	*Pleuromya*	Indeterminate bivalve	*Calcirhynchia calcaria*	Gastropod	Echinoid	Crinoid	Ammonoid	
H63 d	L.M	0	0	0	0	0	2	0	0	
H63 c	D.M	0	0	0	0	0	2	0	0	
H63 b	SHA	0	0	0	0	0	0	0	0	
H63 a	D.M	0	0	0	0	0	7	0	0	
H62	LST	0	0	3	0	0	2	0	0	
H61	D.M	1	0	0	0	0	9	0	0	
H60	LST	0	0	2	0	0	11	0	0	
H59	D.M	0	0	0	0	0	4	0	0	
H58	LST	0	0	1	0	0	1	1	0	
H57	SHA	0	0	0	0	0	2	0	0	
H56	LST	0	0	1	0	0	1	0	1	
H55	D.M	0	0	0	0	0	2	0	0	

BL 8										
Sample	**Lithology**	*Modiolus minimus*	*Chlamys*	*Liostrea*	*Gryphaea*	*Plagiostoma*	*Pseudolimea*	*Antiquilima*	*Pholadomya*	*Pseudopecten*
H54	LST	0	0	0	0	2	0	0	0	0
		Pinna	*Pleuromya*	Indeterminate bivalve	*Calcirhynchia calcaria*	Gastropod	Echinoid	Crinoid	Ammonoid	
		0	0	0	0	0	1	0	0	

BL 7										
Sample	**Lithology**	*Modiolus minimus*	*Chlamys*	*Liostrea*	*Gryphaea*	*Plagiostoma*	*Pseudolimea*	*Antiquilima*	*Pholadomya*	*Pseudopecten*
H53 d	L.M	N/A	N/A	N/A	N/A	N/A	N/A	N/A	N/A	N/A
H53 c	D.M	N/A	N/A	N/A	N/A	N/A	N/A	N/A	N/A	N/A
H53 b	SHA	0	0	0	0	0	0	0	0	0
H53 a	D.M	N/A	N/A	N/A	N/A	N/A	N/A	N/A	N/A	N/A
H52	L.LST	0	0	0	0	0	0	0	0	0
H51	P.S	0	0	0	0	0	0	0	0	0
H50	L.LST	N/A	N/A	N/A	N/A	N/A	N/A	N/A	N/A	N/A
H49	P.S	N/A	N/A	N/A	N/A	N/A	N/A	N/A	N/A	N/A
H48	L.LST	0	0	0	0	0	0	0	0	0
H47	P.S	N/A	N/A	N/A	N/A	N/A	N/A	N/A	N/A	N/A
H46	L.LST	0	0	0	0	0	0	0	0	0
H45 c	D.M	N/A	N/A	N/A	N/A	N/A	N/A	N/A	N/A	N/A
H45 b	P.S	0	0	0	0	0	0	0	0	0
H45 a	D.M	N/A	N/A	N/A	N/A	N/A	N/A	N/A	N/A	N/A
		Pinna	*Pleuromya*	Indeterminate bivalve	*Calcirhynchia calcaria*	Gastropod	Echinoid	Crinoid	Ammonoid	
H53 d	L.M	N/A	N/A	N/A	N/A	N/A	N/A	N/A	N/A	
H53 c	D.M	N/A	N/A	N/A	N/A	N/A	N/A	N/A	N/A	
H53 b	SHA	0	0	0	0	0	0	0	0	
H53 a	D.M	N/A	N/A	N/A	N/A	N/A	N/A	N/A	N/A	
H52	L.LST	0	0	0	0	0	0	0	0	
H51	P.S	0	0	0	0	0	13	0	0	
H50	L.LST	N/A	N/A	N/A	N/A	N/A	N/A	N/A	N/A	
H49	P.S	N/A	N/A	N/A	N/A	N/A	N/A	N/A	N/A	
H48	L.LST	0	0	0	0	0	0	0	0	

H47	P.S	N/A	N/A	N/A	N/A	N/A	N/A	N/A	N/A	
H46	L.LST	0	0	0	0	0	0	0	0	
H45 c	D.M	N/A	N/A	N/A	N/A	N/A	N/A	N/A	N/A	
H45 b	P.S	0	0	0	0	0	0	0	0	
H45 a	D.M	N/A	N/A	N/A	N/A	N/A	N/A	N/A	N/A	

BL 6										
Sample	**Lithology**	*Modiolus minimus*	*Chlamys*	*Liostrea*	*Gryphaea*	*Plagiostoma*	*Pseudolimea*	*Antiquilima*	*Pholadomya*	*Pseudopecten*
H44	LST	0	0	6	0	15	1	1	0	0
H43	D.M	0	0	7	0	3	0	0	0	0
H42	LST	0	0	2	0	3	0	0	0	0
H41	D.M	N/A	N/A	N/A	N/A	N/A	N/A	N/A	N/A	N/A
H40	LST	0	0	4	0	11	0	2	0	0
H39	SHA	0	0	3	0	2	0	0	0	0
H38	LST	0	0	4	0	4	0	0	0	0
H37 b	SHA	N/A	N/A	N/A	N/A	N/A	N/A	N/A	N/A	N/A
H37 a	P.S	0	0	3	0	0	0	0	0	0
		Pinna	*Pleuromya*	Indeterminate bivalve	*Calcirhynchia calcaria*	Gastropod	Echinoid	Crinoid	Ammonoid	
H44	LST	3	0	0	0	0	1	1	3	
H43	D.M	0	0	0	0	0	2	0	0	
H42	LST	0	0	1	0	0	0	1	0	
H41	D.M	N/A	N/A	N/A	N/A	N/A	N/A	N/A	N/A	
H40	LST	0	0	3	0	0	0	1	2	
H39	SHA	0	0	0	0	0	0	1	0	
H38	LST	1	5	0	0	0	2	0	2	
H37 b	SHA	N/A	N/A	N/A	N/A	N/A	N/A	N/A	N/A	
H37 a	P.S	0	0	0	0	0	0	0	0	

BL 5										
Sample	**Lithology**	*Modiolus minimus*	*Chlamys*	*Liostrea*	*Gryphaea*	*Plagiostoma*	*Pseudolimea*	*Antiquilima*	*Pholadomya*	*Pseudopecten*
H36	L.LST	0	0	1	0	0	0	0	0	0
H35	P.S	0	0	0	0	0	0	0	0	0
H34	L.LST	0	0	0	0	0	0	0	0	0
H33	P.S	0	0	1	0	0	0	0	0	0

H32	L.LST	0	0	0	0	0	0	0	0	0
H31	D.M	N/A	N/A	N/A	N/A	N/A	N/A	N/A	N/A	N/A
		Pinna	*Pleuromya*	Indeterminate bivalve	*Calcirhynchia calcaria*	Gastropod	Echinoid	Crinoid	Ammonoid	
H36	L.LST	0	0	3	0	0	0	0	3	
H35	P.S	0	0	0	0	0	0	0	0	
H34	L.LST	0	0	0	0	0	0	0	0	
H33	P.S	0	0	0	0	0	0	0	0	
H32	L.LST	0	0	0	0	0	0	0	0	
H31	D.M	N/A	N/A	N/A	N/A	N/A	N/A	N/A	N/A	

Table 3.2 – Macrofaunal data based on the minimum number of individuals for BL 5 – BL 10. Stratigraphy after the revised lithostratigraphy in Chapter 2. LST = limestone, L.M = light marl, D.M = dark marl, SHA = shale, P.S = paper shale, L.LST = laminated limestone. N/A = no sample.

BL 13 = palaeoecological metrics are consistent with inferred oxygen conditions between adjacent lithologies (fig. 3.7). The single bed of paper shales is without macrofauna (fig. 3.6; table 3.3). Dark marls have a restricted macrofaunal fossil content (average macrofaunal coverage = 2 %) dominated by low diversity epifauna (*Plagiostoma*, *Liostrea*, and echinoids) (fig. 3.6; table 3.3); ammonoids are exclusive to the topmost dark marls (fig. 3.6; table 3.3). Jordan (2016) recorded trace fossils at different heights within BL 13, excluding emplacement in the central paper shales approximating H71b (fig. 3.6).

BL 14 = the microfaunal fossil component of the bioturbated limestones accounts for an irregular proportion of the overall sediment composition (12 – 29 %; fig. 3.6). The percentage of macrofaunal coverage correlates well with lithology and is greater in the bioturbated limestones (average = 6 %) than the dark marl interbeds (average = 2 %) (fig. 3.6). Palaeoecological metrics are lithology non-specific such that MNI and species richness increase with vertical progression (fig. 3.7); the number of different taxa in the limestone beds increases from 3 to 7 in H72 and H76 respectively (fig. 3.7; table 3.3). The limestone fossil assemblage is dominated by *Plagiostoma* and *Liostrea* but contains additional epifaunal bivalves (*Pseudolimea* and *Antiquilima*) and the infaunal genus *Pleuromya* in H76 (fig. 3.6; table 3.3). Dark marl interbeds show low diversity fossil assemblages dominated by *Plagiostoma* and *Liostrea* (fig. 3.6; table 3.3). Ammonoids were present in H73 and H74 (fig. 3.6; table 3.3). It is important to note that the distribution of macrofauna on the bedding surface was not even and scour fills were recognised in H72, H74, and H76 (see also Jordan, 2016). Jordan (2016) identified trace fossils in all of the bioturbated limestone beds as well as the dark marls in H73 (fig. 3.6).

BL 15 = the percentage of macrofaunal coverage in BL 15 is sparse (average = 2 %) and does not correlate with lithology (fig. 3.6). However, species richness and diversity correlate well with inferred oxygen conditions and are consistently greater in the bioturbated limestones (average number of different taxa = 5) compared with the dark marl interbeds (average number of different taxa = 3) (fig. 3.7; table 3.3). The macrofaunal fossil assemblages of both lithologies contain typical, low diversity epifauna (*Plagiostoma*, *Liostrea*, *Pseudolimea*, and echinoids) (fig. 3.6; table 3.3); additional taxa exclusive to the bioturbated limestones include *Antiquilima*, an indeterminate bivalve genus, and ammonoids (fig. 3.6; table 3.3). Jordan (2016) recorded trace fossils in all of the bioturbated limestones and a number of the argillaceous interbeds (fig. 3.6).

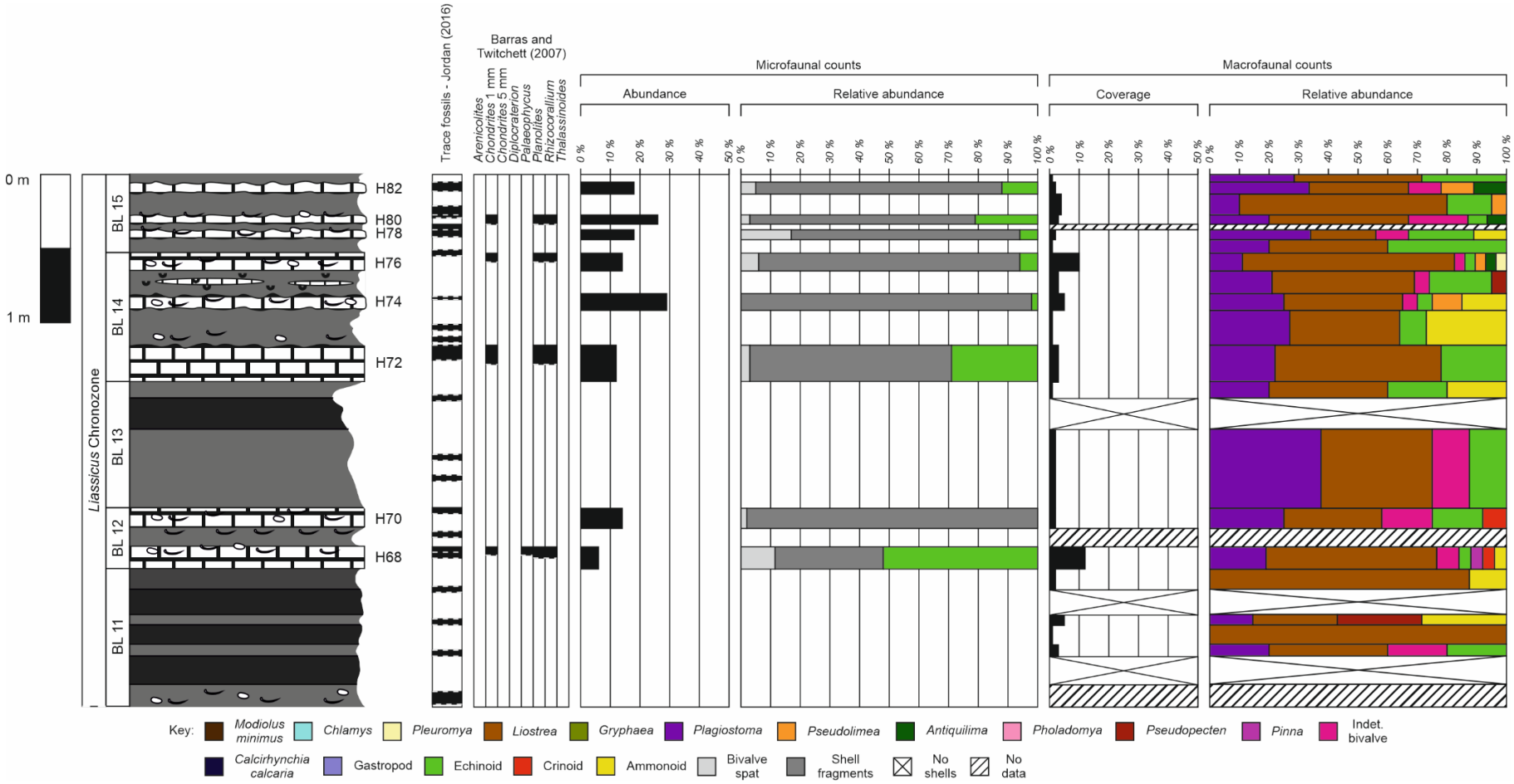

Figure 3.6 – Microfaunal data (proportion of sediment composition/abundance and relative abundance of different bioclasts respectively) and macrofaunal data (percent coverage and relative abundance of different bioclasts from MNI counts respectively) for BL 11 – BL 15. Stratigraphy after the revised lithostratigraphy in Chapter 2. Ichnotaxonomic data after Barras and Twitchett (2007) and Jordan (2016). Components of the micro and macrofaunal counts are shown in the key.

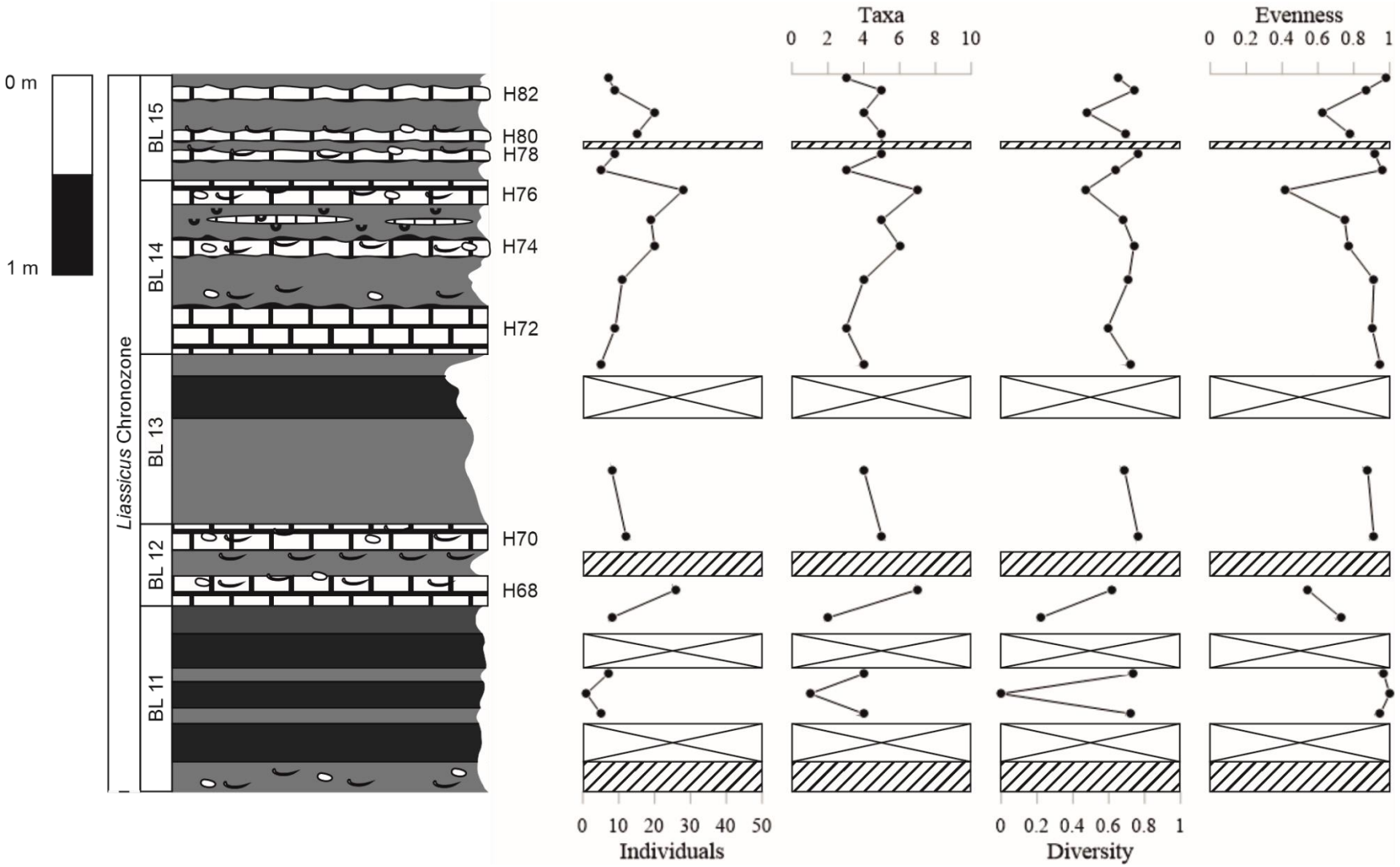

Figure 3.7 – Graphic logs showing the minimum number of individuals, species richness or number of different taxa, diversity, and evenness of the macrofaunal fossil assemblage in BL 11 – BL 15. Stratigraphy after the revised lithostratigraphy in Chapter 2.

BL 15										
Sample	**Lithology**	*Modiolus minimus*	*Chlamys*	*Liostrea*	*Gryphaea*	*Plagiostoma*	*Pseudolimea*	*Antiquilima*	*Pholadomya*	*Pseudopecten*
H83	D.M	0	0	3	0	2	0	0	0	0
H82	LST	0	0	3	0	3	1	1	0	0
H81	D.M	0	0	14	0	2	1	0	0	0
H80	LST	0	0	7	0	3	0	1	0	0
H79	D.M	N/A	N/A	N/A	N/A	N/A	N/A	N/A	N/A	N/A
H78	LST	0	0	2	0	3	0	0	0	0
H77	D.M	0	0	2	0	1	0	0	0	0
		Pinna	*Pleuromya*	Indeterminate bivalve	*Calcirhynchia calcaria*	Gastropod	Echinoid	Crinoid	Ammonoid	
H83	D.M	0	0	0	0	0	2	0	0	
H82	LST	0	0	1	0	0	0	0	0	
H81	D.M	0	0	0	0	0	3	0	0	
H80	LST	0	0	3	0	0	1	0	0	
H79	D.M	N/A	N/A	N/A	N/A	N/A	N/A	N/A	N/A	
H78	LST	0	0	1	0	0	2	0	1	
H77	D.M	0	0	0	0	0	2	0	0	

BL 14										
Sample	**Lithology**	*Modiolus minimus*	*Chlamys*	*Liostrea*	*Gryphaea*	*Plagiostoma*	*Pseudolimea*	*Antiquilima*	*Pholadomya*	*Pseudopecten*
H76	LST	0	0	20	0	3	1	1	0	0
H75	D.M	0	0	9	0	4	0	0	0	1
H74	LST	0	0	8	0	5	2	0	0	0
H73	D.M	0	0	4	0	3	0	0	0	0
H72	LST	0	0	5	0	2	0	0	0	0
		Pinna	*Pleuromya*	Indeterminate bivalve	*Calcirhynchia calcaria*	Gastropod	Echinoid	Crinoid	Ammonoid	
H76	LST	0	1	1	0	0	1	0	0	
H75	D.M	0	0	1	0	0	4	0	0	
H74	LST	0	0	1	0	0	1	0	3	
H73	D.M	0	0	0	0	0	1	0	3	
H72	LST	0	0	0	0	0	2	0	0	

BL 13										
Sample	**Lithology**	*Modiolus minimus*	*Chlamys*	*Liostrea*	*Gryphaea*	*Plagiostoma*	*Pseudolimea*	*Antiquilima*	*Pholadomya*	*Pseudopecten*
H71 c	D.M	0	0	2	0	1	0	0	0	0
H71 b	P.S	0	0	0	0	0	0	0	0	0
H71 a	D.M	0	0	3	0	3	0	0	0	0
		Pinna	*Pleuromya*	Indeterminate bivalve	*Calcirhynchia calcaria*	Gastropod	Echinoid	Crinoid	Ammonoid	
H71 c	D.M	0	0	0	0	0	1	0	1	
H71 b	P.S	0	0	0	0	0	0	0	0	
H71 a	D.M	0	0	1	0	0	1	0	0	

BL 12										
Sample	**Lithology**	*Modiolus minimus*	*Chlamys*	*Liostrea*	*Gryphaea*	*Plagiostoma*	*Pseudolimea*	*Antiquilima*	*Pholadomya*	*Pseudopecten*
H70	LST	0	0	4	0	3	0	0	0	0
H69	D.M	N/A	N/A	N/A	N/A	N/A	N/A	N/A	N/A	N/A
H68	LST	0	0	15	0	5	0	0	0	0
		Pinna	*Pleuromya*	Indeterminate bivalve	*Calcirhynchia calcaria*	Gastropod	Echinoid	Crinoid	Ammonoid	
H70	LST	0	0	2	0	0	2	1	0	
H69	D.M	N/A	N/A	N/A	N/A	N/A	N/A	N/A	N/A	
H68	LST	1	0	2	0	0	1	1	1	

BL 11										
Sample	**Lithology**	*Modiolus minimus*	*Chlamys*	*Liostrea*	*Gryphaea*	*Plagiostoma*	*Pseudolimea*	*Antiquilima*	*Pholadomya*	*Pseudopecten*
H67 g	SHA	0	0	7	0	0	0	0	0	0
H67 f	P.S	0	0	0	0	0	0	0	0	0
H67 e	D.M	0	0	2	0	1	0	0	0	2
H67 d	P.S	0	0	1	0	0	0	0	0	0
H67 c	D.M	0	0	2	0	1	0	0	0	0
H67 b	P.S	0	0	0	0	0	0	0	0	0
H67 a	D.M	N/A	N/A	N/A	N/A	N/A	N/A	N/A	N/A	N/A
		Pinna	*Pleuromya*	Indeterminate bivalve	*Calcirhynchia calcaria*	Gastropod	Echinoid	Crinoid	Ammonoid	
H67 g	SHA	0	0	0	0	0	0	0	1	

H67 f	P.S	0	0	0	0	0	0	0	0	
H67 e	D.M	0	0	0	0	0	0	0	2	
H67 d	P.S	0	0	0	0	0	0	0	0	
H67 c	D.M	0	0	1	0	0	1	0	0	
H67 b	P.S	0	0	0	0	0	0	0	0	
H67 a	D.M	N/A	N/A	N/A	N/A	N/A	N/A	N/A	N/A	

Table 3.3 – Macrofaunal data based on the minimum number of individuals for BL 11 – BL 15. Stratigraphy after the revised lithostratigraphy in Chapter 2. LST = limestone, L.M = light marl, D.M = dark marl, SHA = shale, P.S = paper shale, L.LST = laminated limestone. N/A = no sample.

BL 16 = irrespective of lithology, the extent of macrofaunal coverage throughout the section is poor (1 – 4 %; fig. 3.8). In the bioturbated limestones, MNI is low (average = 7) and there is limited species richness (average number of different taxa = 3) (fig. 3.9; table 3.4). Bivalve genera are restricted to the typical, low diversity epifauna (e.g. *Plagiostoma* and *Liostrea*) except for a single infaunal genus (*Pholadomya*) in H88 (fig. 3.8; table 3.4). The proportion of microfauna decreases from H84 to H90 (19 % – 10 % of the total sediment composition respectively) and whilst the composition of the microfaunal assemblage is generally consistent, H86 is unique in that it contains gastropod spat (fig. 3.8). Of the argillaceous interbeds, light marls have a uniform macrofaunal assemblage restricted to low diversity epifauna (*Plagiostoma*, *Liostrea*, *Pseudolimea*, and echinoids) (fig. 3.8; table 3.4). Contrary to inferred oxygen conditions between adjacent lithologies, dark marls contain the highest average MNI (n = 29) and the greatest species richness (average number of different taxa = 5) (fig. 3.9; table 3.4); this exclusively epifaunal assemblage is comprised of *Plagiostoma*, *Liostrea*, *Pseudolimea*, *Antiquilima*, *Pseudopecten*, and echinoids (fig. 3.8; table 3.4). H85b and H91c, the two shale interbeds in the section, contain sparse single taxon assemblages (ammonoids and *Liostrea* respectively) (fig. 3.8; table 3.4). Barras and Twitchett (2007) record different ichnotaxa in H84 and H86 (*Planolites*/*Rhizocorallium* and *Chondrites* respectively) (fig. 3.8); Jordan (2016) identified a more extensive trace fossil distribution that includes several of the argillaceous interbeds (fig. 3.8).

BL 17 = the percentage of macrofaunal coverage is low irrespective of lithology (average = 1 %; fig. 3.8). Despite the restricted fossil assemblage, other palaeoecological metrics show a good correlation with inferred oxygen conditions (fig. 3.9). Macrofaunal abundance (average MNI = 8) and species richness (average number of different taxa = 4) are greater in the bioturbated limestones than the dark marl interbed, which contains a sparse (MNI = 2), single taxon assemblage (fig. 3.9; table 3.4).

BL 18 = the extent of macrofaunal coverage is loosely correlated to inferred oxygen conditions in that its average is greater in the bioturbated limestones than the dark marl interbeds (5 % and 2 % respectively; fig. 3.8). Palaeoecological metrics are inconsistent and generally lack sustained lithological trends (fig. 3.9). Macrofaunal abundance varies extensively within the bioturbated limestones (MNI = 12 – 39; Brick k and Brick i respectively) and the number of different taxa in a single bed ranges from 3 – 10 (Brick k and Brick i respectively) (fig. 3.9; table 3.4); similar intra-lithology variance occurs within

the dark marls (MNI = 6 – 24; Brick d and Brick n respectively; number of different taxa = 3 – 7; Brick d and Brick j respectively) (fig. 3.9; table 3.4). However, despite the fact that the composition of the macrofaunal assemblage varies extensively on a bed-by-bed basis, the overall fossil assemblage is remarkably consistent between the two lithologies; both contain identical epifaunal bivalve and brachiopod genera (*Plagiostoma, Liostrea, Pseudolimea, Antiquilima, Pseudopecten, and Calcirhynchia*), a single infaunal bivalve genus (*Pholadomya*), echinoids, crinoids, and ammonoids (fig. 3.8; table 3.4). Trace fossils were recorded in a number of the limestone-marl alternations by Barras and Twitchett (2007) and Jordan (2016) (fig. 3.8).

BL 19 = the extent of macrofaunal coverage throughout the section is inconsistent and does not generally correlate with lithology (fig. 3.8). In the bioturbated limestones, there is significant variation in the macrofaunal fossil assemblage and little uniformity to the microfaunal assemblage which accounts for different proportions of the total sediment composition (7 % – 19 %) (fig. 3.8; table 3.4). The macrofaunal assemblage of the basal limestone bed (Soft Bed), which has a total of 8 different taxa including epifaunal and infaunal bivalve genera, is in contrast to that of the limestones immediately above (Lower Venty and Lower Skulls) which contain a restricted fossil assemblage limited to *Plagiostoma* and *Liostrea* only (fig. 3.8; table 3.4). Above this position, the bioturbated limestones have a relatively high proportion of *Calcirhynchia* (maximum relative abundance = 95 % in Under Copper; average = 52 %) (fig. 3.8); the epifaunal bivalve genera vary on a bed-by-bed basis, but include *Plagiostoma, Liostrea, Pseudolimea,* and *Chlamys* (fig. 3.8; table 3.4). There are two instances of infauna recorded from these upper limestones (fig. 3.8; table 3.4); the topmost Lower Skulls limestone bed contains *Pleuromya* and Iron Ledge contains *Pholadomya* (fig. 3.8; table 3.4). Light marls have a moderate species richness (average number of different taxa = 5; fig. 3.9), but the fossil component is limited to epifauna (*Plagiostoma, Liostrea, Pseudolimea, Calcirhynchia*, crinoids and echinoids) albeit with different relative abundances (fig. 3.8; table 3.4). Only the aforementioned epifaunal bivalve and brachiopod genera were present in the single dark marl interbed and, consistent with relative inferred oxygen conditions, the two shale beds (Lower Venty b and Under Copper a) lack macrofauna (fig. 3.8; table 3.4). BL 19 contains a diverse and well-distributed trace fossil assemblage irrespective of lithology (Barras and Twitchett, 2007, Jordan, 2016; fig. 3.8).

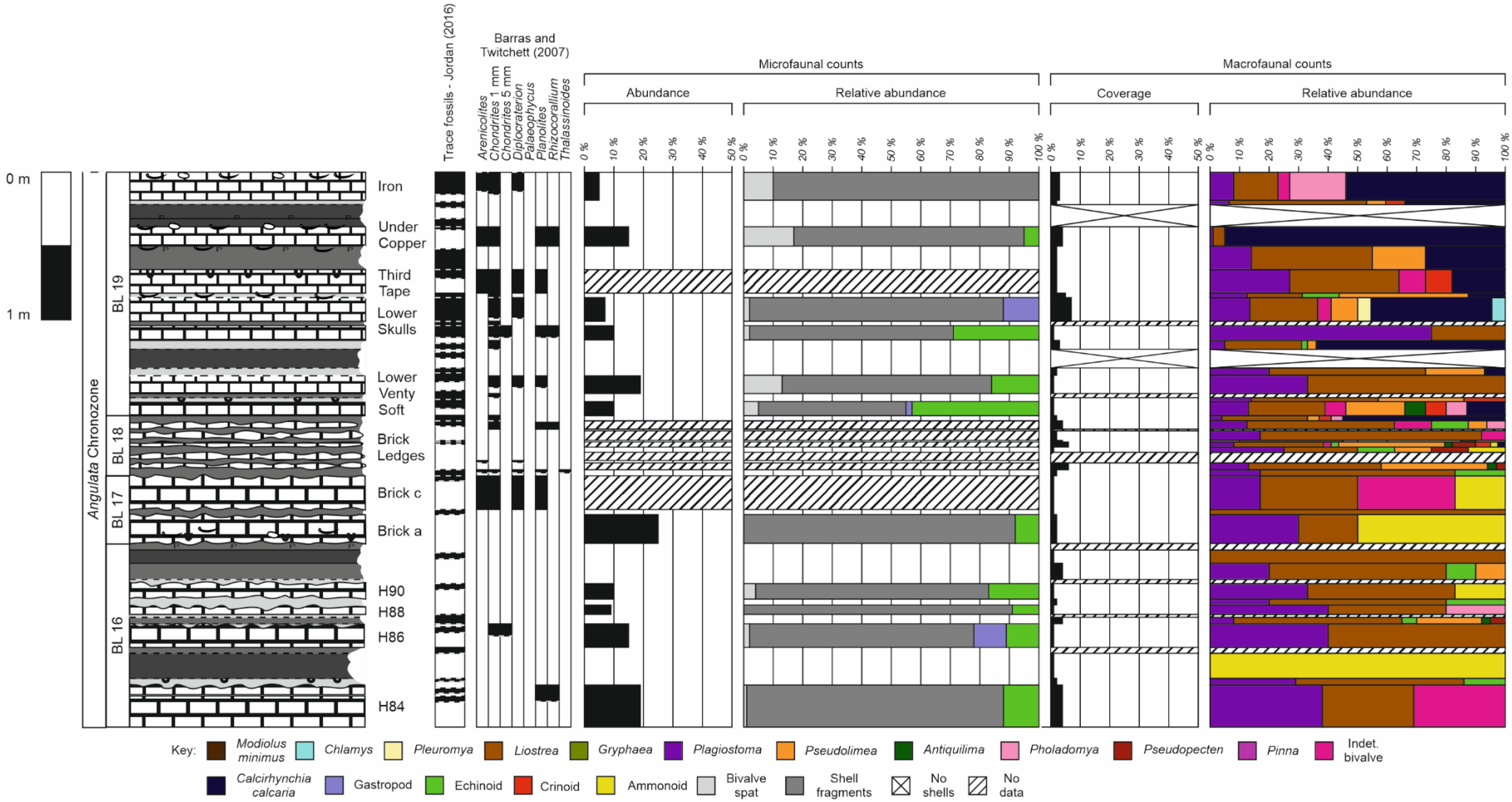

Figure 3.8 – Microfaunal data (proportion of sediment composition/abundance and relative abundance of different bioclasts respectively) and macrofaunal data (percent coverage and relative abundance of different bioclasts from MNI counts respectively) for BL 16 – BL 19. Stratigraphy after the revised lithostratigraphy in Chapter 2. Ichnotaxonomic data after Barras and Twitchett (2007) and Jordan (2016). Components of the micro and macrofaunal counts are shown in the key.

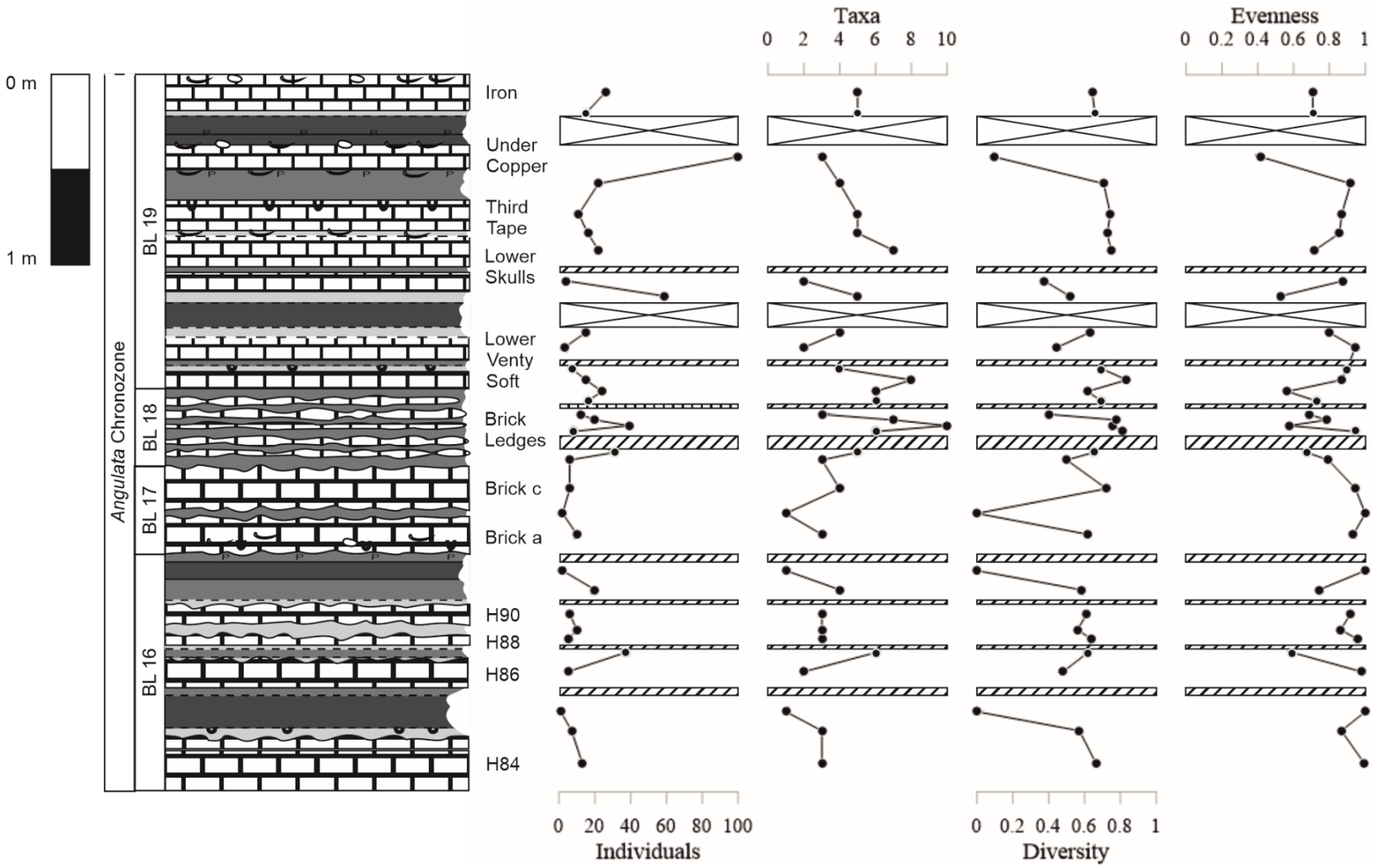

Figure 3.9 – Graphic logs showing the minimum number of individuals, species richness or number of different taxa, diversity, and evenness of the macrofaunal fossil assemblage in BL 16 – BL 19. Stratigraphy after the revised lithostratigraphy in Chapter 2.

BL 19										
Sample	**Lithology**	*Modiolus minimus*	*Chlamys*	*Liostrea*	*Gryphaea*	*Plagiostoma*	*Pseudolimea*	*Antiquilima*	*Pholadomya*	*Pseudopecten*
Iron	LST	0	0	4	0	2	0	0	5	0
Un.Cop b	L.M	0	0	7	0	1	1	0	0	0
Un.Cop a	SHA	0	0	0	0	0	0	0	0	0
Un.Cop	LST	0	0	4	0	1	0	0	0	0
Thi.Tape a	D.M	0	0	9	0	3	4	0	0	0
Thi. Tape	LST	0	0	4	0	3	0	0	0	0
Ab L. Sk c	L.M	0	0	3	0	2	7	0	0	0
Ab L. Sk b	LST	0	1	5	0	3	2	0	0	0
Ab L. Sk a	D.M	N/A	N/A	N/A	N/A	N/A	N/A	N/A	N/A	N/A
L. Sk	LST	0	0	1	0	3	0	0	0	0
L. Vent c	L.M	0	0	15	0	3	2	0	0	0
L. Vent b	SHA	0	0	0	0	0	0	0	0	0
L. Vent a	L.M	0	0	8	0	3	3	0	0	0
L. Vent	LST	0	0	2	0	1	0	0	0	0
Ab Soft b	D.M	N/A	N/A	N/A	N/A	N/A	N/A	N/A	N/A	N/A
Ab Soft a	L.M	0	0	3	0	1	2	0	0	0
Soft	LST	0	0	4	0	2	3	1	1	0
		Pinna	*Pleuromya*	Indeterminate bivalve	*Calcirhynchia calcaria*	Gastropod	Echinoid	Crinoid	Ammonoid	
Iron	LST	0	0	1	14	0	0	0	0	
Un.Cop b	L.M	0	0	0	5	0	0	1	0	
Un.Cop a	SHA	0	0	0	0	0	0	0	0	
Un.Cop	LST	0	0	0	95	0	0	0	0	
Th.Tape a	D.M	0	0	0	6	0	0	0	0	
Thi. Tape	LST	0	0	1	2	0	0	1	0	
Ab L. Sk c	L.M	0	0	0	2	0	2	0	0	
Ab L. Sk b	LST	0	1	1	9	0	0	0	0	
Ab L. Sk a	D.M	N/A	N/A	N/A	N/A	N/A	N/A	N/A	N/A	
L. Sk	LST	0	0	0	0	0	0	0	0	
L. Vent c	L.M	0	0	0	38	0	1	0	0	
L. Vent b	SHA	0	0	0	0	0	0	0	0	
L. Vent a	L.M	0	0	0	1	0	0	0	0	
L. Vent	LST	0	0	0	0	0	0	0	0	
Ab Soft b	D.M	N/A	N/A	N/A	N/A	N/A	N/A	N/A	N/A	

Ab Soft a	L.M	0	0	0	0	0	0	1	0	
Soft	LST	0	0	1	2	0	0	1	0	

BL 18										
Sample	**Lithology**	*Modiolus minimus*	*Chlamys*	*Liostrea*	*Gryphaea*	*Plagiostoma*	*Pseudolimea*	*Antiquilima*	*Pholadomya*	*Pseudopecten*
Brick n	D.M	0	0	7	0	1	1	0	1	0
Brick m	LST	0	0	8	0	2	1	0	1	0
Brick l	D.M	N/A	N/A	N/A	N/A	N/A	N/A	N/A	N/A	N/A
Brick k	LST	0	0	9	0	2	0	0	0	0
Brick j	D.M	0	0	7	0	2	5	1	0	0
Brick i	LST	0	0	12	0	3	14	1	0	3
Brick h	D.M	0	0	2	0	2	1	0	0	1
Brick g	LST	N/A	N/A	N/A	N/A	N/A	N/A	N/A	N/A	N/A
Brick f	D.M	N/A	N/A	N/A	N/A	N/A	N/A	N/A	N/A	N/A
Brick e	LST	0	0	14	0	4	11	1	0	1
Brick d	D.M	0	0	4	0	1	0	0	0	0
		Pinna	*Pleuromya*	Indeterminate bivalve	*Calcirhynchia calcaria*	Gastropod	Echinoid	Crinoid	Ammonoid	
Brick n	D.M	0	0	0	13	0	0	1	0	
Brick m	LST	0	0	2	0	0	2	0	0	
Brick l	D.M	N/A	N/A	N/A	N/A	N/A	N/A	N/A	N/A	
Brick k	LST	0	0	1	0	0	0	0	0	
Brick j	D.M	0	0	1	0	0	2	2	0	
Brick i	LST	0	0	1	1	0	1	2	1	
Brick h	D.M	0	0	0	0	0	1	0	1	
Brick g	LST	N/A	N/A	N/A	N/A	N/A	N/A	N/A	N/A	
Brick f	D.M	N/A	N/A	N/A	N/A	N/A	N/A	N/A	N/A	
Brick e	LST	0	0	0	0	0	0	0	0	
Brick d	D.M	0	0	0	0	0	1	0	0	

BL 17										
Sample	**Lithology**	*Modiolus minimus*	*Chlamys*	*Liostrea*	*Gryphaea*	*Plagiostoma*	*Pseudolimea*	*Antiquilima*	*Pholadomya*	*Pseudopecten*
Brick c	LST	0	0	2	0	1	0	0	0	0
Brick b	D.M	0	0	2	0	0	0	0	0	0
Brick a	LST	0	0	2	0	3	0	0	0	0

		Pinna	*Pleuromya*	Indeterminate bivalve	*Calcirhynchia calcaria*	Gastropod	Echinoid	Crinoid	Ammonoid	
Brick c	LST	0	0	2	0	0	0	0	1	
Brick b	D.M	0	0	0	0	0	0	0	0	
Brick a	LST	0	0	0	0	0	0	0	5	

BL 16										
Sample	**Lithology**	*Modiolus minimus*	*Chlamys*	*Liostrea*	*Gryphaea*	*Plagiostoma*	*Pseudolimea*	*Antiquilima*	*Pholadomya*	*Pseudopecten*
H91 d	D.M	N/A	N/A	N/A	N/A	N/A	N/A	N/A	N/A	N/A
H91 c	SHA	0	0	2	0	0	0	0	0	0
H91 b	D.M	0	0	12	0	4	2	0	0	0
H91 a	L.M	N/A	N/A	N/A	N/A	N/A	N/A	N/A	N/A	N/A
H90	LST	0	0	3	0	2	0	0	0	0
H89	L.M	0	0	6	0	2	0	0	0	0
H88	LST	0	0	2	0	2	0	0	1	0
H87 c	L.M	N/A	N/A	N/A	N/A	N/A	N/A	N/A	N/A	N/A
H87 b	D.M	0	0	21	0	3	8	1	0	2
H87 a	L.M	0	0	3	0	2	3	0	0	0
H86	LST	0	0	3	0	2	0	0	0	0
H85 c	D.M	N/A	N/A	N/A	N/A	N/A	N/A	N/A	N/A	N/A
H85 b	SHA	0	0	0	0	0	0	0	0	0
H85 a	L.M	0	0	4	0	2	0	0	0	0
H84	LST	0	0	4	0	5	0	0	0	0
		Pinna	*Pleuromya*	Indeterminate bivalve	*Calcirhynchia calcaria*	Gastropod	Echinoid	Crinoid	Ammonoid	
H91 d	D.M	N/A	N/A	N/A	N/A	N/A	N/A	N/A	N/A	
H91 c	SHA	0	0	0	0	0	0	0	0	
H91 b	D.M	0	0	0	0	0	2	0	0	
H91 a	L.M	N/A	N/A	N/A	N/A	N/A	N/A	N/A	N/A	
H90	LST	0	0	0	0	0	0	0	1	
H89	L.M	0	0	0	0	0	2	0	0	
H88	LST	0	0	0	0	0	0	0	0	
H87 c	L.M	N/A	N/A	N/A	N/A	N/A	N/A	N/A	N/A	
H87 b	D.M	0	0	0	0	0	2	0	0	
H87 a	L.M	0	0	0	0	0	2	0	0	
H86	LST	0	0	0	0	0	0	0	0	

H85 c	D.M	N/A	N/A	N/A	N/A	N/A	N/A	N/A	N/A	
H85 b	SHA	0	0	0	0	0	0	0	1	
H85 a	L.M	0	0	0	0	0	1	0	0	
H84	LST	0	0	4	0	0	0	0	0	

Table 3.4 – Macrofaunal data based on the minimum number of individuals for BL 16 – BL 19. Stratigraphy after the revised lithostratigraphy in Chapter 2. LST = limestone, L.M = light marl, D.M = dark marl, SHA = shale, P.S = paper shale, L.LST = laminated limestone. N/A = no sample.

BL 20 = macrofaunal coverage is greater on the upper surfaces of the nodular limestones (average = 4 %) than the single dark marl interbed (1 %) (fig. 3.10); palaeoecological metrics also correlate well with inferred oxygen conditions (fig. 3.11). The lower limestone bed contains 6 different taxa, all of which appear to be calcitic or bimineralic epifauna (*Plagiostoma*, *Liostrea*, *Pseudolimea*, *Gryphaea*, an indeterminate bivalve genus, and *Calcirhynchia*) (fig. 3.10; table 3.5). The topmost bioturbated limestone contains a similarly abundant macrofaunal component, but the assemblage is more even and there is greater species richness (number of different taxa = 9) (fig. 3.11; table 3.5); epifaunal bivalves, crinoids, and ammonoids were accounted for (fig. 3.10; table 3.5). Consistent with inferred oxygen conditions between adjacent lithologies, the dark marl interbed contains a restricted macrofaunal assemblage comprised of *Liostrea* and ammonoids (fig. 3.10; table 3.5). Jordan (2016) recorded trace fossils throughout BL 20 (fig. 3.10).

BL 21 = bioturbated limestones exhibit a range of unique palaeoecological characteristics, but the majority are dominated by low diversity epifauna (fig. 3.10; table 3.5); irrespective of lithology, the entire section lacks semi-infaunal and infaunal taxa (fig. 3.10; table 3.5). The two basal limestones (Upper White and Speckety) have high proportions of *Liostrea* (50 % and 60 % respectively) and *Calcirhynchia* (25 % and 20 % respectively) which comprise the majority of the macrofaunal fossil content (fig. 3.10; table 3.5). Above this, the Mongrel limestone bed shows a predominance of *Calcirhynchia* which account for 92 % of the macrofaunal assemblage (fig. 3.10; table 3.5); *Calcirhynchia* are also abundant in the overlaying dark marls (relative abundance = 83 %; figs. 3.1 and 3.10; table 3.5). Top Tape is a concentration lagerstätte dominated by *Metophioceras* ammonoids (approximate relative abundance = 62 %) that result in extensive macrofaunal coverage (34 %) (fig. 3.10; table 3.5). The topmost limestone (Third Quick) contains a high proportion of *Gryphaea* (relative abundance = 47 %) in association with additional epifauna including *Plagiostoma*, *Liostrea*, and *Calcirhynchia* (fig. 3.10; table 3.5). The sampled shale and paper shale interbeds were lacking macrofauna except for a single ammonoid in Mong b (fig. 3.10; table 3.5). Previous authors have described an abundant and diverse trace fossil assemblage in the bioturbated limestones as well as a number of argillaceous interbeds (e.g. Barras and Twitchett, 2007, Jordan, 2016; fig. 3.10).

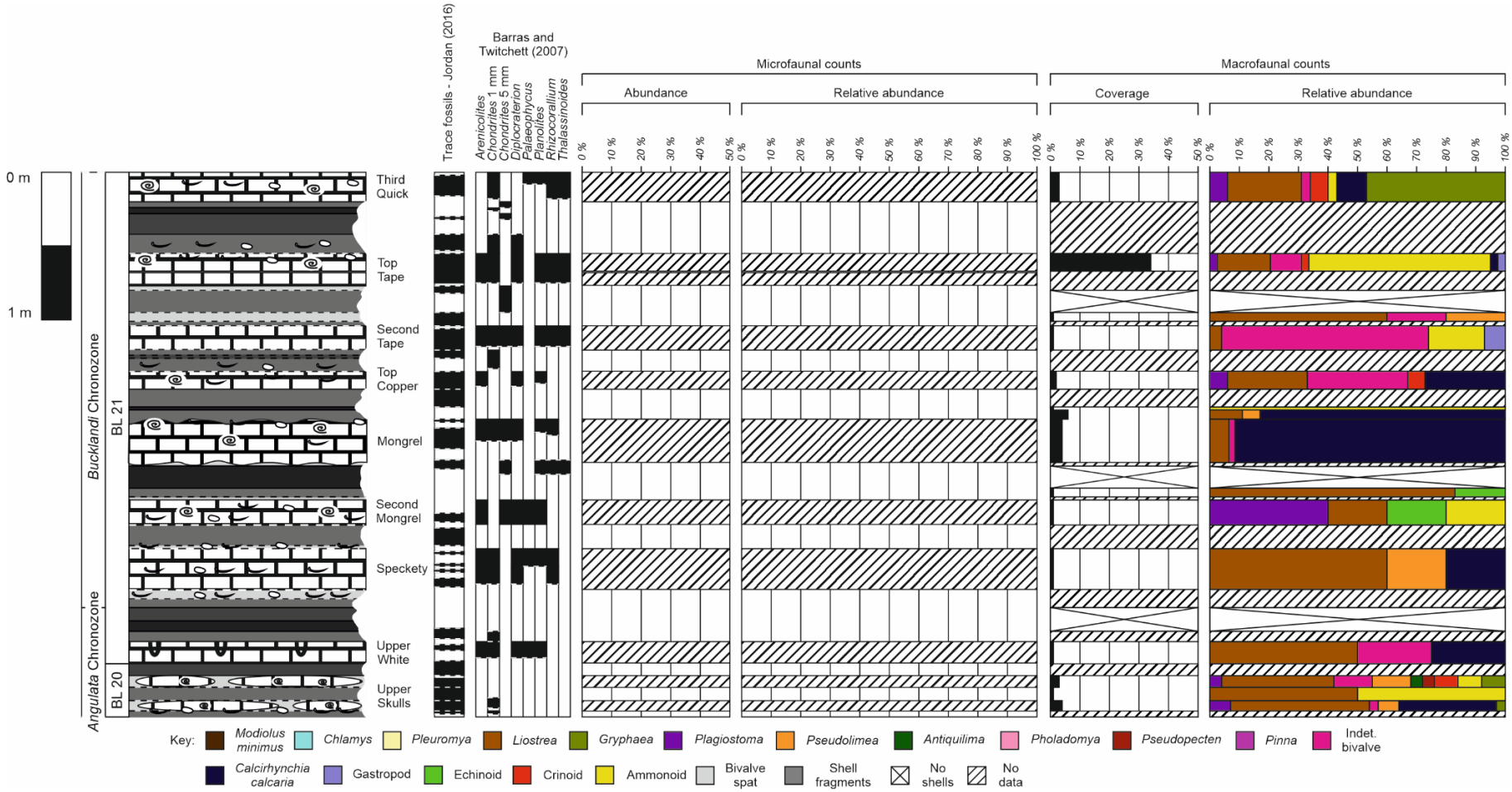

Figure 3.10 – Microfaunal data (proportion of sediment composition/abundance and relative abundance of different bioclasts respectively) and macrofaunal data (percent coverage and relative abundance of different bioclasts from MNI counts respectively) for BL 20 – BL 21. Stratigraphy after the revised lithostratigraphy in Chapter 2. Ichnotaxonomic data after Barras and Twitchett (2007) and Jordan (2016). Components of the micro and macrofaunal counts are shown in the key.

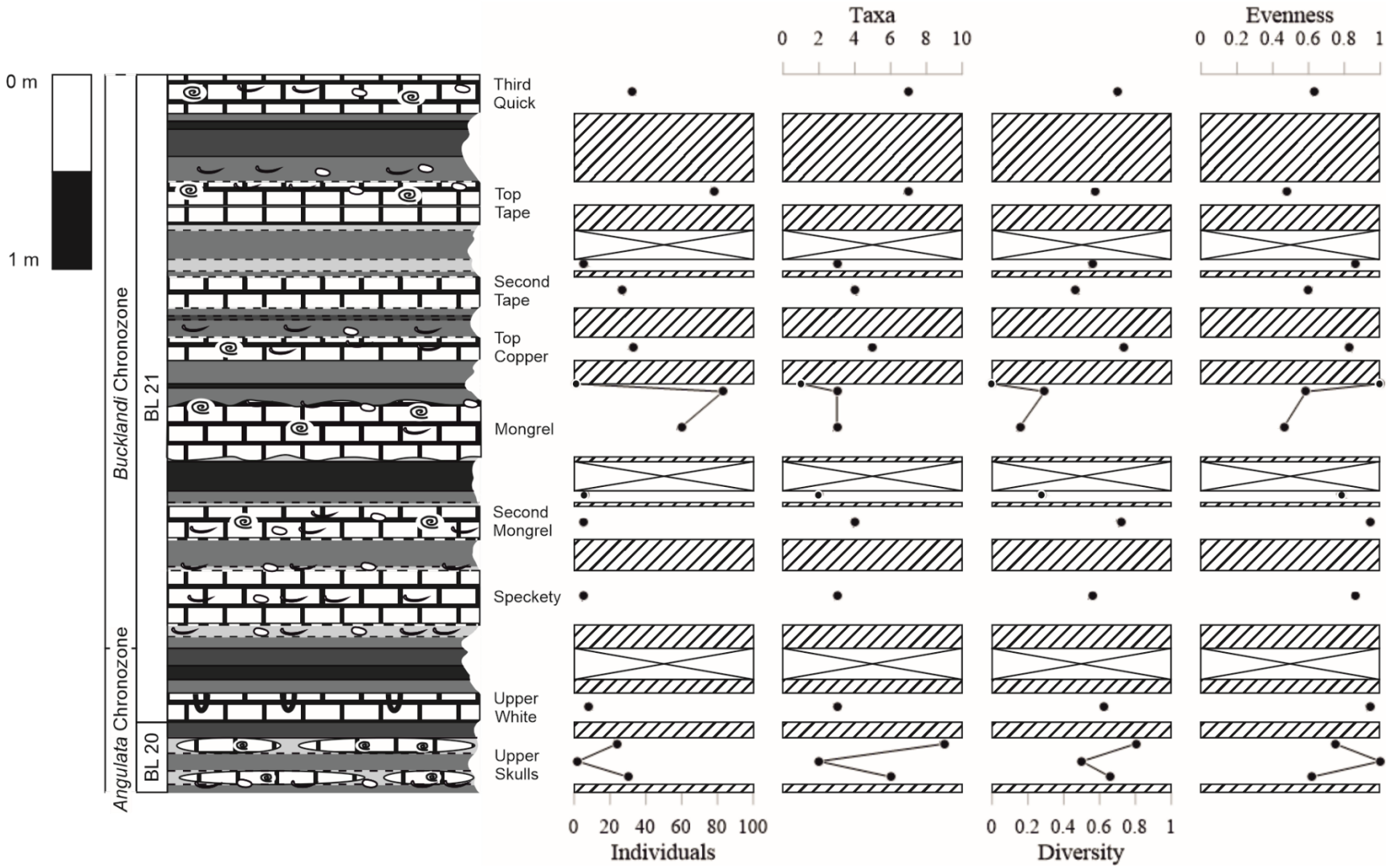

Figure 3.11 – Graphic logs showing the minimum number of individuals, species richness or number of different taxa, diversity, and evenness of the macrofaunal fossil assemblage in BL 20 – BL 21. Stratigraphy after the revised lithostratigraphy in Chapter 2.

BL 21										
Sample	**Lithology**	*Modiolus minimus*	*Chlamys*	*Liostrea*	*Gryphaea*	*Plagiostoma*	*Pseudolimea*	*Antiquilima*	*Pholadomya*	*Pseudopecten*
3rd Quick	LST	0	0	8	15	2	0	0	0	0
Top Tape f	D.M	N/A	N/A	N/A	N/A	N/A	N/A	N/A	N/A	N/A
Top Tape e	P.S	N/A	N/A	N/A	N/A	N/A	N/A	N/A	N/A	N/A
Top Tape d	SHA	N/A	N/A	N/A	N/A	N/A	N/A	N/A	N/A	N/A
Top Tape c	D.M	N/A	N/A	N/A	N/A	N/A	N/A	N/A	N/A	N/A
Top Tape b	LST	0	0	14	0	2	0	0	0	0
Top Tape a	L.M	N/A	N/A	N/A	N/A	N/A	N/A	N/A	N/A	N/A
Top Tape	LST	N/A	N/A	N/A	N/A	N/A	N/A	N/A	N/A	N/A
2nd Tape d	L.M	N/A	N/A	N/A	N/A	N/A	N/A	N/A	N/A	N/A
2nd Tape c	D.M	0	0	0	0	0	0	0	0	0
2nd Tape b	L.M	0	0	3	0	0	1	0	0	0
2nd Tape a	D.M	N/A	N/A	N/A	N/A	N/A	N/A	N/A	N/A	N/A
2nd Tape	LST	0	0	1	0	0	0	0	0	0
Top Cop c	D.M	N/A	N/A	N/A	N/A	N/A	N/A	N/A	N/A	N/A
Top Cop b	SHA	N/A	N/A	N/A	N/A	N/A	N/A	N/A	N/A	N/A
Top Cop a	D.M	N/A	N/A	N/A	N/A	N/A	N/A	N/A	N/A	N/A
Top Cop	LST	0	0	9	0	2	0	0	0	0
Mong c	D.M	N/A	N/A	N/A	N/A	N/A	N/A	N/A	N/A	N/A
Mong b	P.S	0	0	0	0	0	0	0	0	0
Mong a	D.M	0	0	9	0	0	5	0	0	0
Mong	LST	0	0	4	0	0	0	0	0	0
2nd Mong d	L.M	N/A	N/A	N/A	N/A	N/A	N/A	N/A	N/A	N/A
2nd Mong c	P.S	0	0	0	0	0	0	0	0	0
2nd Mong b	D.M	0	0	5	0	0	0	0	0	0
2nd Mong a	L.M	N/A	N/A	N/A	N/A	N/A	N/A	N/A	N/A	N/A
2nd Mong	LST	0	0	1	0	2	0	0	0	0
Speck b	D.M	N/A	N/A	N/A	N/A	N/A	N/A	N/A	N/A	N/A
Speck a	L.M	N/A	N/A	N/A	N/A	N/A	N/A	N/A	N/A	N/A
Speck	LST	0	0	3	0	0	1	0	0	0
Up White e	L.M	N/A	N/A	N/A	N/A	N/A	N/A	N/A	N/A	N/A
Up White d	D.M	N/A	N/A	N/A	N/A	N/A	N/A	N/A	N/A	N/A
Up White c	SHA	0	0	0	0	0	0	0	0	0
Up White b	P.S	0	0	0	0	0	0	0	0	0
Up White a	D.M	N/A	N/A	N/A	N/A	N/A	N/A	N/A	N/A	N/A

Up White	LST	0	0	4	0	0	0	0	0	0
		Pinna	*Pleuromya*	Indeterminate bivalve	*Calcirhynchia calcaria*	Gastropod	Echinoid	Crinoid	Ammonoid	
3rd Quick	LST	0	0	1	3	0	0	2	1	
Top Tape f	D.M	N/A	N/A	N/A	N/A	N/A	N/A	N/A	N/A	
Top Tape e	P.S	N/A	N/A	N/A	N/A	N/A	N/A	N/A	N/A	
Top Tape d	SHA	N/A	N/A	N/A	N/A	N/A	N/A	N/A	N/A	
Top Tape c	D.M	N/A	N/A	N/A	N/A	N/A	N/A	N/A	N/A	
Top Tape b	LST	0	0	8	2	2	0	2	48	
Top Tape a	L.M	N/A	N/A	N/A	N/A	N/A	N/A	N/A	N/A	
Top Tape	LST	N/A	N/A	N/A	N/A	N/A	N/A	N/A	N/A	
2nd Tape d	L.M	N/A	N/A	N/A	N/A	N/A	N/A	N/A	N/A	
2nd Tape c	D.M	0	0	0	0	0	0	0	0	
2nd Tape b	L.M	0	0	1	0	0	0	0	0	
2nd Tape a	D.M	N/A	N/A	N/A	N/A	N/A	N/A	N/A	N/A	
2nd Tape	LST	0	0	19	0	2	0	0	5	
Top Cop c	D.M	N/A	N/A	N/A	N/A	N/A	N/A	N/A	N/A	
Top Cop b	SHA	N/A	N/A	N/A	N/A	N/A	N/A	N/A	N/A	
Top Cop a	D.M	N/A	N/A	N/A	N/A	N/A	N/A	N/A	N/A	
Top Cop	LST	0	0	11	9	0	0	2	0	
Mong c	D.M	N/A	N/A	N/A	N/A	N/A	N/A	N/A	N/A	
Mong b	P.S	0	0	0	0	0	0	0	1	
Mong a	D.M	0	0	0	69	0	0	0	0	
Mong	LST	0	0	1	55	0	0	0	0	
2nd Mong d	L.M	N/A	N/A	N/A	N/A	N/A	N/A	N/A	N/A	
2nd Mong c	P.S	0	0	0	0	0	0	0	0	
2nd Mong b	D.M	0	0	0	0	0	1	0	0	
2nd Mong a	L.M	N/A	N/A	N/A	N/A	N/A	N/A	N/A	N/A	
2nd Mong	LST	0	0	0	0	0	1	0	1	
Speck b	D.M	N/A	N/A	N/A	N/A	N/A	N/A	N/A	N/A	
Speck a	L.M	N/A	N/A	N/A	N/A	N/A	N/A	N/A	N/A	
Speck	LST	0	0	0	1	0	0	0	0	
Up White e	L.M	N/A	N/A	N/A	N/A	N/A	N/A	N/A	N/A	
Up White d	D.M	N/A	N/A	N/A	N/A	N/A	N/A	N/A	N/A	
Up White c	SHA	0	0	0	0	0	0	0	0	
Up White b	P.S	0	0	0	0	0	0	0	0	
Up White a	D.M	N/A	N/A	N/A	N/A	N/A	N/A	N/A	N/A	

Up White	LST	0	0	2	2	0	0	0	0	

BL 20										
Sample	**Lithology**	*Modiolus minimus*	*Chlamys*	*Liostrea*	*Gryphaea*	*Plagiostoma*	*Pseudolimea*	*Antiquilima*	*Pholadomya*	*Pseudopecten*
Up. Sk e	SHA	N/A	N/A	N/A	N/A	N/A	N/A	N/A	N/A	N/A
Up. Sk d	LST	0	0	9	2	1	3	1	0	1
Up. Sk c	D.M	0	0	1	0	0	0	0	0	0
Up. Sk b	LST	0	0	14	1	2	2	0	0	0
Up. Sk a	D.M	N/A	N/A	N/A	N/A	N/A	N/A	N/A	N/A	N/A
		Pinna	*Pleuromya*	Indeterminate bivalve	*Calcirhynchia calcaria*	Gastropod	Echinoid	Crinoid	Ammonoid	
Up. Sk e	SHA	N/A	N/A	N/A	N/A	N/A	N/A	N/A	N/A	
Up. Sk d	LST	0	0	3	0	0	0	2	2	
Up. Sk c	D.M	0	0	0	0	0	0	0	1	
Up. Sk b	LST	0	0	1	10	0	0	0	0	
Up. Sk a	D.M	N/A	N/A	N/A	N/A	N/A	N/A	N/A	N/A	

Table 3.5 – Macrofaunal data based on the minimum number of individuals for BL 20 – BL 21. Stratigraphy after the revised lithostratigraphy in Chapter 2. LST = limestone, L.M = light marl, D.M = dark marl, SHA = shale, P.S = paper shale, L.LST = laminated limestone. N/A = no sample.

3.4. Discussion

3.4.1. Palaeoecology of the Blue Lias Formation in Dorset and East Devon

Tilmanni Chronozone (Base of H1 to the top of H24). The sedimentology and palaeoecology of BL 1 are consistent with a dysaerobic/anoxic depositional environment (*sensu* Hallam and Lang, 1960, Weedon, 1986, Wignall, 2001b); euxinia has also been inferred from geochemical data and the analysis of pyrite framboids (e.g. Wignall, 2001b). A lack of ichnotaxa (e.g. Barras and Twitchett, 2007, Jordan, 2016) and macrobenthos (fig. 3.2) indicates that the sediment surface was generally inhospitable. The single layer of disarticulated *Modiolus* described by Wignall (2001b) points to an allochthonous origin or the potential for short-lived oxic intervals that enabled opportunistic colonisation of the seafloor (*sensu* Jordan, 2016). Planktonic veliger spat preserved in laminated limestone concretions (fig. 3.2) would have been unaffected by bottom water anoxia and their preservation indicates that the sediment/seawater interface was not positioned within the acidic TAZ for a prolonged period of time (*sensu* Cherns et al., 2008).

Above the basal anoxic interval, the remainder of the *Tilmanni* Chronozone contains a high number of thin limestones separated by various argillaceous interbeds (see Chapter 2). The close spacing of limestones has been attributed to condensation via winnowing of fine sediment and organic mud which may have also produced local concentrations of macrofauna (see review by Weedon et al., 2018); as a result, it is important to note that the counted sediment surface is potentially representative of prolonged accumulation and not a single phase of occupation related to stable oxygen conditions.

Up to and including H18, the macrofaunal fossil assemblage is dominated by *Liostrea*, notwithstanding that a number of different beds contain additional taxa including *Plagiostoma*, *Pseudolimea*, and *Modiolus minimus* (fig. 3.2). The *Liostrea* and *Modiolus* assemblage is well known from the basal BLF (Hesselbo et al., 2004, Lord et al., 2010, Pugh et al., 2014, Jordan, 2016). According to Atkinson and Wignall (2019) and Pugh et al. (2014), the dominance of these genera is characteristic of initial faunal recovery following the end-Triassic mass extinction (Recovery Stage 1 *sensu* Twitchett, 2006). Above H18, there is a moderate increase in species richness and whilst the macrofaunal assemblage remains dominated by *Liostrea*, this part of the section marks the first appearance of several additional calcitic and bimineralic epifaunal bivalve genera (*Antiquilima* and *Pseudopecten*) and the semi-infaunal genus *Pinna* (fig. 3.2). Diversification of the bivalve component is a product of further faunal recovery and

improved oxygen conditions. Based on a comparison with observations made by Mander et al. (2008), Pugh et al. (2014) suggest that faunal recovery within the upper *Tilmanni* Chronozone (H19) increases to Recovery Stage 2 (*sensu* Twitchett, 2006) following occupation of the infaunal tier by *Arenicolites* in Barras and Twitchett (2007). The timing of this transition is not disputed based on its consistency with ichnotaxomic trends, but it cannot be recognised within the shelly assemblage (see also Atkinson and Wignall, 2019). Contrasting accounts of the first recorded infaunal bivalve genera are given in Pugh et al. (2014) – *Pteromya tatei* in H2; Atkinson and Wignall (2019) – *Cardinia ovalis* in the *Planorbis* Chronozone; and herein – *Pleuromya* in H28, yet none correlate with a late *Tilmanni* transition to Recovery Stage 2. The poor correlation between macrobenthic and ichnotaxomic palaeoecological trends is the result of taphonomic biases against aragonitic infauna (*sensu* Wright et al., 2003) and indicates that the shelly fossil record is not a reliable representation of original, ecological diversity (see Chapter 7).

Throughout the entire section, only the paper shales of H13a were without macrobenthos (fig. 3.2) and thus indicative of a sustained anoxic interval. Since the remaining argillaceous interbeds contain a similar albeit (typically) restricted variant of the macrofaunal assemblage observed in nearby bioturbated limestones, it is apparent that lithology-specific fluctuations in the extent of bottom water oxygenation were not extreme, and that oxygen availability at the sediment/seawater interface was persistent.

Planorbis Chronozone (Base of H25 to the top of H56). The base of the *Planorbis* Chronozone coincides with the top of BL 2 but unlike the lower part of BL 2, which overlaps with the *Tilmanni* Chronozone, differences in the macrofaunal fossil assemblages of each lithology are more typical of fluctuating bottom water redox conditions (fig. 3.2). The shales of H25 are without macrobenthos (fig. 3.2) and indicate that the sediment/seawater interface was inhospitable owing to a prolonged period of dysaerobic/anoxic deposition. Bioturbated limestones have moderate species richness and macrofaunal abundance (fig. 3.3) which is consistent with aerobic environmental conditions. The bivalve component contains diverse epifauna (e.g. *Plagiostoma*, *Liostrea*, *Pseudolimea*, and *Antiquilima*) and the earliest aragonitic infaunal genus (*Pleuromya*) observed in this study (fig. 3.2). The assemblage lacks shallow infauna and formerly aragonitic epifauna which may be indicative of taphonomic distortion (e.g. Wright et al., 2003; see Chapter 7); *Pleuromya* survived dissolution associated with the Missing Molluscs effect since deep-burrowing infauna were positioned below the shallow-burial

zone of dissolution and early cementation facilitated retention of the mould (e.g. Cherns and Wright, 2009). As a result, H28 marks the first opportunity to identify increased faunal recovery, specifically occupation of the infaunal tier (Recovery Stage 2 *sensu* Twitchett, 2006), within the shelly assemblage of the local BLF. H26 and H28 both contain crinoids which are characteristic of epifaunal tiering and thus indicative of the transition to Recovery Stage 3 (*sensu* Twitchett, 2006); this interpretation is consistent with Pugh et al. (2014). However, whilst it is evidently possible to qualify the relative timing of recovery stages 2 and 3 (*sensu* Twitchett, 2006) using a combination of ichnotaxa and macrofauna, faunal recovery cannot be determined in the BLF of Dorset and East Devon were its recognition to rely solely on the macrofaunal fossil assemblages since the appearance of infaunal bivalves post-dates the first recorded crinoids in BL 2 (fig. 3.2).

In the argillaceous lithology bundle of BL 3, palaeoecological observations reflect different states of bottom water oxygenation (*sensu* Moghadam and Paul, 2000, Weedon, 1986) through the presence or lack of macrofauna and, to some extent, the position of ichnotaxa (e.g. Jordan, 2016) (fig. 3.2). Paper shales are without macrobenthos (fig. 3.2) and thus indicative of sustained anoxic intervals that were inhospitable. In contrast, the thin shale interbed contains a restricted macrofaunal assemblage that would have required periods of oxygen availability during deposition to enable opportunistic colonisation of the seafloor by epifauna (fig. 3.2). Jordan (2016) identified *Chondrites*, *Rhizocorallium*, and *Thalassinoides* in the section which are also characteristic of Recovery Stage 3 (*sensu* Twitchett, 2006).

Several sections in the *Planorbis* Chronozone (BL 4, BL 5, and BL 7) contain lithologies that are generally associated with dysaerobic/anoxic depositional conditions such as paper shales and laminated limestones (e.g. Weedon, 1986, Moghadam and Paul, 2000, Arzani, 2004; see Chapter 2). The macrofaunal fossil content of these sediments supports this interpretation since both typically lack macrobenthos (figs. 3.2 and 3.4). However, the presence of sparse epifauna in H33, H36, and H51 (this study) and ichnotaxa in H30, H32 and H36 (Barras and Twitchett, 2007, Jordan, 2016) (figs. 3.2 and 3.4) indicates that anoxic deposition was punctuated by episodic oxic intervals that enabled colonisation of the seafloor. The influence of this palaeoenvironmental control on the ecological assemblage highlights the need to avoid lithologies associated with dysaerobic/anoxic depositional conditions when attempting to reconstruct faunal recovery since they were

unable to support most characteristic groups associated with different stages of the Twitchett (2006) recovery model.

The bioturbated limestones of BL 6 have an abundant macrofaunal assemblage with high species richness (fig. 3.5); these beds are considered a good reflection of the extent of faunal recovery despite the lack of a shallow infaunal community and aragonitic epifauna, the lack of which is a consequence of taphonomic distortion associated with the Missing Molluscs effect (*sensu* Wright et al., 2003; see Chapter 7). As well as nektonic fauna (ammonoids), epifauna (e.g. *Plagiostoma*, *Liostrea*, *Pseudolimea*, *Antiquilima*, and echinoids), and semi-infauna (*Pinna*), the bioturbated limestones contain infaunal bivalves (*Pleuromya*) and high-tired epifauna (crinoids) (fig. 3.4) which are characteristic of Recovery Stage 3 (*sensu* Twitchett, 2006). On a bed-by-bed basis, the macrofaunal assemblage has a good correlation with inferred oxygen conditions between adjacent lithologies (fig. 3.4); the average number of individuals and different taxa is greatest in the bioturbated limestones and decreases progressively in the dark marls, shales, and paper shales (fig. 3.5; see Results). However, since all of the sampled beds contain macrobenthos, it is evident that despite relative changes in the degree of bottom water oxygenation, oxygen-availability was persistent or at least episodic during deposition. This interpretation is supported by the distribution of ichnotaxa throughout the majority of BL 6, including argillaceous interbeds (e.g. Jordan, 2016). Considering the lithostratigraphical variation (see Chapter 2) and differences in the palaeoecology of individual beds between H25 – H56, it is evident that environmental conditions during deposition of the *Planorbis* Chronozone were highly irregular.

Liassicus Chronozone (Base of H57 to the top of H83). The *Planorbis*/*Liassicus* transition marks a decrease in the relative abundance of limestone beds (Hallam and Lang, 1960, Weedon et al., 2018; see Chapter 2); Weedon et al. (2018) associate poor conditions for limestone formation with sea-level rise. In BL 9 (including that part which overlaps with the *Planorbis* Chronozone), the percentage of macrofaunal coverage and species richness are greatest in the bioturbated limestones and correlate well with inferred oxygen conditions between adjacent lithologies (fig. 3.4). Nonetheless, there is little evidence to suggest that palaeoenvironmental differences were extreme. Throughout the entire section, only the shales of H63b are without macrofauna (fig. 3.4) and therefore indicative of anoxic bottom waters; similar macrofaunal assemblages among the remaining beds points to prolonged, moderately stable oxic intervals during deposition.

In the argillaceous lithology bundles of BL 11 and BL 13, palaeoecological differences between the various lithologies correlate well with inferred oxygen conditions (fig. 3.6). Dysaerobic/anoxic bottom waters associated with organic-rich paper shales (e.g. Weedon, 1986, Moghadam and Paul, 2000, Arzani, 2004; see Chapter 2) are evidenced by a near-total lack of fossils in these beds (fig. 3.6). In contrast, dark marls and shales contain a restricted macrofaunal assemblage, dominated by low diversity epifauna (e.g. *Plagiostoma*, *Liostrea*, and echinoids; fig. 3.6), indicative of low oxygen conditions that were nonetheless sufficient to host macrobenthos. The lack of semi-infauna and infauna (fig. 3.6) suggests that the sediment column was poorly aerated at depth. Ammonoids are present in the dark marl and shale lithologies but since nektonic fauna were unaffected by bottom water anoxia, their omission from the paper shale interbeds is surprising (fig. 3.6). Consistent with macrofaunal distribution, Jordan (2016) identified burrow mottled bed transitions and trace fossils that were emplaced during the non-anoxic intervals (fig. 3.6).

The upper *Liassicus* Chronozone (BL 12, BL 14, and BL 15) is comprised of limestone-dark marl alternations (see Chapter 2). Both lithologies are dominated by typical, low diversity epifauna (*Plagiostoma*, *Liostrea*, and echinoids) and likely reflect relict assemblages following taphonomic loss of vulnerable shelly groups (*sensu* Wright et al., 2003; see Chapter 7). Nonetheless, species richness is consistent with inferred oxygen conditions and greatest in the bioturbated limestones (fig. 3.7). All of the sampled beds contain macrobenthos and as such indicate relatively stable palaeoenvironmental conditions and persistent oxygen availability during deposition. The bioturbated limestones contain the only semi-infaunal (*Pinna*) and infaunal (*Pleuromya*) bivalve genera (fig. 3.6) which would have required deeper aeration of the sediment column. Deep-burrowing anomalodesmatan bivalves survived dissolution in the TAZ via positioning below the zone of shallow dissolution (e.g. Cherns and Wright, 2009; see Chapter 7). Stable bottom water oxygenation is supported by trace fossil distribution since Jordan (2016) recorded ichnotaxa in all of the bioturbated limestones and a high proportion of the dark marl interbeds (fig. 3.6).

Consistent with observations by Pugh et al. (2014), the palaeoecology of the *Liassicus* Chronozone and the range of occupied faunal tiers therein is similar to the underlying *Planorbis* Chronozone. However, the shelly fossil assemblage does not generally correlate with the predicted faunal assemblage, particularly in well-oxygenated environmental conditions, based on taphonomic window fauna that preserve original ecological skeletal

diversity in similar settings (e.g. Wright et al., 2003). Key molluscan components such as aragonitic anomalodesmatan bivalves, shallow infauna, and aragonitic epifaunal gastropods are rare or missing. Whilst the dominance of poorly diverse epifauna (e.g. *Plagiostoma*, *Liostrea*, *Pseudolimea*, and echinoids) may indicate that low oxygen conditions prevented occupation of the sediment column, this relict assemblage is more likely the product of taphonomic distortion which acted to reduce original ecological diversity through the selective dissolution of vulnerable shelly groups (the 'Missing Molluscs' effect *sensu* Cherns and Wright, 2000) (see Chapter 7). Preferential survival of formerly aragonitic, deep-burrowing anomalodesmatan bivalves and ammonoids throughout the BLF is discussed later in the thesis (see Chapter 7).

Angulata Chronozone (Base of H84 to the top of Upper White c). The macrofaunal fossil assemblage at the base of the *Angulata* Chronozone (BL 16) is poorly diverse in comparison to earlier sections. Bioturbated limestones have low species richness and are dominated by epifaunal bivalves (*Plagiostoma* and *Liostrea*) although aragonitic infauna (*Pholadomya*) are also present (fig. 3.8). Contrary to inferred oxygen conditions between different lithologies, dark marls have the highest macrofaunal abundance and greatest species richness (fig. 3.9); however, unlike the bioturbated limestones, these taxa are exclusively epifaunal (*Plagiostoma*, *Liostrea*, *Pseudolimea*, *Antiquilima*, *Pseudopecten*, and echinoids; fig. 3.8) and indicate that the sediment column was not aerated at depth. Shale interbeds are associated with restricted oxygen conditions owing to a predominance of sparse, single taxon macrofaunal assemblages (fig. 3.8); ammonoids in H85b were unaffected by the prevailing bottom water redox state but the lack of epifauna is indicative of a sustained dysaerobic/anoxic interval (fig. 3.8).

There is a significant change in the lithostratigraphy of the central *Angulata* Chronozone (BL 18) where the succession is comprised of irregular, nodular bioturbated limestones separated by dark marl interbeds (see Chapter 2). Minimal spacing between individual limestones has been inferred by previous authors to be the result of condensation via winnowing of fine sediment and organic mud (e.g. Weedon et al., 2018). It is therefore important to note that palaeoenvironmental interpretations based on macrofaunal content are not necessarily representative of a single depositional period but the culmination of prolonged accumulation with potentially varying degrees of bottom water oxygenation. The macrofaunal assemblage does not correlate well with relative changes in inferred oxygen conditions (fig. 3.8); instead, species richness and macrofaunal abundance differ

between different beds of the same lithology (fig. 3.9). The combined range of taxa recorded throughout the section is identical in both the dark marls and bioturbated limestones (fig. 3.8); the assemblage contains diverse epifaunal bivalves (*Plagiostoma*, *Liostrea*, *Pseudolimea*, *Antiquilima*, *Pseudopecten*), *Calcirhynchia*, echinoids, crinoids, and ammonoids (fig. 3.8). Since each bed contains macrobenthos, oxic intervals must have occurred at every stage of deposition; however, the constancy of these palaeoenvironmental conditions cannot be determined since the condensed bioclastic fossil content will include species that reflect maximum faunal diversity in peak oxygen conditions. Palaeoecological variations on a bed by bed basis suggest that the extent of bottom water oxygenation fluctuated despite maintaining minimal background oxygen availability. At the top of the section, the infaunal bivalve genus *Pholadomya* is present in both lithologies (fig. 3.8) and indicates occupation of an aerated sediment column.

Pugh et al. (2014) state that the appearance of deep infaunal bivalve genera such as *Pholadomya* occurred within the *Angulata* Chronozone near to the top of BL 18; whilst *Pholadomya* are known from this horizon herein (fig. 3.8), the first record of this genus is from H56 (*Planorbis* Chronozone; fig. 3.4) and subsequently from H88 (*Angulata* Chronozone; fig. 3.8). Moreover, alternative deep infauna such as *Pleuromya* were identified earlier in the succession from the *Planorbis* (H28 and H38; figs. 3.2 and 3.4 respectively) and *Liassicus* chronozones (H76; fig. 3.6). Pugh et al. (2014) correlate the appearance of *Pholadomya* in BL 18 with an increase in the depth and diversity of ichnotaxa recorded by Barras and Twitchett (2007); the authors suggest that this co-occurrence supports the inference that marine biotic recovery following the end-Triassic mass extinction was achieved in the *Angulata* Chronozone (*sensu* Twitchett and Barras, 2004, Barras and Twitchett, 2007). However, whilst the relative timing of Recovery Stage 4 (*sensu* Twitchett, 2006) is consistent with the ichnotaxonomic assemblage in Twitchett and Barras (2004) and Barras and Twitchett (2007), it is evident from observations herein that it cannot be correlated with the shelly fossil assemblage. Atkinson and Wignall (2019) did not associate Recovery Stage 4 with the *Angulata* Chronozone and suggest that species richness was stable within the *Planorbis* Chronozone.

Following the inferred re-establishment of pre-event palaeoecology (*sensu* Twitchett and Barras, 2004, Barras and Twitchett, 2007, Pugh et al., 2014) in BL 18, the macrofaunal fossil assemblages of BL 19 are highly variable (fig. 3.8). Fossil content in the basal limestone is typical of the predicted faunal assemblage; Soft Bed has high species richness

and contains diverse epifauna (*Plagiostoma*, *Liostrea*, *Pseudolimea*, *Antiquilima*, *Calcirhynchia*), infaunal bivalves (*Pholadomya*), and crinoids (fig. 3.8). In direct contrast, macrofauna from the overlaying Lower Venty and lowermost Lower Skulls limestone beds are restricted to *Plagiostoma* and *Liostrea* (fig. 3.8); since these assemblages are less diverse than in nearby argillaceous lithologies (fig. 3.8), their composition is thought to be the result of selective taphonomic distortion associated with the Missing Molluscs effect (*sensu* Wright et al., 2003) and not low oxygen conditions during deposition. Nonetheless, despite significant variation between the different limestone beds, palaeoecology throughout the remainder of BL 19 is generally consistent with relative inferred oxygen conditions between adjacent lithologies (fig. 3.8). Infaunal bivalve genera are exclusive to the bioturbated limestones (fig. 3.8) and indicate frequent occupation of an aerated sediment column. Light marls have moderate species richness, but an exclusively epifaunal assemblage (*Plagiostoma*, *Liostrea*, *Pseudolimea*, *Calcirhynchia*, crinoids, and echinoids; fig. 3.8) indicates that the depth of oxygen availability was not significant or that taphonomic loss of shallow and deep infauna was complete. Dark marls contain only the aforementioned epifaunal bivalve and brachiopod genera whereas shales are unfossiliferous (fig. 3.8). In the upper part of BL 19 there is an increase in the relative abundance of *Calcirhynchia* (fig. 3.8); whilst this brachiopod genus shares a similar ecological niche and taphonomic survival rate with other bivalves (e.g. *Plagiostoma* and *Liostrea*), the reason for a shift in dominance is unclear. Consistent with an inferred return to pre-event palaeoecology (Recovery Stage 4 *sensu* Twitchett, 2006), BL 19 contains a diverse and abundant trace fossil assemblage within the bioturbated limestones and various argillaceous lithologies (e.g. Barras and Twitchett, 2007, Jordan, 2016; fig. 3.8).

Bucklandi Chronozone (part; Base of Upper White d to the Top of Third Quick). In BL 21, bioturbated limestones exhibit a range of unique palaeoecological characteristics (fig. 3.10). In all of the limestone beds, excluding nektonic ammonoids, the shelly assemblage is limited to epifauna (e.g. *Liostrea*, *Plagiostoma*, *Gryphaea*, *Calcirhynchia*, etc.) and lacks semi-infaunal and infaunal bivalve genera (fig. 3.10). As a result, there is little to correlate the macrofaunal fossil record with pre-event palaeoecology (Recovery Stage 4 *sensu* Twitchett, 2006). The only reliable reflection of inferred faunal recovery (*sensu* Twitchett and Barras, 2004, Barras and Twitchett, 2007, Pugh et al., 2014) is the ichnotaxonomic assemblage which contains deep, abundant, and diverse trace fossils in BL 21 (e.g. Barras and Twitchett, 2007, Jordan, 2016).

3.5. Conclusions

This study provides the most complete bed-by-bed account of the macrofaunal fossil assemblage from the BLF of Dorset and East Devon in over 200 years of palaeontological study. Based on the results presented here, it is now possible to investigate more fully the non-uniform fossil content observed within the succession and examine the control that different factors exerted over the shelly palaeocommunity. These data indicate that the macrobenthic fossil record was influenced by a combination of changing palaeoenvironmental conditions at the T-J boundary interval, fluctuations in the dominant redox state, and taphonomic biases associated with the Missing Molluscs effect.

The degree of bottom water oxygenation controlled the ecological skeletal palaeocommunity and is therefore a key consideration for analyses later in the thesis since lithological alternations in the BLF are widely attributed to fluctuating oxygen conditions (e.g. Weedon, 1986, Moghadam and Paul, 2000, Wignall, 2001b, Hesselbo et al., 2004, Martin, 2004, Paul et al., 2008). In several instances it is apparent that oxygen availability within a single bed was not stable and fossil assemblages may represent time-averaged accumulations including the potential for opportunistic colonisation of the seafloor during short-lived oxic intervals. Non-uniform depositional processes have also altered the fossil assemblage via the concentration of bioclasts and differential or prolonged exposure to acidic conditions within the TAZ during periods of non-deposition.

Within the basal BLF, poor environmental conditions such as low oxygen availability or anoxia are thought to exert a negative palaeoecological control on the benthic assemblage and is associated with a subsequent prolonged or staged biotic recovery (e.g. Barras and Twitchett, 2007, Mander et al., 2008, Pugh et al., 2014); whilst fossil evidence provided herein does not dispute this interpretation, it does show that skeletal macrobenthos are a poor proxy for the reconstruction of a staged recovery model – as is otherwise possible with ichnotaxa (*sensu* Twitchett, 2006) – owing to additional influences such as diagenetic aragonite dissolution.

Taphonomic distortion associated with the Missing Molluscs effect (*sensu* Wright et al., 2003) is examined for the first time at formation scale and for a complete range of lithologies within the BLF of Dorset and East Devon. Shelly fossil assemblages from most lithologies are shown to exhibit some degree of taphonomic bias that manifests as a general lack of formerly aragonitic infaunal bivalves and epifaunal gastropods, eradication of the

shallow infaunal palaeocommunity, selective preservation of large-bodied ammonoids, and/or the predominance of low diversity, calcitic and bimineralic pteriomorph bivalves. Consequently, the use of infauna as an indicator of biotic recovery is particularly unreliable since these groups are more vulnerable to selective dissolution. This control is discussed in more detail later in the thesis (see Chapter 7).

CHAPTER 4

4. AN IRON PALAEOREDOX PROXY APPROACH TO RECONSTRUCT REDOX CONDITIONS IN AN EARLY JURASSIC, ALTERNATING LIMESTONE-MUDROCK SUCCESSION IN DORSET AND EAST DEVON, UK

4.1. Introduction

During the Early Jurassic, deposition of fossiliferous mudrocks throughout southern Britain was coincident with regularly fluctuating bottom water redox conditions. It has been inferred by previous authors that different (pre-diagenetic) lithologies represent varying degrees of bottom water oxygenation (e.g. Weedon, 1986, Moghadam and Paul, 2000) which ranged from anoxic and sulphide-rich (euxinic) to fully oxic. This study attempts to characterise these changes within the BLF of Dorset and East Devon using the Fe_{HR}/Fe_T and Fe_{Py}/Fe_{HR} ratios.

Iron speciation, specifically the Indicator of Anoxicity (*sensu* Raiswell et al., 2001) or the highly reactive iron (Fe_{HR}) to total iron (Fe_T) ratio (Fe_{HR}/Fe_T), is used to reconstruct bottom water redox conditions in modern and ancient marine settings (Raiswell and Canfield, 1998, Raiswell et al., 2001, Poulton and Raiswell, 2002, Lyons and Severmann, 2006, Poulton and Canfield, 2011, Clarkson et al., 2014, Raiswell et al., 2018; see Chapter 1). During deposition beneath an anoxic water column, Fe_{HR} is enriched with respect to Fe_T (Canfield et al., 1996, Raiswell and Canfield, 1998) so that $Fe_{HR}/Fe_T > 0.38$ (Raiswell and Canfield, 1998, Raiswell et al., 2018). Fe_{HR} enrichment is the product of iron mobilisation from the oxic continental shelf via intra-basinal transport (Wijsman et al., 2001, Anderson and Raiswell, 2004, Lyons and Severmann, 2006, Severmann et al., 2008, Clarkson et al., 2014, Raiswell et al., 2018; see Chapter 1). Beneath well-oxygenated bottom waters, without Fe_{HR} enrichment, Fe_{HR}/Fe_T ratios plot below the 0.38 threshold (Raiswell and Canfield, 1998) and more definitively, below a recently defined 0.22 threshold (Poulton and Canfield, 2011, Raiswell et al., 2018).

In conjunction with Fe_{HR}/Fe_T, the pyrite (Fe_{Py}) to Fe_{HR} ratio (Fe_{Py}/Fe_{HR}) can be used to differentiate euxinic and ferruginous conditions (sulphide-rich and FeII-rich respectively) (Poulton et al., 2004, Canfield et al., 2008, Poulton and Canfield, 2011, Raiswell et al., 2018; see Chapter 1). Where Fe_{HR} enrichment coincides with sulphidic bottom waters, iron reacts with dissolved sulphide to precipitate pyrite (Canfield et al., 1996, Raiswell and Canfield, 1998, Wijsman et al., 2001, Anderson and Raiswell, 2004, Lyons and Severmann, 2006, Severmann et al., 2008); this results in Fe_{Py}/Fe_{HR} ratios that exceed the 0.8 euxinic threshold (Canfield et al., 2008, Raiswell et al., 2018), although recent studies indicate a revised 0.7 threshold may be more suitable (Poulton and Canfield, 2011, Raiswell et al., 2018). In ferruginous anoxic bottom waters, iron is preferentially precipitated as unsulphidised minerals including $Fe_{Oxyhydroxides}$ (Fe_{Oxy}) as well as $Fe_{Carbonates}$

(Fe_{Carb}) (Poulton and Canfield, 2011); this results in Fe_{Py}/Fe_{HR} ratios that plot below the 0.8 threshold (Canfield et al., 2008) or, more conclusively, below the revised 0.7 threshold (Poulton and Canfield, 2011, Raiswell et al., 2018). Crucially, Fe_{Py}/Fe_{HR} is only applicable where $Fe_{HR}/Fe_T > 0.38$ (Poulton et al., 2004, Poulton and Canfield, 2011).

Diagenetic iron mobilisation and enrichment are important considerations in Jurassic marine mudrocks, particularly alternating limestone-marl successions, since lithologically distinct horizons were subject to different diagenetic processes (see review by Raiswell et al., 2018). Bottrell and Raiswell (1989) describe the potential for diagenetic iron migration in the BLF based on the adjacence of (pre-diagenetic) carbonate-poor and carbonate-rich horizons. The authors suggest that the relative abundance of pyrite was a function of the proportion of $CaCO_3$ in the sediment as carbonate dissolution was required to buffer acidity produced during bioturbational pyrite oxidation and maintain porewater supersaturation with respect to sulphides (Bottrell and Raiswell, 1989); this process occurred in carbonate-rich limestone horizons but not in the alternating, carbonate-poor argillaceous lithologies where pore-waters quickly became acidic and iron-rich (Bottrell and Raiswell, 1989). Different states of iron and sulphide availability subsequently enabled iron mobilisation from carbonate-poor to carbonate-rich horizons (Bottrell and Raiswell, 1989) which contributed to diagenetic Fe_{HR} enrichment. Clarkson et al. (2014) reviewed the applicability of iron speciation on carbonate-rich, oxic sediments and found that samples with low total iron content (< 0.5 % wt) and low organic carbon content (< 0.5 % wt) were susceptible to Fe_{HR} enrichment that propagated false anoxic Fe_{HR}/Fe_T ratios (see review by Raiswell et al., 2018). Additional diagenetic Fe_{HR} enrichment mechanisms are potentially significant and include the preferential incorporation of iron during carbonate cementation (e.g. Clarkson et al., 2014).

4.2. Material and methods

4.2.1. Sampling

A high-resolution, iron palaeoredox analysis was conducted on the Early Jurassic BLF of Dorset and East Devon, South England (see Chapter 2 for locality details). A total of 204 samples were taken in order to account for the majority of individual lithological horizons, incorporating limestones and argillaceous lithologies (see Chapter 2 for revised lithostratigraphic log). Approximately 50 mm^3 of sediment was taken from fresh exposures

in order to minimise the effects of weathering which can result in the loss of pyrite via oxidative decay (Raiswell et al., 2018); this was conducted intermittently over a period of two years owing to the variable nature of this locality.

4.2.2. Iron palaeoredox analysis

In preparation for all analyses, samples were dried in a furnace at 30°C for 12 hours to remove excess moisture; dried sediments were then ground to an approximate coarseness of 1 – 3 mm before being processed into a 4 μm powder. It is important to note that these represent the carbonate-containing sediment fraction and data presented later in the chapter have not been corrected for dilution by carbonate nor organic matter. Analyses reference the relative abundance of individual iron pools with respect to total iron and thus correction for dilution was not necessary (Anderson and Raiswell, 2004, Clarkson et al., 2014).

Sequential iron extractions. The sequential extraction procedure of Poulton and Canfield (2005) was used to quantify different iron-bearing mineral phases within each of the reactive iron pools: Fe_{HR} = Fe_{Carb}, Fe_{Oxy}, $Fe_{Magnetite}$ (Fe_{Mag}), and $Fe_{Hematite}$ (Fe_{Hem}) as well as $Fe_{PoorlyReactive}$ (Fe_{PR}) = $Fe_{SheetSilicates}$ (Fe_{SS}) (table 4.1). The extractions were undertaken on a 50 mg powdered sediment sample that was drained and reused after each stage; prior to the Fe_{SS} extraction, the sediment was drained and dried for 48 hours. In order to prepare the extraction solution for analysis, 250 μl was separated and diluted to 10 ml with MQ-H_2O.

Sequential iron extraction procedures (Poulton and Canfield, 2005)	
Fe_{Carb}	10 ml of a 1 mol sodium acetate (CH_3COONa) solution, buffered to pH 4.5 with acetic acid, was applied to the sample and shaken for 48 hours at 50°C.
Fe_{Oxy}	10 ml of a 50 g/l sodium dithionite ($Na_2S_2O_4$) solution, buffered to pH 4.8 with 0.35 mol acetic acid/0.2 mol sodium citrate, was applied to the sample and shaken for 2 hours at room temperature.
Fe_{Mag}	10 ml of an ammonium oxalate solution ($C_2H_{10}N_2O_5.H_2O$) at 0.2 mol ammonium oxalate monohydrate/0.17 mol oxalic acid was applied to the sample and shaken for 6 hours at room temperature.
Fe_{Hem}	The sodium dithionite extraction as for Fe_{Oxy} was applied to the sample but shaken for 6 hours at room temperature.
Fe_{SS}	5 ml of concentrated HCl was applied to the sample and boiled for 2 minutes. The solution was diluted to a known volume and left to react for 1 hour at room temperature.

Table 4.1 – Sequential iron extraction protocols for Fe_{Carb}, Fe_{Oxy}, Fe_{Mag}, Fe_{Hem}, and Fe_{SS} (Poulton and Canfield, 2005).

Total iron extraction. Using an extraction procedure based on Poulton and Canfield (2005), 100 mg of sediment was combusted at 520ºC for 8 hours. 5 ml of 6 mol HCl was added to the sample and left for 48 hours at 80ºC. The solution was taken up to a known volume with MQ-H_2O and left to stand for 1 hour. In order to prepare the extraction solution for analysis, 250 µl was separated and diluted to 10 ml with MQ-H_2O.

Ferrozine test. Following the sequential extraction procedure (after Poulton and Canfield, 2005), iron measurements were determined via atomic absorption using the ferrozine test (applied by Poulton and Canfield, 2005, after Stookey, 1970, Viollier et al., 2000). Spectrophotometric analyses were performed on a Cary 50 Probe UV–vis spectrophotometer at Cardiff University; the reaction between iron and ferrozine was measured spectrophotometrically at 562 nm wavelength (Stookey, 1970) and plotted against a calibration curve of dilutions from an iron standard solution. The procedure required in order to prepare the extraction solution for analysis is detailed in Table 4.2 (applied by Poulton and Canfield, 2005, after Stookey, 1970, Viollier et al., 2000). The method detection limit is 0.3 µmol/l Fe with a 10 mm cuvette (Viollier et al., 2000).

Ferrozine test procedure (applied by Poulton and Canfield, 2005, after Stookey, 1970, Viollier et al., 2000)	
Ferrozine	100 µl of ferrozine reagent, comprised of a 10^{-2} mol ferrozine ($C_{20}H_{13}N_4NaO_6S_2$) solution in 10^{-1} mol ammonium acetate ($C_2H_7NO_2$), was applied to 1 ml of sample solution.
Reducing agent	150 µl of reducing agent, comprised of a 1.4 mol hydroxylamine hydrochloride ($H_2NOH.HCl$) solution in 2 mol HCl, was applied to 800 µl of sample solution and rested for 10 minutes.
Buffer solution	50 µl of buffer solution, comprised of a 10 mol ammonium acetate ($C_2H_7NO_2$) solution adjusted to pH 9.5 with 30 % ammonium hydroxide (NH_4OH), was added to the sample solution.

Table 4.2 – Ferrozine test protocol for the spectrophotometric determination of iron (applied by Poulton and Canfield, 2005, after Stookey, 1970, Viollier et al., 2000).

Chromous chloride reduction method. The chromous chloride reduction method of Newton et al. (1995), (modified from Canfield et al., 1986) was used to determine Fe_{Py} for use in association with the sequential iron extraction procedure. This method quantifies the reduced inorganic sulphur forms: pyrite, acid volatile sulphides (AVS), and elemental sulphur (Canfield et al., 1986). It is important to note that AVS typically transformed to pyrite during diagenesis (Raiswell et al., 2018) and was not identified in test samples. The

principal behind the procedure is that inorganic sulphur species are liberated as hydrogen sulphide (H_2S) from the sediment sample following decomposition in solution by hydrochloric acid (HCl) and chromous chloride ($CrCl_2$) (Canfield et al., 1986, Newton et al., 1995). H_2S is subsequently precipitated as copper sulphide (CuS) in the collecting head (fig. 4.1) following reaction with copper chloride ($CuCl_2$) (Newton et al., 1995). The amount of CuS is directly proportionate to inorganic sulphur (pyrite) in the sediment sample which can be determined by quantifying the remaining copper (Cu) via titration (Newton et al., 1995).

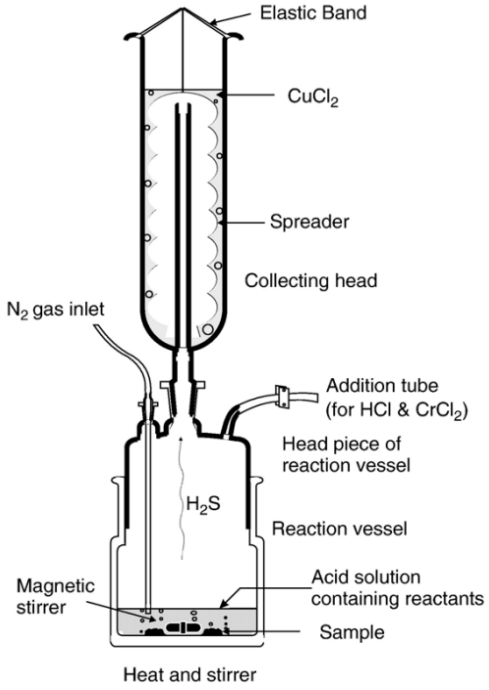

Figure 4.1 – Illustration of the apparatus and experiment set-up used in the chromous chloride reduction method (Rickard et al., 2006, after Newton et al., 1995).

The apparatus used in the chromous chloride reduction method were modified by Rickard et al. (2006), (after Newton et al., 1995) (fig. 4.1). Prior to each procedure, the apparatus were assembled containing 1 g of sediment sample and approximately 10 ml of ethanol (after Canfield et al., 1986). A 'Jones reductor' (Kolthoff and Sandell, 1963, in Canfield et al., 1986) was used to prepare chromous chloride ($CrCl_2$) for the experiment (after Canfield et al., 1986). The reductor comprised a 50 ml burette, plugged at the base with a fibrous mesh, that was filled to the 30 ml mark with a granular zinc amalgam – zinc in an acidic 2 % mercury nitrate ($Hg[NO_3]_2$) solution (after Canfield et al., 1986); the reductor was activated using 10 % HCl. Chromous (II) chloride ($CrCl_2$) was made by passing a 1 mol solution of chromium (III) chloride hexahydrate ($Cl_3CrH_{12}O_6$) in 10 % HCl through

the zinc amalgam column (after Canfield et al., 1986); the reduced solution was stored in glass bottles flushed with nitrogen.

Chromous chloride reduction method (Newton et al., 1995, modified from Canfield et al., 1986)	
Working copper	25 ml of a 0.1 mol copper chloride ($CuCl_2$) solution was added to the collecting head (fig. 4.1). The experiment apparatus was then flushed with nitrogen gas (approximately 2 – 3 bubbles per second) and left for ten minutes.
Conc. HCl	20 ml of concentrated HCl was added to the reaction vessel.
Chromous chloride	40 ml of the chromous chloride ($CrCl_2$) solution was added to the reaction vessel before it was heated to boiling point and left for 90 minutes to react.

Table 4.3 – Chromous chloride reduction method protocol for the determination of Fe_{Py} (Newton et al., 1995, modified from Canfield et al., 1986).

To prepare samples for titration, both the spreader and the collecting head (fig. 4.1) were emptied into a conical flask via a filtration system (after Rickard et al., 2006); both pieces of apparatus were rinsed over the same filter paper with $MQ.H_2O$ in order to retrieve all of the solution (after Rickard et al., 2006). 25 ml of a copper sulphate pentahydrate ($CuSO_4.5H_2O$) solution (6 g/l) was used as a standard (after Rickard et al., 2006).

Titration method (Newton et al., 1995, Rickard et al., 2006)	
Buffer solution	70 ml of a 1 mol sodium acetate (CH_3COONa) solution, made to pH 5.5 with acetic acid, was added to the conical flask containing the sample solution.
Indicator	5 drops of a 0.5 % aqueous solution of Glycine Cresol red was added to the conical flask containing the sample solution and stirred.
EDTA	The sample was then titrated against a 0.1 mol EDTA solution; completion was evident by a colour change from blue to green.

Table 4.4 – Titration protocol for the determination of Fe_{Py} (Newton et al., 1995, Rickard et al., 2006).

4.3. Results and interpretations

Fe_{HR}/Fe_T ratios from (inferred) oxic lithologies that do not meet the $Fe_T > 0.5$ wt % screening criterion applied to carbonate-rich oxic sediments by Clarkson et al. (2014) were still plotted; these measurements are spurious, but have been included for discussion later in the chapter. Fe_{HR}/Fe_T ratios > 1 were considered analytical errors and not plotted. Non-applicable Fe_{Py}/Fe_{HR} ratios, i.e. where $Fe_{HR}/Fe_T < 0.38$, were included for discussion later in the chapter but do not correspond to original depositional conditions.

BL 1 = At the base of the BLF, measurements of Fe_{Py} (885.79 – 13430.52 ppm) and Fe_T (2973.13 – 30943.92 ppm) have a large range (table 4.5); minimum values were recorded in the central laminated limestones (table 4.5). Despite this variation, Fe_{HR}/Fe_T ratios plot uniformly above the anoxic 0.38 threshold (fig. 4.2; table 4.5); Fe_{HR}/Fe_T in the laminated limestones (0.469) is marginally less than the paper shales above and below (average = 0.552) (fig. 4.2; table 4.5). Fe_{Py}/Fe_{HR} consistently plots below the euxinic 0.8 threshold (fig. 4.2; table 4.5).

BL 2 = The majority of bioturbated limestone beds, except for H10 (Fe_{HR}/Fe_T = 0.182) and H20 (Fe_{HR}/Fe_T = 0.177), plot above the anoxic 0.38 threshold (fig. 4.2; table 4.5). Fe_T measurements in the limestones are persistently low (2501.84 – 8745.59 ppm; table 4.5); 7 of the 13 samples do not meet the Fe_T > 0.5 wt % screening criterion (table 4.5) applied to carbonate-rich sediments by Clarkson et al. (2014) and are therefore considered potentially spurious. Fe_T measurements in the remaining limestone samples that marginally exceed the screening criterion should be carefully considered with supporting palaeontological and sedimentological evidence. The Fe_{Py}/Fe_{HR} ratio, excluding oxic samples (Fe_{HR}/Fe_T < 0.38), is similarly variable (fig. 4.2; table 4.5). Below H21, Fe_{Py}/Fe_{HR} in the bioturbated limestones has a large range (0.392 – 0.944; fig. 4.2; table 4.5) and spans the ferruginous and euxinic fields (fig. 4.2; table 4.5). In contrast, limestones above H21 uniformly plot above the euxinic 0.8 threshold (fig. 4.2; table 4.5).

Fe_{HR}/Fe_T ratios in argillaceous sediments generally plot above the 0.38 anoxic threshold but the extent of relative Fe_{HR} enrichment does not correlate with lithology (fig. 4.2; table 4.5). Nonetheless, there are few instances where serial Fe_{HR}/Fe_T measurements mirror relative changes in inferred oxygen conditions between adjacent lithologies e.g. H5a – H5b and H19c – H20 (fig. 4.2; table 4.5). Fe_{Py}/Fe_{HR} ratios in argillaceous sediments below H22, excluding oxic samples, have a large range (0.144 – 0.867) but the majority plot beneath the 0.8 euxinic threshold (average = 0.665) (fig. 4.2; table 4.5). In contrast, argillaceous sediment samples above H22 occur uniformly within the euxinic field (average Fe_{Py}/Fe_{HR} = 0.914) (fig. 4.2; table 4.5).

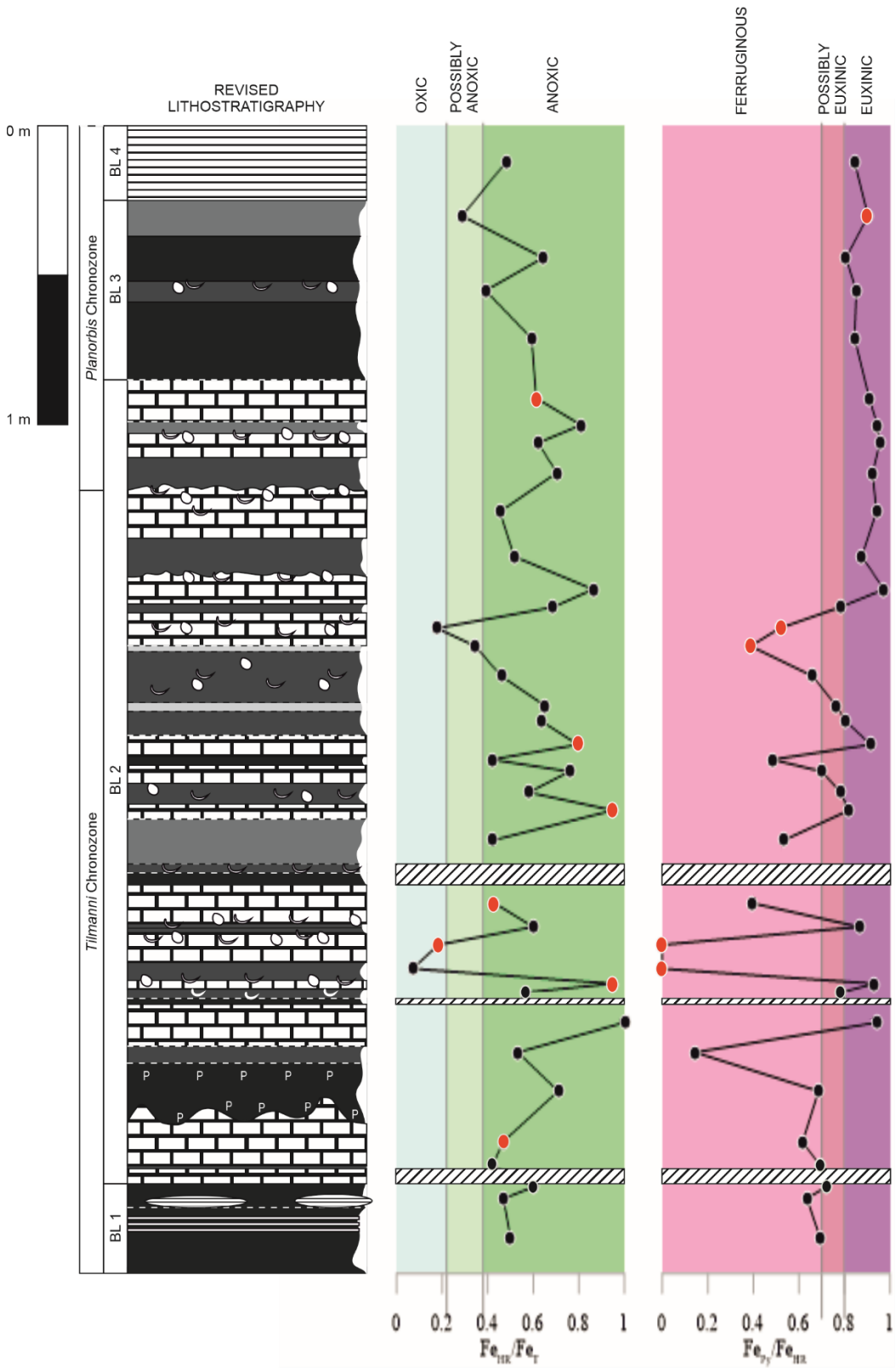

Figure 4.2 – Iron speciation plots (Fe_{HR}/Fe_T ratio and Fe_{Py}/Fe_{HR} ratio respectively) for the basal BLF (BL 1 – BL 4). Fe_{HR}/Fe_T ratios in (inferred) oxic lithologies that do not meet the Fe_T > 0.5 wt % screening criterion described by Clarkson et al. (2014) as well as non-applicable Fe_{Py}/Fe_{HR} ratios i.e. where Fe_{HR}/Fe_T < 0.38, are highlighted in red. For a detailed description of the revised lithostratigraphy see Chapter 2. The Fe_{HR}/Fe_T thresholds are taken at 0.22 and 0.38. The Fe_{Py}/Fe_{HR} thresholds are taken at 0.7 and 0.8.

BL 4										
Sample	**Lithology**	**Fe_{Py}**	**Fe_{Carb}**	**Fe_{Oxy}**	**Fe_{Mag}**	**Fe_{Hem}**	**Fe_{SS}**	**Fe_{T}**	**IoA**	**IoE**
H30	L.LST	798.46	48.78	97.93	0.00*	0.00*	154.22	1970.95	0.480	0.845

BL 3										
Sample	**Lithology**	**Fe_{Py}**	**Fe_{Carb}**	**Fe_{Oxy}**	**Fe_{Mag}**	**Fe_{Hem}**	**Fe_{SS}**	**Fe_{T}**	**IoA**	**IoE**
H29 d	D.M	2133.58	116.73	111.54	0.00*	0.00*	872.73	8221.21	0.287	0.903
H29 c	P.S	12236.21	349.67	2587.82	0.00*	0.00*	1206.30	23596.94	0.643	0.806
H29 b	SHA	2630.08	116.44	325.81	0.00*	15.01	552.15	7912.04	0.390	0.852
H29 a	P.S	5208.73	137.92	779.75	0.00*	38.21	1047.92	10401.51	0.593	0.845

BL 2										
Sample	**Lithology**	**Fe_{Py}**	**Fe_{Carb}**	**Fe_{Oxy}**	**Fe_{Mag}**	**Fe_{Hem}**	**Fe_{SS}**	**Fe_{T}**	**IoA**	**IoE**
H28	LST	1949.85	70.27	124.48	0.00*	0.00*	358.93	3502.27	0.612	0.909
H27	D.M	8391.08	116.80	357.26	0.00*	22.06	N/A	10977.67	0.810	0.944
H26	LST	3566.22	69.65	96.14	0.00*	0.00*	320.94	6009.44	0.621	0.956
H25	SHA	13551.35	283.67	833.12	0.00*	9.96	1355.47	20877.78	0.703	0.923
H24	LST	2748.32	98.94	75.71	0.00*	0.00*	472.65	6450.76	0.453	0.940
H23	SHA	8879.80	129.68	1110.37	0.00*	18.92	1569.26	19651.19	0.516	0.876
H22	LST	6776.36	55.81	127.52	0.00*	0.00*	374.04	8066.32	0.863	0.974
H21	SHA	10974.38	161.11	2932.97	0.00*	0.00*	N/A	20521.36	0.686	0.780
H20	LST	796.02	69.84	678.22	0.00*	0.00*	655.25	8745.59	0.177	0.516
H19 d	L.M	2852.63	276.42	4227.66	0.00*	0.00*	N/A	21315.18	0.345	0.388
H19 c	SHA	8537.37	120.96	4227.81	0.00*	69.20	1140.57	28265.10	0.458	0.659
H19 b	L.M	3276.58	84.22	926.26	0.00*	0.00*	324.06	6578.40	0.652	0.764
H19 a	SHA	8808.92	133.47	1964.74	0.00*	46.68	955.19	17309.76	0.633	0.804
H18	LST	3625.31	55.22	281.63	0.00*	0.00*	545.35	4976.64	0.796	0.915
H17	P.S	4398.03	45.20	4585.33	0.00*	66.25	1431.95	21824.10	0.417	0.484
H16	LST	2678.13	32.51	1109.22	0.00*	0.00*	291.44	5032.40	0.759	0.701
H15	SHA	10751.57	156.11	2677.03	0.00*	143.76	1014.96	23677.88	0.580	0.783
H14	LST	2968.01	54.42	598.45	0.00*	0.00*	226.00	3807.69	0.951	0.820
H13 c	D.M	3828.69	47.93	3295.63	0.00*	0.00*	1140.93	16945.47	0.423	0.534
H13 b	SHA	N/A	N/A	N/A	N/A	N/A	N/A	N/A	N/A	N/A
H13 a	P.S	N/A	N/A	N/A	N/A	N/A	N/A	N/A	N/A	N/A
H12	LST	690.61	19.71	1052.59	0.00*	0.00*	257.39	4107.83	0.429	0.392
H11	SHA	11549.57	144.10	1575.33	0.00*	59.85	1169.71	22259.28	0.599	0.867
H10	LST	0.00*	41.72	414.74	0.00*	0.00*	315.88	2501.84	0.182	0.000
H9	SHA	0.00*	250.68	1418.75	0.00*	86.40	1405.88	25057.40	0.070	0.000
H8	LST	4091.93	70.49	227.12	0.00*	0.00*	322.01	4628.48	0.948	0.932
H7 b	SHA	8190.27	119.78	2142.41	0.00*	0.00*	704.74	18538.62	0.564	0.784

H7 a	P.S	N/A	N/A	N/A	N/A	N/A	N/A	N/A	N/A	N/A
H6	LST	6201.74	82.44	283.67	0.00*	0.00*	243.86	6555.01	1.002	0.944
H5 b	SHA	306.35	73.97	1572.67	0.00*	179.26	N/A	4006.32	0.532	0.144
H5 a	P.S	7783.72	140.38	3354.67	65.64	0.00*	N/A	16001.68	0.709	0.686
H4	LST	991.47	77.58	540.85	0.00*	0.00*	216.46	3448.75	0.467	0.616
H3	SHA	4671.10	108.30	1948.50	0.00*	0.00*	850.18	16006.36	0.420	0.694
H2	LST	N/A	N/A	N/A	N/A	N/A	N/A	N/A	N/A	N/A
BL 1										
Sample	**Lithology**	**Fe_{Py}**	**Fe_{Carb}**	**Fe_{Oxy}**	**Fe_{Mag}**	**Fe_{Hem}**	**Fe_{SS}**	**Fe_{T}**	**IoA**	**IoE**
H1 c	P.S	13430.52	218.02	4985.75	0.00*	28.84	1093.42	30943.92	0.603	0.720
H1 b	L.LST	885.79	65.50	443.28	0.00*	0.00*	417.57	2973.13	0.469	0.635
H1 a	P.S	4924.08	129.22	2054.59	0.00*	0.00*	817.05	14227.72	0.500	0.693

Table 4.5 – Iron speciation data for BL 1 – BL 4. Data presented includes: Fe_{Py}, Fe_{Carb}, Fe_{Oxy}, Fe_{Mag}, Fe_{Hem}, Fe_{SS}, and Fe_{T} (measured in parts per million). * = Below method detection limit. The Fe_{HR}/Fe_{T} (IoA) and Fe_{Py}/Fe_{HR} (IoE) ratios are given also. L.LST = laminated limestone, LST = limestone, P.S = paper shale, SHA = shale, D.M = dark marl, and L.M = light marl. See Chapter 2 for the revised lithostratigraphy; bed numbers/nomenclature after Lang (1924).

BL 3 = Serial Fe_{HR}/Fe_T ratios are consistent with relative changes in inferred oxygen conditions between adjacent lithologies (paper shales [average] = 0.618 > shales = 0.39 > dark marls = 0.287) (fig. 4.2; table 4.5). Fe_{HR}/Fe_T values for the shale and dark marl samples plot near to or below the anoxic 0.38 threshold whereas both paper shale samples occur within the anoxic field (fig. 4.2; table 4.5). Fe_{Py}/Fe_{HR} ratios plot within the euxinic field irrespective of lithology (fig. 4.2; table 4.5).

BL 4 = The single laminated limestone bed plots within the anoxic (Fe_{HR}/Fe_T = 0.48) and euxinic (Fe_{Py}/Fe_{HR} = 0.845) fields (fig. 4.2; table 4.5).

BL 5 = Fe_{HR}/Fe_T ratios plot uniformly above the anoxic 0.38 threshold, but do not correlate with lithology (fig. 4.3; table 4.6). In contrast, Fe_{Py}/Fe_{HR} ratios correlate well with lithological alternations such that values are greater in the laminated limestones (average = 0.904) than in the paper shale interbeds (average = 0.728) (fig. 4.3; table 4.6). Laminated limestone samples plot uniformly within the euxinic field (fig. 4.3; table 4.6).

BL 6 = It is important to note that Fe_T measurements in the bioturbated limestones are low (3860.21 - 6203.31 ppm; table 4.6); 2 of the 4 samples do not reach the Fe_T screening criterion described by Clarkson et al. (2014) and the remainder only marginally exceed it (table 4.6). As a result, these values are spurious and should be considered with supporting palaeontological evidence. Fe_{HR}/Fe_T is generally inverted with respect to inferred oxygen conditions such that Fe_{HR}/Fe_T ratios in the bioturbated limestone lithology – excluding samples where Fe_T < 0.5 wt % – are greater than those in the argillaceous alternations (average = 0.511 and 0.44 respectively) (fig. 4.3; table 4.6). Excluding oxic samples, Fe_{Py}/Fe_{HR} ratios are also greater in the bioturbated limestones (average = 0.916) than in the combined argillaceous lithologies (average = 0.824) (fig. 4.3; table 4.6).

BL 7 = Laminated limestones consistently plot below the oxic 0.22 and/or anoxic 0.38 thresholds (fig. 4.3; table 4.6), contrary to inferred oxygen conditions. Fe_{HR}/Fe_T ratios in the paper shale interbeds are greater (average = 0.437) and most occur within the anoxic field (fig. 4.3; table 4.6). Fe_{Py}/Fe_{HR} ratios show no correlation with lithological alternations and whilst the range of values is large (Fe_{Py}/Fe_{HR} = 0 – 0.835), 8 of the 9 samples plots below the euxinic 0.8 threshold (fig. 4.3; table 4.6).

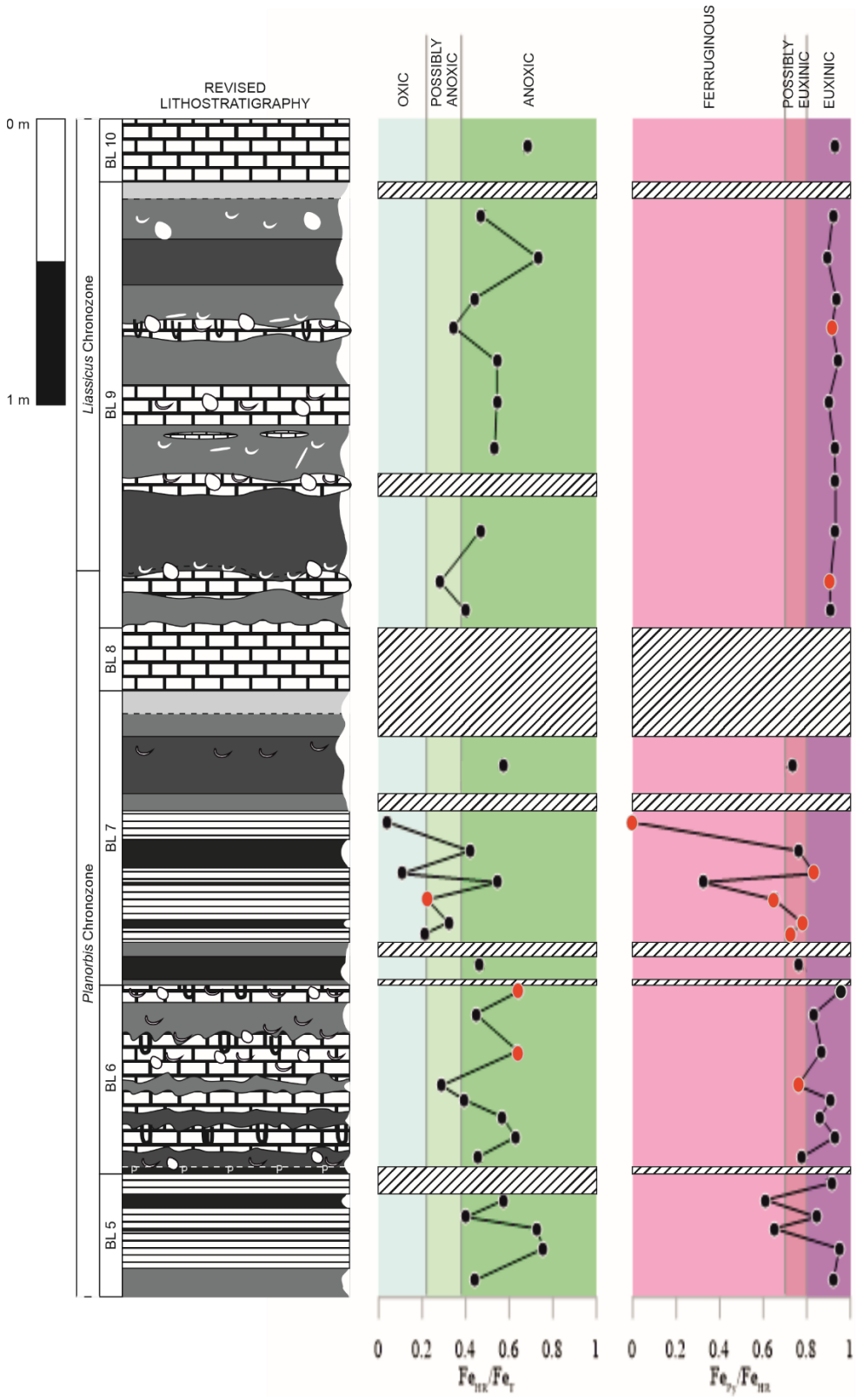

Figure 4.3 – Iron speciation plots (Fe_{HR}/Fe_T ratio and Fe_{Py}/Fe_{HR} ratio respectively) for the BLF (BL 5 – BL 10). Fe_{HR}/Fe_T ratios in (inferred) oxic lithologies that do not meet the Fe_T > 0.5 wt % screening criterion described by Clarkson et al. (2014) as well as non-applicable Fe_{Py}/Fe_{HR} ratios i.e. where Fe_{HR}/Fe_T < 0.38, are highlighted in red. For a detailed description of the revised lithostratigraphy see Chapter 2. The Fe_{HR}/Fe_T thresholds are taken at 0.22 and 0.38. The Fe_{Py}/Fe_{HR} thresholds are taken at 0.7 and 0.8.

BL 10										
Sample	**Lithology**	**Fe_{Py}**	**Fe_{Carb}**	**Fe_{Oxy}**	**Fe_{Mag}**	**Fe_{Hem}**	**Fe_{SS}**	**Fe_{T}**	**IoA**	**IoE**
H66	LST	5115.51	81.90	313.19	0.00*	0.00*	410.15	8073.36	0.683	0.928

BL 9										
Sample	**Lithology**	**Fe_{Py}**	**Fe_{Carb}**	**Fe_{Oxy}**	**Fe_{Mag}**	**Fe_{Hem}**	**Fe_{SS}**	**Fe_{T}**	**IoA**	**IoE**
H63 d	L.M	N/A	N/A	N/A	N/A	N/A	N/A	N/A	N/A	N/A
H63 c	D.M	10967.04	247.74	651.00	0.00*	70.81	1835.68	25377.73	0.470	0.919
H63 b	SHA	26429.23	461.11	2559.63	0.00*	48.33	1630.58	40104.23	0.736	0.896
H63 a	D.M	10026.93	170.90	487.65	0.00*	38.91	1838.03	24332.32	0.441	0.935
H62	LST	2730.68	41.77	197.26	0.00*	13.92	496.91	8657.23	0.345	0.915
H61	D.M	13091.81	212.77	526.38	0.00*	25.56	1526.23	25496.38	0.543	0.945
H60	LST	3779.49	74.77	346.00	0.00*	0.00*	484.59	7744.04	0.542	0.900
H59	D.M	11335.00	289.29	534.63	0.00*	81.30	1450.55	22959.15	0.533	0.926
H58	LST	3342.83	79.39	163.79	0.00*	0.00*	455.98	689.60	//5.200//	0.932
H57	SHA	11613.69	226.29	539.00	0.00*	86.95	1786.04	26627.61	0.468	0.932
H56	LST	2105.66	33.43	180.95	0.00*	0.00*	479.43	8202.56	0.283	0.908
H55	D.M	7372.49	160.68	539.28	0.00*	63.47	1597.23	20486.36	0.397	0.906

BL 8										
Sample	**Lithology**	**Fe_{Py}**	**Fe_{Carb}**	**Fe_{Oxy}**	**Fe_{Mag}**	**Fe_{Hem}**	**Fe_{SS}**	**Fe_{T}**	**IoA**	**IoE**
H54	LST	N/A	N/A	N/A	N/A	N/A	N/A	N/A	N/A	N/A

BL 7										
Sample	**Lithology**	**Fe_{Py}**	**Fe_{Carb}**	**Fe_{Oxy}**	**Fe_{Mag}**	**Fe_{Hem}**	**Fe_{SS}**	**Fe_{T}**	**IoA**	**IoE**
H53 d	L.M	N/A	N/A	N/A	N/A	N/A	N/A	N/A	N/A	N/A
H53 c	D.M	N/A	N/A	N/A	N/A	N/A	N/A	N/A	N/A	N/A
H53 b	SHA	13581.10	423.24	4422.74	0.00*	82.89	1159.25	32205.32	0.575	0.734
H53 a	D.M	N/A	N/A	N/A	N/A	N/A	N/A	N/A	N/A	N/A
H52	L.LST	0.00*	205.25	210.14	0.00*	0.00*	862.05	10293.21	0.040	0.000
H51	P.S	4141.43	229.53	1037.18	0.00*	22.28	853.33	12982.77	0.418	0.763
H50	L.LST	967.05	64.84	126.75	0.00*	0.00*	477.94	10724.33	0.108	0.835
H49	P.S	923.81	271.32	1677.06	0.00*	0.00*	N/A	5235.98	0.549	0.322
H48	L.LST	549.09	70.29	225.18	0.00*	0.00*	289.27	3789.64	0.223	0.650
H47	P.S	4115.21	286.61	887.36	0.00*	15.01	878.10	16606.30	0.319	0.776
H46	L.LST	860.17	73.13	245.13	0.00*	0.00*	224.47	5561.48	0.212	0.730
H45 c	D.M	N/A	N/A	N/A	N/A	N/A	N/A	N/A	N/A	N/A
H45 b	P.S	10575.81	478.82	2697.52	0.00*	115.93	826.41	29960.72	0.463	0.763
H45 a	D.M	N/A	N/A	N/A	N/A	N/A	N/A	N/A	N/A	N/A

BL 6										
Sample	**Lithology**	**Fe_{Py}**	**Fe_{Carb}**	**Fe_{Oxy}**	**Fe_{Mag}**	**Fe_{Hem}**	**Fe_{SS}**	**Fe_{T}**	**IoA**	**IoE**
H44	LST	2378.56	71.68	42.78	0.00*	0.00*	272.56	3860.21	0.646	0.954
H43	D.M	6378.24	263.22	1019.01	0.00*	0.00*	948.35	17211.99	0.445	0.833
H42	LST	2417.29	58.98	305.88	0.00*	0.00*	350.27	4356.27	0.639	0.869
H41	D.M	1532.20	93.45	393.83	0.00*	0.00*	522.33	6997.24	0.289	0.759
H40	LST	2216.37	71.68	146.05	0.00*	0.00*	363.91	6203.31	0.392	0.911
H39	SHA	5481.20	113.05	767.86	0.00*	0.00*	554.05	11203.32	0.568	0.861
H38	LST	3301.56	71.39	181.46	0.00*	0.00*	301.68	5646.95	0.629	0.929
H37 b	SHA	3342.08	179.27	728.16	0.00*	42.51	581.68	9406.53	0.456	0.779
H37 a	P.S	N/A	N/A	N/A	N/A	N/A	N/A	N/A	N/A	N/A
BL 5										
Sample	**Lithology**	**Fe_{Py}**	**Fe_{Carb}**	**Fe_{Oxy}**	**Fe_{Mag}**	**Fe_{Hem}**	**Fe_{SS}**	**Fe_{T}**	**IoA**	**IoE**
H36	L.LST	2660.84	58.63	185.15	0.00*	0.00*	334.98	2446.48	//1.187//	0.916
H35	P.S	1659.41	176.45	880.62	0.00*	0.00*	N/A	4711.86	0.577	0.611
H34	L.LST	734.34	69.38	64.67	0.00*	0.00*	231.04	2162.96	0.401	0.846
H33	P.S	2660.42	131.48	1303.70	0.00*	0.00*	N/A	5635.02	0.727	0.650
H32	L.LST	4102.84	110.44	107.86	0.00*	0.00*	458.62	5721.68	0.755	0.949
H31	D.M	8329.87	310.35	389.26	0.00*	0.00*	1718.74	20383.90	0.443	0.923

Table 4.6 – Iron speciation data for BL 5 – BL 10. Data presented includes: Fe_{Py}, Fe_{Carb}, Fe_{Oxy}, Fe_{Mag}, Fe_{Hem}, Fe_{SS}, and Fe_{T} (measured in parts per million). * = Below method detection limit. The Fe_{HR}/Fe_{T} (IoA) and Fe_{Py}/Fe_{HR} (IoE) ratios are given also. Fe_{HR}/Fe_{T} ratios > 1 were not plotted. L.LST = laminated limestone, LST = limestone, P.S = paper shale, SHA = shale, D.M = dark marl, and L.M = light marl. See Chapter 2 for the revised lithostratigraphy; bed numbers/nomenclature after Lang (1924).

BL 8 = There was no data for BL 8 (fig. 4.3; table 4.6).

BL 9 = Serial Fe_{HR}/Fe_T ratios in BL 9 correspond well with relative changes in inferred oxygen conditions between adjacent lithologies (fig. 4.3; table 4.6). Moreover, the limestone beds of H56 ($Fe_{HR}/Fe_T = 0.283$) and H62 ($Fe_{HR}/Fe_T = 0.345$) (fig. 4.3; table 4.6) plot beneath the anoxic 0.38 threshold which indicates a consistency with palaeoecological evidence presented elsewhere in the thesis (see Chapter 3). Fe_{Py}/Fe_{HR} ratios have a limited range (0.896 – 0.945), do not correlate with lithological alternations and uniformly plot above the euxinic 0.8 threshold (fig. 4.3; table 4.6).

BL 10 = The single tabular limestone bed plots within the anoxic ($Fe_{HR}/Fe_T = 0.683$) and euxinic ($Fe_{Py}/Fe_{HR} = 0.928$) fields (fig. 4.3; table 4.6).

BL 11 = Serial Fe_{HR}/Fe_T ratios in BL 11 correlate well with relative changes in inferred oxygen conditions between adjacent lithologies (fig. 4.4; table 4.7). H67c ($Fe_{HR}/Fe_T = 0.216$) occurs within the oxic field, but the remaining dark marl samples plot above the anoxic 0.38 threshold (average $Fe_{HR}/Fe_T = 0.509$) as do the paper shale interbeds (average $Fe_{HR}/Fe_T = 0.737$) (fig. 4.4; table 4.7). Fe_{Py}/Fe_{HR} has no correlation with lithology and data span the ferruginous and euxinic fields (fig. 4.4; table 4.7).

BL 12 = Samples plot within the anoxic field irrespective of lithology (fig. 4.4; table 4.7).

BL 13 = Samples in BL 13 plot uniformly above the anoxic 0.38 threshold irrespective of lithology (fig. 4.4; table 4.7). Fe_{Py}/Fe_{HR} ratios have a limited range (0.82 – 0.92) within the euxinic field (fig. 4.4; table 4.7).

BL 14 = The Fe_{HR}/Fe_T ratio has a limited range (0.443 – 0.511) and does not reflect alternations between carbonate-poor and carbonate-rich lithologies (fig. 4.4; table 4.7); all samples plot above the anoxic 0.38 threshold (fig. 4.4; table 4.7). Fe_{Py}/Fe_{HR} ratios have a narrow range (0.937 – 0.97) and all plot within the euxinic field (fig. 4.4; table 4.7).

BL 15 = In the dark marl lithology, Fe_{HR}/Fe_T ratios generally plot within the anoxic field (average = 0.582) except for H81 ($Fe_{HR}/Fe_T = 0.277$) which occurs below the anoxic 0.38 threshold (fig. 4.4; table 4.7). In contrast, Fe_{Py}/Fe_{HR} ratios correspond well to carbonate-poor and carbonate-rich alternations (fig. 4.4); excluding oxic samples, Fe_{Py}/Fe_{HR} is greater in the bioturbated limestones (average = 0.969) than the dark marl interbeds (average = 0.857) (fig. 4.4; table 4.7).

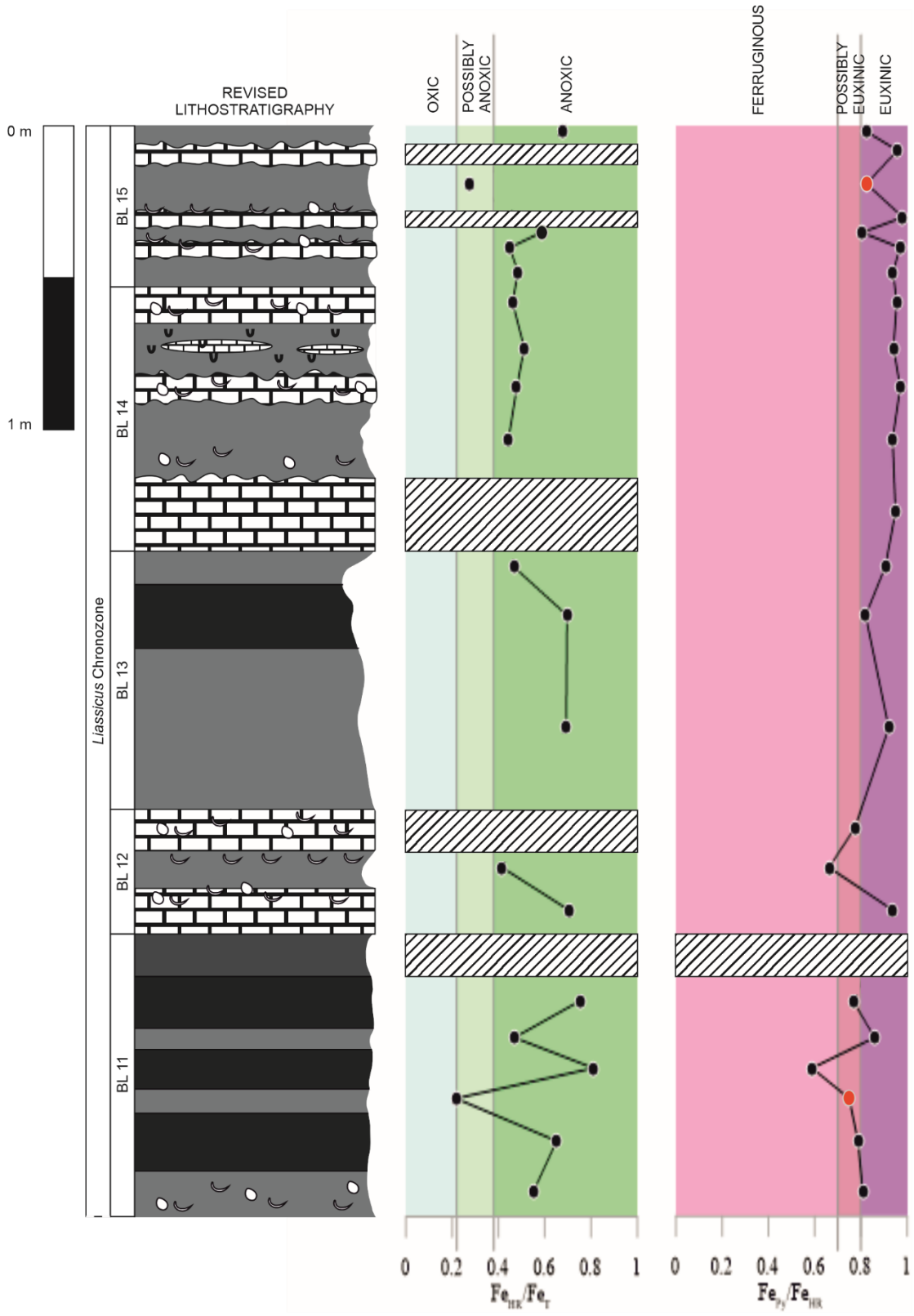

Figure 4.4 – Iron speciation plots (Fe_{HR}/Fe_T ratio and Fe_{Py}/Fe_{HR} ratio respectively) for the BLF (BL 11 – BL 15). Fe_{HR}/Fe_T ratios in (inferred) oxic lithologies that do not meet the Fe_T > 0.5 wt % screening criterion described by Clarkson et al. (2014) as well as non-applicable Fe_{Py}/Fe_{HR} ratios i.e. where Fe_{HR}/Fe_T < 0.38, are highlighted in red. For a detailed description of the revised lithostratigraphy see Chapter 2. The Fe_{HR}/Fe_T thresholds are taken at 0.22 and 0.38. The Fe_{Py}/Fe_{HR} thresholds are taken at 0.7 and 0.8.

BL 15										
Sample	**Lithology**	**Fe_{Py}**	**Fe_{Carb}**	**Fe_{Oxy}**	**Fe_{Mag}**	**Fe_{Hem}**	**Fe_{SS}**	**Fe_{T}**	**IoA**	**IoE**
H83	D.M	12984.13	335.16	2042.63	139.47	200.52	N/A	23191.04	0.677	0.827
H82	LST	6414.02	93.74	160.72	0.00*	30.21	887.93	6329.17	//1.058//	0.958
H81	D.M	7008.45	320.57	1133.08	43.63	0.00*	N/A	30722.77	0.277	0.824
H80	LST	7715.29	110.76	40.56	0.00*	0.00*	571.53	5962.01	//1.319//	0.981
H79	D.M	9816.44	306.03	1833.51	141.60	107.54	N/A	20867.56	0.585	0.804
H78	LST	4261.62	83.27	45.75	0.00*	12.17	300.60	9814.31	0.449	0.968
H77	D.M	9584.20	275.18	324.29	0.00*	24.19	1398.95	21069.82	0.484	0.939
BL 14										
Sample	**Lithology**	**Fe_{Py}**	**Fe_{Carb}**	**Fe_{Oxy}**	**Fe_{Mag}**	**Fe_{Hem}**	**Fe_{SS}**	**Fe_{T}**	**IoA**	**IoE**
H76	LST	2724.04	52.26	79.16	0.00*	0.00*	598.40	6197.33	0.461	0.954
H75	D.M	10873.59	121.09	402.72	0.00*	159.65	1547.91	22605.66	0.511	0.941
H74	LST	2952.11	65.45	27.40	0.00*	0.00*	410.19	6353.87	0.479	0.970
H73	D.M	9459.92	213.14	400.98	0.00*	25.30	1306.67	22777.16	0.443	0.937
H72	LST	6500.47	127.76	220.69	0.00*	0.00*	647.00	4711.65	//1.454//	0.949
BL 13										
Sample	**Lithology**	**Fe_{Py}**	**Fe_{Carb}**	**Fe_{Oxy}**	**Fe_{Mag}**	**Fe_{Hem}**	**Fe_{SS}**	**Fe_{T}**	**IoA**	**IoE**
H71 c	D.M	11440.86	269.84	850.99	37.38	38.45	N/A	27146.36	0.466	0.905
H71 b	P.S	18625.92	588.47	3263.00	159.96	77.31	N/A	32647.25	0.696	0.820
H71 a	D.M	15141.44	494.67	802.76	0.00*	18.08	N/A	23752.84	0.693	0.920
BL 12										
Sample	**Lithology**	**Fe_{Py}**	**Fe_{Carb}**	**Fe_{Oxy}**	**Fe_{Mag}**	**Fe_{Hem}**	**Fe_{SS}**	**Fe_{T}**	**IoA**	**IoE**
H70	LST	2948.44	110.71	728.28	0.00*	25.44	740.73	3721.44	//1.025//	0.773
H69	D.M	8352.89	225.20	3855.16	171.34	17.15	N/A	30395.80	0.415	0.662
H68	LST	5836.45	104.71	286.37	0.00*	0.00*	770.13	8845.11	0.704	0.937
BL 11										
Sample	**Lithology**	**Fe_{Py}**	**Fe_{Carb}**	**Fe_{Oxy}**	**Fe_{Mag}**	**Fe_{Hem}**	**Fe_{SS}**	**Fe_{T}**	**IoA**	**IoE**
H67 g	SHA	N/A	N/A	N/A	N/A	N/A	N/A	N/A	N/A	N/A
H67 f	P.S	27090.65	924.46	5307.92	1721.32	270.82	N/A	47057.16	0.750	0.767
H67 e	D.M	11178.07	258.61	1234.15	190.74	158.13	N/A	27773.23	0.469	0.859
H67 d	P.S	22192.34	825.76	13466.49	1169.55	62.56	N/A	46531.13	0.811	0.588
H67 c	D.M	3927.57	267.21	974.82	22.46	51.27	N/A	24269.11	0.216	0.749
H67 b	P.S	12097.54	312.60	2955.53	0.00*	0.00*	N/A	23607.67	0.651	0.787
H67 a	D.M	10001.72	390.13	1243.50	128.59	612.38	N/A	22542.67	0.549	0.808

Table 4.7 – Iron speciation data for BL 11 – BL 15. Data presented includes: Fe_{Py}, Fe_{Carb}, Fe_{Oxy}, Fe_{Mag}, Fe_{Hem}, Fe_{SS}, and Fe_T (measured in parts per million). * = Below method detection limit. The Fe_{HR}/Fe_T (IoA) and Fe_{Py}/Fe_{HR} (IoE) ratios are given also. Fe_{HR}/Fe_T ratios > 1 were not plotted. L.LST = laminated limestone, LST = limestone, P.S = paper shale, SHA = shale, D.M = dark marl, and L.M = light marl. See Chapter 2 for the revised lithostratigraphy; bed numbers/nomenclature after Lang (1924).

BL 16 = Serial Fe_{HR}/Fe_T ratios correlate well with relative changes in inferred oxygen conditions between adjacent lithologies (fig. 4.5; table 4.8). A number of the bioturbated limestone beds, including H84 (Fe_{HR}/Fe_T = 0.28) and H90 (Fe_{HR}/Fe_T = 0.302), plot below or near to the anoxic 0.38 threshold (fig. 4.5; table 4.8). Fe_{HR}/Fe_T ratios in the argillaceous interbeds, irrespective of lithology, plot within the anoxic field (fig. 4.5; table 4.8). Fe_{Py}/Fe_{HR} ratios, excluding oxic samples, have a limited range (0.889 – 0.95) and all plot above the 0.8 euxinic threshold (fig. 4.5; table 4.8).

BL 17 = Unlike in BL 16, Fe_{HR}/Fe_T ratios in limestones from BL 17 uniformly plot above the 0.38 anoxic threshold (Brick a = 0.405 and Brick c = 0.972) (fig. 4.5; table 4.8); both samples have low Fe_T (5738.63 and 4293.71 ppm respectively; table 4.8) that is below or close to the screening criterion established by Clarkson et al. (2014). Fe_{Py}/Fe_{HR} ratios plot above the 0.8 euxinic threshold irrespective of lithology (fig. 4.5; table 4.8).

BL 18 = Fe_{HR}/Fe_T ratios are generally lower in the bioturbated limestones (average = 0.463) than in the dark marl interbeds (average = 0.538) (fig. 4.5; table 4.8). Fe_{Py}/Fe_{HR} ratios plot above the 0.8 euxinic threshold irrespective of lithology (fig. 4.5; table 4.8).

BL 19 = Fe_{HR}/Fe_T ratios in BL 19 are highly variable and generally do not correlate with lithology (fig. 4.5; table 4.8). In the bioturbated limestones, Fe_{HR}/Fe_T ratios have a large range (0.132 – 0.915) and are scattered between the oxic and anoxic fields (fig. 4.5; table 4.8). Fe_T measurements are greater in the limestone samples that plot below the 0.38 anoxic threshold (average = 8800.15 ppm) than those that plot above it (average = 6843.07 ppm) (table 4.8). Fe_{HR}/Fe_T in argillaceous lithologies is similarly variable (fig. 4.5; table 4.8). Below the basal Lower Skulls limestone bed (inclusive), Fe_{Py}/Fe_{HR} has a limited range (0.894 – 0.967) and samples plot exclusively within the euxinic field (fig. 4.5; table 4.8). Fe_{Py}/Fe_{HR} ratios above this position, excluding oxic samples, have a significantly greater range (0.678 – 0.968) with measurements spanning the euxinic and ferruginous fields (fig. 4.5; table 4.8); these values also show no correlation with lithology (fig. 4.5).

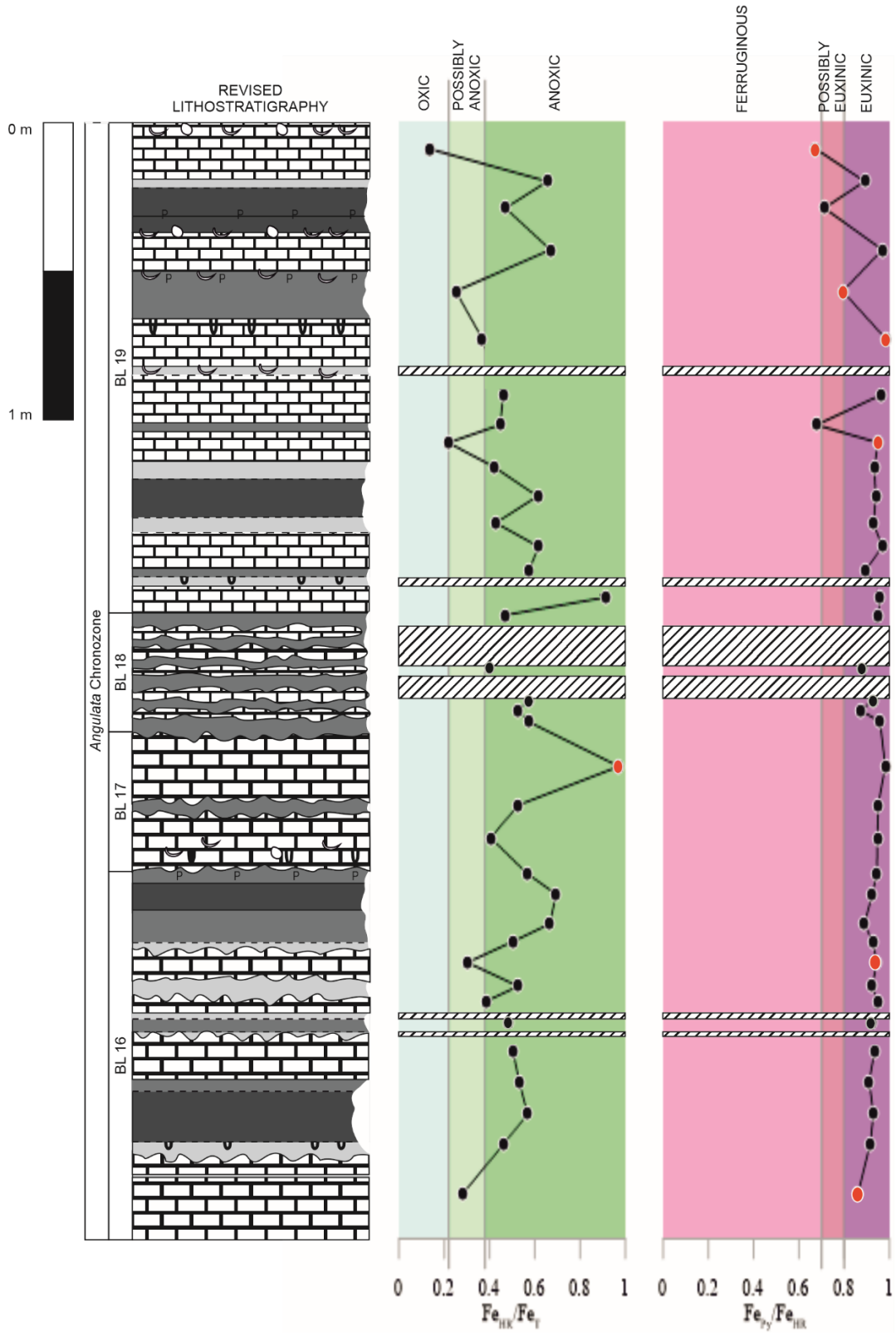

Figure 4.5 – Iron speciation plots (Fe_{HR}/Fe_T ratio and Fe_{Py}/Fe_{HR} ratio respectively) for the BLF (BL 16 – BL 19). Fe_{HR}/Fe_T ratios in (inferred) oxic lithologies that do not meet the $Fe_T > 0.5$ wt % screening criterion described by Clarkson et al. (2014) as well as non-applicable Fe_{Py}/Fe_{HR} ratios i.e. where $Fe_{HR}/Fe_T < 0.38$, are highlighted in red. For a detailed description of the revised lithostratigraphy see Chapter 2. The Fe_{HR}/Fe_T thresholds are taken at 0.22 and 0.38. The Fe_{Py}/Fe_{HR} thresholds are taken at 0.7 and 0.8.

BL 19										
Sample	**Lithology**	**Fe_{Py}**	**Fe_{Carb}**	**Fe_{Oxy}**	**Fe_{Mag}**	**Fe_{Hem}**	**Fe_{SS}**	**Fe_{T}**	**IoA**	**IoE**
Iron	LST	549.90	99.71	166.89	0.00*	0.00*	644.68	6180.35	0.132	0.673
Un.Cop b	L.M	13585.19	383.69	1269.68	0.00*	20.20	N/A	23285.32	0.655	0.890
Un.Cop a	SHA	9563.78	914.42	2527.38	356.38	64.73	N/A	28568.34	0.470	0.712
Un.Cop	LST	4486.92	57.29	59.90	0.00*	29.69	1659.59	6929.43	0.669	0.968
Thi.Tape a	D.M	4800.72	380.64	716.63	58.45	95.84	N/A	24134.09	0.251	0.793
Thi. Tape	LST	4073.04	66.77	0.00*	0.00*	0.00*	886.81	11246.94	0.368	0.984
Ab L. Sk c	L.M	N/A	N/A	N/A	N/A	N/A	N/A	N/A	N/A	N/A
Ab L. Sk b	LST	4094.43	103.71	68.30	0.00*	0.00*	761.51	9260.27	0.461	0.960
Ab L.Sk a	D.M	7897.66	510.77	2841.12	265.47	134.02	N/A	26115.18	0.446	0.678
L. Sk	LST	1856.53	78.77	0.00*	0.00*	18.47	769.47	8973.15	0.218	0.950
L. Vent c	L.M	7488.60	292.60	215.97	0.00*	29.52	1925.07	19244.64	0.417	0.933
L. Vent b	SHA	14040.49	473.07	356.48	0.00*	76.39	1085.37	24434.40	0.612	0.939
L. Vent a	L.M	7069.64	248.56	282.65	0.00*	0.00*	1330.82	17779.32	0.428	0.930
L. Vent	LST	3353.68	88.07	25.70	0.00*	0.00*	683.70	5619.92	0.617	0.967
Ab Soft b	D.M	10049.67	358.54	828.78	0.00*	0.00*	N/A	19600.04	0.573	0.894
Ab Soft a	L.M	N/A	N/A	N/A	N/A	N/A	N/A	N/A	N/A	N/A
Soft	LST	4876.74	157.47	57.53	0.00*	0.00*	981.48	5562.65	0.915	0.958

BL 18										
Sample	**Lithology**	**Fe_{Py}**	**Fe_{Carb}**	**Fe_{Oxy}**	**Fe_{Mag}**	**Fe_{Hem}**	**Fe_{SS}**	**Fe_{T}**	**IoA**	**IoE**
Brick n	D.M	9059.01	224.01	171.76	0.00*	76.30	1707.87	20219.72	0.471	0.950
Brick m	LST	N/A	N/A	N/A	N/A	N/A	N/A	N/A	N/A	N/A
Brick l	D.M	N/A	N/A	N/A	N/A	N/A	N/A	N/A	N/A	N/A
Brick k	LST	N/A	N/A	N/A	N/A	N/A	N/A	N/A	N/A	N/A
Brick j	D.M	N/A	N/A	N/A	N/A	N/A	N/A	N/A	N/A	N/A
Brick i	LST	9158.27	303.83	947.10	0.00*	0.00*	N/A	26066.85	0.399	0.880
Brick h	D.M	N/A	N/A	N/A	N/A	N/A	N/A	N/A	N/A	N/A
Brick g	LST	N/A	N/A	N/A	N/A	N/A	N/A	N/A	N/A	N/A
Brick f	D.M	9754.45	236.02	262.01	0.00*	273.20	1231.72	18465.16	0.570	0.927
Brick e	LST	2458.57	111.14	184.88	0.00*	67.20	N/A	5357.83	0.527	0.871
Brick d	D.M	12687.96	231.97	216.82	0.00*	97.65	1371.72	23060.81	0.574	0.959

BL 17										
Sample	**Lithology**	**Fe_{Py}**	**Fe_{Carb}**	**Fe_{Oxy}**	**Fe_{Mag}**	**Fe_{Hem}**	**Fe_{SS}**	**Fe_{T}**	**IoA**	**IoE**
Brick c	LST	4092.33	79.59	0.00*	0.00*	0.00*	464.14	4293.71	0.972	0.981
Brick b	D.M	9919.45	235.79	267.94	0.00*	16.43	1333.38	19822.94	0.527	0.950
Brick a	LST	2200.56	86.54	37.51	0.00*	0.00*	470.92	5738.63	0.405	0.947

BL 16										
Sample	**Lithology**	**Fe_{Py}**	**Fe_{Carb}**	**Fe_{Oxy}**	**Fe_{Mag}**	**Fe_{Hem}**	**Fe_{SS}**	**Fe_{T}**	**IoA**	**IoE**
H91 d	D.M	13459.99	291.28	453.88	0.00*	43.52	N/A	25234.56	0.565	0.945
H91 c	SHA	21262.53	783.98	841.52	0.00*	128.51	1331.68	33166.11	0.694	0.924
H91 b	D.M	15550.11	292.98	1628.32	0.00*	14.98	N/A	26265.44	0.666	0.889
H91 a	L.M	9073.84	372.61	259.87	0.00*	92.75	N/A	19547.50	0.501	0.926
H90	LST	2656.16	85.56	68.07	0.00*	0.00*	1527.71	9297.26	0.302	0.945
H89	L.M	11089.38	400.30	533.73	0.00*	0.00*	N/A	22830.79	0.527	0.922
H88	LST	3278.87	90.26	81.15	0.00*	0.00*	541.20	8938.58	0.386	0.950
H87 c	L.M	N/A	N/A	N/A	N/A	N/A	N/A	N/A	N/A	N/A
H87 b	D.M	11068.44	298.05	632.20	0.00*	0.00*	1474.12	24858.56	0.483	0.922
H87 a	L.M	N/A	N/A	N/A	N/A	N/A	N/A	N/A	N/A	N/A
H86	LST	2653.13	87.57	100.51	0.00*	0.00*	286.01	5639.93	0.504	0.934
H85 c	D.M	13375.54	295.49	888.81	0.00*	134.44	1068.10	27709.89	0.530	0.910
H85 b	SHA	13234.06	530.44	381.39	0.00*	92.41	1080.70	25066.02	0.568	0.929
H85 a	L.M	5719.51	94.54	362.89	0.00*	74.23	763.31	13481.77	0.464	0.915
H84	LST	1799.80	95.33	197.42	0.00*	0.00*	554.88	7473.79	0.280	0.860

Table 4.8 – Iron speciation data for BL 16 – BL 19. Data presented includes: Fe_{Py}, Fe_{Carb}, Fe_{Oxy}, Fe_{Mag}, Fe_{Hem}, Fe_{SS}, and Fe_{T} (measured in parts per million). * = Below method detection limit. The Fe_{HR}/Fe_{T} (IoA) and Fe_{Py}/Fe_{HR} (IoE) ratios are given also. L.LST = laminated limestone, LST = limestone, P.S = paper shale, SHA = shale, D.M = dark marl, and L.M = light marl. See Chapter 2 for the revised lithostratigraphy; bed numbers/nomenclature after Lang (1924).

BL 20 = Serial Fe_{HR}/Fe_T ratios correlate well with relative changes in inferred oxygen conditions between adjacent lithologies (fig. 4.6; table 4.9). Fe_{HR}/Fe_T in the topmost Upper Skulls limestone bed plots within the oxic field ($Fe_{HR}/Fe_T = 0.125$) whereas the argillaceous lithologies all plot above the anoxic 0.38 threshold (fig. 4.6; table 4.9). Fe_{Py}/Fe_{HR} in the argillaceous lithologies has a narrow range (0.776 – 0.863) that occurs close to or above the 0.8 euxinic threshold (fig. 4.6; table 4.9).

BL 21 = Serial Fe_{HR}/Fe_T ratios in the lower-middle part of the section (between Upper White a – Mongrel c) correlate well with relative changes in inferred oxygen conditions between adjacent lithologies (fig. 4.6; table 4.9); in the remainder of BL 21 there is no trend between Fe_{HR}/Fe_T and lithology (fig. 4.6; table 4.9). Two of the bioturbated limestone beds, Speckety and Mongrel, plot within the oxic field ($Fe_{HR}/Fe_T = 0.096$ and 0.254 respectively), whereas the remaining limestone samples occur above the 0.38 anoxic threshold (average $Fe_{HR}/Fe_T = 0.691$) (fig. 4.6; table 4.9). In the argillaceous sediments, lithology specific average Fe_{HR}/Fe_T ratios generally mirror relative inferred oxygen conditions (light marls = 0.499 < dark marls = 0.507 < paper shales = 0.719) despite the fact that Fe_{HR}/Fe_T ratios from each lithology show extensive range (fig. 4.6; table 4.9). Fe_{Py}/Fe_{HR} ratios do not correlate with lithology and are scattered between the euxinic and ferruginous fields with no clear pattern (fig. 4.6; table 4.9).

BL 22 = Whilst all samples in BL 22 plot above the anoxic 0.38 threshold, serial Fe_{HR}/Fe_T ratios correlate well with relative changes in inferred oxygen conditions between adjacent lithologies (fig. 4.7; table 4.10); the overall range of Fe_{HR}/Fe_T is small (0.591 – 0.69) (fig. 4.7; table 4.10). The Fe_{Py}/Fe_{HR} ratio also corresponds to lithological alternations but is inversely proportionate to Fe_{HR}/Fe_T (fig. 4.7; table 4.10). Fe_{Py}/Fe_{HR} in the paper shale lithology is consistently low (average = 0.522) and both samples plot within the ferruginous field (fig. 4.7; table 4.10); in contrast, both the shales (average = 0.797) and dark marls (average = 0.82) have much greater Fe_{Py}/Fe_{HR} values and all samples plot above the 0.7 threshold (fig. 4.7; table 4.10).

BL 23 = Both the Fe_{HR}/Fe_T and Fe_{Py}/Fe_{HR} ratios are greater in the bioturbated limestone beds (average = 0.654 and 0.869 respectively) than the paper shale interbed (0.615 and 0.724 respectively) (fig. 4.7; table 4.10).

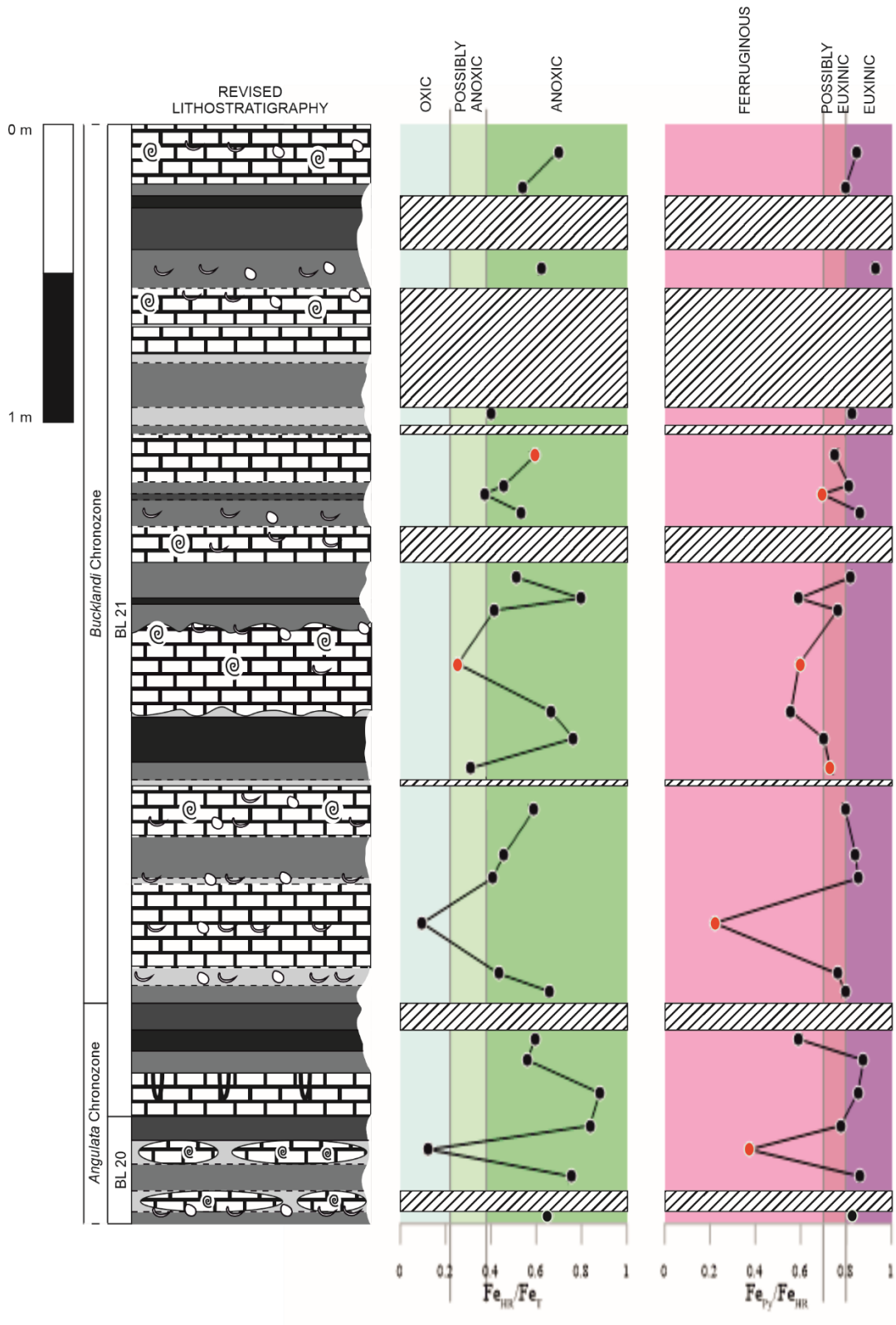

Figure 4.6 – Iron speciation plots (Fe_{HR}/Fe_T ratio and Fe_{Py}/Fe_{HR} ratio respectively) for the BLF (BL 20 – BL 21). Fe_{HR}/Fe_T ratios in (inferred) oxic lithologies that do not meet the Fe_T > 0.5 wt % screening criterion described by Clarkson et al. (2014) as well as non-applicable Fe_{Py}/Fe_{HR} ratios i.e. where Fe_{HR}/Fe_T < 0.38, are highlighted in red. For a detailed description of the revised lithostratigraphy see Chapter 2. The Fe_{HR}/Fe_T thresholds are taken at 0.22 and 0.38. The Fe_{Py}/Fe_{HR} thresholds are taken at 0.7 and 0.8.

BL 21										
Sample	**Lithology**	**Fe_{Py}**	**Fe_{Carb}**	**Fe_{Oxy}**	**Fe_{Mag}**	**Fe_{Hem}**	**Fe_{SS}**	**Fe_{T}**	**IoA**	**IoE**
3rd Quick	LST	4335.74	203.97	561.69	0.00*	0.00*	N/A	7312.83	0.698	0.850
Top Tape f	D.M	8727.56	400.82	1696.37	84.12	34.33	N/A	20207.98	0.542	0.798
Top Tape e	P.S	N/A	1148.73	4693.66	662.86	30.07	N/A	29246.60	N/A	N/A
Top Tape d	SHA	N/A	1421.10	2975.87	0.00*	0.00*	N/A	26988.55	N/A	N/A
Top Tape c	D.M	8639.63	301.24	299.21	0.00*	54.33	1394.10	14883.15	0.624	0.930
Top Tape b	LST	N/A	N/A	N/A	N/A	N/A	N/A	N/A	N/A	N/A
Top Tape a	L.M	N/A	N/A	N/A	N/A	N/A	N/A	N/A	N/A	N/A
Top Tape	LST	N/A	N/A	N/A	N/A	N/A	N/A	N/A	N/A	N/A
2nd Tape d	L.M	N/A	393.98	944.90	11.37	83.42	N/A	16925.20	N/A	N/A
2nd Tape c	D.M	N/A	902.44	3100.69	421.81	82.89	N/A	27160.55	N/A	N/A
2nd Tape b	L.M	5249.93	319.23	792.49	0.00*	0.00*	N/A	15969.31	0.398	0.825
2nd Tape a	D.M	N/A	1791.70	4712.17	655.78	156.89	N/A	30905.53	N/A	N/A
2nd Tape	LST	2171.13	150.91	568.82	0.00*	0.00*	N/A	4858.07	0.595	0.751
Top Cop c	D.M	6227.71	778.81	655.74	0.00*	0.00*	N/A	16678.76	0.459	0.813
Top Cop b	SHA	4041.86	332.02	1377.93	0.00*	66.00	994.62	15708.47	0.370	0.695
Top Cop a	D.M	6992.46	297.42	838.85	0.00*	0.00*	N/A	15314.09	0.531	0.860
Top Cop	LST	N/A	N/A	N/A	N/A	N/A	N/A	N/A	N/A	N/A
Mong c	D.M	6986.75	341.98	1202.01	0.00*	0.00*	N/A	16713.74	0.510	0.819
Mong b	P.S	15191.20	512.80	9379.55	485.92	41.29	N/A	32101.38	0.798	0.593
Mong a	D.M	3654.96	247.46	888.95	0.00*	0.00*	N/A	11551.88	0.415	0.763
Mong	LST	691.92	205.40	269.13	0.00*	0.00*	N/A	4595.68	0.254	0.593
2nd Mong d	L.M	9456.36	656.33	5564.72	1120.53	185.72	N/A	25579.56	0.664	0.557
2nd Mong c	P.S	15841.94	717.38	6010.40	15.58	0.00*	N/A	29526.98	0.765	0.701
2nd Mong b	D.M	3902.48	387.61	1047.28	0.00*	0.00*	N/A	17351.25	0.308	0.731
2nd Mong a	L.M	N/A	N/A	N/A	N/A	N/A	N/A	N/A	N/A	N/A
2nd Mong	LST	4565.40	226.85	859.26	13.70	63.52	N/A	9713.70	0.590	0.797
Speck b	D.M	6917.07	666.28	624.58	0.00*	0.00*	N/A	17892.81	0.459	0.843
Speck a	L.M	5320.86	483.73	429.52	0.00*	0.00*	N/A	15424.61	0.404	0.854
Speck	LST	139.19	192.63	303.45	0.00*	0.00*	N/A	6611.05	0.096	0.219
Up White e	L.M	7611.46	552.10	1343.22	321.44	160.11	N/A	22956.05	0.435	0.762
Up White d	D.M	11241.58	685.20	2182.73	0.00*	0.00*	N/A	21352.51	0.661	0.796
Up White c	SHA	N/A	682.96	2120.97	265.92	51.62	N/A	21390.57	N/A	N/A
Up White b	P.S	8659.48	765.39	5147.74	80.32	0.00*	N/A	24698.80	0.593	0.591
Up White a	D.M	8684.80	345.89	861.81	0.00*	0.00*	N/A	17661.28	0.560	0.878
Up White	LST	4309.67	244.93	509.24	0.00*	0.00*	N/A	5756.46	0.880	0.851

BL 20										
Sample	**Lithology**	**Fe_{Py}**	**Fe_{Carb}**	**Fe_{Oxy}**	**Fe_{Mag}**	**Fe_{Hem}**	**Fe_{SS}**	**Fe_{T}**	**IoA**	**IoE**
Up. Sk e	SHA	22286.31	731.30	4575.74	1012.22	115.37	N/A	34351.71	0.836	0.776
Up. Sk d	LST	333.60	265.63	294.66	0.00*	0.00*	N/A	7149.95	0.125	0.373
Up. Sk c	D.M	18570.14	644.58	2308.07	0.00*	0.00*	N/A	28570.06	0.753	0.863
Up. Sk b	LST	N/A	N/A	N/A	N/A	N/A	N/A	N/A	N/A	N/A
Up. Sk a	D.M	13726.25	613.07	2315.12	0.00*	0.00*	N/A	25533.15	0.652	0.824

Table 4.9 – Iron speciation data for BL 20 – BL 21. Data presented includes: Fe_{Py}, Fe_{Carb}, Fe_{Oxy}, Fe_{Mag}, Fe_{Hem}, Fe_{SS}, and Fe_{T} (measured in parts per million). * = Below method detection limit. The Fe_{HR}/Fe_{T} (IoA) and Fe_{Py}/Fe_{HR} (IoE) ratios are given also. L.LST = laminated limestone, LST = limestone, P.S = paper shale, SHA = shale, D.M = dark marl, and L.M = light marl. See Chapter 2 for the revised lithostratigraphy; bed numbers/nomenclature after Lang (1924).

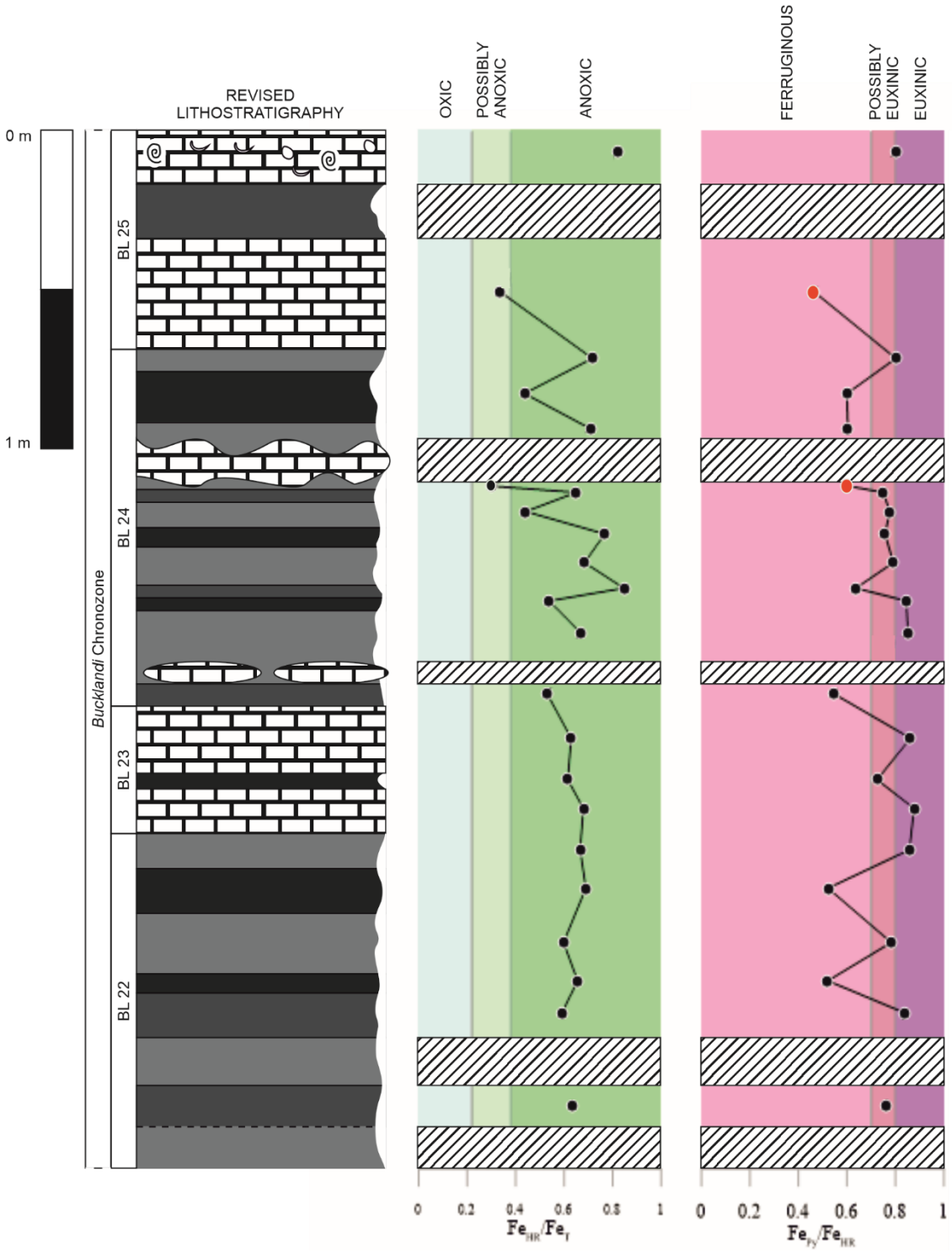

Figure 4.7 – Iron speciation plots (Fe_{HR}/Fe_T ratio and Fe_{Py}/Fe_{HR} ratio respectively) for the BLF (BL 22 – BL 25). Fe_{HR}/Fe_T ratios in (inferred) oxic lithologies that do not meet the Fe_T > 0.5 wt % screening criterion described by Clarkson et al. (2014) as well as non-applicable Fe_{Py}/Fe_{HR} ratios i.e. where Fe_{HR}/Fe_T < 0.38, are highlighted in red. For a detailed description of the revised lithostratigraphy see Chapter 2. The Fe_{HR}/Fe_T thresholds are taken at 0.22 and 0.38. The Fe_{Py}/Fe_{HR} thresholds are taken at 0.7 and 0.8.

BL 25										
Sample	**Lithology**	**Fe_{Py}**	**Fe_{Carb}**	**Fe_{Oxy}**	**Fe_{Mag}**	**Fe_{Hem}**	**Fe_{SS}**	**Fe_{T}**	**IoA**	**IoE**
Best	LST	3760.10	156.87	778.13	0.00*	0.00*	N/A	5707.90	0.823	0.801
Second a	SHA	N/A	N/A	N/A	N/A	N/A	N/A	N/A	N/A	N/A
Second	LST	946.01	172.25	928.10	0.00*	0.00*	N/A	6143.89	0.333	0.462

BL 24										
Sample	**Lithology**	**Fe_{Py}**	**Fe_{Carb}**	**Fe_{Oxy}**	**Fe_{Mag}**	**Fe_{Hem}**	**Fe_{SS}**	**Fe_{T}**	**IoA**	**IoE**
2nd Quic n	D.M	9571.39	537.69	1836.90	0.00*	0.00*	N/A	16674.16	0.716	0.801
2nd Quic m	P.S	3842.47	413.84	1769.01	86.13	293.58	N/A	14685.30	0.436	0.600
2nd Quic l	D.M	9036.78	585.53	4518.54	759.29	70.31	N/A	21164.65	0.707	0.604
2^{nd} Quic k	LST	N/A	N/A	N/A	N/A	N/A	N/A	N/A	N/A	N/A
2nd Quic j	D.M	2823.44	476.49	1312.01	36.49	22.87	N/A	15681.40	0.298	0.604
2nd Quic i	SHA	13374.53	1469.03	2940.24	42.01	29.83	N/A	27512.12	0.649	0.749
2nd Quic h	D.M	6452.83	491.98	1322.27	18.90	19.47	N/A	18816.06	0.441	0.777
2nd Quic g	P.S	16664.74	697.92	3725.62	853.22	84.48	N/A	28704.54	0.767	0.757
2nd Quic f	D.M	13625.26	796.82	2096.38	120.56	575.86	N/A	25168.78	0.684	0.791
2nd Quic e	SHA	7082.56	350.61	3651.92	42.57	0.00*	N/A	13151.90	0.846	0.636
2nd Quic d	P.S	7978.53	475.52	990.96	0.00*	0.00*	N/A	17539.71	0.538	0.845
2nd Quic c	D.M	11144.73	516.33	1292.69	103.27	41.16	N/A	19634.85	0.667	0.851
2nd Quic b	LST	N/A	N/A	N/A	N/A	N/A	N/A	N/A	N/A	N/A
2nd Quic a	SHA	5117.38	484.52	3677.00	66.95	60.13	N/A	17774.51	0.529	0.544

BL 23										
Sample	**Lithology**	**Fe_{Py}**	**Fe_{Carb}**	**Fe_{Oxy}**	**Fe_{Mag}**	**Fe_{Hem}**	**Fe_{SS}**	**Fe_{T}**	**IoA**	**IoE**
2nd Quic	LST	4467.07	432.99	282.91	0.00*	0.00*	N/A	8245.09	0.629	0.862
Gump a	P.S	11375.69	612.07	2923.05	663.32	143.27	N/A	25553.38	0.615	0.724
Gump	LST	4500.55	401.68	232.47	0.00*	0.00*	N/A	7561.89	0.679	0.876

BL 22										
Sample	**Lithology**	**Fe_{Py}**	**Fe_{Carb}**	**Fe_{Oxy}**	**Fe_{Mag}**	**Fe_{Hem}**	**Fe_{SS}**	**Fe_{T}**	**IoA**	**IoE**
3rd Quic h	D.M	10990.38	386.30	1294.63	52.04	102.78	N/A	19255.51	0.666	0.857
3rd Quic g	P.S	11246.81	283.73	7198.20	2666.52	164.60	N/A	31265.99	0.690	0.522
3rd Quic f	D.M	9246.18	543.11	1778.93	73.30	172.21	N/A	19786.91	0.597	0.783
3rd Quic e	P.S	7544.47	590.16	5357.91	912.34	82.84	N/A	22106.88	0.655	0.521
3rd Quic d	SHA	10317.75	565.13	1252.72	130.83	81.70	N/A	20906.63	0.591	0.836
3rd Quic c	D.M	N/A	N/A	N/A	N/A	N/A	N/A	N/A	N/A	N/A
3rd Quic b	SHA	10385.75	760.33	2547.17	0.00*	0.00*	N/A	21581.04	0.635	0.758
3rd Quic a	D.M	N/A	N/A	N/A	N/A	N/A	N/A	N/A	N/A	N/A

Table 4.10 – Iron speciation data for BL 22 – BL 25. Data presented includes: Fe_{Py}, Fe_{Carb}, Fe_{Oxy}, Fe_{Mag}, Fe_{Hem}, Fe_{SS}, and Fe_T (measured in parts per million). * = Below method detection limit. The Fe_{HR}/Fe_T (IoA) and Fe_{Py}/Fe_{HR} (IoE) ratios are given also. L.LST = laminated limestone, LST = limestone, P.S = paper shale, SHA = shale, D.M = dark marl, and L.M = light marl. See Chapter 2 for the revised lithostratigraphy; bed numbers/nomenclature after Lang (1924).

BL 24 = In the argillaceous lithologies of BL 24, Fe_{HR}/Fe_T ratios have a large range (0.298 – 0.846) with all but one sample (2nd Quick j) plotting above the anoxic 0.38 threshold (fig. 4.7; table 4.10). Serial Fe_{HR}/Fe_T measurements in the middle part of the section (2nd Quick e – 2nd Quick j) correlate well with relative changes in inferred oxygen conditions between adjacent lithologies, but samples in the upper and lower parts do not (fig. 4.7; table 4.10). Fe_{Py}/Fe_{HR} ratios have a moderate- range (0.544 – 0.851) and do not correspond to lithological alternations (fig. 4.7; table 4.10); the majority of samples plot below the 0.8 euxinic threshold (fig. 4.7; table 4.10).

BL 25 = Bioturbated limestones in the section are contrasting; Second Bed plots below the 0.38 anoxic threshold (Fe_{HR}/Fe_T = 0.333) whereas Best Bed plots within the anoxic (Fe_{HR}/Fe_T = 0.823) and euxinic (Fe_{Py}/Fe_{HR} = 0.801) fields (fig. 4.7; table 4.10).

BL 26 = An exclusively argillaceous lithology bundle, serial Fe_{HR}/Fe_T ratios in BL 26 correlate well with relative changes in inferred oxygen conditions between adjacent lithologies (fig. 4.8; table 4.11). Moreover, despite the fact that all samples plot above the anoxic 0.38 threshold, lithology specific average Fe_{HR}/Fe_T ratios mirror relative inferred bottom water oxygen conditions (light marls = 0.544 < dark marls = 0.58 < shales = 0.612 < paper shales = 0.713) (fig. 4.8; table 4.11). Fe_{Py}/Fe_{HR} has a large range (0.376 – 0.929) but does not correspond to lithological alternations (fig. 4.8; table 4.11); measurements are scattered between the euxinic and ferruginous fields (fig. 4.8; table 4.11).

BL 27 = Sampling of the section was limited, but measurements uniformly plot above the anoxic 0.38 threshold and below the 0.8 euxinic threshold irrespective of lithology (fig. 4.8; table 4.11).

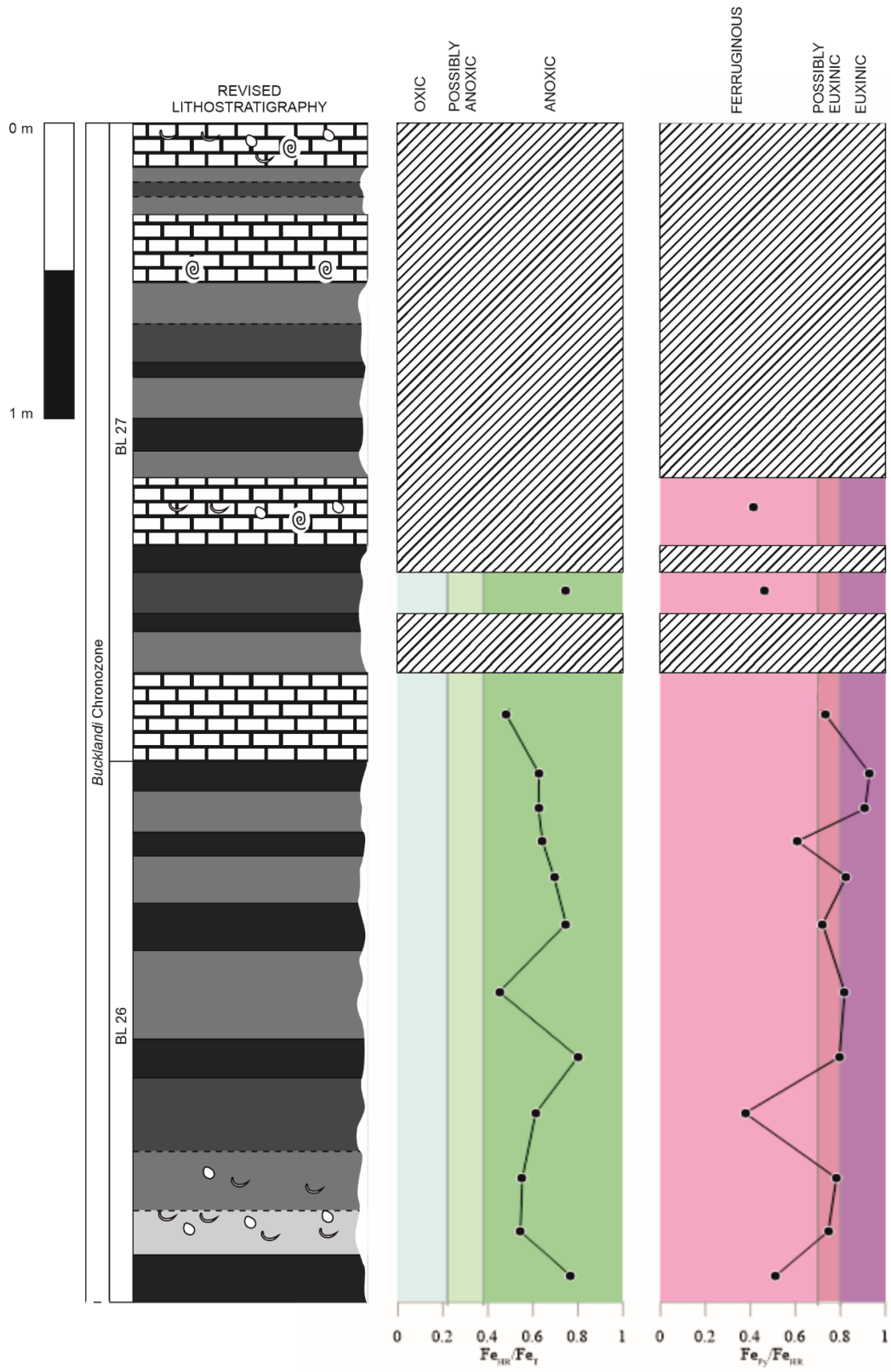

Figure 4.8 – Iron speciation plots (Fe_{HR}/Fe_T ratio and Fe_{Py}/Fe_{HR} ratio respectively) for the BLF (BL 26 – BL 27). Fe_{HR}/Fe_T ratios in (inferred) oxic lithologies that do not meet the Fe_T > 0.5 wt % screening criterion described by Clarkson et al. (2014) as well as non-applicable Fe_{Py}/Fe_{HR} ratios i.e. where Fe_{HR}/Fe_T < 0.38, are highlighted in red. For a detailed description of the revised lithostratigraphy see Chapter 2. The Fe_{HR}/Fe_T thresholds are taken at 0.22 and 0.38. The Fe_{Py}/Fe_{HR} thresholds are taken at 0.7 and 0.8.

BL 27										
Sample	**Lithology**	**Fe_{Py}**	**Fe_{Carb}**	**Fe_{Oxy}**	**Fe_{Mag}**	**Fe_{Hem}**	**Fe_{SS}**	**Fe_{T}**	**IoA**	**IoE**
Grey Led	LST	N/A	N/A	N/A	N/A	N/A	N/A	N/A	N/A	N/A
Glass c	D.M	N/A	N/A	N/A	N/A	N/A	N/A	N/A	N/A	N/A
Glass b	SHA	N/A	N/A	N/A	N/A	N/A	N/A	N/A	N/A	N/A
Glass a	D.M	N/A	N/A	N/A	N/A	N/A	N/A	N/A	N/A	N/A
Glass	LST	N/A	N/A	N/A	N/A	N/A	N/A	N/A	N/A	N/A
Top Qui f	D.M	N/A	N/A	N/A	N/A	N/A	N/A	N/A	N/A	N/A
Top Qui e	SHA	N/A	N/A	N/A	N/A	N/A	N/A	N/A	N/A	N/A
Top Qui d	P.S	N/A	N/A	N/A	N/A	N/A	N/A	N/A	N/A	N/A
Top Qui c	D.M	N/A	N/A	N/A	N/A	N/A	N/A	N/A	N/A	N/A
Top Qui b	P.S	N/A	N/A	N/A	N/A	N/A	N/A	N/A	N/A	N/A
Top Qui a	D.M	N/A	N/A	N/A	N/A	N/A	N/A	N/A	N/A	N/A
Top Qui	LST	5976.07	191.53	910.11	0.00*	7413.52	N/A	8837.68	//1.640//	0.412
Venty d	P.S	N/A	N/A	N/A	N/A	N/A	N/A	N/A	N/A	N/A
Venty c	SHA	7655.01	409.02	8397.06	155.99	0.00*	N/A	22279.38	0.746	0.461
Venty b	P.S	N/A	N/A	N/A	N/A	N/A	N/A	N/A	N/A	N/A
Venty a	D.M	N/A	N/A	N/A	N/A	N/A	N/A	N/A	N/A	N/A
Venty	LST	3028.05	209.55	901.12	0.00*	0.00*	N/A	8628.07	0.480	0.732
BL 26										
Sample	**Lithology**	**Fe_{Py}**	**Fe_{Carb}**	**Fe_{Oxy}**	**Fe_{Mag}**	**Fe_{Hem}**	**Fe_{SS}**	**Fe_{T}**	**IoA**	**IoE**
Best k	P.S	21706.44	471.60	1088.13	20.43	73.86	N/A	37328.27	0.626	0.929
Best j	D.M	16223.92	375.16	1068.18	155.67	22.78	N/A	28564.05	0.625	0.909
Best i	P.S	9573.68	524.67	5449.34	197.91	0.00*	N/A	24527.87	0.642	0.608
Best h	D.M	14709.17	390.12	2449.77	188.31	71.06	N/A	25704.79	0.693	0.826
Best g	P.S	8383.64	268.61	2985.93	0.00*	0.00*	N/A	15575.91	0.747	0.720
Best f	D.M	9565.97	393.64	1613.19	110.62	0.00*	N/A	26000.46	0.449	0.819
Best e	P.S	9528.29	444.42	1892.34	90.00	30.06	N/A	14986.93	0.800	0.795
Best d	SHA	5899.29	301.86	9136.61	347.88	10.71	N/A	25653.27	0.612	0.376
Best c	D.M	10086.21	352.37	2351.80	53.35	55.37	N/A	23352.92	0.552	0.782
Best b	L.M	8417.51	301.11	2445.32	124.91	0.00*	N/A	20746.60	0.544	0.746
Best a	P.S	4027.95	242.69	3578.45	0.00*	0.00*	N/A	10234.87	0.767	0.513

Table 4.11 – Iron speciation data for BL 26 – BL 27. Data presented includes: Fe_{Py}, Fe_{Carb}, Fe_{Oxy}, Fe_{Mag}, Fe_{Hem}, Fe_{SS}, and Fe_{T} (measured in parts per million). * = Below method detection limit. The Fe_{HR}/Fe_{T} (IoA) and Fe_{Py}/Fe_{HR} (IoE) ratios are given also. Fe_{HR}/Fe_{T} ratios > 1 were not plotted. L.LST = laminated limestone, LST = limestone, P.S = paper shale, SHA = shale, D.M = dark marl, and L.M = light marl. See Chapter 2 for the revised lithostratigraphy; bed numbers/nomenclature after Lang (1924).

4.4. Discussion

4.4.1. Lithological trends in iron speciation

When separated into different lithological classifications – excluding samples that do not meet the Fe_T > 0.5 wt. % screening criterion applied to oxic carbonate-rich sediments by Clarkson et al. (2014) – the range of Fe_{HR}/Fe_T ratios shows extensive overlap (fig. 4.9): limestones = 0.096 – 0.915, light marls = 0.345 – 0.664, dark marls = 0.216 – 0.81, shales = 0.07 – 0.846, paper shales = 0.319 – 0.811, and laminated limestones = 0.04 – 0.755 (fig. 4.9; see Results). Mean Fe_{HR}/Fe_T ratios in non-limestone lithologies correlate well with relative inferred oxygen conditions (light marls = 0.495 < dark marls = 0.519 < shales = 0.57 < paper shales = 0.629) but there is no such correlation in the carbonate-rich lithologies (limestones = 0.496 and laminated limestones = 0.352) (fig. 4.9; see Results).

Excluding oxic samples (Fe_{HR}/Fe_T < 0.38), Fe_{Py}/Fe_{HR} ratios show similar overlap between different lithologies (fig. 4.9): limestones = 0.392 – 0.981, light marls = 0.557 – 0.933, dark marls = 0.534 – 0.959, shales = 0.144 – 0.939, paper shales = 0.322 – 0.929, and laminated limestones = 0.635 – 0.949 (fig. 4.9; see Results). In the carbonate-poor sediments, mean Fe_{Py}/Fe_{HR} ratios show a weak inverse correlation with inferred oxygen conditions (light marls = 0.835, dark marls = 0.853, shales = 0.75, paper shales = 0.68) (fig. 4.9; see Results). There is no such correlation in the carbonate-rich lithologies (limestones = 0.875 and laminated limestones = 0.838) (fig. 4.9; see Results).

Based on a comparison of Fe_{HR}/Fe_T ratios and sedimentological/palaeontological evidence presented elsewhere in the thesis (see chapters 2, 3, and 7), it appears that iron palaeoredox proxies are a poor representation of bottom water redox conditions throughout most of the BLF, particularly when plotted against defined parameters to distinguish oxic and anoxic deposition. These data show that there are infrequent samples which reflect inferred oxygen conditions (both oxic and anoxic), but that the majority of sediments from (inferred) non-anoxic depositional environments plot above the anoxic 0.38 threshold (fig. 4.9) and are therefore difficult to corroborate. Nonetheless, whilst it is difficult to support the direct validity of most Fe_{HR}/Fe_T ratios, particularly in oxic carbonate-rich sediments, mean Fe_{HR}/Fe_T ratios in non-limestone lithologies correlate well with inferred oxygen conditions and serial Fe_{HR}/Fe_T ratios in parts of the succession correlate well with relative changes in inferred oxygen conditions between adjacent lithologies; these observations indicate the need to determine possible controls that may have contributed to the alteration and/or obscuration of original Fe_{HR}/Fe_T ratios at a bed-by-bed or lithology-specific scale.

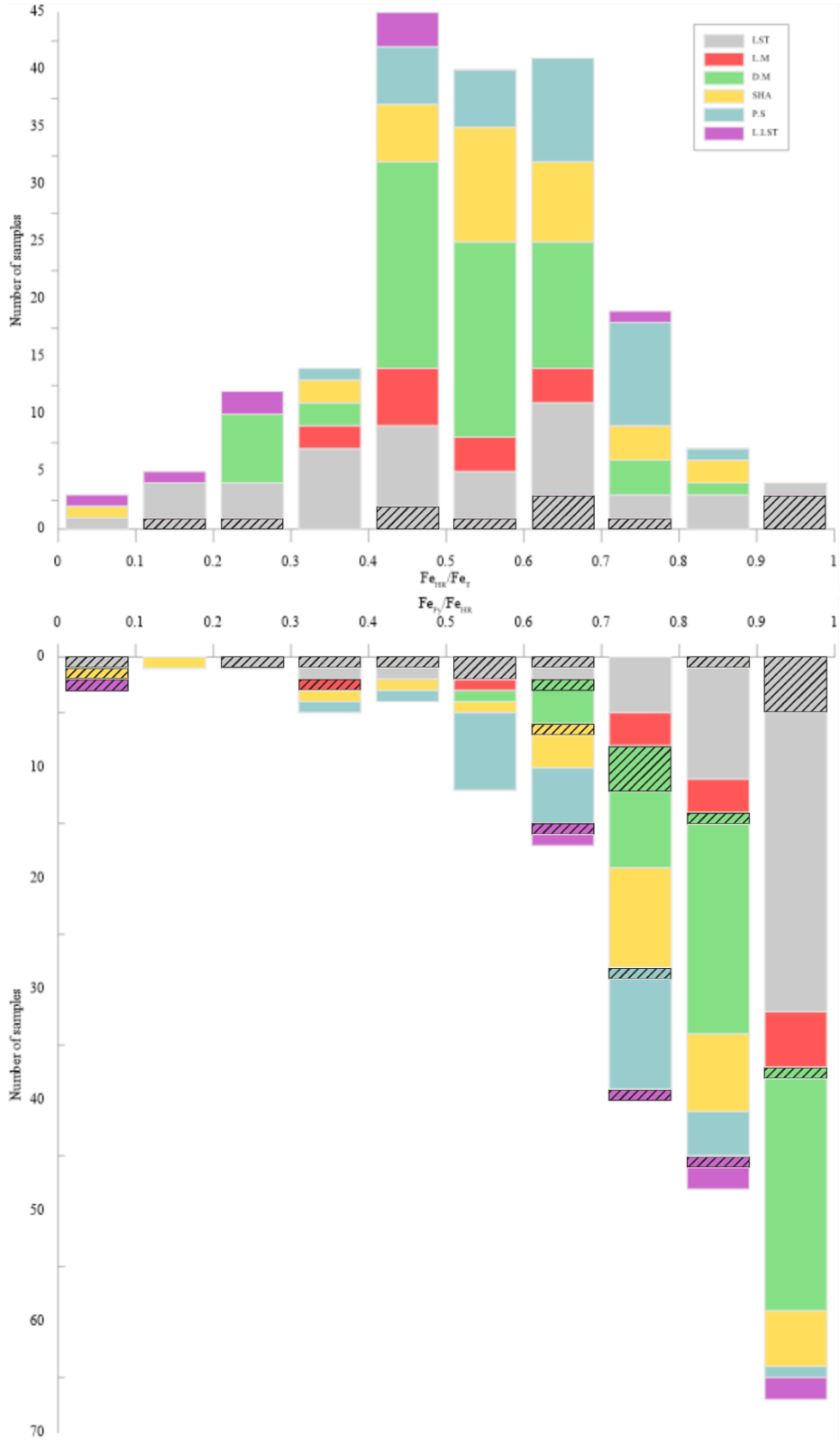

Figure 4.9 – The range of Fe_{HR}/Fe_T and Fe_{Py}/Fe_{HR} ratios measured within different lithologies from the BLF of Dorset and East Devon. Fe_{HR}/Fe_T ratios in (inferred) oxic carbonate-rich lithologies (bioturbated limestones) that do not meet the Fe_T > 0.5 wt. % screening criterion described by Clarkson et al. (2014) as well as non-applicable Fe_{Py}/Fe_{HR} ratios i.e. where Fe_{HR}/Fe_T < 0.38, are highlighted. LST = limestone, L.M = light marl, D.M = dark marl, SHA = shale, P.S = paper shale, and L.LST = laminated limestone.

4.4.2. Controls on the validity of iron palaeoredox proxies in the Blue Lias Formation of Dorset and East Devon

Whilst there is an opportunity to interpret Fe_{HR}/Fe_T and Fe_{Py}/Fe_{HR} ratios on a bed-by-bed basis using data presented in this thesis, it is important to also consider the validity of the method's application to the BLF and discuss the potential controls that may have influenced the results shown. Iron palaeoredox proxies, including the Fe_{HR}/Fe_T and Fe_{Py}/Fe_{HR} ratios, do not always exclusively represent depositional redox conditions but can be altered by a number of factors including: sedimentation rates, minor fluctuations in bottom water redox conditions, diagenetic iron mobilisation, etc (see reviews by Raiswell et al., 2018, Poulton, 2021). Some of these variables may be distinguished through the use of alternative geochemical proxies (e.g. Fe_T/Al ratios), but this was not within the scope of the project; instead, the use of iron palaeoredox proxies is contrasted with palaeoecological and sedimentological evidence (see chapters 2 and 3).

Secondary Fe_{HR} enrichment in oxic carbonate-rich sediments. The first major control concerns the validity of Fe_{HR}/Fe_T ratios in oxic carbonate-rich sediments (*sensu* Clarkson et al., 2014). Clarkson et al. (2014) recognised the potential for false anoxic Fe_{HR}/Fe_T ratios in oxic carbonate-rich lithologies as a result of increased sensitivity to secondary Fe_{HR} enrichment – i.e. not a product of water column anoxia – since the proportion of detrital sediment influx, and therefore the amount of Fe_{HR} and Fe_T, was low (Clarkson et al., 2014). The authors describe a number of potential secondary Fe_{HR} enrichment mechanisms such as the preferential incorporation of reactive iron during oxic carbonate precipitation and the mobilisation of dissolved iron during burial diagenesis (Clarkson et al., 2014). In the BLF, Bottrell and Raiswell (1989) account for varying degrees of pyrite formation and iron migration in adjacent (pre-diagenetic) carbonate-poor and carbonate-rich horizons. The authors infer that the extent of pyrite formation was a function of carbonate content which acted as a buffer to consume acidity, produced during bioturbational pyrite oxidation, and enable prolonged sulphide supersaturation in carbonate-rich sediments (Bottrell and Raiswell, 1989); porewaters within carbonate-poor sediments lacked this buffering capacity and quickly became acidic as well as iron-rich (Bottrell and Raiswell, 1989). Following prolonged BSR in the former, iron was able to diffuse from carbonate-poor to carbonate-rich horizons (Bottrell and Raiswell, 1989) and ultimately contribute to diagenetic Fe_{HR} enrichment. Given the size of the respective iron pools (carbonate-rich < carbonate-poor), diagenetic Fe_{HR} enrichment in carbonate-rich sediments would have had a

greater influence on Fe_{HR}/Fe_T than the loss of Fe_{HR} would have exerted on Fe_{HR}/Fe_T in the carbonate-poor sediment source. Prolonged BSR and pyrite formation in carbonate-rich horizons are expected to influence Fe_{Py}/Fe_{HR} ratios also.

In order to identify false anoxic Fe_{HR}/Fe_T ratios in oxic carbonate-rich sediments, Clarkson et al. (2014) established the use of screening criterion for the method's application; the authors determined that Fe_{HR}/Fe_T was only valid where $Fe_T > 0.5$ wt. % (Clarkson et al., 2014). Furthermore, it was suggested that an additional 0.5 wt. % TOC threshold be used to distinguish low Fe_T oxic from low Fe_T anoxic sediments (Clarkson et al., 2014); however, since this mainly concerns bioturbated and laminated limestones respectively in the BLF, the use of sedimentological and palaeontological evidence to separate the two was deemed sufficient.

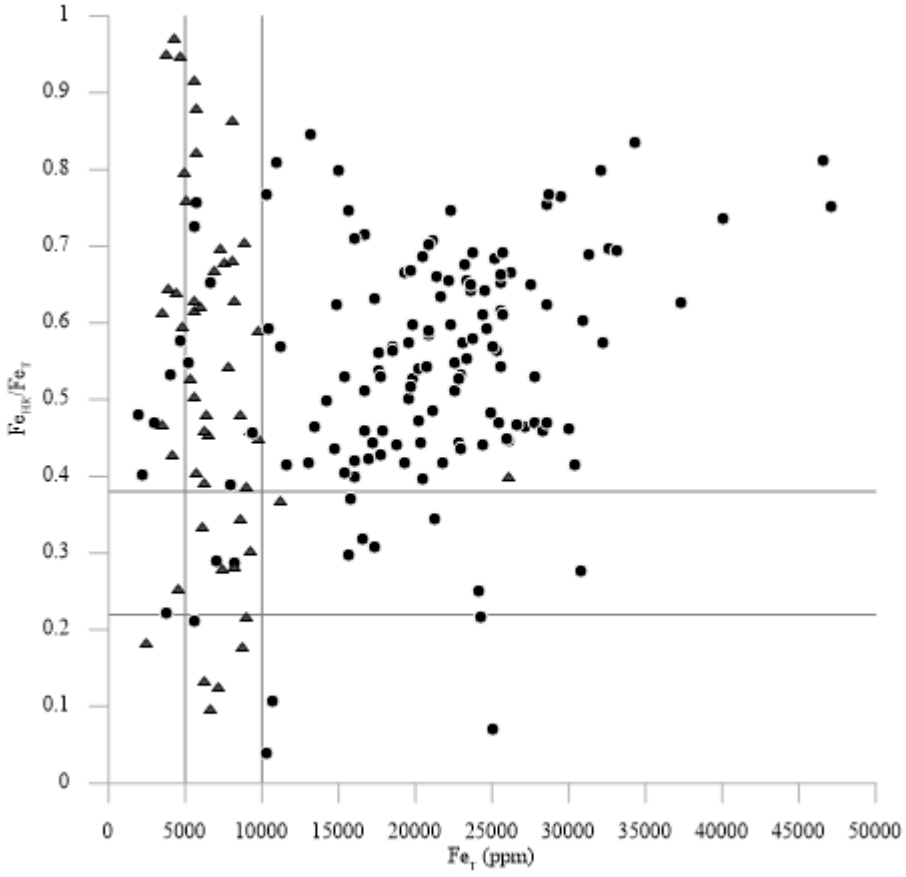

Figure 4.10 – Scatter plot illustrating the correlation between Fe_T and Fe_{HR}/Fe_T in inferred oxic carbonate-rich sediments i.e. bioturbated limestones (triangles) versus the remaining lithologies i.e. light marls, dark marls, shales, paper shales, and laminated limestones (circles). The Fe_{HR}/Fe_T thresholds were taken at 0.22 and 0.38. The $Fe_T > 0.5$ wt. % screening criterion of Clarkson et al. (2014) and a revised $Fe_T > 1$ wt. % criterion are also marked. Fe_T is given in parts per million.

In this study, a total of 22 samples did not meet the Fe_T > 0.5 wt. % screening criterion determined by Clarkson et al. (2014) (fig. 4.10; see Results). When separated into different lithological classifications, the number of samples was as follows: limestones (n = 15), light marls (n = 0), dark marls (n = 0), shales (n = 1), paper shales (n = 1), and laminated limestones (n = 5) (see Results). Within this subset, samples were removed where Fe_{HR}/Fe_T was greater than 1, less than the anoxic 0.38 threshold, or inferred to represent true anoxic deposition; 10 oxic carbonate-rich sediments that did not meet the screening criterion and evidenced false anoxic Fe_{HR}/Fe_T ratios remained. However, application of this screening criterion did not adequately isolate spurious data (fig. 4.10). A further 28 inferred oxic carbonate-rich sediment samples (i.e. bioturbated limestones) exceed the Fe_T > 0.5 wt. % screening criterion yet show false anoxic Fe_{HR}/Fe_T ratios (fig. 4.10); in order to separate these data, the parameter required revision to Fe_T > 1 wt. % (fig. 4.10). This creates further uncertainty regarding the validity of Fe_{HR}/Fe_T ratios from this setting since the revised Fe_T > 1 wt. % screening criterion, and occasionally the Fe_T > 0.5 wt. % criterion, does not reliably distinguish between oxic and false anoxic Fe_{HR}/Fe_T ratios (fig. 4.10).

Time-averaging. Poulton (2021) refers to the potential for inconsistencies to exist between palaeontological evidence – specifically the presence of a benthic fossil assemblage – and iron speciation data as a function of the sampling resolution. The example cited by Poulton (2021) was the euxinic origin given for the Alum Shale (late Cambrian) by Gill et al. (2011) and the conflicting presence of benthic biota in the same strata; Poulton (2021) describes how this paradox was resolved by Dahl et al. (2019) following the recognition of short-lived oxic intervals that enabled the sediment surface to be colonised by species tolerant of poorly hospitable conditions during predominantly euxinic deposition (see review by Poulton, 2021). According to Poulton (2021), this example indicates how some applications of iron speciation should be considered time-averaged representations of original redox conditions. Similarly, Raiswell et al. (2018) cited earlier work by Boyer et al. (2011) to demonstrate how analysis can blend short-lived fluctuations in depositional redox conditions and produce results that are inconsistent with palaeontological evidence (see review by Raiswell et al., 2018). Resolution of this control requires that the sediment package remains finely stratified in order to preserve small-scale fluctuations. Whilst opportunistic benthic colonisation in the paper shale lithology (e.g. Paul et al., 2008, Jordan, 2016; see Chapter 3) provides comparable palaeontological evidence for the existence of unresolved, short-lived oxic intervals within anoxic sediments, the majority of

lithologies from the BLF are bioturbated and/or homogenised which limits the potential for lower sampling resolutions to have produced time-averaged results.

There is also significant potential for bioturbation and sediment mixing throughout the BLF to have altered original Fe_{HR}/Fe_T ratios (*sensu* Poulton, 2021) since the succession is comprised of alternations that were deposited under fluctuating redox conditions. Variance is a product of physical mixing that either diluted anoxic Fe_{HR}/Fe_T ratios via the addition of oxic sediment or – evidently more manifest in the local strata – provided a source of Fe_{HR} enrichment to oxic Fe_{HR}/Fe_T ratios by blending earlier anoxic intervals into the sediment profile (see Poulton, 2021); the influence of Fe_{HR} enrichment in originally oxic sediments is more pronounced since the proportion of detrital sediment influx, and therefore the amount of Fe_{HR} and Fe_T, was low (Clarkson et al., 2014). Poulton (2021) suggests that this mixing control was influenced by the duration and frequency of oxic versus anoxic intervals, the extent and depth of bioturbation, as well as the degree of anoxic Fe_{HR} enrichment (Poulton, 2021). In the BLF, it is practical to assume that these factors are, at least in part, indicated by the types of sediments that have been emplaced and/or mixed together. Where burrows are clearly defined, appropriate sampling practice can help to mitigate any physical alteration; this is not possible where the sediment has been homogenised and therefore, in this instance, analyses record a time-averaged representation of redox conditions.

The distribution of ichnotaxa and the extent of bioturbation have been examined in the BLF by a number of previous authors (Moghadam and Paul, 2000, Martin, 2004, Twitchett and Barras, 2004, Barras and Twitchett, 2007, Jordan, 2016). Nonetheless, calculating the influence of bioturbation on a bed-by-bed basis was not possible since theoretical unmixing of bioturbated or homogenised sediments would require quantification of the factors that Poulton (2021) indicates would have influenced the mixing control (see above) as well as baseline Fe_{HR}/Fe_T measurements that represent depositional redox conditions for component sediments. It is not appropriate to average the influence of bioturbation for different sections and therefore qualify its potential impact since sediment mixing was not a uniform process; distribution of ichnotaxa was controlled by palaeoenvironmental and palaeoecological factors including the degree of bottom water oxygenation (e.g. Moghadam and Paul, 2000, Martin, 2004, Barras and Twitchett, 2007). Instead, it is only practical to identify parts of the BLF where iron speciation may be spurious and requires

the use of supporting palaeoecological and sedimentological evidence to examine the validity of subsequent interpretations.

Several authors have demonstrated that the extent of bioturbation correlates with lithology as a function of original oxygen conditions (e.g. Moghadam and Paul, 2000, Martin, 2004). In the *Angulata*/*Bucklandi* and *Bucklandi* chronozones respectively, Moghadam and Paul (2000) and Martin (2004) observed that laminated shales were without ichnotaxa and were not subject to bioturbation at the time of deposition. The relative diversity, intensity, depth, and diameter of burrows increases progressively in the marl and limestone lithologies (Moghadam and Paul, 2000, Martin, 2004). Jordan (2016) stated that light marls were the most regularly bioturbated argillaceous lithology whereas laminated shales were the least. The influence of bioturbation was compounded in oxic carbonate-rich lithologies since those sediments that were especially sensitive to Fe_{HR} enrichment were the most conducive to occupation. Barras and Twitchett (2007) also showed that ichnofauna exhibit a progressive or staged recovery throughout the succession owing to anoxia at the T-J boundary interval. This trend manifests as an increase in diversity, relative abundance, diameter, and depth of burrows with vertical progression (Barras and Twitchett, 2007). In the authors account, the lower part of the *Tilmanni* Chronozone lacked ichnotaxa and the degree of bioturbation was limited, whereas the upper part had few trace fossils and bioturbation was locally extensive (Barras and Twitchett, 2007). Barras and Twitchett (2007) recognised thoroughly disturbed bedding or complete homogenisation in limestones above the *Tilmanni* Chronozone. Maximum ichnotaxonomic diversity was recorded in the *Angulata* Chronozone coincident with significantly deeper and larger burrows that subsequently reach their maximum by the *Bucklandi* Chronozone (Barras and Twitchett, 2007). Jordan (2016) also recognised that the proportion of horizons with evidence for bioturbation and/or burrowing increases with vertical progression.

The majority of samples in this study were taken from sediments that show some degree of bioturbation and/or contain macrobenthos (see Chapter 3); despite evidence for an oxic depositional environment, most have Fe_{HR}/Fe_T ratios that plot above the anoxic 0.38 threshold (fig. 4.9). Notwithstanding the potential for false anoxic Fe_{HR}/Fe_T ratios to develop in oxic carbonate-rich lithologies as a result of secondary Fe_{HR} enrichment (e.g. Bottrell and Raiswell, 1989, Clarkson et al., 2014), this supporting sedimentological and palaeontological evidence indicates that bioturbational mixing – which provided an additional source of Fe_{HR} through the blending of earlier anoxic intervals into the sediment

profile (*sensu* Poulton, 2021) – was a controlling factor locally and resulted in the obscuration of original oxic signals. It is beyond the scope of this study to ascertain the ratio of oxic to anoxic deposition within individual beds, but it is important to note that the relative proportion of anoxic sediment required to produce false anoxic Fe_{HR}/Fe_T ratios in time-averaged sections would be relatively small. Nonetheless, since Fe_{HR} enrichment via bioturbation and sediment mixing would have required a source of anoxic sediments, it is necessary that inferred oxic lithologies were not constantly oxygenated.

Where inferred oxic deposition was subject to unresolved anoxic intervals, it is possible that the local faunal assemblage may have been relatively poorly developed. Moreover, the palaeocommunity may reflect specific or short-lived depositional redox conditions within a longer, time-averaged period that was affected by variable or contrasting states of bottom water oxygenation. This palaeoecological causality could account for specific beds being dominated by individual species or low diversity assemblages of calcitic and bimineralic epifaunal bivalve genera (e.g. *Liostrea* and *Plagiostoma*) that colonised opportunistically (see Chapter 3).

The examples discussed above do not constitute an exhaustive list of the lithological/sedimentological controls with the potential to alter Fe_{HR}/Fe_T ratios in the BLF; increased weathering, rapid sedimentation, physical reworking, and the conversion of Fe_{HR} to unreactive Fe_{SS} are important additional considerations (see review by Raiswell et al., 2018).

4.5. Conclusions

This study attempts to utilise an iron palaeoredox proxy approach, specifically the application of Fe_{HR}/Fe_T and Fe_{Py}/Fe_{HR} ratios, to characterise changes in bottom water redox conditions within an alternating limestone-marl succession. This is the first time that a multi-disciplinary, iron palaeoredox and palaeontological (Chapter 3) investigation has been conducted at this scale in the BLF of Dorset and East Devon in order to examine whether the method can be used to determine the influence of bottom water redox conditions on the abundance and diversity of the skeletal palaeocommunity, as well as the impact of the Missing Molluscs effect.

The results show that samples infrequently reflect inferred oxygen conditions based on palaeontological and sedimentological evidence presented elsewhere within the thesis (see

chapters 2 and 3). The ranges of lithology specific Fe_{HR}/Fe_T ratios overlap extensively and the majority of samples from (inferred) non-anoxic depositional environments plot spuriously above the anoxic 0.38 threshold. Nonetheless, mean Fe_{HR}/Fe_T ratios in non-limestone lithologies correlate well with relative inferred oxygen conditions. Excluding oxic samples ($Fe_{HR}/Fe_T < 0.38$), Fe_{Py}/Fe_{HR} ratios show similar overlap between different lithologies; mean Fe_{Py}/Fe_{HR} ratios in the argillaceous lithologies share an inverse correlation with inferred oxygen conditions. These data indicate that original Fe_{HR}/Fe_T ratios have been significantly altered, likely as a result of multiple established controls, and are therefore a poor representation of bottom water redox conditions throughout most of the BLF, particularly when plotted against defined parameters to distinguish oxic and anoxic deposition.

A major influence on the validity of these data concerns the use of Fe_{HR}/Fe_T ratios in oxic carbonate-rich sediments (*sensu* Clarkson et al., 2014). The precise cause of secondary Fe_{HR} enrichment remains unclear, but multiple factors including diagenetic iron mobilisation have been described elsewhere (e.g. Bottrell and Raiswell, 1989, Clarkson et al., 2014). The recommended $Fe_T > 0.5$ wt. % screening criterion of Clarkson et al. (2014) was applied to the bioturbated limestone samples but did not adequately isolate spurious data; the parameter was subsequently revised to $Fe_T > 1$ wt. %. As a result of these observations, oxic carbonate-rich sediments in the BLF appear inappropriate for the evaluation of water column redox conditions.

In the remaining lithologies, time-averaging – either as a function of sampling resolution or bioturbation and sediment mixing (*sensu* Poulton, 2021) – impacts the validity of Fe_{HR}/Fe_T ratios. Palaeontological evidence from inferred anoxic sediments suggests opportunistic colonisation of the seafloor occurred during short-lived oxic intervals, yet this was not resolved in the iron speciation data owing to a lower sampling resolution. Whilst this issue is addressed by increasing the sampling frequency in finely laminated lithologies, the majority of sediments in the BLF are bioturbated and/or homogenised which limits the preservation potential of small-scale fluctuations. Bioturbation furthers obscuration of original Fe_{HR}/Fe_T ratios since the succession is comprised of alternations that were deposited under regularly fluctuating redox conditions. Variance is a product of physical mixing that either diluted anoxic Fe_{HR}/Fe_T ratios via the addition of oxic sediment or – evidently more manifest in the local strata – provided a source of Fe_{HR} enrichment to oxic Fe_{HR}/Fe_T ratios by blending earlier anoxic intervals into the sediment profile (see Poulton,

2021). Calculating the influence of bioturbation and sediment mixing on a bed-by-bed basis was not possible and the extent of these processes was not uniform throughout the succession. Nonetheless, since Fe_{HR} enrichment required a source of anoxic sediment, these data suggest that inferred oxic lithologies were not constantly oxygenated. As a result, interpretations based on the correlation of iron speciation data and fossil content are uncertain since the palaeocommunity may reflect specific or short-lived depositional conditions within a longer, time-averaged period that was affected by variable or contrasting states of bottom water oxygenation.

It is evident that further work is needed before palaeoenvironmental redox conditions can be reliably reconstructed on a bed-by-bed basis in the BLF of Dorset and East Devon – and perhaps in similar alternating limestone-marl successions – using iron speciation; future investigations would also benefit from the use of alternative geochemical analyses including sulphur isotopes, framboid measurements, and Fe_T/Al ratios.

CHAPTER 5

5. PYRITE PRESERVATION OF AMMONOIDS IN THE CHARMOUTH MUDSTONE FORMATION (EARLY JURASSIC) OF DORSET, UK

5.1. Introduction

Pyrite replacement of molluscan fossils is common in Jurassic marine mudrocks (e.g. Hudson and Palframan, 1968, Hudson, 1982, Fisher, 1986, Andrew et al., 2010, Paul, 2011, Paul, 2015) and its nature was described in detail by Hudson (1982) and Hudson and Palframan (1968). In many settings, the formation of well-preserved pyritic internal moulds occurs in non-anoxic conditions where pyritisation is confined to reducing micro-environments such as the internal voids of shells (e.g. Hudson and Palframan, 1968, Hudson, 1982, Fisher, 1986). In euxinic marine conditions, pyritisation is concentrated within the sediment and rarely associated with fossil preservation (Hudson, 1982).

Pyritised molluscs are common in the CMF of Dorset (e.g. Lang and Spath, 1926, Andrew et al., 2010, Lord et al., 2010, Andrew et al., 2011) and similar fossils are known from these strata outside of the study area (e.g. Paul, 2011, Paul and Simms, 2012, Paul, 2015). The current assemblage of pyritised ammonoid moulds allows for assessment of the timing and nature of pyrite replacement following deposition and during early burial. Based on these observations, the potential for pyritisation to preserve a true, characteristic assemblage of vulnerable shelly groups is considered (see Chapter 7). Preservation of an originally aragonitic fauna in the marine fossil record implies survival through the TAZ and replacement prior to aragonite dissolution. In similar Jurassic offshore carbonate ramp settings, selective dissolution of vulnerable groups is responsible for an approximate 80 % loss in original, ecological diversity (Wright et al., 2003).

5.2. Material and methods

The majority of specimens (SPM_01-23 and SPM_M_01-27) were collected *ex situ* by CR and M. Harrison at Charmouth, Dorset and likely originated from BVM 15 or BVM 17 in the upper part of the BVM (see Chapter 2 for locality details); a single specimen of *Caenisites* (SPM_M_28) was collected *ex situ* by CR from the SWB at Lyme Regis, Dorset (see Chapter 2 for locality details). BVM 15 and BVM 17 are made up of conchoidal dark marls (see Chapter 2); they contain abundant pyritic ammonoid moulds as well as epifaunal and infaunal bivalve genera throughout the section (e.g. Lang and Spath, 1926, Lord et al., 2010). The conchoidal sediment texture indicates that original planar laminae were rarely preserved owing to bioturbation and sediment mixing (see Chapter 2).

Sampled specimens include the well-preserved, pyritic internal moulds of 23 *Promicroceras* ammonoids (SPM_01-23; table 5.1) and a further 28 individuals (SPM_M_01-28; tables 5.2 and 5.3) of various genera where evidence of poor and/or irregular replacement was observed. Pyrite replacement was described from the outer surface of ammonoid moulds and, for most specimens, from a transverse cross-section through the ventral axis. This process required the fossils to be held horizontally in a greased plastic tube and set in an Araldite 2-part epoxy resin. Once dry, resin blocks were progressively polished in order to achieve a reflective finish before being made into polished thin sections. Photomicrographs were taken using a Leica DM750P microscope with reflected light module attachment and Leica LAS (Leica Application Suite) Imaging Software; the variable use of plane-polarised, cross-polarised, and reflected light microscopy is indicated in individual figures.

5.3. Results

The nature of pyritisation in ammonoid moulds from Jurassic marine mudrocks was described and categorised by Hudson (1982); it concerns two key factors – the texture of pyrite crystals and the setting for pyrite replacement (termed 'habits' herein).

5.3.1. Pyrite textures

Two of Hudson's (1982) four primary replacement textures are present in the current ammonoid assemblage – aggregated and equant pyrite (fig. 5.1).

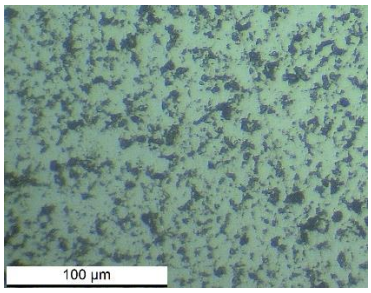

Aggregated pyrite (SPM_02): The most common replacement texture in pyritic fossils is aggregated pyrite (Hudson, 1982). In the current assemblage it occurs within the body chamber and phragmocone of ammonoid moulds. Small (5 – 20 µm), aggregated crystals are possibly a product of the coalescence of an earlier equant texture.

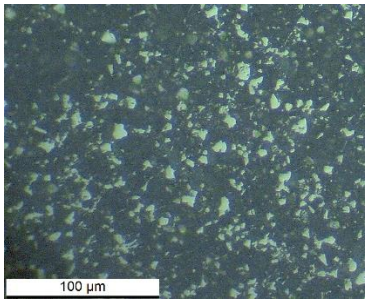

Equant pyrite (SPM_01): There are two types of equant pyrite and each coincides with a specific part of the ammonoid shell. The first is typically found within external sediments near to the aperture and is comprised of small (5 – 20 µm), uniform crystals with an approximately cubic habit. Hudson (1982) suggests that this texture generally corresponds to euhedral pyrite *sensu* Raiswell and Plant (1980).

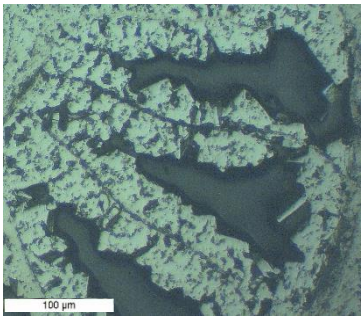

Equant pyrite (SPM_02): The second type of equant pyrite is associated with chamber-linings and is exclusive to the phragmocone. It is made up of large (30 – 100 µm) cubic crystals that rarely coalesce; this texture coats the inner shell and septal walls as well as the upper surface of pyritic internal precipitate (see Section 5.3.2). Both equant textures form without restriction by other minerals (Hudson, 1982).

Figure 5.1 – Pyrite replacement textures observed in pyritic ammonoid moulds from the BVM of Charmouth, Dorset. Specimens were photographed under reflected light microscopy. Scale = 100 µm.

5.3.2. Pyrite habits

In order to assess the timing and nature of pyrite replacement, it is important to separate primary and secondary pyrite habits (or 'settings' *sensu* Hudson, 1982). Primary habits are responsible for good preservation of the original shell microstructure and/or mould (fig. 5.2) whereas secondary habits result in poor preservation of the mould that does not reflect the original internal structure and/or obscures surface details (fig. 5.3).

Primary replacement habits observed in the SWB and BVM of Dorset were pyritic internal precipitate (or 'internal sediments' *sensu* Hudson, 1982), chamber-lining pyrite, and direct shell replacement; these classifications were first described in detail by Hudson (1982). Secondary replacement habits include over-pyrite and clustered concretionary pyrite; incipient over-pyritisation was described by Hudson (1982).

Figure 5.2 (From left to right: SPM_21, SPM_22, and SPM_23) – Examples of pyritic *Promicroceras* that show good replacement of the mould. Note that some specimens are preserved with a thin lens of hardened marl covering the outer surface. Scale = 10 mm.

Figure 5.3 – A cluster of poorly-preserved pyritic ammonoid moulds exposed *in situ* on the foreshore ledges beneath mean low water at Charmouth. Note that pyrite replacement has not produced a good mould of the shell's original structure and surface details are obscured. Scale = 40 mm.

a. Primary replacement

Pyritic internal precipitate. In the 'open' body chamber of ammonoid moulds, the nature of pyritic internal precipitate is variable (fig. 5.4). At the anterior of the body chamber, near to the aperture, pyrite is generally associated with clays, carbonate mud, or bioclasts that have washed into the ammonoid shell (fig. 5.4). The relative proportion of pyritic internal precipitate is low (approximately < 25 %) but increases adapically and at the shell margins (approximately 25 – 95 %) such that the amount of pyrite is inversely proportional to the amount of external sediment (fig. 5.4). At the anterior of the body chamber and in association with external sediment, pyrite precipitate is comprised of small (10 – 20 μm), equant crystals that are gradually replaced by similarly sized (10 – 20 μm), aggregated crystals in the posterior portion and at the shell margins.

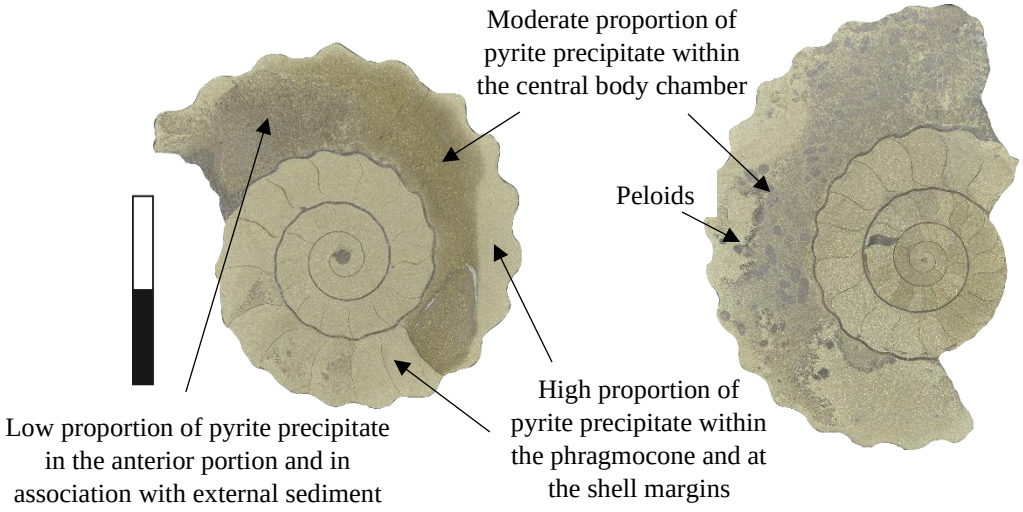

Figure 5.4 – Left (SPM_01): variable proportions of pyritic internal precipitate within the body chamber of a *Promicroceras*. Note that the relative proportions of pyrite precipitate are marked by different colour tones. Right (SPM_05): *Promicroceras* with peloids in the body chamber replaced by sparry calcite cement. There is extensive damage at the posterior of the body chamber. Scale = 10 mm.

Within the 'closed' gas chambers of the phragmocone, pyritic internal precipitate is bright and highly reflective (fig. 5.5). There is little variation in the overall proportion of pyrite (approximately 80 – 95 %) owing to the lack of external sediment (fig. 5.5); its texture is dominated by small (10 – 20 μm), aggregated crystals. Incomplete pyritisation of the phragmocone is common (fig. 5.6) and individual gas chambers are often incompletely filled by geopetal pyrite (fig. 5.5).

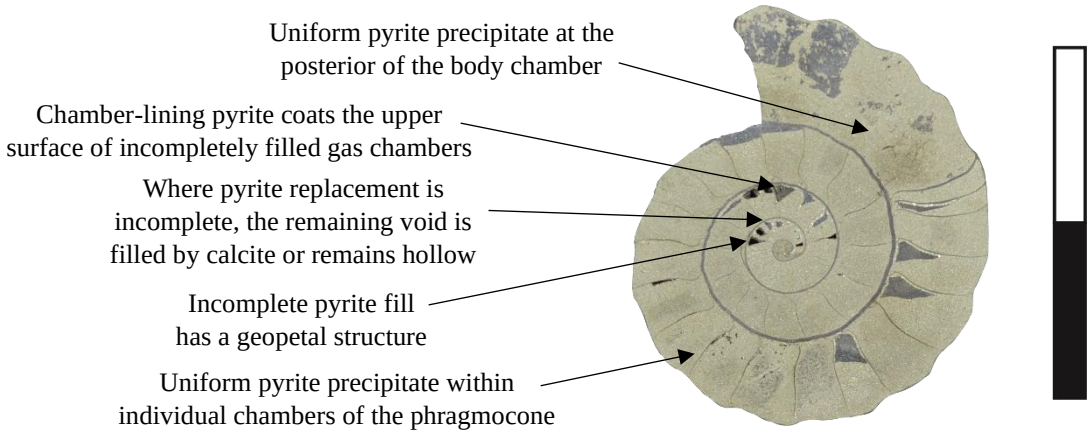

Figure 5.5 (SPM_06) – A pyritic mould of *Promicroceras* with many incompletely filled gas chambers that show geopetal structures. Chamber-lining pyrite overlays pyritic internal precipitate and coats the inner shell and septal walls within incompletely filled gas chambers. The remaining void is filled with calcite cement in the outer whorl and remains hollow in the nucleus. Scale = 10 mm.

Chamber-lining pyrite. Chamber-lining pyrite is made up of coarse (30 – 100 μm) cubic crystals (fig. 5.1) and occurs within the phragmocone, either in the nucleus or in the outer whorl near to the final septa (figs. 5.5 and 5.6). It typically coats the inner shell surface and septal walls of individual gas chambers to produce a mould of the phragmocone's original, internal chambered structure (fig. 5.5); this observation is consistent with studies of similar pyritic fossils (e.g. Hudson and Palframan, 1968, Hudson, 1982). Chamber-lining pyrite overlays the upper surface of pyritic internal precipitate within incompletely filled gas chambers (*sensu* Hudson, 1982); the remaining void was then filled by calcite spar (figs. 5.5 and 5.6) or left empty (fig. 5.5). It rarely coats sections of the internal shell surface without the septal walls (fig. 5.6).

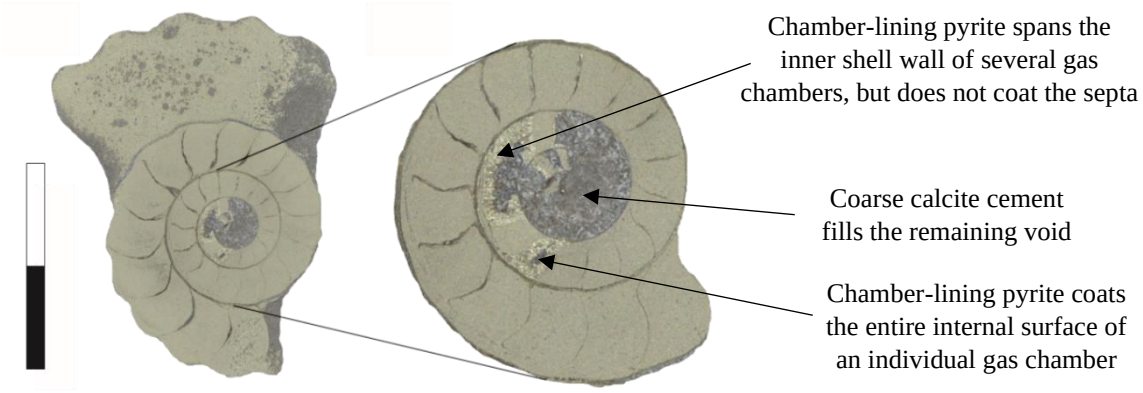

Figure 5.6 (SPM_14) – Variable replacement by chamber-lining pyrite in a single *Promicroceras*. Note that pyritisation is incomplete and calcite spar fills the remainder of the phragmocone. Replacement in this habit is non-uniform and indicates complex relative timings. Scale = 10 mm.

Direct shell replacement. Pyritisation of original shell microstructure is inferred from the preservation of fine (< 100 μm), impersistent linear features that occur centrally within the shell wall between whorls (fig. 5.7). In this assemblage, direct shell replacement appears to be more simplistic than its counterpart in pyritic moulds described by Hudson (1982). Owing to the nature and position of these features, it is assumed that they represent replacement of the organic-rich, nacreous layer of shell microstructure between the inner and outer prismatic layers (e.g. Kulicki, 1996). The remaining shell wall was subsequently replaced by calcite spar (fig. 5.7). In addition, portions of the siphuncular wall are preserved by a pyritic veneer and pyrite precipitate within the previous void (fig. 5.7). The siphuncle is present in gas chambers that have been replaced by pyritic internal precipitate as well as calcite cement (fig. 5.7); in both cases the siphuncle is fragmented (fig. 5.7).

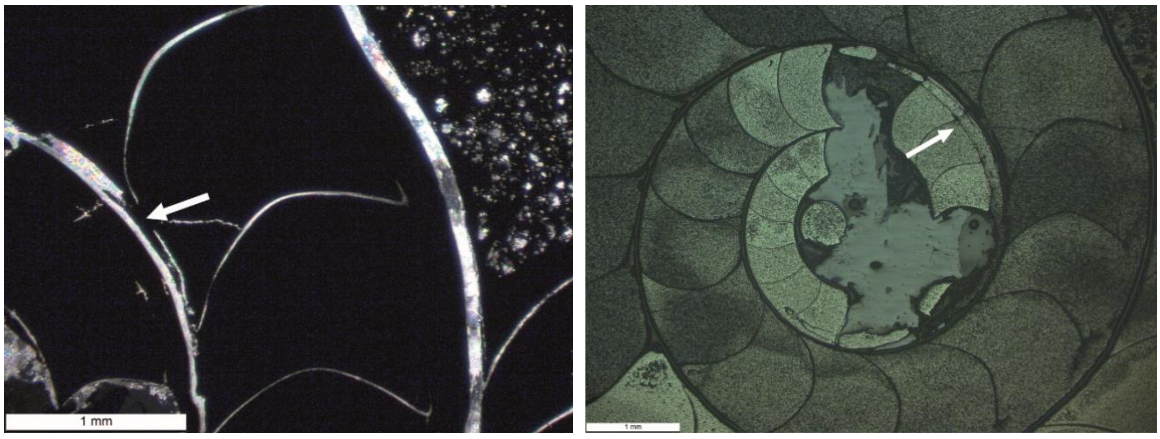

Figure 5.7 (SPM_03) – Left: direct pyrite replacement of shell microstructure (highlighted by arrow) in a *Promicroceras* viewed under cross-polarised light. Right: replacement of the siphuncle by pyrite viewed under reflected light microscopy. Scale = 1 mm.

b. Secondary replacement

Over-pyrite. The most common form of secondary replacement in the current assemblage, over-pyrite is an irregular surface texture comprised of random pyritic clusters nucleated at fractures in the ammonoid shell (*sensu* Hudson, 1982) (fig. 5.8). This habit does not produce an internal mould (Hudson, 1982). Over-pyrite is the result of progressive outward growth that can be traced to compaction of specific parts of the ammonoid shell – the body chamber, phragmocone, or its entirety; each part facilitates a unique replacement pathway.

i. Over-pyritisation facilitated by compaction of the body chamber. The most common condition for development of over-pyrite is compaction of the body chamber. This pathway is typically in conjunction with a pyritic phragmocone that was well preserved by primary replacement habits (fig. 5.8). Compaction of the body chamber is particularly common in the eoderoceratids (e.g. *Eoderoceras* and *Crucilobiceras*) which possess a thin-walled shell. In this pathway, the extent of over-pyritisation is variable and corresponds to a series of growth phases:

> **Phase 1:** Limited over-pyrite growth at the body chamber where fracturing of the shell wall acts as the nucleus for over-pyritisation.
> **Phase 2:** Continued outward growth of over-pyrite resulting in the total obscuration of the body chamber.
> **Phase 3:** Expansion of over-pyrite beyond the body chamber to less than one complete whorl of the phragmocone.
> **Phase 4:** Continued growth of over-pyrite resulting in moderate to major obscuration of the phragmocone.
> **Phase 5:** Entire obscuration of the ammonoid shell by over-pyrite.

Phase 1: Limited over-pyrite growth is concentrated at fractures in the body chamber (fig. 5.8); the extent of over-pyritisation is a function of the degree of compaction. Primary replacement habits are generally associated with good mouldic preservation of the phragmocone and remaining body chamber (fig. 5.8).

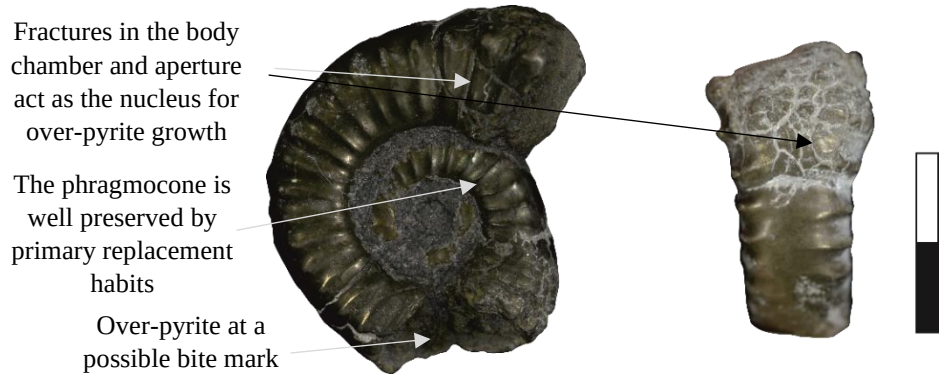

Figure 5.8 (SPM_M_10) – Phase 1 over-pyrite growth in the body chamber of a *Promicroceras*; over-pyrite nucleates at compactional fractures in the body chamber and at the aperture. Scale = 10 mm.

Phase 2: Over-pyrite growth obscures the entire external surface of the body chamber (fig. 5.9) as a result of continued discharge from existing fractures or preferentially following its total compaction. In cross-section, some shell fragments appear to retain their original aragonitic biomineralogy (fig. 5.9).

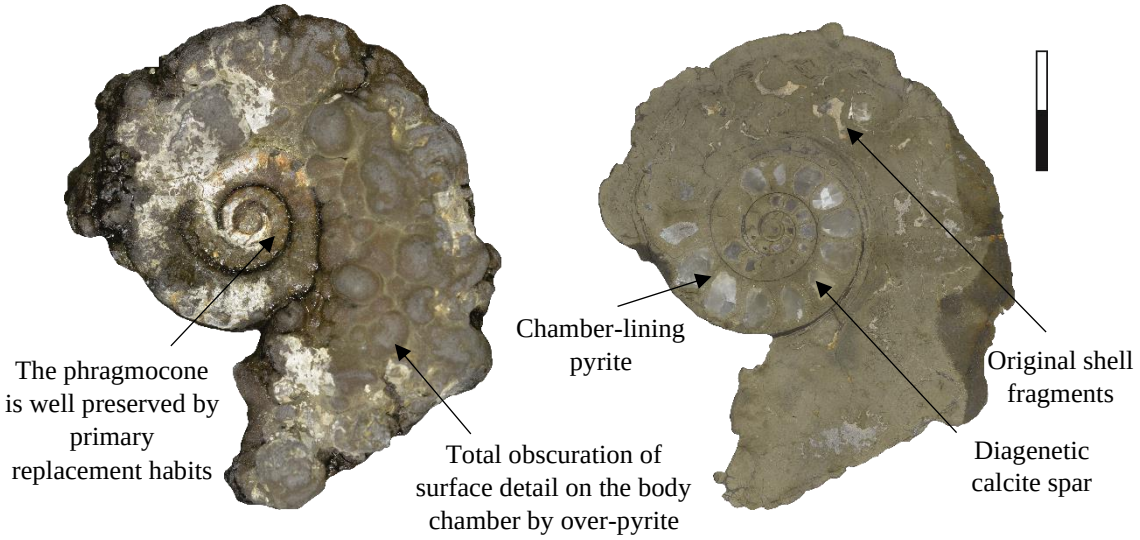

Figure 5.9 (SPM_M_06) – Phase 2 over-pyrite in an *Eoderoceras* has resulted in obscuration of the body chamber. White patches across the surface are evidence of pyrite degradation. Scale = 20 mm.

Phase 3: Over-pyrite growth is no longer localised to the body chamber and expands outward to the outer surface of the phragmocone (fig. 5.10). This is a superficial process and does not require compaction of the phragmocone which typically remains intact following prior primary replacement (fig. 5.10). In this phase, over-pyritisation is limited to the area immediately adjacent to the final septum or in recesses upon the shell structure e.g. covering the umbilicus (fig. 5.10).

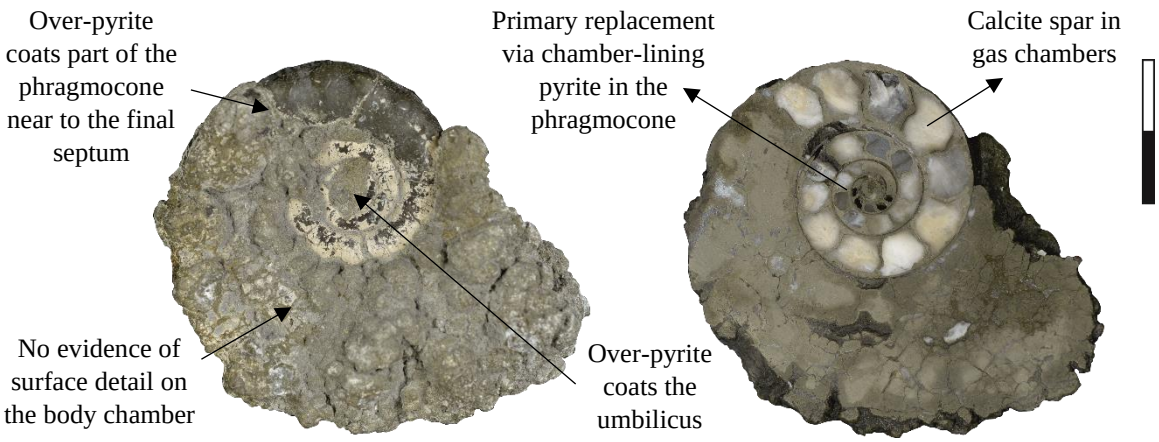

Figure 5.10 (SPM_M_05) – Phase 3 over-pyrite shows total obscuration of the body chamber (as in Phase 2) and additional growth at the final septum coating part of the first whorl of the phragmocone. Note the presence of over-pyrite in the recesses between the whorls and at the umbilicus. Scale = 20 mm.

Phase 4: Over-pyrite covers the majority of the phragmocone (fig. 5.11), but there is often a disparity in the volume of pyrite between the two faces. Phases 3 and 4 are poorly constrained and reflect the approximate extent to which over-pyrite has obscured the phragmocone. Phase 4 is generally taken to represent near-total obscuration that does not include the nucleus (fig. 5.11).

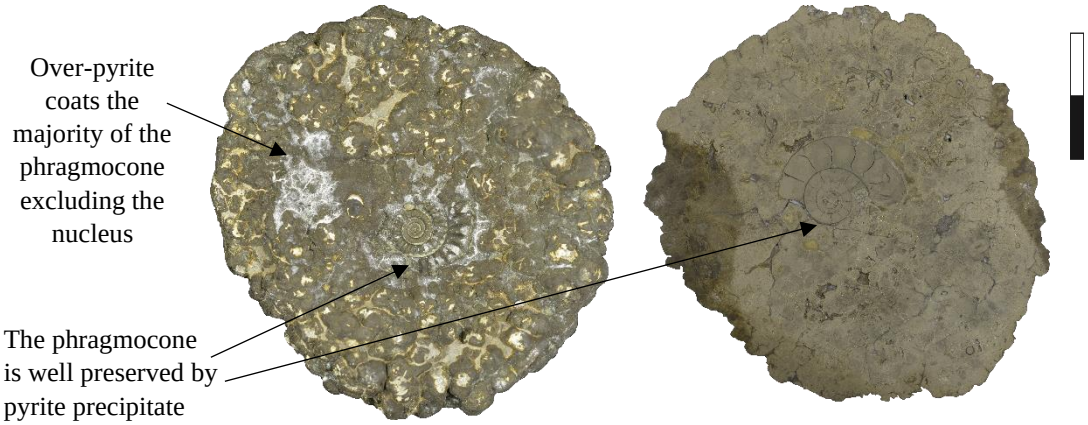

Figure 5.11 (SPM_M_09) – Phase 4 over-pyrite growth coats the majority of the phragmocone in a *Crucilobiceras?* mould; the nucleus is relatively well preserved by pyrite precipitate. Scale = 20 mm.

Phase 5: Total obscuration of the ammonoid mould indicates completion of phased over-pyrite growth facilitated by compaction of the body chamber (fig. 5.12). Despite the external morphology of the shell being difficult to recognise, the internal structure of the phragmocone remains relatively well preserved (fig. 5.12). Dissolution of the septa is common (fig. 5.12) although the cause remains uncertain.

Figure 5.12 (SPM_M_04) – Complete over-pyritisation of an unknown ammonoid genus. The shell's surface is entirely obscured by over-pyrite, but the phragmocone remains relatively intact in cross-section. The phragmocone lacks definition of the internal chambered structure and septal walls. Scale = 10 mm.

ii. Over-pyritisation facilitated by compaction of the phragmocone. In pyritic moulds of *Caenisites* from the SWB, over-pyritisation follows compaction of the phragmocone and not the body chamber; over-pyrite completely obscures the inner whorls (fig. 5.13). Whilst the body chamber is generally well preserved by primary replacement habits, there is often minor superficial over-pyrite across the venter following outward growth from the phragmocone (fig. 5.13).

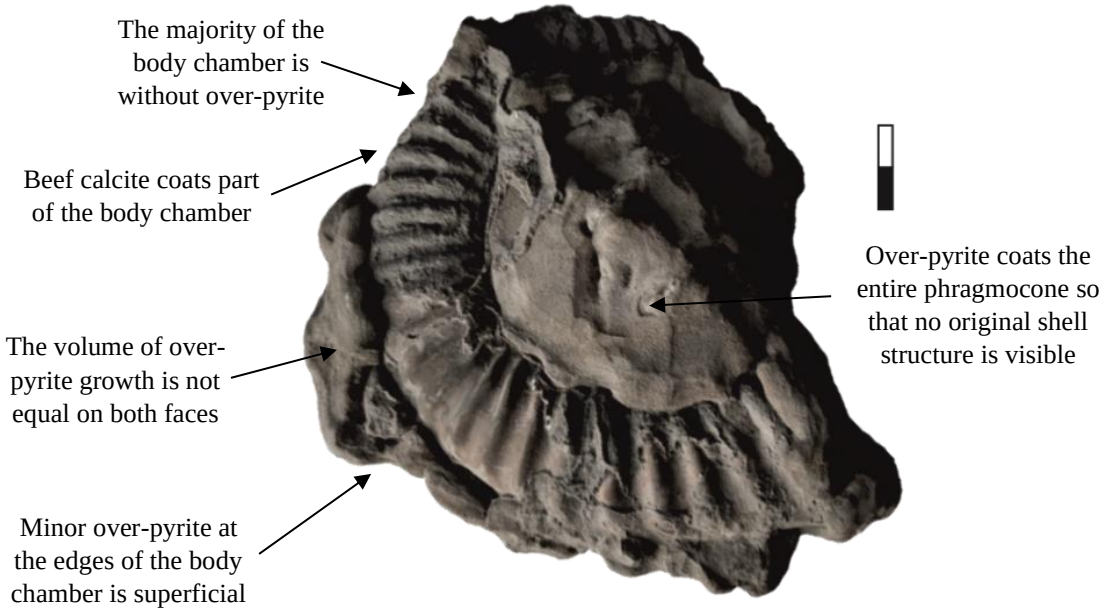

Figure 5.13 (SPM_M_28) – Over-pyritisation of a *Caenisites* facilitated by compaction of the phragmocone. The inner whorls are entirely obscured by over-pyrite that has subsequently expanded outward on to the venter of the body chamber. Scale = 20 mm.

iii. Over-pyritisation facilitated by total compaction of the shell. Entire obscuration by over-pyrite is not exclusive to the final phase of the replacement pathway facilitated by

compaction of the body chamber (fig. 5.12) but can instead follow total compaction of the ammonoid shell (fig. 5.14). External surface features are unrecognisable following the growth of over-pyrite clusters (fig. 5.14). In cross-section, the internal chambered structure of the phragmocone is not recognisable (fig. 5.14).

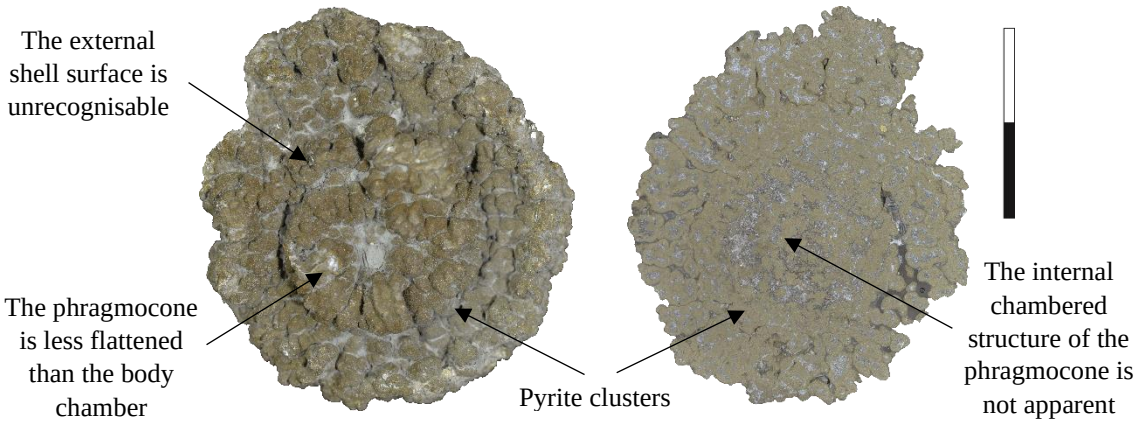

Figure 5.14 (SPM_M_03) – Complete obscuration of an unknown ammonoid genus by over-pyrite. The cross-section shows coarse, calcitic cementation of original shell fragments enveloped by thick (approximately 2 mm) pyritic lenses. The internal chambered structure of the phragmocone is unrecognisable. Scale = 20 mm.

Although the original internal chambered structure of the ammonoid is broken and unrecognisable, survival of aragonitic shell fragments is common in association with this replacement habit (fig. 5.15). Surviving shell aragonite has been altered and is preserved as a white/brown, crystalline material enveloped by pyrite clusters (fig. 5.15).

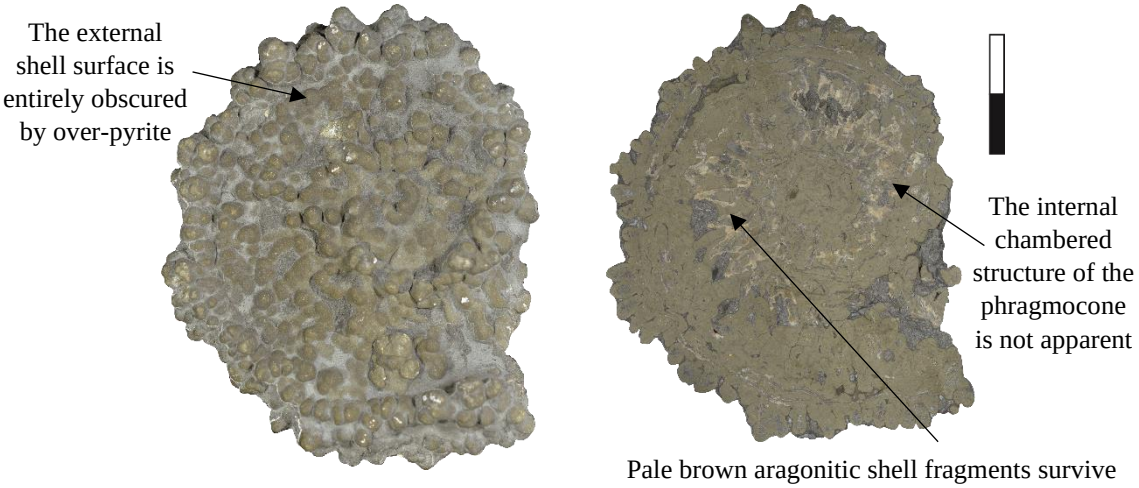

Figure 5.15 (SPM_M_01) – Complete obscuration of an unknown ammonoid genus by over-pyrite. Pale brown aragonitic shell fragments do not preserve the internal chambered structure of the phragmocone. Scale = 20 mm.

Clustered concretionary pyrite. In several instances, irregular pyrite concretions envelop clusters of pyritic ammonoid moulds (fig. 5.16); the complete association is referred to herein as clustered concretionary pyrite. Additional types of inorganic pyritic concretion, similar to features described by Hudson (1982), are present in the CMF but not considered in this study. Concretions are not a product of atypically high concentrations of pyrite within the host sediment and lack an interstitial argillaceous component (fig. 5.16).

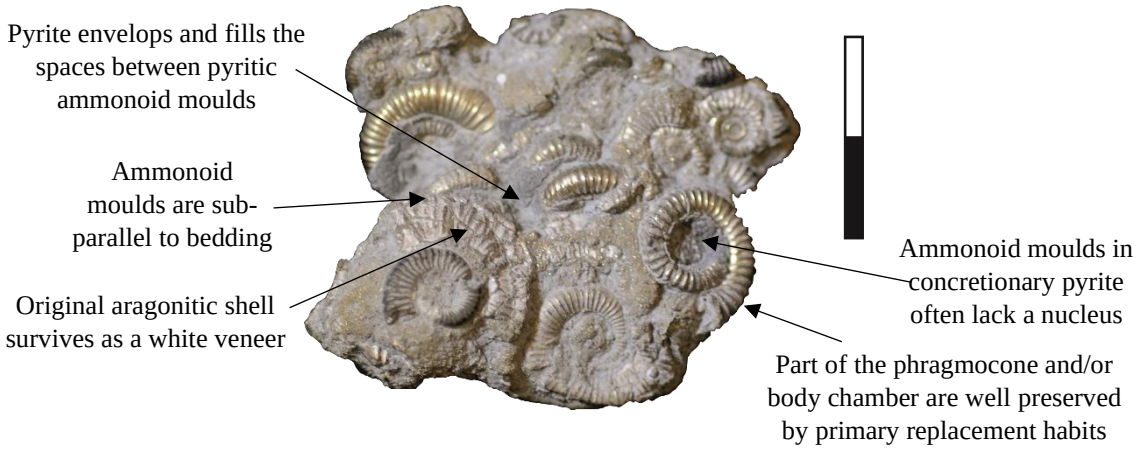

Figure 5.16 (SPM_M_27) – Clustered concretionary pyrite containing multiple *Crucilobiceras*. Part of the phragmocone is preserved by primary habits, but the nucleus is often missing. Scale = 20 mm.

Fragments of clustered concretionary pyrite contain numerous pyritic ammonoid moulds that are generally arranged sub-parallel to original bedding (fig. 5.16). Primary habits replace a variable amount of the phragmocone – as well as the body chamber – although the nucleus is often missing (fig. 5.16). Whilst ammonoid moulds are typically well preserved, breakage of the phragmocone and/or body chamber is not uncommon and can manifest as disarticulation of individual gas chambers (figs. 5.16 and 5.17); separation is at the septal walls and results in marginal displacement between each chamber (fig. 5.17).

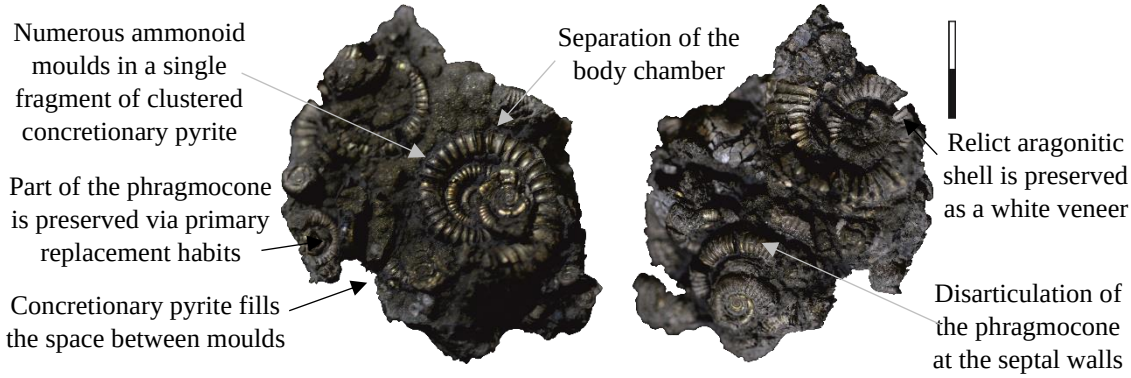

Figure 5.17 (SPM_M_26) – Pyritic *Crucilobiceras* within clustered concretionary pyrite. Ammonoid moulds are preserved by pyrite precipitate and disarticulated at the septal walls. Scale = 10 mm.

5.3.3. Non-pyritic preservation associated with pyritic ammonoid moulds

Calcite cementation. A final stage of calcite cementation is observed in the current assemblage of pyritic ammonoid moulds (fig. 5.18; tables 5.1 and 5.2); there are a number of different replacement contexts and multiple can occur within a single specimen (fig. 5.18). Coarse (100 μm – 1 mm), undulous calcite spar fills the remaining void within incompletely filled gas chambers, often where the internal surfaces were coated by chamber-lining pyrite prior to cementation (fig. 5.18). Calcite cement also fills irregular portions of the phragmocone without replicating the internal chambered structure of the nucleus (fig. 5.18); in this instance, septal dissolution occurred prior to calcite precipitation. In the majority of specimens, calcite cement replaces the shell wall between whorls but does not preserve original shell microstructure (fig. 5.18). There is no evidence of calcite cement replacing the outer shell wall which indicates that the external surface of the mould was in contact with the surrounding sediment. Cementation textures are consistent with those described by Curtis et al. (2000) in calcitic moulds from the CMF and generally correspond to late diagenetic cements (*sensu* Curtis et al., 2000).

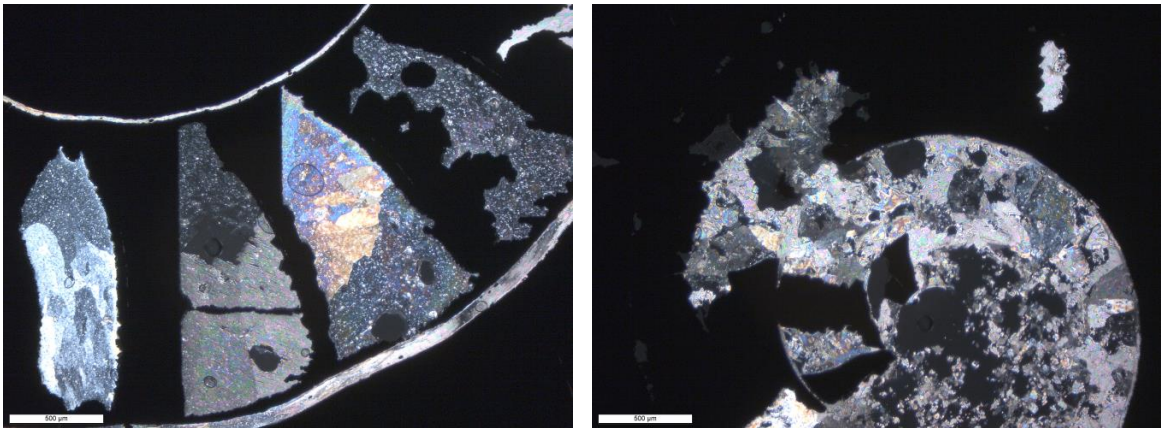

Figure 5.18 (SPM_18 and SPM_14) – Calcite cementation associated with pyritic ammonoid moulds. Left: coarse (100 μm – 1 mm) calcite cement filling the previous void spaces of individual gas chambers as well as the shell wall between whorls. Right: cementation of the nucleus that does not replicate the original, internal chambered structure of the phragmocone. Scale = 500 μm.

Original shell aragonite. Relict aragonitic shell is retained in several specimens, preserved as a powdered white veneer on the external surface of the pyritic internal mould (fig. 5.19); it lacks the nacreous lustre typically associated with shell aragonite (see Chapter 6) as a result of alteration and/or deterioration during burial diagenesis. There is no consistency regarding the extent nor position of relict shell aragonite although it is generally associated with secondary pyrite replacement habits (fig. 5.19).

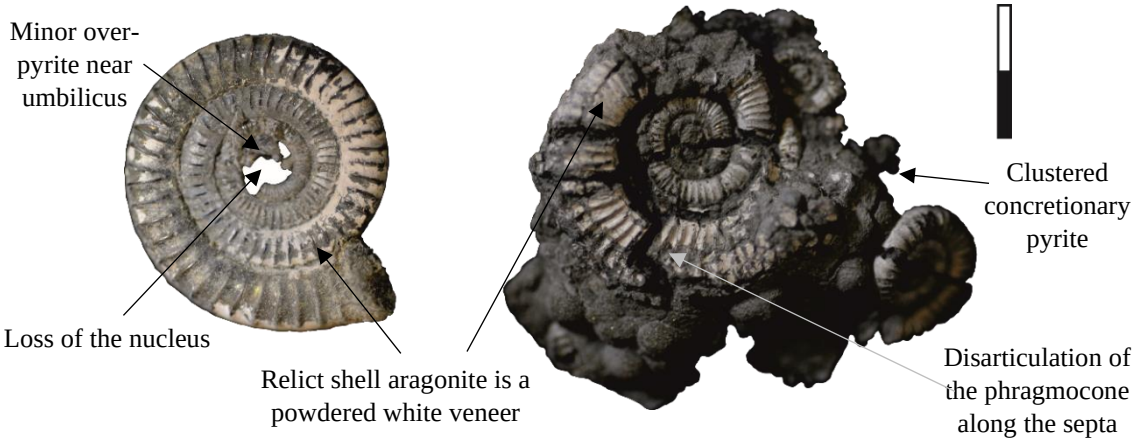

Figure 5.19 – Left (SPM_M_07): a pyritic *Crucilobiceras* with extensive relict aragonitic shell preserved as a powdered white veneer. Right (SPM_M_25): relict aragonitic shell on numerous pyritic *Crucilobiceras* within a fragment of clustered concretionary pyrite. Scale = 10 mm.

		Body chamber				Phragmocone						Shell		
Specimen	Diameter (mm)	Pyrite precipitate (sparse)	Pyrite precipitate (dense)	Calcite	Hollow	Pyrite precipitate (sparse)	Pyrite precipitate (dense)	Pyrite precipitate (geopetal)	Chamber-lining pyrite	Calcite	Hollow	Direct shell replacement	Calcite	Notes
SPM_01	22	/	/	-	-	-	/	-	-	/	-	/	/	Relict ghost structure; aptychi
SPM_02	14	/	/	?	-	-	/	-	/	/	-	/	/	Peloids in body chamber; broken phragmocone
SPM_03	17	/	/	/	-	/	/	-	-	/	-	/	/	Relict ghost structure; siphuncle preserved
SPM_04	22	/	/	?	-	/	/	-	-	-	-	/	/	Damage at posterior of body chamber; peloids
SPM_05	24	/	/	?	-	-	/	-	-	/	-	/	/	Major damage in phragmocone; siphuncle
SPM_06	12	-	/	/	-	-	/	/	/	/	/	-	/	Broken body chamber; geopetal pyrite
SPM_07	18	/	/	-	-	/	/	-	-	-	/	/	/	Broken body chamber and phragmocone
SPM_08	16	/	/	?	?	-	/	-	-	-	/	/	/	Uniform replacement in phragmocone
SPM_09	14	/	/	-	-	-	/	-	-	/	-	-	/	Broken body chamber; calcite in nucleus
SPM_10	12	/	/	-	-	-	/	-	-	-	-	-	/	Bivalve lodged in body chamber
SPM_11	18	/	/	?	-	-	/	-	-	-	-	/	/	Uniform replacement in phragmocone
SPM_12	13	/	/	-	-	/	/	-	-	/	-	/	/	Uniform replacement
SPM_13	23	-	/	/	-	/	/	/	/	/	/	/	/	Damage to posterior of the body chamber
SPM_14	18	/	/	-	-	-	/	-	/	/	/	/	/	Irregular replacement in the nucleus
SPM_15	17	/	/	?	-	-	/	-	-	-	-	-	/	Uniform replacement
SPM_16	13	-	/	-	?	-	/	-	/	/	/	-	/	Part of body chamber is missing
SPM_17	16	/	/	-	/	-	/	-	-	/	/	/	-	Uniform replacement; siphuncle preserved
SPM_18	22	/	/	-	-	/	/	/	/	/	/	/	/	Variable replacement
SPM_19	20	-	/	-	-	-	/	-	-	-	/	/	/	Damage at posterior of body chamber
SPM_20	18	/	/	?	-	-	/	-	-	-	-	/	/	Uniform replacement
SPM_21	15	N/A	N/A	N/A	N/A	N/A	N/A	N/A	N/A	N/A	N/A	N/A	N/A	Not sectioned
SPM_22	20	N/A	N/A	N/A	N/A	N/A	N/A	N/A	N/A	N/A	N/A	N/A	N/A	Not sectioned
SPM_23	23	N/A	N/A	N/A	N/A	N/A	N/A	N/A	N/A	N/A	N/A	N/A	N/A	Not sectioned

Table 5.1 – Types of replacement observed in the cross-sections of well-preserved, pyritic *Promicroceras* from the BVM of Dorset (SPM_01 – SPM_23). Primary pyrite replacement habits include: pyritic internal precipitate (sparse = approximately < 70 % pyrite, dense = approximately > 70 % pyrite, and geopetal), chamber-lining pyrite, and direct shell replacement. Non-pyritic replacement habits include: calcite (not associated with peloids/external sediment) and hollows. / = present, dash (-) = absent.

		Body chamber				Phragmocone						Shell		
Specimen	Diameter (mm)	Pyrite precipitate (sparse)	Pyrite precipitate (dense)	Calcite	Hollow	Pyrite precipitate (sparse)	Pyrite precipitate (dense)	Pyrite precipitate (geopetal)	Chamber-lining pyrite	Calcite	Hollow	Direct shell replacement	Calcite	Notes
SPM_M_01	78	-	/	/	/	-	/	N/A	N/A	/	-	/	/	Poor internal structure; aragonite shell
SPM_M_02	42	/	/	/	-	-	/	N/A	N/A	/	-	-	/	Poor internal structure; aragonite shell
SPM_M_03	42	-	/	/	/	-	/	N/A	N/A	/	?	-	-	Poor internal structure; no shell
SPM_M_04	23	/	/	/	-	/	/	N/A	N/A	/	-	/	/	Phragmocone lacks chambered structure
SPM_M_05	61	/	/	/	/	-	/	-	/	/	/	/	/	Uniform, coarse calcite cement
SPM_M_06	85	/	/	/	-	-	/	-	/	/	-	/	/	Siphuncle; aragonite shell
SPM_M_07	25	N/A	N/A	N/A	N/A	N/A	N/A	N/A	N/A	N/A	N/A	N/A	N/A	Not sectioned
SPM_M_08	131	N/A	N/A	N/A	N/A	N/A	N/A	N/A	N/A	N/A	N/A	N/A	N/A	Not sectioned
SPM_M_09	68	/	/	/	/	/	/	-	/	/	/	/	/	Part of phragmocone missing; siphuncle
SPM_M_10	22	/	/	/	-	/	/	/	/	/	/	-	/	Fracturing and disarticulation of body chamber
SPM_M_11	23	-	/	/	-	-	/	-	/	/	-	-	/	Variable replacement in phragmocone
SPM_M_12	23	/	/	?	-	/	/	-	-	-	/	/	/	Uniform replacement; ghost structure
SPM_M_13	21	?	/	?	-	/	/	-	/	/	/	/	/	Damaged body chamber; peloids in opening
SPM_M_14	20	-	/	/	-	-	/	-	/	/	/	-	/	Distorted body chamber and phragmocone
SPM_M_15	15	/	/	/	-	/	/	-	/	/	/	-	/	Damaged body chamber; missing nucleus
SPM_M_16	23	/	/	/	-	/	/	-	/	/	/	/	/	Damaged/disarticulated body chamber
SPM_M_17	20	/	/	?	?	/	/	-	-	/	-	/	/	Septa reverse orientation
SPM_M_18	14	/	/	/	-	/	/	-	-	/	-	/	/	Different replacement across shell
SPM_M_19	21	N/A	N/A	N/A	N/A	N/A	N/A	N/A	N/A	N/A	N/A	N/A	N/A	Not sectioned
SPM_M_20	17	/	/	-	-	/	/	/	/	/	/	-	/	Variable replacement
SPM_M_21	26	/	/	?	?	-	/	-	-	?	?	/	/	Fragmented shell structure
SPM_M_22	17	/	/	/	-	/	/	-	/	/	-	/	/	Damaged body chamber
SPM_M_23	19	-	/	/	-	-	/	-	/	/	/	/	/	Extensive damage to shell structure
SPM_M_24	45	/	/	/	/	/	/	-	/	/	?	/	/	Extensive damage by over-pyrite
SPM_M_25	N/A	N/A	N/A	N/A	N/A	N/A	N/A	N/A	N/A	N/A	N/A	N/A	N/A	Not sectioned
SPM_M_26	N/A	N/A	N/A	N/A	N/A	N/A	N/A	N/A	N/A	N/A	N/A	N/A	N/A	Not sectioned
SPM_M_27	N/A	N/A	N/A	N/A	N/A	N/A	N/A	N/A	N/A	N/A	N/A	N/A	N/A	Not sectioned
SPM_M_28	155	N/A	N/A	N/A	N/A	N/A	N/A	N/A	N/A	N/A	N/A	N/A	N/A	Not sectioned

Table 5.2 – Types of replacement observed in the cross-sections of poorly-preserved, pyritic ammonoid moulds of various genera (see table 5.3) from the CMF of Dorset (SPM_M_01 – SPM_M_28). Primary pyrite replacement habits include: pyritic internal precipitate (sparse = approximately < 70 % pyrite, dense = approximately > 70 % pyrite, and geopetal), chamber-lining pyrite, and direct shell replacement. Non-pyritic replacement habits include: calcite (not associated with peloids/external sediment) and hollows. / = present, dash (-) = absent.

		Over-pyrite facilitated by compaction of the body chamber					Over-pyrite facilitated by compaction of the body chamber	Over-pyrite facilitated by total shell compaction	Clustered concretionary pyrite		General		
Specimen	Genus	Over-pyrite 1	Over-pyrite 2	Over-pyrite 3	Over-pyrite 4	Over-pyrite 5			Single face	Both faces	Original shell	Incomplete structure	Notes
SPM_M_01	N/A	-	-	-	-	-	-	/	-	-	-	-	No external shell structure
SPM_M_02	N/A	-	-	-	-	?	-	?	-	-	-	-	No external shell structure
SPM_M_03	N/A	-	-	-	-	-	-	/	-	-	-	-	Raised phragmocone on one side
SPM_M_04	N/A	-	-	-	-	/	-	-	-	-	-	-	No external shell structure
SPM_M_05	*Eod*	-	-	/	-	-	-	-	-	-	/	-	Body chamber obscured
SPM_M_06	*Eod*	-	/	-	-	-	-	-	-	-	-	-	Body chamber obscured
SPM_M_07	*Cruci*	/	-	?	-	-	-	-	-	-	/	/	Over-pyrite at the aperture
SPM_M_08	*Eod*	-	-	/	?	-	-	-	-	-	/	-	Tubercles visible through over-pyrite
SPM_M_09	*Cruci?*	-	-	-	/	-	-	-	-	-	-	-	Differential growth on each face
SPM_M_10	*Prom*	/	-	-	-	-	-	-	-	-	-	/	Over-pyrite at damage and aperture
SPM_M_11	*Cruci*	-	-	/	-	-	-	-	-	-	-	/	Missing parts of the shell on one side
SPM_M_12	*Prom*	/	-	?	-	-	-	-	-	-	-	-	Over-pyrite at aperture
SPM_M_13	*Prom*	/	-	-	-	-	-	-	-	-	-	/	Over-pyrite at damage and aperture
SPM_M_14	*Cruci*	-	-	/	-	-	-	-	-	-	-	/	Over-pyrite at damage to body chamber
SPM_M_15	*Cruci*	/	-	?	-	-	-	-	-	-	-	/	Missing nucleus; pyrite rot
SPM_M_16	*Prom*	-	/	-	-	-	-	-	-	-	-	/	Over-pyrite at damage to body chamber
SPM_M_17	*Cruci*	/	-	-	-	-	-	-	-	-	-	/	Damaged; no nucleus on one side
SPM_M_18	*Prom*	-	-	-	-	-	-	-	-	-	-	/	Different replacement across shell
SPM_M_19	*Cruci*	-	-	-	-	-	-	-	-	/	-	-	Differential growth on both sides
SPM_M_20	*Prom*	-	-	-	-	-	-	-	-	-	-	/	Missing parts of the shell on one side
SPM_M_21	N/A	-	-	-	-	-	-	-	?	-	-	-	Shell is flattened
SPM_M_22	*Prom*	-	-	-	-	-	-	-	-	-	-	-	Beef coating surface
SPM_M_23	*Cruci*	/	-	?	-	-	-	-	-	-	-	-	Small over-pyrite clusters

SPM_M_24	*Glev*	-	-	/	-	-	-	-	-	-	-	-	Differential growth on both sides
SPM_M_25	*Cruci*	-	-	-	-	-	-	-	-	/	/	-	Disarticulation of the shell
SPM_M_26	*Cruci*	-	-	-	-	-	-	-	-	/	/	-	Disarticulation of the shell
SPM_M_27	*Cruci*	-	-	-	-	-	-	-	-	/	/	/	Ammonoid moulds without nuclei
SPM_M_28	*Caen*	-	-	-	-	-	/	-	-	-	-	-	Extensive over-pyrite

Table 5.3 – Types of replacement observed on the external surface of poorly-preserved, pyritic ammonoid moulds of various genera from the CMF of Dorset (SPM_M_01 – SPM_M_28). Secondary pyrite replacement habits include: over-pyrite (facilitated by compaction of the body chamber, facilitated by compaction of the phragmocone, and facilitated by total shell compaction) and clustered concretionary pyrite. Other notable features include preservation of the original aragonitic shell and the loss of parts of the shell structure. *Eod* = *Eoderoceras*, *Cruci* = *Crucilobiceras*, *Prom* = *Promicroceras*, *Glev* = *Gleviceras*, *Caen* = *Caenisites*. / = present, dash (-) = absent.

5.4. Discussion

The paragenetic sequence in pyritic ammonoid moulds from the CMF of Dorset exhibits a range of replacement minerals, textures, and habits. By understanding the nature of their interaction, the relative timing for each phase of the replacement pathway can be inferred. Furthermore, by determining the exact conditions for survival of formerly aragonitic fauna within the TAZ, pyritisation is established as a taphonomic window (*sensu* Cherns et al., 2008) that preserves a truer representation of vulnerable shelly groups (see Chapter 7).

5.4.1. Primary replacement pathway

The replacement pathway for the current assemblage of well-preserved pyritic ammonoid moulds is generally consistent with relative timings proposed by Hudson (1982). A significant portion of the reaction pathway established by Coleman and Raiswell (1995) for pyrite formation in carbonate concretions can be applied to pyrite replacement of aragonitic ammonoid shells herein despite differences in their respective settings. The primary replacement pathway is as follows:

Stage 1: Following post-mortem deposition of the ammonoid shell, soft tissues retained in the body chamber acted as a blockage to prevent major external sediment ingress (*sensu* Cope and Sole, 2000, Curtis et al., 2000) (fig. 5.20 – Stage 1). Shortly after deposition, during the time in which the shell was surrounded by non-anoxic sediments, micro-reducing conditions developed within the enclosed void of the body chamber (*sensu* Hudson and Palframan, 1968, Hudson, 1982, Fisher, 1986) (fig. 5.20 – Stage 2). In this model, reducing micro-environments are the product of a greater rate of aerobic oxygen consumption by bacteria – or associated metabolic products i.e. hydrogen sulphide – compared to the rate of oxygen diffusion into the enclosed void (*sensu* Jørgensen, 1977). This imbalance is intensified by the concentration of digestible organic matter that exists within the shell. Whilst constant, uni-directional diffusion of oxygen into the enclosed void is restricted by the shell's microstructure; furthermore, the integrity of the reducing micro-environment is sustained since the shell and sediment ingress at the aperture act as a physical barrier to prevent the introduction of aerated sediment via bioturbation and sediment mixing. Supporting evidence that points to accumulation in non-anoxic conditions is inferred from the lack of pyrite in the surrounding sediment that would typically be associated with a reducing environment (e.g. Hudson, 1982, Fisher and Hudson, 1985).

Stage 2: BSR was initiated in micro-reducing conditions within the ammonoid shell after minor burial (fig. 5.20 – Stage 2); organic matter was derived from the surviving soft tissues and sulphate was supplied by overlying seawater. The first stage of replacement comprised the precipitation of sparse, equant pyrite within the external sediment at the apertural margin (fig. 5.20 – Stage 2). The reaction pathway is based on initial euhedral pyrite formation in Coleman and Raiswell (1995). *In situ* iron sources were utilised to precipitate pyrite directly (Coleman and Raiswell, 1995 - eqs. 11 and 12) but were insufficient to react with all available sulphide and so additional H_2S was lost from the system (Coleman and Raiswell, 1995). Alkalinity was generated where S^0 production occurred via *in situ* iron reduction (Coleman and Raiswell, 1995 - eq. 8). There is no evidence to suggest that pyrite precipitation in the reducing micro-environment progressed via an FeS intermediate since monosulphides were typically associated with framboidal textures (Sweeney and Kaplan, 1973, Hudson, 1982, Coleman and Raiswell, 1995) and these were not present in the current assemblage.

It is likely that the majority of early BSR proceeded without iron to form pyrite since it was not naturally present within the shell and only a finite amount could be sourced from external sediments in the body chamber; moreover, without reducing conditions in the surrounding sediment, iron was immobile/unable to diffuse in to the semi-enclosed void (Fisher, 1986). Coleman (1985) established that iron limitation during sulphate reduction contributed to supersaturation and/or precipitation of carbonate (eq. 5 in Coleman, 1985, eq. 4 in Fisher, 1986) since sulphide was hydrolised, not precipitated, and able to diffuse from the system as H_2S (eq. 4 in Coleman, 1985, eq. 2 and 3 in Fisher, 1986). The local buffering effects imposed both by iron limitation during sulphate reduction (*sensu* Coleman, 1985, Fisher, 1986, Coleman and Raiswell, 1995) and by direct pyrite precipitation using *in situ* sources of iron to form S^0 via iron reduction (*sensu* Coleman and Raiswell, 1995) protected the vulnerable aragonitic shell from acidic conditions in the TAZ. Acidity was generated via aerobic, microbial organic decay and oxidation of products associated with BSR in the surrounding sediment (Wright et al., 2003 and references therein).

Stage 3: The transition away from preliminary pyritisation in the reducing micro-environment (fig. 5.20 – Stage 2) occurred once widespread reducing conditions were established in the sediment column (fig. 5.20 – Stage 3). However, since the extent of initial pyrite precipitation cannot be correlated with the scale of the *in situ* iron source, it is

not possible to ascertain whether the main phase of pyrite replacement (fig. 5.20 – stages 3, 4, and 5) could have initially proceeded via the reaction pathway in Stage 2. For the purposes of this model, it is generally assumed that *in situ* iron was exhausted within the reducing micro-environment.

The main phase of primary pyrite replacement commenced with pyritic internal precipitate in the body chamber (fig. 5.20 – Stage 3). The proportion of pyrite increases towards the posterior of this semi-enclosed void and is inversely proportional to the amount of external sediment; this trend is coincident with a gradual transition from an equant to aggregated texture. Assuming *in situ* sources of iron were exhausted within the reducing micro-environment, the reaction pathway for all subsequent stages of pyrite precipitation are based on the second phase of euhedral pyrite formation in Coleman and Raiswell (1995). Iron reduction (eq. 3 in Coleman and Raiswell, 1995) and S^0 production (eq. 8 in Coleman and Raiswell, 1995) occurred outside of the ammonoid shell; both reactants diffused inward where they reacted with H_2S (supplied by BSR) to directly precipitate pyrite (Coleman and Raiswell, 1995 - eq. 16). Access to reactants was facilitated across the aperture and the reaction was sustained by organic matter in the body chamber; anoxic conditions in the surrounding sediment were essential to enable inward diffusion of reduced iron (Fisher, 1986). The reaction pathway generated acidity (via H^+) that was buffered by incomplete dissolution of the originally aragonitic shell (Coleman and Raiswell, 1995).

Stage 4: Commencement of pyritisation in the phragmocone followed partial or complete replacement of the body chamber. Preservation of the shell's original, internal chambered structure indicates that total aragonite dissolution had not yet been achieved. Pyritic internal precipitate is the earliest primary habit evident in the phragmocone (fig. 5.20 – Stage 4); it replaced gas chambers located in the final whorl first and progressed adapically around the shell (fig. 5.20 – Stage 4). The extent of pyritic internal precipitate is inconsistent across the assemblage and whilst this variability likely represents differential reactant availability, the precise cause remains uncertain; approximately 30 % of moulds lack pyrite precipitate in the innermost whorls, yet elsewhere it completely fills the phragmocone. Where individual gas chambers are partially filled, the presence of geopetal structures support Hudson's (1982) interpretation that pyrite settled from an organic-rich fluid source.

It is not possible to determine a precise relative timing for loss of the siphuncle since it varies across the assemblage, but the earliest opportunity to confirm its widespread exclusion from the replacement pathway is at the end of pyritic internal precipitate formation (fig. 5.20 – Stage 4) or the initiation of chamber-lining pyritisation (fig. 5.20 – Stage 5). Despite the fact that the siphuncle is not evident in most specimens, and thus its dissolution must have occurred prior to pyritisation of the phragmocone, fragments of the siphuncular tube were sometimes replaced by pyrite precipitate (fig. 5.7) which requires that it occasionally survived to this stage of the replacement pathway. The siphuncle is never associated with chamber-lining pyrite which helps to pinpoint a relative timing for its elimination from the phragmocone. Whilst dissolution of the siphuncular tube may have contributed to increased access for pyritising fluids to the internal gas chambers, there are no obvious differences between phragmocones with or without the siphuncle.

Stage 5: Cessation of pyritic internal precipitate formation was followed by chamber-lining pyritisation that coated the inner surfaces of the shell and septal walls as well as the upper surface of pyrite precipitate within incompletely filled gas chambers (*sensu* Hudson and Palframan, 1968) (fig. 5.20 – Stage 5). The cause of this shift in the dominant primary replacement habit remains unclear. The potential for dual habits to coexist within an individual gas chamber was discussed by Hudson (1982); the author suggests that pyritic internal precipitate settled at the base of the chamber from a fluid source containing the products of bacterial autolysis and was followed by a subsequent phase of slow, *in situ* chamber-lining precipitation from an aqueous solution (Hudson, 1982). This habit does not occur in all of the chambers not filled previously, nor is it exclusive to the early whorls of the phragmocone. Previous authors have inferred that chamber-lining pyrite abutting the septa was in contact with the organic septal lining (Bayer, 1975, in Hudson, 1982) and not the aragonitic septum following partial decay of the former (Hudson, 1982). Good preservation of the phragmocone's original, internal chambered structure indicates that replacement typically occurred prior to complete aragonite dissolution (*sensu* Hudson and Palframan, 1968, Hudson, 1982) (fig. 5.20 – Stage 5). A single specimen (SPM_14) exhibits chamber-lining pyrite that coats irregular portions of the inner shell wall without the septa (notwithstanding septa shared with chambers that had already been replaced by pyrite precipitate) (fig. 5.6); in this instance, chamber-lining pyrite post-dates septal dissolution, but pre-dates loss of the main aragonitic shell. Chamber-lining pyrite was

formed via the reaction pathway in Stage 3 but may represent particularly slow precipitation as iron sources in the surrounding porewaters were consumed.

Stage 6: Ammonoid moulds were not always completely filled prior to the termination of pyrite replacement. However, since no subsequent stages of the paragenetic sequence preserved the internal chambered structure of the phragmocone, this point in the replacement pathway indicates the earliest opportunity to recognise total dissolution of the ammonoid shell where it occurred (fig. 5.20 – Stage 6). This relationship was discussed by Coleman and Raiswell (1995) who suggested that consumption of acidity by carbonate dissolution was essential to continued direct pyrite precipitation and so the lack of a carbonate buffer following loss of the ammonoid shell could terminate pyrite formation via increased acidity and sulphide undersaturation. The subsequent phase of calcite precipitation observed within the assemblage requires that carbonate supersaturation be achieved at a later stage (i.e. fig. 5.20 – Stage 7).

Stage 7: The final stage of the replacement pathway was the precipitation of calcite cement within incompletely filled gas chambers and/or irregular portions of the nucleus (fig. 5.20 – Stage 7). Calcite cement also replaced the septa and innermost shell walls (fig. 5.20 – Stage 7). Cementation textures are generally consistent with late, diagenetic/inorganic cements identified by Curtis et al. (2000). Calcite precipitation required that the sediment be supersaturated with respect to carbonate following the termination of pyrite precipitation although the exact cause of this porewater geochemistry is not clear. If applied to Coleman and Raiswell's (1995) model for direct pyrite precipitation, alkalinity could have been generated away from the mould, at the same time as sedimentary pyrite formation, by iron reduction and S^0 formation within the surrounding sediment (Coleman and Raiswell, 1995 - eq. 3 and 8). Once pyrite formation had ceased within the mould owing to complete dissolution of the carbonate buffer, the lack of acidity being generated by direct precipitation (Coleman and Raiswell, 1995 - eq. 16) means local supersaturation could be sustained; exhaustion of *in situ* and nearby sources of iron may have also contributed to continued BSR without iron availability and thus increased the potential for carbonate precipitation (*sensu* Coleman, 1985 - eq. 5, Fisher, 1986).

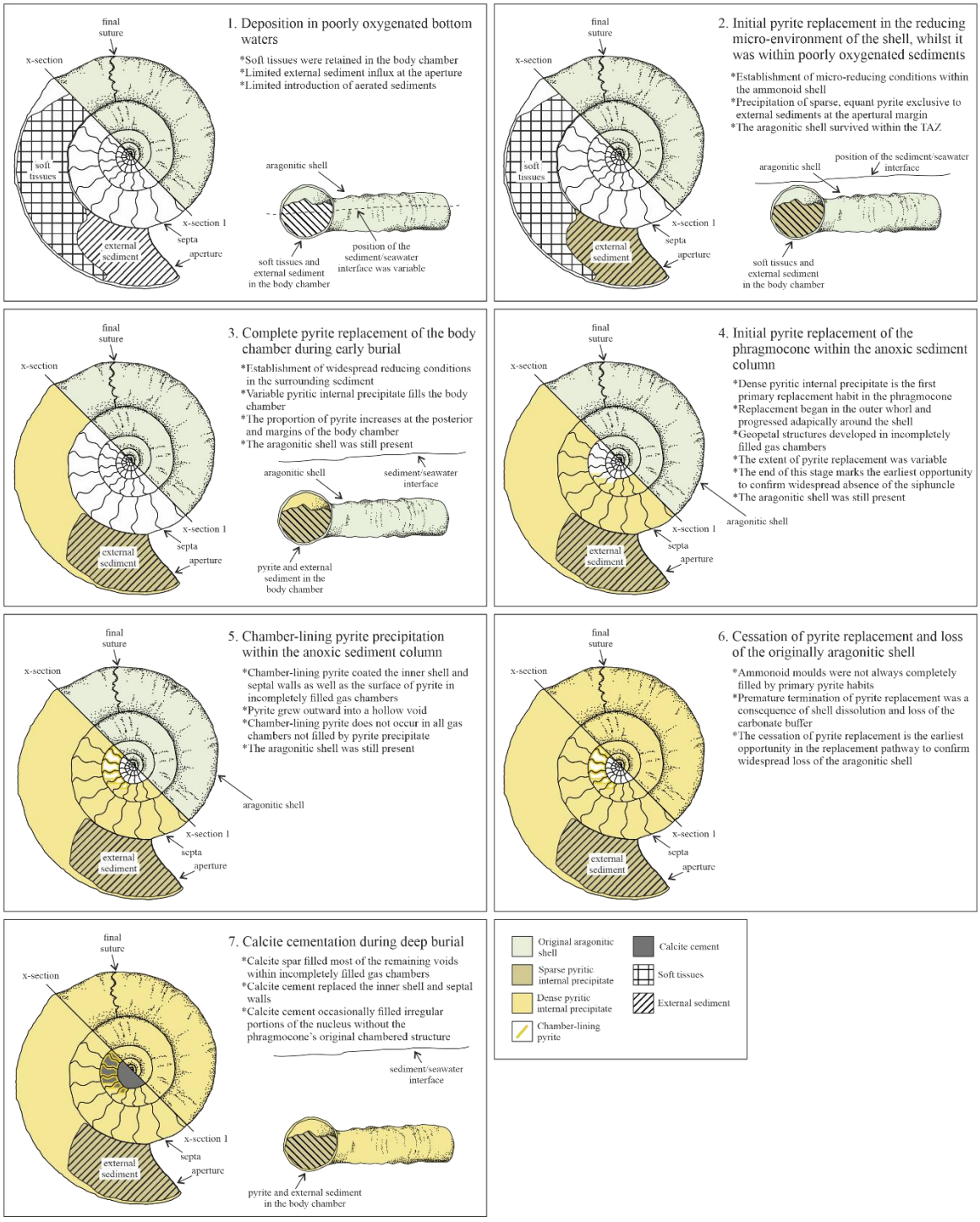

Figure 5.20 – The primary replacement pathway in pyritic ammonoid moulds from the CMF of Dorset. Sketches indicate the relative timing of replacement and dissolution on the outer surface of the shell versus a ventral cross-section to illustrate internal replacement (line of division between the two views = x-section). The shell's relative position within the sediment column is also shown. Key in figure.

5.4.2. Secondary replacement pathways

An important consideration for both secondary replacement habits is the cause of divergence from primary pyrite replacement. The timing of secondary replacement with

respect to the primary replacement pathway was also variable, but the majority of specimens – except for those that were totally compacted prior to pyritisation – were subject to partial preservation of the ammonoid mould by pyritic internal precipitate or chamber-lining pyrite (e.g. fig. 5.20 – stages 2, 3, 4, and 5).

Over-pyrite. Over-pyritisation required compaction and fracturing of the ammonoid shell that Hudson (1982) suggests would have occurred whilst the surviving internal void remained chemically distinct from the surrounding sediment. The author attributes compaction to moderately deep burial (up to several metres in depth) and indicates that both fracturing and over-pyritisation post-date precipitation of primary pyrite habits but pre-date calcite cementation (Hudson, 1982). In contrast, Fisher (1986) does not ascribe precise conditions to shell compaction and recognised that it varied between individuals owing to a number of different factors including size and the extent of prior replacement. In the current assemblage, different conditions for compaction – including relative timings – are inferred from the part of the shell that was flattened:

i. Over-pyritisation facilitated by compaction of the body chamber. Compaction of the body chamber is a common trait in ammonoid shells from the CMF, particularly among the thin-walled eoderoceratids, irrespective of their preservation as pyritic internal moulds or calcitic moulds contained within diagenetic carbonate concretions. Some evidence for the relative timing of compaction can be inferred from Curtis et al. (2000), who suggested that compression (of peloids) in the latter must have occurred prior to early calcite precipitation during manganese, iron, and sulphate reduction since cementation would have prevented subsequent compression; by applying this relative timing to pyritic ammonoid moulds, assuming that the eoderoceratids were comparably resistant to burial pressures regardless of their genera, compaction of the body chamber occurred prior to or contemporaneously with (in the case of micro-reducing conditions) pyrite precipitation (fig. 5.21 – Stage 2). Whilst the depositional setting was different, it is reasonable to assume that since the threshold for compaction was exceeded in laminated paper shales associated with carbonate concretions, it would have also been exceeded in the dark marls containing pyritic ammonoid moulds where suitable conditions for manganese, iron, and sulphate reduction occurred comparatively slower and at greater depths. Pyritisation of the body chamber was the earliest stage of the primary replacement pathway and it is therefore doubtful that compaction occurred after significant pyrite precipitation (fig. 5.20 – Stage 3) owing to the inherent resistance afforded by mouldic preservation.

ii. Over-pyritisation facilitated by compaction of the phragmocone. Compaction of the phragmocone in exclusivity was rare among pyritic ammonoid moulds in the assemblage (table 5.3). When considered with respect to the primary replacement pathway, this phenomenon likely required significant compression to have occurred between stages of pyrite replacement i.e. after sediment influx and early pyritisation provided a resistant, localised internal structure that prevented compaction of the body chamber (fig. 5.20 – stages 2 and 3) but before pyritisation commenced within the phragmocone (fig. 5.20 – Stage 4) such that it was without internal support during burial.

iii. Over-pyritisation facilitated by total compaction of the shell. Rapid burial processes associated with storm events or sediment draping may have led to overburden pressure and subsequent compression, but there is no lithological evidence to support this interpretation. Instead, the timing and nature of compaction are inferred from a lack of prior replacement which indicates that total shell compression occurred before pyrite precipitation. Without pyritisation in the reducing micro-environment, potentially as a result of the delayed onset of BSR or a lack of retained soft tissues, the aragonitic ammonoid shell did not benefit from the buffering effects associated with BSR and early pyrite precipitation; instead, the shell was retained within the TAZ and exposed to acidic conditions for an uncertain period of time. Partial dissolution of the shell microstructure coupled with a lack of initial internal support would have limited its ability to resist compaction.

Despite the variable nature and timing of compression, over-pyritisation facilitated by compaction of the body chamber and by compaction of the phragmocone share a number of similarities, including that over-pyrite was accompanied by partial preservation of the ammonoid mould by primary replacement habits. In both instances, the commencement of over-pyritisation (e.g. fig. 5.21 – Stage 4) was preceded by initial pyrite formation within micro-reducing conditions inside the body chamber (e.g. figs. 5.20 – Stage 2 and 5.21 – Stage 3) – provided that fractures had not damaged the integrity of the micro-environment – and pyritic internal precipitate that filled its remaining void space (e.g. figs. 5.20 – Stage 3 and 5.21 – Stage 4). Alternatively, following total compaction of the body chamber, over-pyrite post-dated replacement of any surviving internal structure. Over-pyritisation facilitated by compaction of the phragmocone would have also likely required pyrite to have filled the damaged shell interior prior to any outward growth. Where the internal chambered structure of the phragmocone remained intact, subsequent stages of primary replacement occurred after the onset of over-pyritisation in the body chamber (fig. 5.21 –

Stage 4), but there is no way to correlate these to specific phases of over-pyrite growth (fig. 5.21 – stages 5, 6, 7, 8). Total compaction of the shell was unique in that over-pyritisation was initiated at fractures in the body chamber and phragmocone simultaneously.

Over-pyrite was the result of progressive outward growth that nucleated at compression fractures (*sensu* Hudson, 1982), regardless of their position, and expanded outward to superficially cover a variable proportion of the remaining ammonoid shell (e.g. fig. 5.21 – stages 4, 5, 6, 7, and 8). The potential maximum extent of over-pyritisation was total obscuration of the mould (e.g. fig. 5.21 – Stage 8), but its range in the current assemblage is inconsistent and completion was rarely achieved except where over-pyrite was facilitated by total compaction of the shell. The cause of cessation of over-pyritisation (both premature and following complete obscuration of the shell) is uncertain. In the primary replacement pathway (fig. 5.20), a plausible causal mechanism for the prevention of pyrite precipitation was the lack of a carbonate buffer following loss of the ammonoid shell. Whilst this model may be applicable to some moulds with over-pyrite, many specimens showing incomplete over-pyritisation nonetheless retained portions of relict aragonitic shell. Instead of a dependence on the carbonate buffer to prolong pyrite formation, it is possible that the larger/thicker shells of some ammonoids provided an overabundance of consumable carbonate such that pyrite precipitation was instead limited by reactant availability (iron) as a consequence of voluminous pyrite over-growth. In relative terms, the termination of over-pyritisation – regardless of its extent – frequently appears to post-date cessation of primary pyrite replacement as evidenced by over-pyrite coating parts of the shell replaced by pyritic internal precipitate and chamber-lining pyrite; as such, incomplete pyritisation of the phragmocone, where it had otherwise remained intact, is surprising since pyrite precipitation had evidently continued elsewhere. Notwithstanding the potential for aragonite dissolution or a complete lack of reactants to prevent primary pyrite replacement of the phragmocone, over-pyrite on the outside of the shell would have preferentially consumed iron and S^0 based on the direction of diffusion from surrounding sediments; relatively late over-pyritisation that consumed depleted reactants equal to the rate at which they were supplied could have inhibited continued pyrite formation within the shell. Calcite cementation did not preserve the internal chambered structure of the phragmocone and therefore indicates the earliest opportunity to recognise total dissolution of the ammonoid shell where it occurred (fig. 5.21 – Stage 9).

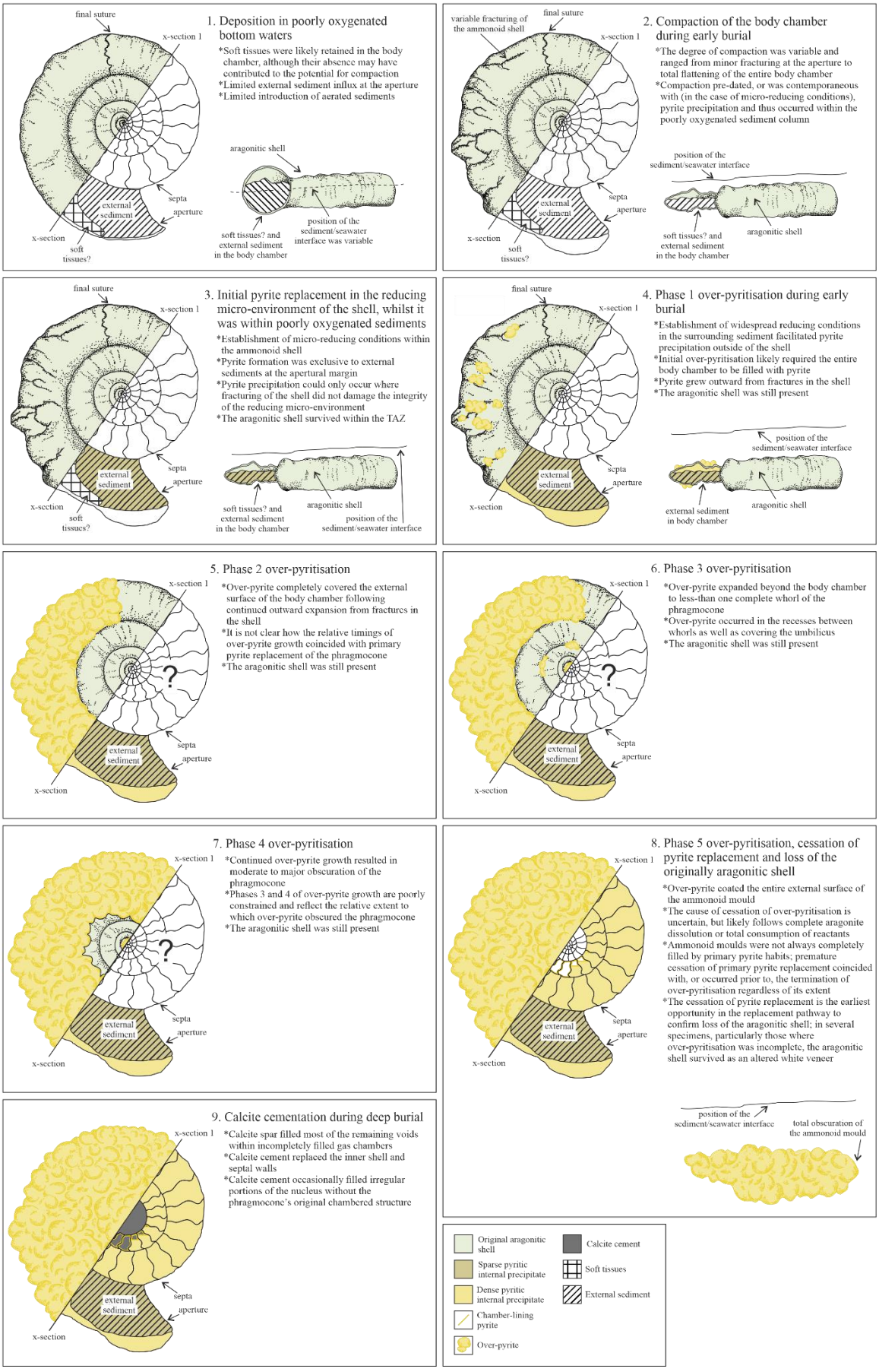
1. Deposition in poorly oxygenated bottom waters
*Soft tissues were likely retained in the body chamber, although their absence may have contributed to the potential for compaction
*Limited external sediment influx at the aperture
*Limited introduction of aerated sediments
final suture
x-section 1
septa
aperture
external sediment
x-section
soft tissues?
aragonitic shell
soft tissues? and external sediment in the body chamber
position of the sediment/seawater interface was variable
2. Compaction of the body chamber during early burial
*The degree of compaction was variable and ranged from minor fracturing at the aperture to total flattening of the entire body chamber
*Compaction pre-dated, or was contemporaneous with (in the case of micro-reducing conditions), pyrite precipitation and thus occurred within the poorly oxygenated sediment column
variable fracturing of the ammonoid shell
position of the sediment/seawater interface
soft tissues? and external sediment in the body chamber
aragonitic shell
3. Initial pyrite replacement in the reducing micro-environment of the shell, whilst it was within poorly oxygenated sediments
*Establishment of micro-reducing conditions within the ammonoid shell
*Pyrite formation was exclusive to external sediments at the apertural margin
*Pyrite precipitation could only occur where fracturing of the shell did not damage the integrity of the reducing micro-environment
*The aragonitic shell survived within the TAZ
4. Phase 1 over-pyritisation during early burial
*Establishment of widespread reducing conditions in the surrounding sediment facilitated pyrite precipitation outside of the shell
*Initial over-pyritisation likely required the entire body chamber to be filled with pyrite
*Pyrite grew outward from fractures in the shell
*The aragonitic shell was still present
external sediment in body chamber
5. Phase 2 over-pyritisation
*Over-pyrite completely covered the external surface of the body chamber following continued outward expansion from fractures in the shell
*It is not clear how the relative timings of over-pyrite growth coincided with primary pyrite replacement of the phragmocone
*The aragonitic shell was still present
6. Phase 3 over-pyritisation
*Over-pyrite expanded beyond the body chamber to less-than one complete whorl of the phragmocone
*Over-pyrite occurred in the recesses between whorls as well as covering the umbilicus
*The aragonitic shell was still present
7. Phase 4 over-pyritisation
*Continued over-pyrite growth resulted in moderate to major obscuration of the phragmocone
*Phases 3 and 4 of over-pyrite growth are poorly constrained and reflect the relative extent to which over-pyrite obscured the phragmocone
*The aragonitic shell was still present
8. Phase 5 over-pyritisation, cessation of pyrite replacement and loss of the originally aragonitic shell
*Over-pyrite coated the entire external surface of the ammonoid mould
*The cause of cessation of over-pyritisation is uncertain, but likely follows complete aragonite dissolution or total consumption of reactants
*Ammonoid moulds were not always completely filled by primary pyrite habits; premature cessation of primary pyrite replacement coincided with, or occurred prior to, the termination of over-pyritisation regardless of its extent
*The cessation of pyrite replacement is the earliest opportunity in the replacement pathway to confirm loss of the aragonitic shell; in several specimens, particularly those where over-pyritisation was incomplete, the aragonitic shell survived as an altered white veneer
position of the sediment/seawater interface
total obscuration of the ammonoid mould
9. Calcite cementation during deep burial
*Calcite spar filled most of the remaining voids within incompletely filled gas chambers
*Calcite cement replaced the inner shell and septal walls
*Calcite cement occasionally filled irregular portions of the nucleus without the phragmocone's original chambered structure
Original aragonitic shell
Sparse pyritic internal precipitate
Dense pyritic internal precipitate
Chamber-lining pyrite
Over-pyrite
Calcite cement
Soft tissues
External sediment

Figure 5.21 – The idealised secondary replacement pathway for over-pyrite facilitated by compaction of the body chamber in pyritic ammonoid moulds from the CMF of Dorset. Sketches indicate the relative timing of replacement on the outer surface of the shell versus a ventral cross-section to illustrate internal replacement (line of division between the two views = x-section). The shell's relative position within the sediment column is also shown. Key in figure.

Clustered concretionary pyrite. The only replacement habit to incorporate pyrite that was independent of ammonoid preservation, clustered concretionary pyrite is an aggregate comprised of ammonoid moulds partially enveloped by irregular, interstitial pyritic concretions (fig. 5.16). The cause of this incidental growth is uncertain, but its relative timing can be inferred. Contained ammonoid moulds are consistent with primary pyrite replacement by pyritic internal precipitate and chamber-lining pyrite (fig. 5.20 – stages 2, 3, 4, and 5) but there is moderate separation between individually preserved gas chambers at the septa (fig. 5.17). The nature of this breakage indicates that the formation of pyrite concretions occurred after partial dissolution of the aragonitic shell (fig. 5.20 – Stage 6) but prior to calcite cementation (fig. 5.20 – Stage 7). Disarticulation of the mould accounts for specimens lacking calcite cementation of the nucleus.

5.4.3. Soft tissue relicts in pyritic ammonoid moulds

Evidence for the post-mortem retention of soft tissues is known from calcitic ammonoid moulds in the CMF of Dorset (e.g. Cope and Sole, 2000, Curtis et al., 2000, Andrew et al., 2010); the same phenomenon is now described in pyritic ammonoid moulds from these strata. In the former, Curtis et al. (2000) state that this rare taphonomic occurrence was the product of a resuspended sediment package that engulfed and buried a life assemblage of ammonoids with their soft tissues intact. There is, however, no sedimentological evidence that supports this interpretation in the dark marls containing pyritic ammonoid moulds; moreover, this depositional process would not be conducive to the development of stable micro-reducing conditions required for early pyritisation. In order to account for the presence of soft tissues during early pyrite replacement, it is suggested that ammonoid shells were simply deposited with the soft parts *in situ* more frequently than previously anticipated (e.g. Cope and Sole, 2000), but that soft tissues did not survive the fossilisation process/are not recognised without exceptional preservation.

Retention of the ammonoid body is inferred from limited sediment ingress, restricted to the anterior portion of the body chamber, where soft tissues acted as a blockage to prevent external sediment influx (Cope and Sole, 2000, Curtis et al., 2000) (fig. 5.22). Ammonoid

jaw structures preserved within the body chamber were also used by Cope and Sole (2000) to demonstrate that soft parts remained *in situ* during burial, and comparable features are evident in pyritic ammonoid moulds (fig. 5.22). By occupying the available space within the body chamber, the retained ammonoid body limited the volume of internal pyrite precipitation and subsequently produced a relict structure that replicates the shape and position of the ammonoid soft parts (fig. 5.22).

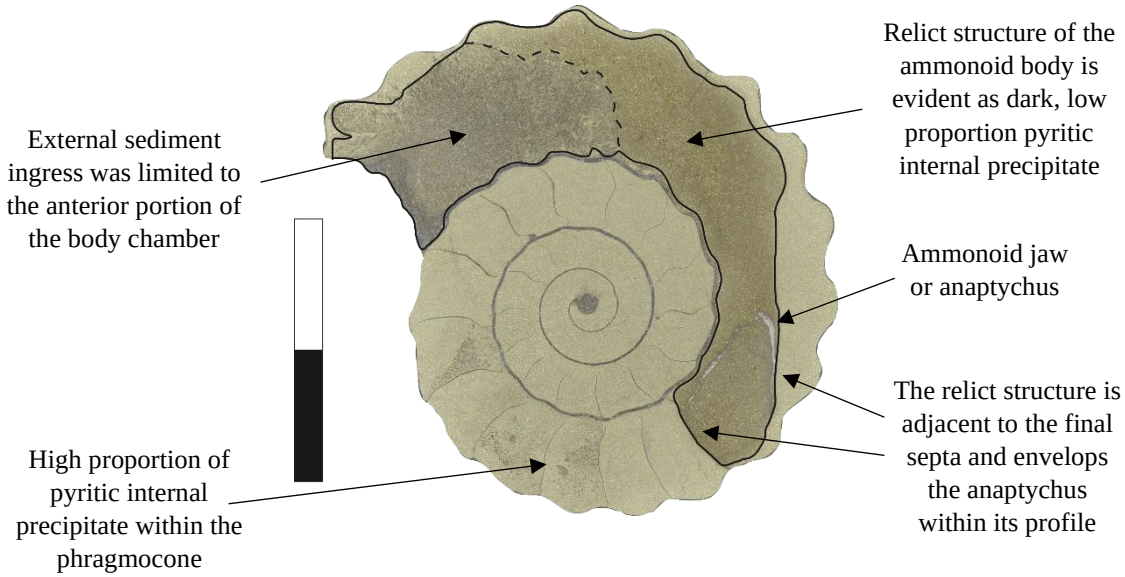

Figure 5.22 (SPM_01) – A pyritic *Promicroceras* that retained a relict structure of the ammonoid body preserved as dark, low proportion pyrite precipitate within the body chamber. The posterior of the relict structure contains the sectioned calcitic jaw structure (anaptychus). Scale = 10 mm.

The relict structure of the ammonoid body was preserved as a result of the primary pyrite replacement pathway (fig. 5.20). During early burial in poorly-oxygenated bottom waters, introduction of a substantial volume of organic matter – via *in situ* soft tissues – resulted in rapid microbial consumption of available oxygen and the establishment of a reducing micro-environment within the shell that prevented complete aerobic decomposition of the body. Subsequent primary pyrite precipitation continued whilst the ammonoid body occupied part of the body chamber resulting in a low proportion of pyritic internal precipitate that mirrored the shape and position of retained soft parts.

5.5. Conclusions

This study provides the first detailed examination of pyrite replacement in ammonoids from the CMF of Dorset despite the notability and relative abundance of these fossils. A

complex local paragenetic sequence is presented that shows a range of different replacement minerals, textures, and habits, most of which are consistent with previous descriptions of pyrite replacement from various strata (e.g. Hudson, 1982). Using a number of newly collected specimens from several different ammonoid genera, it was possible to describe multiple primary pyrite habits that produce good preservation of the internal mould or shell microstructure such as pyritic internal precipitate, chamber-lining pyrite, and direct shell replacement as well as secondary replacement habits such as over-pyrite and clustered concretionary pyrite that poorly preserve the shell's original structure and obscure surface details. Evidence of original shell aragonite associated with pyritic ammonoid moulds is also described for the first time locally.

The primary pyrite replacement pathway followed post-mortem deposition of the ammonoid with soft tissues contained in the body chamber; new evidence is presented for soft tissue retention in pyritic ammonoid moulds including hitherto undescribed relict structures of the ammonoid body. Aerobic decay of organic matter consumed available oxygen and facilitated the development of a reducing micro-environment within the enclosed void of the shell whilst it was surrounded by non-anoxic sediments. Subsequent BSR resulted in the precipitation of sparse, equant pyrite within the external sediment at the apertural margin. Dissolution of the aragonitic shell within the TAZ was prevented by local buffering effects imposed both by direct pyrite precipitation using *in situ* sources of iron to form S^0 via iron reduction and iron limitation during BSR (*sensu* Coleman, 1985, Fisher, 1986, Coleman and Raiswell, 1995). The potential for these processes to function as a taphonomic window is examined later (see Chapter 7).

The remainder of the primary replacement pathway, and all secondary pyrite replacement, occurred once widespread reducing conditions were established during burial and required reactants – iron and S^0 – to diffuse inward from the surrounding sediment (*sensu* Coleman and Raiswell, 1995). The reaction pathway generated acidity (via H^+) that was buffered by dissolution of the originally aragonitic shell (Coleman and Raiswell, 1995). Primary pyrite replacement continued with pyritic internal precipitate in the body chamber that progressed adapically into the phragmocone, followed by chamber-lining pyritisation that coated the inner surfaces of the shell and septal walls. Ammonoid moulds were not always completely filled prior to the termination of pyrite replacement; a plausible causal mechanism for the prevention of pyrite formation was the lack of a carbonate buffer following loss of the ammonoid shell, required to buffer acidity generated by direct pyrite precipitation (*sensu*

Coleman and Raiswell, 1995). The final stage of the replacement pathway was precipitation of calcite cement within incompletely filled gas chambers and/or irregular portions of the nucleus; calcite also replaced the septa and innermost shell walls.

Examination of complex secondary pyrite replacement habits shows that the relative timing of over-pyrite and clustered concretionary pyrite, with respect to the primary replacement pathway, was variable; nonetheless, the majority of these specimens – except for those that were totally compacted prior to pyritisation – were subject to partial preservation of the ammonoid mould by pyritic internal precipitate or chamber-lining pyrite. The nature of over-pyrite correlates with different conditions for compaction – including relative timing and the part of the shell that was flattened – and is most commonly associated with progressive or staged growth facilitated by compaction of the body chamber. The cause of cessation of over-pyritisation during burial is uncertain but appears to variably be the result of total shell dissolution (as per the primary replacement pathway) or reactant unavailability. The potential for over-pyrite to preferentially consume reactants owing to the direction of the diffusion gradient and subsequently terminate any associated primary pyrite replacement prematurely is also discussed. Finally, previously undescribed aggregates made up of pyritic ammonoid moulds and interstitial pyrite concretions were examined in order to better understand the timing and nature of pyrite replacement.

CHAPTER 6

6. SOFT TISSUE ATTACHMENT SCARS IN AMMONOIDS (EODEROCERATIDAE AND ARIETITIDAE) FROM THE CHARMOUTH MUDSTONE FORMATION (EARLY JURASSIC), DORSET AND THEIR TAPHONOMIC IMPLICATIONS

6.1. Introduction

Evidence for muscle attachment in ammonoid shells is well documented from a range of geological and geographical settings (Doguzhaeva and Mutvei, 1996). These features have been recognised in a number of different Mesozoic ammonoid genera (e.g. Crick, 1898, Jordan, 1968, Landman and Bandel, 1985, Weitschat and Bändel, 1991, Richter, 2002, Richter and Fischer, 2002, Klug et al., 2007, Andrew et al., 2010, Paul, 2011, Mironenko, 2014). Muscle attachment scars are classified according to their position or correlation with specific muscle groups (see review by Doguzhaeva and Mutvei, 1996) and include the paired dorsal scar, unpaired ventral scar, unpaired middorsal scar, paired lateral attachment scars, lateral sinus, and anterior lateral sinus (e.g. Crick, 1898, Jones, 1961, Jordan, 1968, Bandel, 1982, Landman and Bandel, 1985, Doguzhaeva and Mutvei, 1991, Weitschat and Bändel, 1991, Doguzhaeva and Mutvei, 1996, Richter, 2002, Richter and Fischer, 2002, Klug et al., 2007, Mironenko, 2014).

In this study, muscle attachment scars preserved as aragonitic veneers on calcitic ammonoid moulds are described from the CMF of Dorset. Andrew et al. (2015) were the first to address these features in the current assemblage and whilst the authors discussed their potential to represent sites of muscle attachment, this could not be confirmed owing to a lack of defining features consistent with earlier descriptions. A re-examination of some previously figured specimens coupled with new material presented herein provides an opportunity to review their origin and identify specific attachment sites with respect to existing classifications. Muscle attachment scars are discussed in the eoderoceratids *Microderoceras* and *Promicroceras* as well as the arietitid *Asteroceras*. Attachment scars are known from the eoderoceratid genus *Eoderoceras* – the middorsal unpaired attachment scar was identified by Rakus (1978), (in Doguzhaeva and Mutvei, 1996) and the paired dorsal attachment scar was recognised in pyritic internal moulds by Andrew et al. (2010). In the arietitids, muscle scars were recorded in *Asteroceras* (*Arietites obtusus*) by Crick (1898) and paired dorsal attachment scars were identified in the genus by Jordan (1968), (in Doguzhaeva and Mutvei, 1996).

The preservation of ammonoid muscle attachment scars required the atypical survival of this vulnerable, formerly aragonitic group through the Taphonomically Active Zone (TAZ) (*sensu* Wright et al., 2003) as well as the retention of original shell biomineralogy. This study assesses the unique local taphonomic conditions responsible for facilitating the

prolonged survival of aragonite during burial diagenesis, and its consequences for the Missing Molluscs effect.

6.2. Material and methods

6.2.1. Samples

Ammonoid moulds that preserve evidence of muscle attachment scars were collected from diagenetic carbonate concretions in the CMF of Dorset (see Chapter 2 for locality details; see also Andrew et al., 2015). The sedimentological composition of these limestones is variable, but most are peloidal wackestones with irregular proportions of bioclasts, clays, pyrite, and other detrital minerals (see Chapter 2). Attachment scars are present on the external surface of uncrushed, calcitic internal moulds as well as the inner surface of the replaced shell following separation from the former. In both instances, these features are preserved as a thin aragonite veneer. Studied specimens were collected by a number of different individuals (see below). Several ammonoid moulds collected by Andrew et al. (2015) (LYMPH_2015/9 – 2015/12), J. Carroll (NMW_2021.2.G1), and CR (NMW_2021.2.G5 and G7) were revealed using mechanical preparatory techniques, but there has been little to no attempt to further prepare the majority of specimens following initial separation of the part and counterpart. A single unregistered *Promicroceras* was broken into small pieces in order to examine and photograph the cross-section of the attachment scar using scanning electron microscopy.

Microderoceras. A single internal mould of an immature *Microderoceras birchi* (NMW_2021.2.G1; table 6.1) was examined from the *Birchi* Bed at the top of the SWB (see Chapter 2). The specimen was found by J. Carroll and donated to the National Museum Wales (NMW).

Promicroceras. The internal moulds of 19 *Promicroceras* were examined (table 6.1). 6 new specimens were contributed to this study collectively by CR (NMW_2021.2.G2, G4, and G7), D. Sole (NMW_2021.2.G3 and G5), and J. Carroll (NMW_2021.2.G6) (table 6.1) prior to being deposited in the NMW. 5 specimens (LYMPH_2015/7, 2015/9 –2015/12; table 6.1) were re-examined following description and deposition in Lyme Regis Philpott Museum by Andrew et al. (2015). A further 8 specimens were examined, most following initial description by Andrew et al. (2015), from the J. F. Jackson Collection at the NMW (NMW_60.510.G596, G598 – G601, G606, G4490, and a single specimen with an

unknown accession number; table 6.1). 5 additional *Promicroceras* external moulds that show the inner surface of the separated shell were collected by CR (NMW_2021.2.G8) and D. Sole (NMW_2021.2.G9 – G12) (table 6.1) prior to being deposited in the NMW. NMW_2021.2.G2 and G8 are a part and counterpart. *Promicroceras* originate from a number of concretionary horizons including the Yellowstone, Woodstone, Flatstone, and Topstone beds of the CMF (see Chapter 2; see also Andrew et al., 2015).

Asteroceras. A single internal mould of *Asteroceras obtusum* (NMW_60.510.G3518; table 6.1) was re-examined following initial description by Andrew et al. (2015). The specimen likely originates from the Flatstone Bed of the central BVM (see Chapter 2) and resides in the J. F. Jackson Collection at the NMW.

6.2.2. Angular Approach Method

The Angular Approach method (after Klompmaker et al., 2009 and Andrew et al., 2015) was used to determine the position and length of muscle attachment scars, both in degrees and as a function of the total length of the body chamber (fig. 6.1; see Klompmaker et al., 2009). In order to process these data, photographs of the ammonoid mould's lateral face were traced into CorelDraw software; it is important to note that previously published photographs of LYMPH_2015/7 and 2015/9 – 2015/12 were used from Andrew et al. (2015) owing to access restrictions during the Covid-19 pandemic.

From the umbilicus, or an estimation of its position where it remained obscured by sediment, lines were drawn to the ventral position of the final septum and to the aperture (fs and a respectively; fig. 6.1; see Klompmaker et al., 2009). Lines were also drawn to the anterior and posterior margins of each muscle attachment scar e.g. iridescent paired lateral attachment scar ($pls[i]^1$ – $pls[i]^2$) (fig. 6.1); these two lines account for the maximum extent of the attachment area. Where the muscle scar was in contact with the final septum, the posterior line was drawn to the ventral position of the final septum (fs; fig. 6.1) in order to ensure consistency across the assemblage owing to the irregular surface expression of the final suture. From these landmarks, the relative position and angular extent of different features could be calculated accordingly (see Klompmaker et al., 2009). Andrew et al. (2015) also used this method to map iridescent features on specimens that were subsequently re-examined in this study.

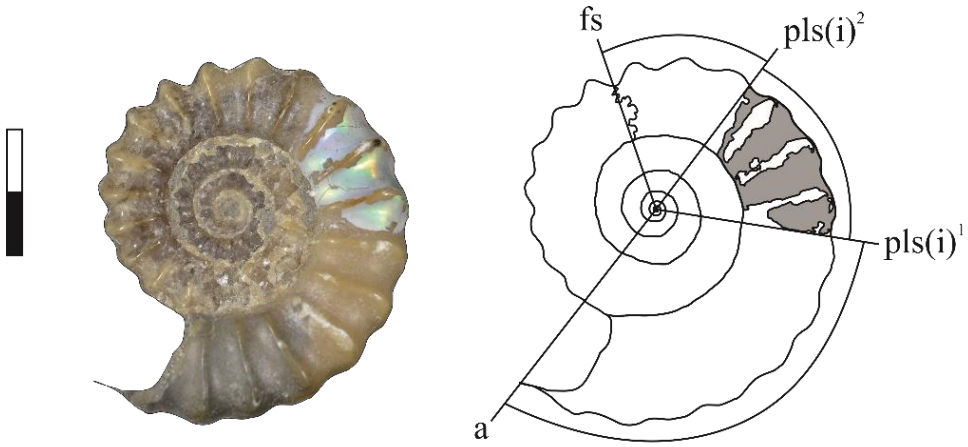

Figure 6.1 (NMW_60.510.G606) – Illustration of the Angular Approach method (after Klompmaker et al., 2009 and Andrew et al., 2015). The position of the attachment scar's anterior margin (pls[i][1]) is measured in degrees from the aperture (a) and the position of the posterior margin (pls[i][2]) is measured in degrees from the final septum (fs). The length of the attachment scar is measured between pls[i][1] and pls[i][2].

6.3. Results

6.3.1. Preservation of muscle attachment scars

There are two types of preservation associated with muscle attachment scars in the current assemblage – the first is an iridescent, nacreous veneer and the second is a transparent, poorly-iridescent layer. The surviving shell aragonite is preserved in contact with the internal mould of the body chamber (fig. 6.2) and/or the inner shell surface of the outer mould, both of which were replaced by calcite cement; it is important to note that the exposed attachment areas are likely to be incomplete owing to poor separation (Andrew et al., 2015). These features are generally associated with ammonoids that show limited sediment ingress beyond the aperture (e.g. Andrew et al., 2015) and little to no sediment within the posterior of the body chamber where the attachment scar is located (e.g. fig. 6.1). In the few specimens that counter this trend and contain sediment beneath the attachment area, it is not a uniform fill, and the body chamber was still mostly replaced by calcite cement (e.g. NMW_60.510.G600; fig. 6.5iv).

Scanning electron microscopy of the iridescent paired lateral attachment scar shows a series of stacked, interlocking hexagonal microcrystals (fig. 6.2). In Kulicki et al. (2015), this texture is attributed to the basic form of the nacreous layer of shell microstructure. However, since the characteristic lustre is not uniform across all of the different muscle

attachment scars, those associated with the transparent veneer are thought to be preserved on the inner prismatic layer instead (*sensu* Mironenko, 2014) and that poor separation of the mould resulted in differential exposure of the shell's microstructure. Detailed assessment of the nature and microstructural origin of the attachment areas is beyond the scope of this study.

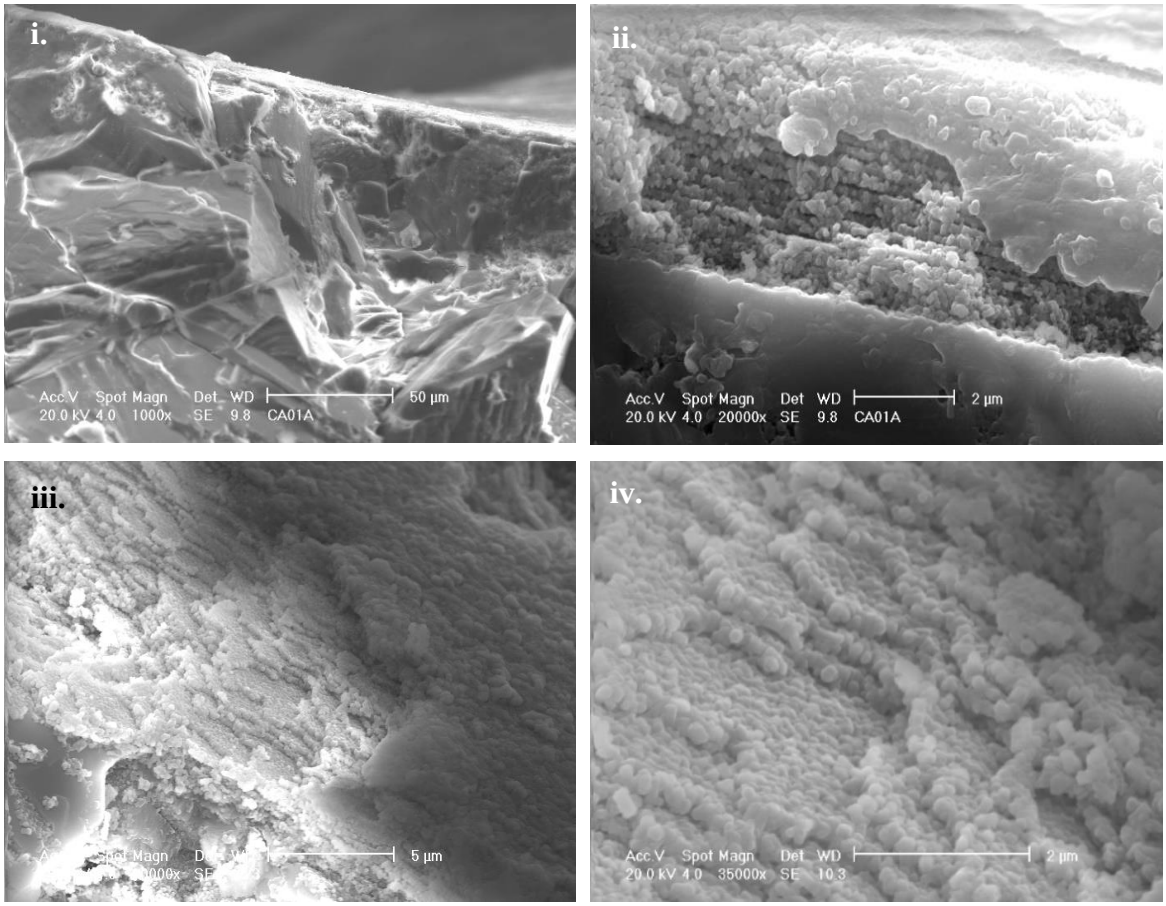

Figure 6.2 – Scanning electron photomicrographs, under various magnifications, of a cross-section through the iridescent paired lateral attachment scar in an unregistered *Promicroceras*. Note the laminated hexagonal microcrystals in the aragonitic shell microstructure. See images for scale.

6.3.2. Muscle attachment scars

Paired lateral attachment scars. In *Microderoceras*, the paired lateral attachment scar is an iridescent aragonitic veneer positioned near to the rear of the body chamber (fig. 6.3). The anterior margin is 146° from the aperture and the posterior margin is 40° from the final septum (fig. 6.3; table 6.1). The angular extent of the attachment area is 68°, which accounts for 27 % of the total length of the body chamber (fig. 6.3; table 6.1). There is a minor adaperturally directed lobe at the anterior border whereas the rear approximates an inverse sigmoid curve with ventrolateral projection towards the final septum (fig. 6.3). The

paired lateral attachment scar extends to the dorsum and crosses the venter (fig. 6.3), but it was not possible to determine its bilateral symmetry since the opposing lateral face is not exposed.

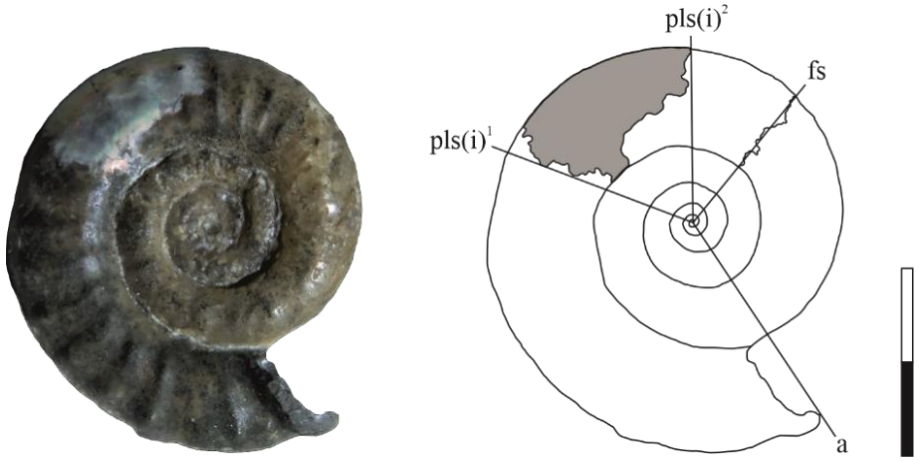

Figure 6.3 (NMW_2021.2.G1) – Preservation of the iridescent paired lateral attachment scar in an immature *Microderoceras birchi*. a = aperture, fs = final septum, pls = paired lateral attachment scar, i = iridescent. Scale = 10 mm.

The morphology and position of paired lateral attachment scars in *Promicroceras* is generally consistent amongst the studied specimens (table 6.1). Attachment areas are preserved as an aragonitic veneer at the posterior of the body chamber (fig. 6.4), but lack the clearly defined form associated with these features in other studies (e.g. Mironenko, 2014). Paired lateral attachment scars are approximately bilaterally symmetrical, cross the venter (Andrew et al., 2015), and most connect with the dorsum on the lateral face (fig. 6.5). The angular extent of the iridescent attachment area varies significantly within the assemblage (maximum = 141° in NMW_60.510.G4490; minimum = 28° in NMW_60.510.G598) and it covers an irregular proportion of the body chamber (maximum = 63 % in NMW_60.510.G4490; minimum = 12 % in NMW_2021.2.G6 and NMW_60.510.G598) (table 6.1). The transparent paired lateral attachment scar was not present in all specimens (table 6.1); moreover, the anterior border was often obscured by its iridescent counterpart and so the feature's angular extent could not always be determined (table 6.1). In specimens where both the anterior and posterior border were present, its maximum angular extent was 151° (NMW_60.510.G4490) and its minimum 25° (NMW_2021.2.G6) (table 6.1).

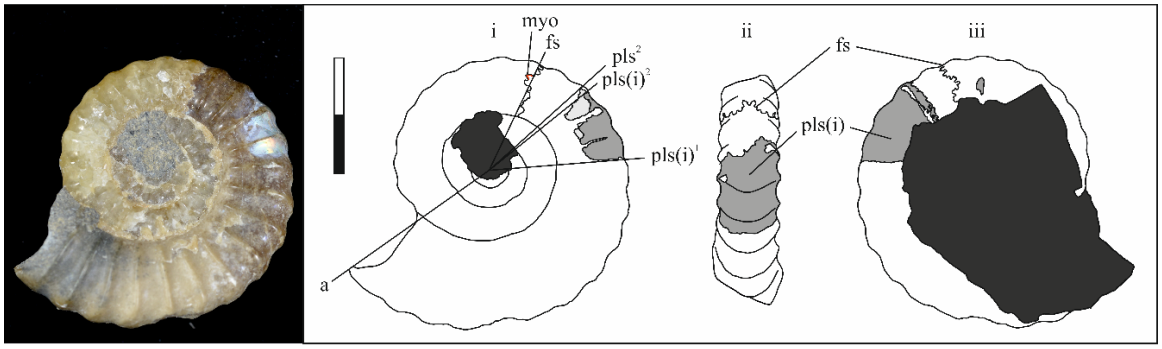

Figure 6.4 (NMW_60.510.G601) – Ventral and lateral position of the iridescent and transparent paired lateral attachment scar as well as the myoadhesive band in a single *Promicroceras*. a = aperture, fs = final septum, pls = paired lateral attachment scar, myo = myoadhesive band, i = iridescent. Obscuring matrix is blocked out as dark grey fill. Scale = 10 mm.

The anterior margins of 'aragonitic veneers' (paired lateral attachment scars) were discussed in detail by Andrew et al. (2015). The authors describe these linear features as a series of differently angled borders that are generally closest to the aperture ventrolaterally (e.g. NMW_60.510.G600; Andrew et al., 2015; fig. 6.5iv); this morphology is consistent with several additional specimens presented herein. Andrew et al. (2015) also recognised that the typical orientation of the angled anterior border was infrequently inverted such that its lateral position is closest to the aperture dorsolaterally; additional specimens were observed in this study that exhibit a similar inversion (e.g. NMW_2021.2.G10). The morphology of the paired lateral attachment scar's anterior border is difficult to characterise since it is usually incomplete (e.g. NMW_2021.2.G5; fig. 6.5iii) and there is significant variation within the assemblage (fig. 6.5). Several of the apparently intact anterior boundaries are approximately linear (e.g. LYMPH 2015/7; see Andrew et al., 2015), rounded (e.g. NMW_60.510.G596; fig. 6.5ii), or have a minor ventro-lateral projection (e.g. NMW_60.510.G600; fig. 6.5iv). The position of the iridescent paired lateral attachment scar's anterior margin ranges from 75° – 168° away from the aperture (average = 132°) (table 6.1); this equates to an average of 91° from the final septum (table 6.1) which is consistent with earlier measurements by Andrew et al. (2015). The anterior boundary of the transparent paired lateral attachment scar is rarely observed since it is often obscured by the former (table 6.1). Where present, it occurs close to – either behind or in front of – the iridescent anterior boundary (average angular distance from the aperture = 128°; table 6.1) and loosely mirrors its form (fig. 6.6).

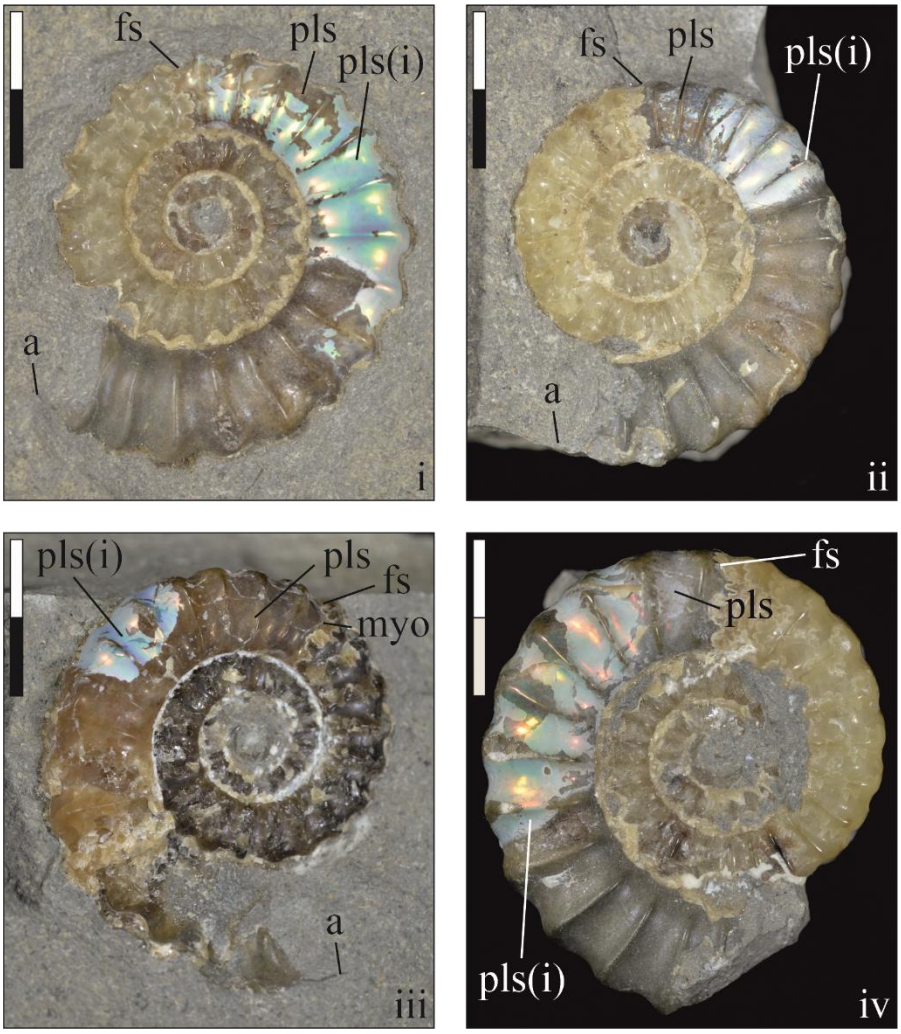

Figure 6.5 (i = NMW_60.510.G4490, ii = NMW_60.510.G596, iii = NMW_2021.2.G5, and iv = NMW_60.510.G600) – Evidence for muscle attachment in *Promicroceras*. The paired lateral attachment scar is typically preserved as an irregular iridescent or transparent veneer at the posterior of the body chamber; its angular extent varies significantly. a = aperture, fs = final septum, pls = paired lateral attachment scar, myo = myoadhesive band, i = iridescent. The myo is not visible on all specimens at this scale. Scale = 10 mm.

The position of the paired lateral attachment scar's posterior boundary varies extensively (e.g. fig. 6.5; table 6.1); moreover, its placement is inconsistent between the two different types of preservation (table 6.1). In two specimens, LYMPH 2015/10 and the inner shell surface of NMW_2021.2.G11, the iridescent attachment scar contacts the final septum (table 6.1; see also Andrew et al., 2015). In all other specimens, the posterior border is located away from the rear of the body chamber (maximum angular distance from the final septum = 56° in NMW_60.510.G606; minimum non-zero angular distance from the final septum = 2° in LYMPH 2015/7; average = 28°; table 6.1). The posterior boundary of the transparent paired lateral attachment scar, where this feature is preserved, is positioned

behind its iridescent counterpart and close to the final septum (excluding NMW_2021.2.G6, average angular distance from the final septum = 4°; table 6.1); on 7 out of 18 measured lateral faces, it is in direct contact with the final septum (e.g. fig. 6.5iii; table 6.1). Based on the irregular, often incomplete preservation of the paired lateral attachment scar, and the consistency with which transparent attachment areas contact the final septum, support is given to the inference made in Andrew et al. (2015) that the original posterior limit of these features was located at the final septum. This interaction is particularly evident in NMW_2021.2.G2 and G8 since the transparent paired lateral attachment scar follows the final suture in its entirety (fig. 6.6).

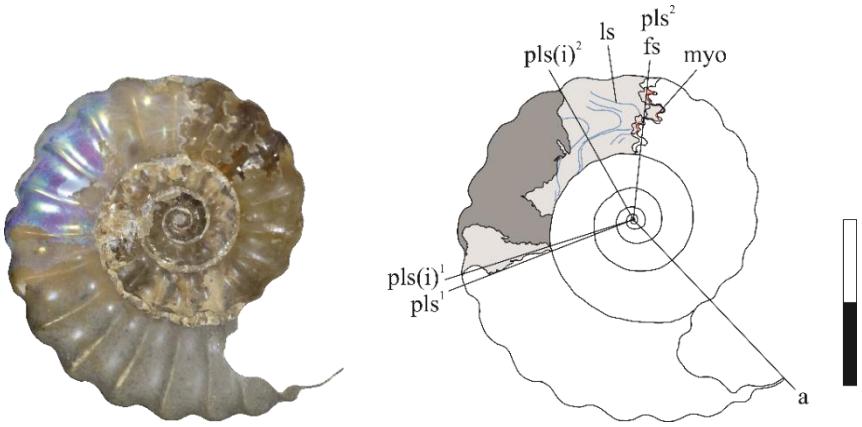

Figure 6.6 (NMW_2021.2.G2) – Preservation of the paired lateral attachment scar, lateral sinus, and myoadhesive band in a single *Promicroceras* mould. The lateral sinus is preserved as thin, nacreous lines that progress incrementally around the body chamber. a = aperture, fs = final septum, pls = paired lateral attachment scar, myo = myoadhesive band, ls = lateral sinus, i = iridescent. Scale = 10 mm.

In *Asteroceras*, the paired lateral attachment scar is preserved as a nacreous aragonitic veneer at the posterior of the body chamber and lacks the transparent layer observed in some *Promicroceras* (fig. 6.7). The iridescent attachment area is an irregular feature measuring 32° and covering 19 % of the body chamber (fig. 6.7; table 6.1). The anterior border forms an adaperturally directed lobe and is positioned 133° from the aperture (fig. 6.7; table 6.1) whilst the posterior border crudely mirrors the final septum (fig. 6.7; see also Andrew et al., 2015). The attachment scar is not bilaterally symmetrical (fig. 6.7); there is a powdered white veneer approximating the position of the attachment area on the opposing lateral face (fig. 6.7), but this cannot be conclusively ascribed to soft tissue attachment. The paired lateral attachment scar does not cross the venter, nor does it contact the dorsum (fig. 6.7); the keel marks the ventral limit of the attachment area (fig. 6.7).

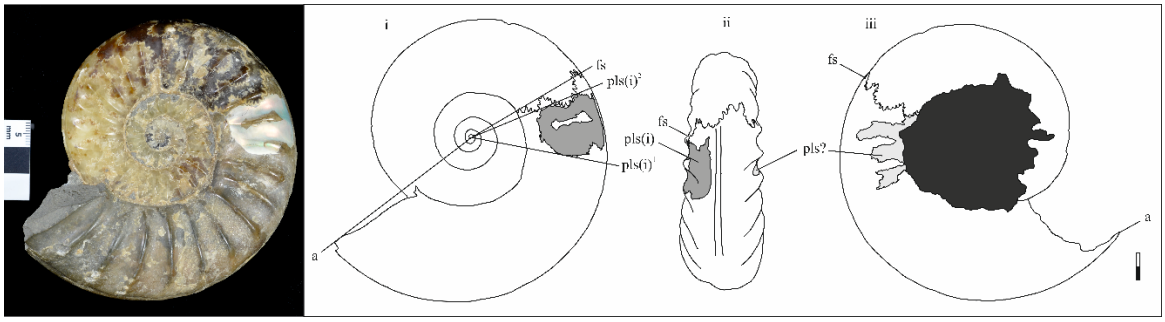

Figure 6.7 (NMW_60.510.G3518) – Ventral and lateral position of the iridescent paired lateral attachment scar in a single *Asteroceras* mould. There is a powdered white veneer approximating the attachment area on the opposing lateral face that may represent poor preservation of the attachment scar. a = aperture, fs = final septum, pls = paired lateral attachment scar, i = iridescent. Obscuring matrix is blocked out as dark grey fill. Scale = 10 mm.

Specimen	Width (mm)	a - fs	a – pls(i)^1	pls(i)^1 – pls(i)^2	pls(i)^2 – fs	a – pls^1	pls^1 – pls^2	pls^2 – fs
Microderoceras								
NMW_2021.2.G1	24	254°	146°	68°	40°	N/A	N/A	N/A
Promicroceras								
NMW_2021.2.G2	23	229°	116°	78°	35°	113°	116°	0°
NMW_2021.2.G3	22	214°	146°	54°	14°	-	-	0°
NMW_2021.2.G4	30	236°	146°	52°	38°	-	-	4°
NMW_2021.2.G5	27	232°	134°	43°	55°	120°	112°	0°
NMW_2021.2.G6*	25	245°	168°	29°	48°	177°	25°	43°
NMW_2021.2.G7	17	207°	129°	50°	28°	N/A	N/A	N/A
//NMW_2021.2.G8//	-	224°	-	-	-	-	-	0°
//NMW_2021.2.G9//	27	-	-	-	-	-	-	-
//NMW_2021.2.G10//	-	-	139°	-	-	146°	-	-
//NMW_2021.2.G11//	-	208°	121°	87°	0°	-	-	-
//NMW_2021.2.G12//	-	-	-	-	-	-	-	-
NMW_60.510.G596	26	214°	139°	48°	27°	-	-	5°
NMW_60.510.G598*	29	228°	162°	28°	38°	153°	75°	0°
NMW_60.510.G598(b)	29	223°	144°	54°	25°	-	-	8°
NMW_60.510.G599	26	210°	127°	60°	23°	106°	103°	1°
NMW_60.510.G600	-	-	-	90°	22°	-	-	9°
NMW_60.510.G601	26	209°	149°	34°	26°	-	-	23°
NMW_60.510.G606	30	237°	119°	62°	56°	N/A	N/A	N/A
NMW_60.510.G4490	27	223°	75°	141°	7°	71°	151°	1°
NMW_Unknown*	-	-	-	-	36°	-	-	0°
NMW_Unknown.(b)*	-	-	-	-	40°	-	-	0°
LYMPH 2015/7	23	224°	132°	90°	2°	-	-	0°
LYMPH 2015/9	25	219°	101°	96°	22°	-	-	4°
LYMPH 2015/10	23	229°	132°	97°	0°	N/A	N/A	N/A
LYMPH 2015/11	21	209°	103°	93°	13°	-	-	2°
LYMPH 2015/12	31	232°	156°	45°	31°	154°	64°	14°
Asteroceras								
NMW_60.510.G3518	110	172°	133°	32°	7°	N/A	N/A	N/A

Table 6.1 – Data for paired lateral attachment scars in *Microderoceras*, *Promicroceras, and Asteroceras*. a = aperture, fs = final septum, pls(i) = iridescent paired lateral attachment scar, pls = transparent paired

lateral attachment scar, N/A = without feature, dashed line (-) = data not measurable and/or incomplete, * = position of umbilicus estimated, // = internal surface of the external mould (not included in calculations).

Lateral sinus. Lateral sinus lines are infrequent in *Promicroceras* and occur on both internal and external moulds (table 6.2). This particular attachment scar was not observed in *Microderoceras* or *Asteroceras* (table 6.2). In *Promicroceras*, lateral sinuses are evident as a series of nacreous lines that incrementally progress around the body chamber (figs. 6.6 and 6.8); the number of individual sinus lines varies between specimens. The attachment area is positioned at the posterior of the body chamber and overlaps the transparent and/or iridescent paired lateral attachment scars (figs. 6.6 and 6.8). Consistent with previous descriptions (e.g. Jordan, 1968, Doguzhaeva and Mutvei, 1996), its form is an adorally open lobe although many of the sinus lines observed in the current assemblage are incomplete (figs. 6.6 and 6.8). The anterior boundary of the lateral sinus does not extend past the anterior limit of the paired lateral attachment scar in any of the studied specimens. In NMW_2021.2.G2, the anterior boundary of the lateral sinus is positioned 145° degrees from the aperture and its angular extent measures 84° (fig. 6.6; table 6.2); in the same specimen, and its counterpart NMW_2021.2.G8, the posterior boundary is interrupted by the final septum (fig. 6.6; table 6.2).

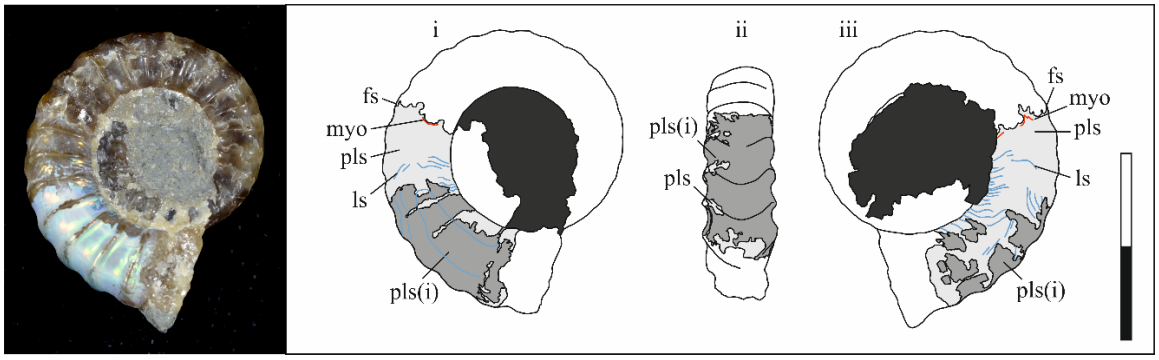

Figure 6.8 (NMW_Unknown) – Preservation of the paired lateral attachment scar, lateral sinus, and myoadhesive band in a single *Promicroceras*. The lateral sinus lines overlap the iridescent and transparent paired lateral attachment scar. fs = final septum, pls = paired lateral attachment scar, ls = lateral sinus, myo = myoadhesive band, i = iridescent. Obscuring matrix is blocked out as dark grey fill. Scale = 10 mm.

Myoadhesive band. In the majority of *Promicroceras* there is a thin nacreous line positioned at the posterior of the body chamber that follows the final septum (e.g. figs. 6.6 and 6.8; table 6.2); it is plausible that this feature represents the septal myoadhesive band, a component of the annular elevation (see review by Doguzhaeva and Mutvei, 1996). Similar attachment areas were not observed in *Microderoceras* or *Asteroceras* (table 6.2).

Microderoceras					
Specimen	Width (mm)	a – sin^1	sin^1 – sin^2	sin^2 - fs	myo
NMW_2021.2.G1	24	N/A	N/A	N/A	N/A
Promicroceras					
NMW_2021.2.G2	23	145°	84°	0°	Y
NMW_2021.2.G3	22	N/A	N/A	N/A	Y
NMW_2021.2.G4	30	N/A	N/A	N/A	N/A
NMW_2021.2.G5	27	N/A	N/A	N/A	Y
NMW_2021.2.G6*	25	N/A	N/A	N/A	N/A
NMW_2021.2.G7	17	N/A	N/A	N/A	N/A
//NMW_2021.2.G8//	-	-	-	0°	Y
//NMW_2021.2.G9//	27	-	-	-	N/A
//NMW_2021.2.G10//	-	146°	-	-	Y
//NMW_2021.2.G11//	-	N/A	N/A	N/A	Y
//NMW_2021.2.G12//	-	-	-	-	N/A
NMW_60.510.G596	26	N/A	N/A	N/A	N/A
NMW_60.510.G598*	29	N/A	N/A	N/A	Y
NMW_60.510.G598(b)	29	N/A	N/A	N/A	Y
NMW_60.510.G599	26	N/A	N/A	N/A	Y
NMW_60.510.G600	-	-	-	-	Y
NMW_60.510.G601	26	N/A	N/A	N/A	Y
NMW_60.510.G606	30	N/A	N/A	N/A	N/A
NMW_60.510.G4490	27	N/A	N/A	N/A	Y
NMW_Unknown*	-	-	-	11°	Y
NMW_Unknown.(b)*	-	-	-	20°	Y
LYMPH 2015/7	23	N/A	N/A	N/A	Y
LYMPH 2015/9	25	N/A	N/A	N/A	N/A
LYMPH 2015/10	23	-	-	0°	N/A
LYMPH 2015/11	21	N/A	N/A	N/A	N/A
LYMPH 2015/12	31	N/A	N/A	N/A	N/A
Asteroceras					
NMW_60.510.G3518	110	N/A	N/A	N/A	N/A

Table 6.2 – Data for the lateral sinus and myoadhesive band in *Microderoceras*, *Promicroceras*, and *Asteroceras*. a = aperture, fs = final septum, sin = lateral sinus, myo = myoadhesive band, N/A = without feature, dashed line (-) = data not measurable and/or incomplete, * = position of umbilicus estimated, // = internal surface of the external mould (not included in calculations), Y = present.

6.4. Discussion

The preservation of ammonoid muscle attachment scars varies in different geological and sedimentological settings (e.g. Dagys and Keupp, 1998, Richter, 2002, Richter and Fischer, 2002, Klug et al., 2007, Andrew et al., 2010, Paul, 2011, Mironenko, 2014, Andrew et al., 2015) as a function of the depositional environment, replacement context of the ammonoid mould, and/or the type of structural attachment area (e.g. Mironenko, 2014). Mironenko (2014) summarised two types of preservation associated with muscle attachment scars – yellow or black pyrite on pyritic internal moulds (e.g. Dagys and Keupp, 1998, Richter,

2002, Richter and Fischer, 2002, Andrew et al., 2010, Paul, 2011) and surface features on non-pyritic internal moulds where preservation of different muscle scars can (generally) be correlated either to the presence of the nacreous layer of shell microstructure or to a lack thereof (e.g. Klug et al., 2007, Mironenko, 2014, Andrew et al., 2015; see Results).

Regardless of the replacement context, preservation of muscle attachment scars required that the vulnerable aragonitic ammonoid shell survived passage through and/or deposition within the acidic TAZ. Curtis et al. (2000) determined that this particular ammonoid assemblage was subject to rapid burial following fallout from a suspended sediment package. Therefore, since anoxic conditions were established shortly after deposition (Curtis et al., 2000), prolonged residency within acidic porewaters was prevented as was complete shell dissolution (*sensu* Cherns et al., 2008). However, these depositional conditions do not account for the occasional retention of unaltered shell aragonite at sites of soft tissue attachment, a phenomenon that was lacking in the majority of otherwise identical ammonoid moulds from the same strata as well as individuals in close association (e.g. Andrew et al., 2015).

For preservation of aragonitic muscle attachment scars to have occurred, it was essential that original shell aragonite associated with these features survived short-lived exposure to acidity within the TAZ, even accounting for the rapid onset of anoxia (*sensu* Curtis et al., 2000). Furthermore, it required the selective prevention of neomorphism considering that the remainder of the ammonoid shell and internal mould were replaced by calcite cement. The exact conditions for preservation remain ambiguous; based on these observations it was not possible to establish whether soft tissue attachment sites routinely survived with the main ammonoid shell such that the preservation of original aragonite was a product of selective prevention of neomorphism or, that the microstructural nature and position of attachment areas meant that they were especially vulnerable to acidic dissolution, independent of the main shell, resulting in their loss from most ammonoid moulds. The latter does not address the survival of original shell aragonite and would have nonetheless required the selective prevention of neomorphism. Regardless of the cause, the unlikely survival of aragonitic muscle attachment scars may be addressed where loss of these features – by selective dissolution, neomorphism, or a combination of both – was prevented by atypical conditions within the body chamber.

Cope and Sole (2000) recognised evidence for soft tissue retention within the body chambers of ammonoid moulds from the same strata. The authors described *in situ* jaw apparatuses and limited sediment ingress that were attributed to the persistence of soft parts within the shell (Cope and Sole, 2000). Jaw structures (e.g. LYMPH 2015/10 in Andrew et al., 2015, NMW_2021.2.G7, NMW_60.510.G600) and comparable sediment infill were also observed in specimens that preserve muscle attachment scars (see Results; see also Andrew et al., 2015). Assuming that the aragonitic attachment site was especially vulnerable to acidity within the TAZ, prolonged connection of the ammonoid musculature to the inner shell surface would have provided a physical barrier to prevent contact with acidic porewaters. Moreover, limited aerobic microbial decay – immediately after deposition and prior to the establishment of anoxic conditions in the surrounding sediment – would have facilitated the development of a reducing micro-environment within the body chamber that prevented early aragonite dissolution (see Chapter 5). However, whilst it is apparent that the retention of soft tissues had a significant control on localised geochemistry within the ammonoid shell, exactly how this influenced the prevention of neomorphism at sites of muscle attachment remains unclear. This model also fails to account for the relative paucity of aragonitic attachment scars compared with evidence for retained soft parts.

6.5. Conclusions

Calcitic ammonoid moulds found in carbonate concretions from the CMF of Dorset preserve a range of different muscle attachment scars. In the arietitid *Asteroceras*, and for the first time in the eoderoceratids *Microderoceras* and *Promicroceras*, paired lateral attachment scars are recognised as iridescent or transparent aragonitic veneers at the posterior of the body chamber. The lateral sinus is identified in *Promicroceras* as a series of nacreous lines that incrementally progress around the body chamber and overlap the paired lateral attachment scars. The septal myoadhesive band is evident in the majority of *Promicroceras* as a thin nacreous line that follows the final septum. This study shows that preservation of muscle attachment scars on calcitic ammonoid moulds (locally) is associated with both the nacreous and inner prismatic layers of shell microstructure, with the distinction between them being based on visual differences, specifically the occurrence of an iridescent, nacreous veneer and a transparent, poorly-iridescent layer respectively.

For the preservation of muscle attachment scars to have occurred, it was necessary that the vulnerable aragonitic ammonoid shell survived acidity within the TAZ. This was achieved via a limited residency time owing to rapid burial and the establishment of anoxia in the surrounding sediment (Curtis et al., 2000). However, these depositional conditions do not account for the occasional retention of unaltered shell aragonite at sites of soft tissue attachment; this phenomenon required that the inner shell surface associated with these features remained intact following short-lived exposure to acidic porewaters whilst also being subject to the selective prevention of neomorphism. Although the precise nature of this preservation model remains uncertain, this study shows it can be addressed where loss of aragonitic attachment areas – by selective dissolution, neomorphism, or a combination of both – was prevented by atypical conditions within the body chamber.

Based on evidence presented elsewhere in the thesis, post-mortem retention of soft tissues is known to exert a significant control over porewater geochemistry within the ammonoid shell (see Chapter 5); therefore, since most ammonoid moulds that preserve aragonitic muscle attachment scars also show evidence consistent with retained soft parts, it is suggested that the persistence of organic matter during early burial diagenesis acted as a hitherto unknown mechanism to promote the atypical survival of unaltered shell aragonite. Assuming that the attachment site was especially vulnerable to acidity in the TAZ, prior to the onset of anoxia, limited aerobic microbial decay of retained soft tissues would have facilitated the formation of a reducing micro-environment within the body chamber that prevented aragonite dissolution. Furthermore, prolonged connection of the ammonoid musculature to the inner shell surface provided a physical barrier to prevent contact with acidic porewaters. However, exactly how original aragonite survived at the site of soft tissue attachment, considering the remainder of the shell was neomorphosed to calcite, remains uncertain. Recognition of the potential for physical biological factors to influence or enhance molluscan preservation, specifically the survival of a known vulnerable biomineralogy, warrants further investigation and has implications for the Missing Molluscs effect.

CHAPTER 7

7. DIFFERENTIAL TAPHONOMIC DISTORTION OF FOSSIL MARINE SHELLY COMMUNITIES AS A FUNCTION OF BOTTOM WATER OXYGENATION IN THE BLUE LIAS AND CHARMOUTH MUDSTONE FORMATIONS (EARLY JURASSIC) OF DORSET AND EAST DEVON, UK.

7.1. Introduction

Taphonomic distortion of fossil marine shelly communities via early diagenetic aragonite dissolution is widely accepted in modern literature (e.g. Cherns and Wright, 2000, Wright et al., 2003, Bush and Bambach, 2004, James et al., 2005, Cherns et al., 2008, Cherns and Wright, 2009, Hendy, 2011, Foote et al., 2015, Jordan et al., 2015). Selective dissolution of originally aragonitic groups is by microbially induced acidity in the TAZ, a product of the aerobic bacterial decay of organic matter (e.g. Canfield and Raiswell, 1991a) strengthened by oxidation of hydrogen sulphide produced in the sulphate reduction zone (e.g. Aller, 1982, Canfield and Raiswell, 1991a, Sanders, 2003, Sanders, 2004) (see review by Cherns et al., 2008). In similar Early Jurassic offshore carbonate ramp settings, taphonomic distortion is potentially responsible for the loss of up to approximately 80 % of original ecological diversity among skeletal fauna (Wright et al., 2003). Nonetheless, the preservation of aragonitic fossils in a range of different geological and geographical settings (e.g. Wilcox and Lockley, 1981, Webby and Percival, 1983, Noe-Nygaard et al., 1987, Oschmann, 1988, Oschmann, 1991, Oschmann, 1993, Cherns and Wright, 2000, Nelson and James, 2000, Radley and Barker, 2000, Fürsich and Pandey, 2003, Nelson et al., 2003, Wright et al., 2003, Wheeley and Twitchett, 2005, Cherns and Wright, 2009, see review by Cherns et al., 2008) indicates that the loss of these groups was not ubiquitous.

Depositional conditions that preserve a truer representation of original ecological skeletal diversity and abundance were defined as ‘taphonomic windows’ by Cherns et al. (2008). Early silica replacement was recognised as one such example from Silurian (Cherns and Wright, 2000) and Jurassic (Wright et al., 2003) sediments. Cherns et al. (2008) subsequently expanded the categorisation of taphonomic window fauna to include storm beds, shell plasters or other shell beds of dysaerobic/anoxic environments, and hardgrounds. In the Early Jurassic of Dorset, Jordan et al. (2015) and Jordan (2016) described the atypical survival of an abundant ammonoid assemblage in Bed 29 as per Lang (1924), which the authors interpreted to be the product of temporary anoxic conditions that limited oxidation of hydrogen sulphide and consequent aragonite dissolution.

The aim of this chapter is to assess differential taphonomic distortion of the fossil marine shelly community for each lithology in the Early Jurassic of Dorset and East Devon and therefore qualify its influence as a function of the extent of bottom water oxygenation. Taphonomic distortion is measured as the difference between the predicted faunal

assemblage minus the typical fossil assemblage; an estimate of the former is given for oxic, restricted, and dysaerobic/anoxic conditions based on observations of an early silicified fauna in Wright et al. (2003). The degree of bottom water oxygenation is theorised to influence taphonomic bias since it controls the palaeoecology of a given faunal assemblage as well as the strength and position of the TAZ; in a rhythmic sedimentary succession such as the BLF, these factors are highly variable and specific to individual lithologies (e.g. Weedon, 1986, Moghadam and Paul, 2000). The extent to which different taphonomic windows preserve true ecological abundance and diversity is also considered.

7.2. Material and methods

The BLF was examined in coastal cliff outcrops and on the exposed foreshore reefs between Lyme Regis, Dorset and Pinhay Bay, Devon. The overlying SWB and BVM were examined in cliff outcrops between Lyme Regis and Charmouth, Dorset. See Chapter 2 for locality details and a revised lithostratigraphy of each succession.

The total fossil assemblage for each of the different lithologies (bioturbated limestones, light marls, dark marls, shales, paper shales, and laminated limestones; see Chapter 2) was calculated as the sum of MNI counts from all sampled beds of that type (see Chapter 3 for data); different taxa were expressed as a proportion of the total fossil assemblage. The relative abundance of specific fossil groups (i.e. bivalves, ammonoids, etc) was given separately, as was the combined shelly component divided according to original shell biomineralogy (i.e. aragonitic, calcitic, and bimineralic [calcite + aragonite]). Indeterminate bivalves were not included in the latter since shell composition could not be determined. These results were based on data collected exclusively from the BLF, but interpretations were applied to the CMF nonetheless; this approach was necessitated by poor exposure of the CMF and was deemed an appropriate qualification since the two successions share comparable lithologies (see Chapter 2). It is important to note that this method does not account for the vertical distribution or delayed appearance of different taxa within the BLF (see Chapter 3). Taxa were considered part of the typical fossil assemblage where they occurred in over 5 % of the sampled horizons.

The analysis of taphonomic windows is based on field/hand specimen observations, palaeontology, and petrography of polished thin sections. Owing to difficulties associated with the finite sampling potential of many of these features, a qualitative approach was

taken in order to offer comparison against the respective, lithology-specific typical fossil assemblages.

7.3. Results and interpretations

7.3.1. Fossil assemblages from different lithologies in the Early Jurassic of Dorset and East Devon

Bioturbated limestones. A total of 57 limestone beds were sampled throughout the BLF (table 7.1; see Chapter 3). This lithology has the highest species richness (number of different taxa = 17; fig. 7.1a) and the greatest average MNI per bed (table 7.1). Bivalves are the dominant fossil group (relative abundance = 70 %; fig. 7.2, 1a) and epifaunal genera such as *Liostrea* and *Plagiostoma* account for a significant proportion of the overall fossil assemblage (relative abundance = 35 % and 15 % respectively; fig. 7.1a); additional surficial suspension feeders include *Pseudolimea*, *Chlamys*, *Gryphaea*, *Antiquilima*, and *Pseudopecten* (fig. 7.1a; table 7.1). Semi-infaunal bivalves are a relatively minor component and limited to *Pinna* and *Modiolus* (fig. 7.1a; table 7.1). The deep infaunal bivalves *Pleuromya* and *Pholadomya* are also rare (relative abundance = 1 % and 1 %; fig. 7.1a; table 7.1). Brachiopods are represented by the genus *Calcirhynchia* (fig. 7.1a; table 7.1) which shares a similar ecological niche with common epifaunal bivalves; despite occurring for the first time in the *Angulata* Chronozone (see Chapter 3), it is the second most abundant fossil group (relative abundance = 18 %; fig. 7.2, 1a). Ammonoids account for a total of 7 % of the overall fossil assemblage (fig. 7.2, 1a) although their relative abundance is influenced by significant local concentrations e.g. Bed 29 (see Jordan et al., 2015; see Chapter 3). Echinoids, crinoids, and gastropods are the least abundant fossils (3 %, 2 %, and > 1 % respectively; fig. 7.2, 1a; table 7.1). When the shelly component is considered as a function of original biomineralogy, calcitic groups are most abundant (relative abundance = 63 %) followed by bimineralic (27 %) and aragonitic (10 %, mostly ammonoids) forms (fig. 7.2, 1b). Originally aragonitic, deep-burrowing bivalves are typically preserved as articulated mud-filled steinkerns; the aragonite biomineralogy does not remain and total shell dissolution is common. There are rare instances of mouldic replacement in which neomorphism of the aragonitic shell to calcite has been observed. Ammonoids are generally preserved as mud-filled and/or calcitic internal moulds although partial pyrite replacement is also common (Paul et al., 2008).

Light marls. Macrofauna were present in all 10 of the light marl samples (see Chapter 3). Species richness (total number of different taxa = 7) and the average number of individuals

per bed is lower than in the bioturbated limestone lithology (fig. 7.1b; table 7.1). The fossil assemblage is bivalve dominated (relative abundance = 62 %; fig. 7.2, 2a) and includes low diversity surficial suspension feeders such as *Liostrea* (36 %), *Pseudolimea* (13 %), and *Plagiostoma* (12 %) (fig. 7.1b; table 7.1); there are no semi-infaunal nor infaunal bivalve genera (fig. 7.1b; table 7.1). Brachiopods (*Calcirhynchia*) are the second most abundant fossil group (relative abundance = 30 %) (fig. 7.2, 2a; table 7.1). Remaining taxa include echinoids (7 %) and crinoids (1 %) (fig. 7.2, 2a; table 7.1). There are no originally aragonitic shelly fossils within the assemblage (fig. 7.2, 2b); calcitic forms are dominant (relative abundance = 75 %), but there is also a small proportion of bimineralic forms (25 %) (fig. 7.2, 2b).

Dark marls. Macrofauna were recorded in all but one of the dark marl beds (2nd Tape c) and the number of individuals in the remaining samples varied extensively (range of non-zero MNI values = 2 – 83) (see Chapter 3). The total fossil assemblage shows high species richness (total number of different taxa = 12; fig. 7.1c; table 7.1). Bivalves are the dominant fossil group (64 %; fig. 7.2, 3a) and common epifaunal genera (*Liostrea*, *Plagiostoma*, and *Pseudolimea*) account for similar proportions of the overall fossil assemblage as in the light marl lithology (relative abundance = 38 %, 14 %, and 9 % respectively; fig. 7.1c; table 7.1). Additional surficial suspension feeders, specifically *Pseudopecten* and *Antiquilima*, are rare (fig. 7.1c; table 7.1). There are single occurrences of semi-infaunal (*Pinna*) and deep infaunal (*Pholadomya*) bivalve genera (fig. 7.1c; table 7.1). Brachiopods, represented by the epifaunal genus *Calcirhynchia*, are the second most abundant fossil group (relative abundance = 21 %; fig. 7.2, 3a; table 7.1). In order of decreasing relative abundance, echinoids (12 %); ammonoids (2 %); and crinoids (1 %) are also present (fig. 7.2, 3a; table 7.1). Originally calcitic shelly fossils are dominant (relative abundance = 68 %), followed by bimineralic (29 %) and aragonitic (3 %, mostly ammonoids) forms (fig. 7.2, 3b). Ammonoids are typically preserved as mud-filled, compacted moulds although pyritic internal moulds were observed in H73 (see also Jordan, 2016); both types lack original shell aragonite.

Shales. 8 out of 14 shale beds contained macrofossils (see Chapter 3). The combined fossil assemblage has a total of 8 different taxa (fig. 7.1d; table 7.1). The most abundant fossil group are bivalves (relative abundance = 90 %; fig. 7.2, 4a); epifaunal genera such as *Liostrea* and *Plagiostoma* are dominant (relative abundance = 69 % and 15 % respectively) although the semi-infaunal genus *Modiolus* (relative abundance = 1 %) occurs in the

Tilmanni Chronozone (fig. 7.1d; table 7.1; see Chapter 3). In order of decreasing relative abundance, additional taxa include echinoids (6 %), crinoids (2 %), and ammonoids (2 %) (fig. 7.2, 4a). Calcitic groups remain dominant (relative abundance = 79 %) compared with bimineralic and aragonitic forms (19 % and 2 % respectively) (fig. 7.2, 4b). Ammonoid shells are preserved as mud-filled, compacted moulds without relict aragonite.

Paper shales. Out of a total of 17 paper shale beds, 6 contained macrofauna (see Chapter 3). The combined fossil content is dominated by echinoids (relative abundance = 65 %; fig. 7.2, 5a) although this is the artefact of an atypical concentration in H51 (MNI = 13; see Chapter 3) and is not representative of the ecological macrofaunal assemblage; all other paper shales lack echinoids (see Chapter 3). Other beds contain single taxon assemblages limited to *Liostrea* or ammonoids (see Chapter 3); *Liostrea* accounts for the greater proportion of the total fossil content (30 % and 5 % respectively; fig. 7.1e; table 7.1).

Laminated limestones. The fossil assemblage of the laminated limestone lithology is taken from H36, the only sample that contained macrofauna (see Chapter 3); the remaining 6 out of 7 laminated limestones were unfossiliferous (see Chapter 3). Bivalves are the most common fossil group (relative abundance = 57 %; fig. 7.2, 6a) and whilst a single *Liostrea* valve was identified, the remaining individuals could not be attributed to a specific genus and were therefore clumped into an indeterminate group (see Chapter 3). Ammonoids account for the remaining 43 % of the fossil assemblage (fig. 7.2, 6a; table 7.1). When examined under magnification, the laminated limestone samples also contain sparse shell fragments as well as intact veliger spat (see Chapter 3).

Figure 7.1 (below) – Pie diagrams showing the relative abundance of different taxa for each lithology in the BLF of Dorset and East Devon. The total fossil assemblage was calculated as the sum of MNI counts from all sampled beds of that type (table 7.1; see Chapter 3). Key in figure.

Total taxa

a. Bioturbated limestones

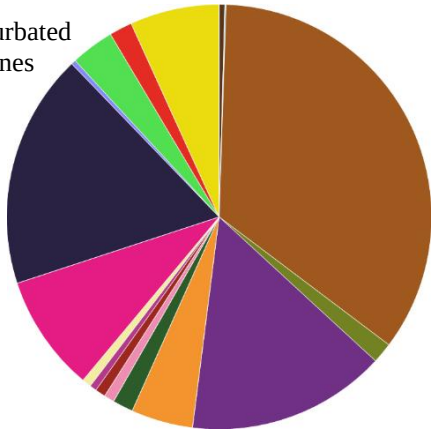

No. of different taxa = 17; MNI = 1148

b. Light marls

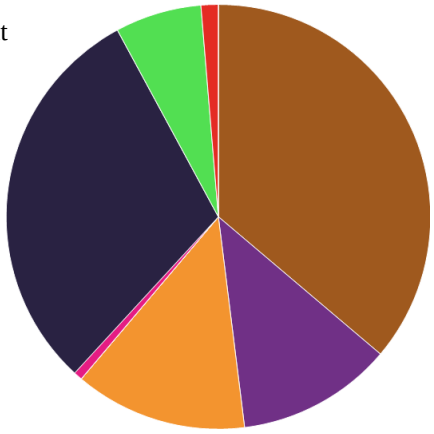

No. of different taxa = 7; MNI = 152

c. Dark marls

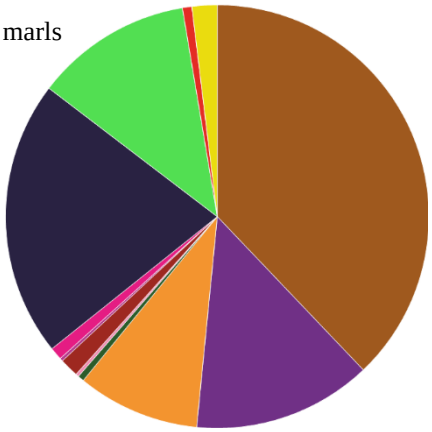

No. of different taxa = 12; MNI = 417

d. Shales

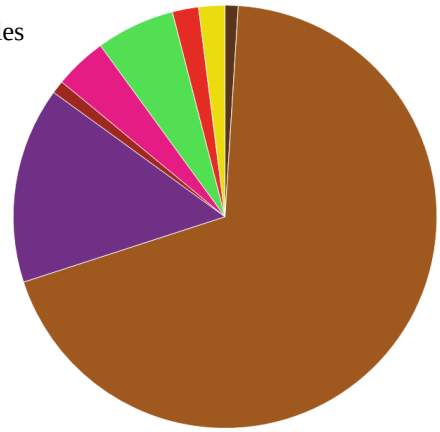

No. of different taxa = 8; MNI = 100

e. Paper shales

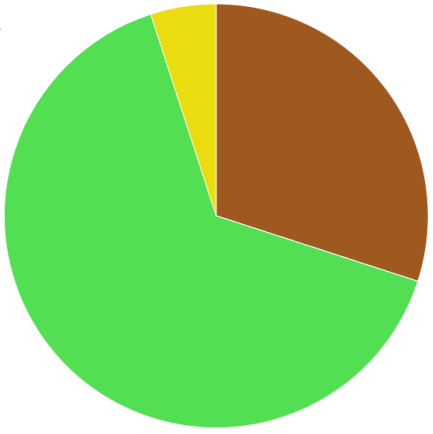

No. of different taxa = 3; MNI = 20

f. Laminated limestones

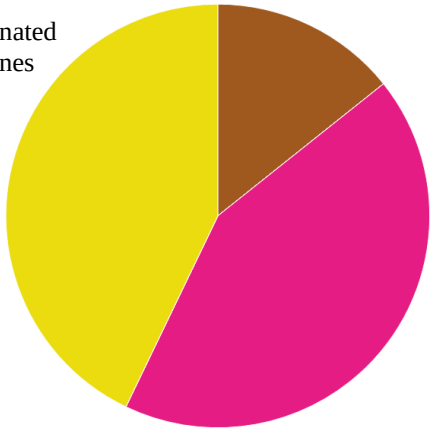

No. of different taxa = 3; MNI = 7

Modiolus minimus *Chlamys* *Liostrea* *Gryphaea* *Plagiostoma*
Pseudolimea *Antiquilima* *Pholadomya* *Pseudopecten* *Pinna*
Pleuromya Indet. bivalve *Calcirhynchia calcaria* Gastropod Echinoid
Crinoid Ammonoid

Total fauna

Shelly fossil abundance and mineral composition

1a. Bioturbated limestones

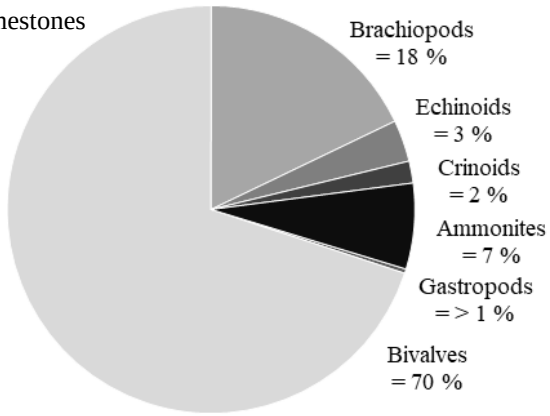

No. of different taxa = 17; MNI = 1148

1b.

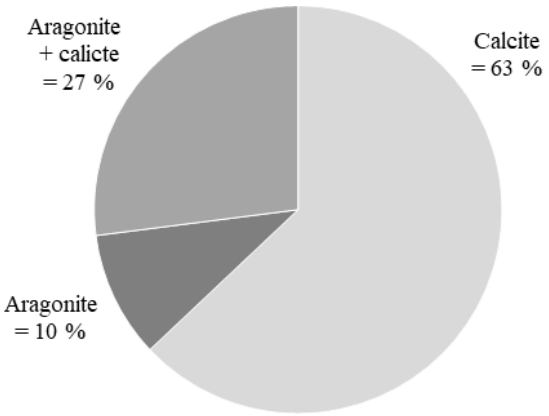

No. of different shelly taxa = 14;
MNI of shelly fauna = 988

2a. Light marls

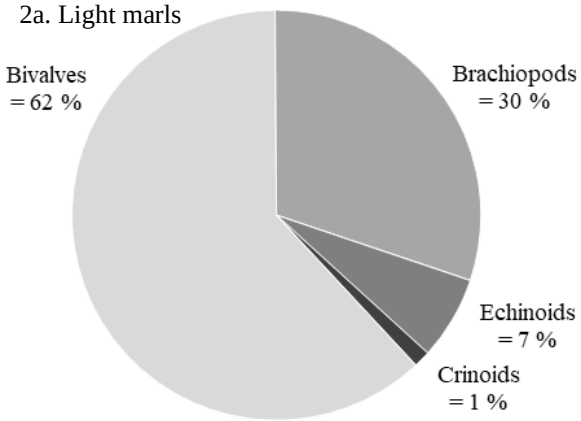

No. of different taxa = 7; MNI = 152

2b.

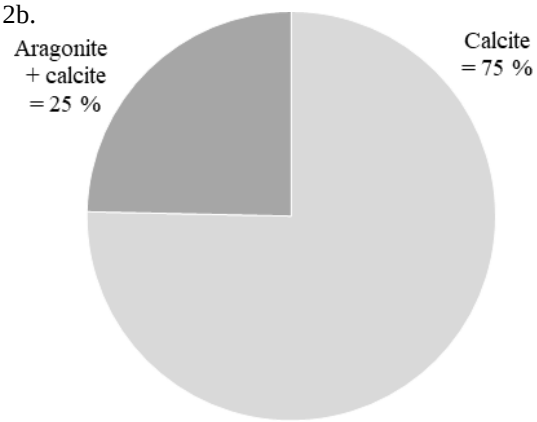

No. of different shelly taxa = 4;
MNI of shelly fauna = 139

3a. Dark marls

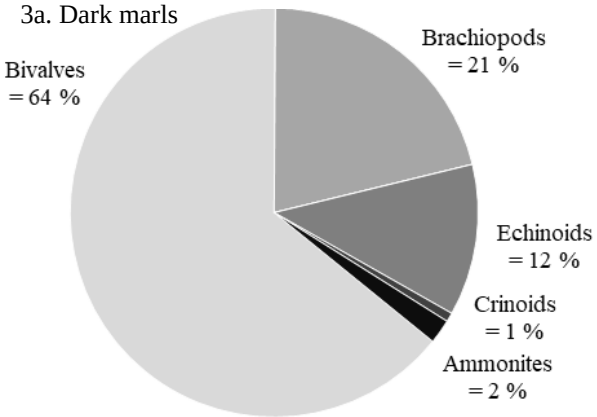

No. of different taxa = 12; MNI = 417

3b.

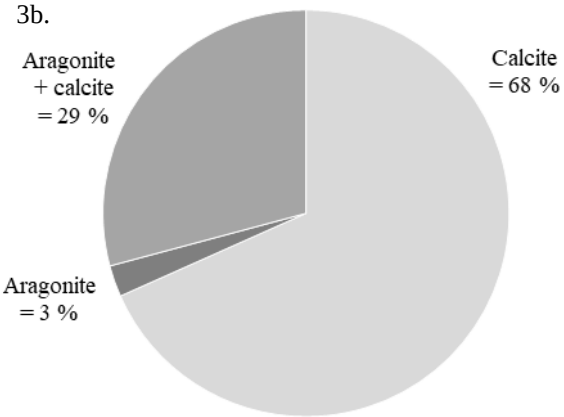

No. of different shelly taxa = 9;
MNI of shelly fauna = 360

4a. Shales

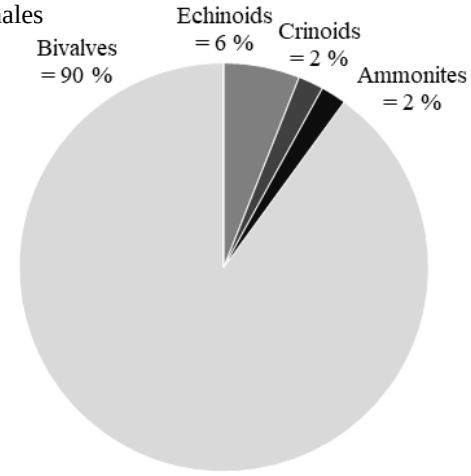

No. of different taxa = 8; MNI = 100

4b.

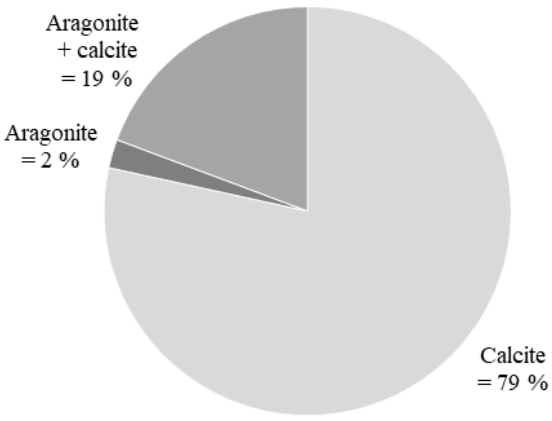

No. of different shelly taxa = 5;
MNI of shelly fauna = 88

5a. Paper shales

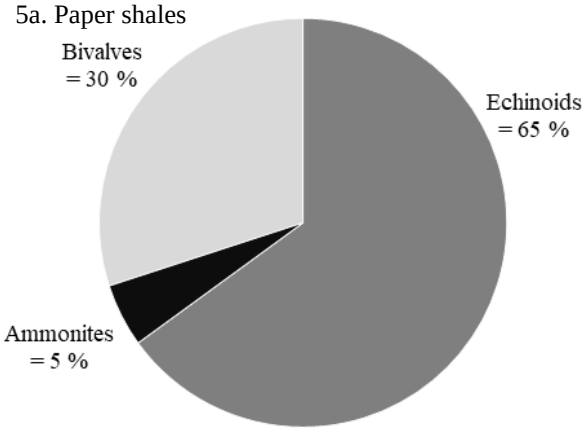

No. of different taxa = 3; MNI = 20

5b.

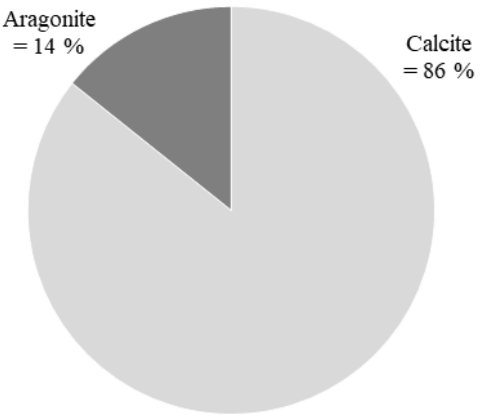

No. of different shelly taxa = 2;
MNI of shelly fauna = 7

6a. Laminated limestones

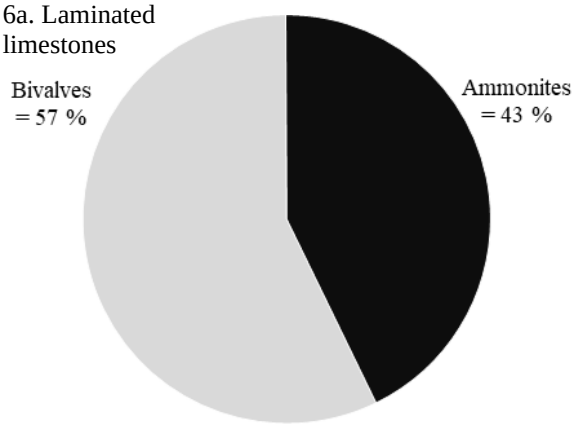

No. of different taxa = 3; MNI = 7

6b.

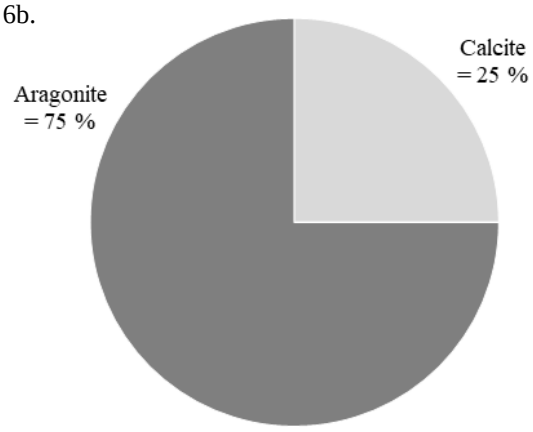

No. of different shelly taxa = 2
MNI of shelly fauna = 4

Figure 7.2 – Pie diagrams showing the proportion of different fossil groups within the total fossil assemblage (1a – 6a) as well as the shelly fossil abundance and mineral composition (1b – 6b) for each lithology in the BLF of Dorst and East Devon (table 7.1; see Chapter 3).

LITHOLOGY-SPECIFIC PALAEOECOLOGY										
Lithology	MNI	*Modiolus minimus*	*Chlamys*	*Liostrea*	*Gryphaea*	*Plagiostoma*	*Pseudolimea*	*Antiquilima*	*Pholadomya*	*Pseudopecten*
LST	1148	5	1	399	18	174	54	18	9	9
L.M	152	0	0	55	0	18	20	0	0	0
D.M	417	0	0	158	0	57	39	2	1	6
SHA	100	1	0	69	0	15	0	0	0	1
P.S	20	0	0	6	0	0	0	0	0	0
L.LST	7	0	0	1	0	0	0	0	0	0
	No. of beds	*Pinna*	*Pleuromya*	Indeterminate bivalve	*Calcirhynchia calcaria*	Gastropod	Echinoid	Crinoid	Ammonoid	
LST	57	6	8	102	205	4	38	20	78	
L.M	10	0	0	1	46	0	10	2	0	
D.M	28	1	0	4	88	0	50	3	8	
SHA	14	0	0	4	0	0	6	2	2	
P.S	17	0	0	0	0	0	13	0	1	
L.LST	7	0	0	3	0	0	0	0	3	

Table 7.1 – The sum of macrofaunal MNI counts for different lithologies in the BLF of Dorset and East Devon. For individual data refer to Chapter 3. LST = limestone, L.M = light marl, D.M = dark marl, SHA = shale, P.S = paper shale, L.LST = laminated limestone.

7.3.2. Fossil assemblages from different taphonomic windows in the Early Jurassic of Dorset and East Devon

Storm beds. Cherns et al. (2008) described the potential for storm beds to preserve a truer representation of original ecological molluscan diversity despite typically being associated with the disarticulation and fragmentation of fossils (e.g. Kidwell and Bosence, 1991). The authors discuss multiple factors that contribute to the survival of aragonitic groups in this setting such as winnowing of fine grained sediment and organic matter that acts to restrict microbially induced acidity (Wright et al., 2003), rapid burial that limits dissolution by positioning vulnerable shells below the TAZ, and selective dissolution of shell fragments to buffer porewater acidity (see review by Cherns et al., 2008).

a. BLF (general). True storm beds were not observed in the BLF of Dorset and East Devon which, according to previous authors, was positioned below storm wave base (e.g. Paul et al., 2008, Radley, 2008, Jordan, 2016). Whilst there is abundant evidence for comparable storm-related depositional and erosive processes operating in various lithologies within the succession (e.g. Hallam and Lang, 1960, Weedon, 1986, Weedon, 1987, Paul et al., 2008, Jordan, 2016, Weedon et al., 2018), these do not appear to have been associated with the preferential preservation of originally aragonitic molluscs. In comparison with the model described by Cherns et al. (2008), storm scours – required to entrain epifauna and prospective shallow burrowers – are evident (e.g. Martin, 2004, Paul et al., 2008, Jordan, 2016, Weedon et al., 2018) and subsequent transportation is typified by the disarticulation, fragmentation, and random orientation of bioclasts (Hallam and Lang, 1960, Paul et al., 2008, Jordan, 2016). However, many of the beds that contain evidence for storm-related deposition also exhibit homogenisation of the surrounding sediment and/or the presence of trace fossils; this indicates that rapid deposition, in juxtaposition to the taphonomic window described by Cherns et al. (2008), rarely buried shells below the redox boundary and therefore outside of the acidic influence of the TAZ. The preservation potential of originally aragonitic fauna in these non-anoxic settings was further reduced by the winnowing of fine grained sediment and organic matter that regularly followed storm-related deposition in the BLF (*sensu* Weedon et al., 2018); periods of non-deposition would have prolonged residency time within the TAZ and therefore sustained selective dissolution of vulnerable shelly groups. Consistent with these interpretations, winnowed shell layers are common (see also Hallam, 1964, Weedon, 1986, Weedon, 1987, Jordan,

2016, Weedon et al., 2018) and contain macrofaunal assemblages dominated by calcitic and bimineralic forms.

Weedon et al. (2018) discussed an alternative preservation model in which rapid, storm-related deposition was a contributing factor to the preservation of originally aragonitic fauna – particularly ammonoids – but that it required a subsequent period of non-deposition to initiate early limestone cementation prior to aragonite dissolution. Whilst Weedon et al. (2018) succeeded in demonstrating that this could improve the preservation potential of some vulnerable shelly groups, the predominance of large-bodied ammonoid fossils and bioturbation of the host sediment indicate that selective dissolution of small-bodied individuals could have occurred in the period of time between rapid deposition and non-deposition/limestone formation. Cherns and Wright (2011) recognised that taphonomic distortion is closely linked to the size of the shell and that small forms/micromolluscs, irrespective of biomineralisation, are vulnerable to dissolution in the TAZ (Cherns and Wright, 2011).

b. Black Arnioceras Bed, SWB. At the base of SB 12 (*sensu* Gallois, 2008a), in the western part of Black Ven, there is a thick bed (average = 0.37 m) of limestone-bearing paper shales known locally as the Black *Arnioceras* Bed (see Chapter 2). Black *Arnioceras* concretions are unique in that they preserve a densely packed layer of originally aragonitic molluscs dominated by *Arnioceras* ammonoids (fig. 7.3); according to Gallois (2008a), the latter reflect a range of different ontogenetic development stages including eggs (not observed in this study), post-embryonic, and mature individuals. Small (0.1 – 1 mm), articulated spat of the aragonitic cardiid bivalve genus *Protocardia* are mixed with similar fragmented and disarticulated valves (fig. 7.3). Turreted gastropod spat are also present (fig. 7.3).

All taxa had a nektonic or planktonic (at the time of death) mode of life and were therefore unaffected by inferred dysaerobic/anoxic bottom water conditions associated with the paper shale and laminated limestone lithologies (e.g. Weedon, 1986, Moghadam and Paul, 2000, Arzani, 2004; see Chapter 2). The lack of formerly aragonitic groups otherwise considered typical of this taphonomic window, particularly shallow infaunal bivalves (e.g. Cherns et al., 2008), was a product of prevailing environmental conditions and not taphonomic bias. Benthos were ill-suited to environments with low levels of oxygen availability and sediments lacking oxygen.

Owing to the relative abundance of randomly orientated fossils (up to approximately 60 % of the total sediment composition; fig. 7.3), previous authors attribute the Black *Arnioceras* shell layer to an episode of high energy storm deposition (e.g. Gallois, 2008a). Fragmentation and disarticulation of bioclasts is consistent with post-mortem transport, but the presence of intact spat points to a separate, additional stage of planktotrophic settling during a short-lived quiescent period. Black *Arnioceras* concretions are sedimentologically similar to other laminated limestones from the CMF described by Curtis et al. (2000), indicating they likely share a comparable depositional/diagenetic origin; according to Curtis et al. (2000), concretions are the product of rapid burial, following deposition of a suspended sediment package, that resulted in the onset of anoxia and initiated early calcite cementation. In the Black *Arnioceras* Bed, the causal sediment drape was evidently sufficient to trap and bury a significantly greater quantity of shelly fauna. The formational model described by Curtis et al. (2000) is consistent with processes attributed to increased preservation potential in storm beds by Cherns et al. (2008). Early cementation (*sensu* Curtis et al., 2000) would have also promoted the survival of originally aragonitic fauna during burial diagenesis (*sensu* Cherns et al., 2008).

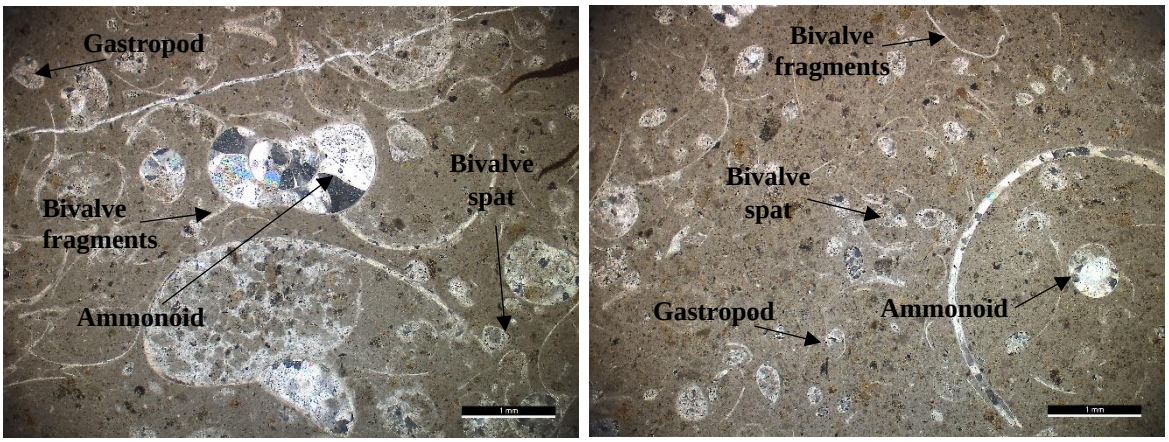

Figure 7.3 – Photomicrographs of the Black *Arnioceras* concretions under cross-polarised light. Ammonoids, indeterminate shell fragments, and intact veliger spatfall (bivalves and gastropods) are abundant, preserved by coarse (50 – 500 μm) calcite spar. Scale = 1 mm.

Shell plasters and other shell beds of dysaerobic/anoxic environments. Cherns et al. (2008) recognised the potential for dysaerobic/anoxic conditions to facilitate the survival of originally aragonitic infauna and epifauna owing to a limited residency time within the acidic TAZ. Irrespective of the causal mechanism, elevation of the redox boundary prevents microbially induced acidity and bioturbational re-oxidation of the sediment column – processes known to result in the selective dissolution of aragonitic shells (Cherns

and Wright, 2000, Wright et al., 2003, Cherns et al., 2008). Episodic anoxia within settings prone to fluctuating redox conditions was capable of causing the death and preservation of autochthonous molluscan assemblages (Cherns et al., 2008); the authors also assert that transport and deposition of aragonitic shells into these environments via storm events or planktotrophic spatfall would have increased the preservation potential of vulnerable shelly groups (Cherns et al., 2008).

a. BLF (general). Inferred dysaerobic/anoxic sediments in the BLF do not appear to be associated with the preservation of originally aragonitic bivalves (see Chapter 3). Thin shell pavements resulting from the upward migration and mortality of infauna during anaerobic intervals (*sensu* Oschmann, 1991, Cherns et al., 2008) were not observed. *Liostrea* valves present in multiple paper shale beds (e.g. Paul et al., 2008; see Chapter 3) point to the potential for anoxia to terminate opportunistic benthic colonies (Jordan, 2016), but there were no aragonitic groups preserved in this way. Since originally aragonitic bivalves in these strata were predisposed to an infaunal mode of life (e.g. *Pleuromya* and *Pholadomya*), a lack of these shells in dysaerobic/anoxic environments is attributed to palaeoecological factors, not taphonomic distortion. Jordan et al. (2015) and Jordan (2016) discussed a taphonomic model based on Bed 29 of the BLF (*sensu* Lang, 1924) that facilitated the preservation of a concentration lagerstätte dominated by formerly aragonitic *Metophioceras* ammonoids (see also Chapter 3); this model can be applied more widely to cover nektonic and planktonic aragonitic molluscan fauna. The authors suggest that deposition and burial of aragonitic shells during anoxic intervals increased their preservation potential since processes associated with acidity in the TAZ, including the bioturbational oxidation of sulphides, were restricted (Jordan et al., 2015, Jordan, 2016).

b. Spittles Arnioceras Bed, BVM. The Spittles *Arnioceras* Bed is positioned near to the top of BVM 7 and is exclusive to the Spittles Landslide Section of the Black Ven exposure (see Chapter 2). It occurs as a thin layer (30 mm) of pyritic limestones contained within pyritiferous paper shales (see Chapter 2). Each concretion is comprised of a laminated limestone core surrounded by an irregular pyritic rim up to 10 mm in thickness (fig. 7.4; see Chapter 2). The molluscan fossil assemblage contains *Arnioceras* ammonoids of various ontogenetic development stages as well as veliger spat of the cardiid bivalve genus *Protocardia* and an indeterminate, turreted gastropod genus (fig. 7.4). Molluscan fauna are exclusive to originally aragonitic, nektonic and planktonic groups. Fossils in the limestone core are preserved as internal moulds replaced by coarse calcite spar (100 μm – 2 mm; fig.

7.4); cement textures are consistent with those described by Curtis et al. (2000). In the pyritic rim, replacement is via a combination of pyrite (as internal precipitate and chamber-lining pyrite; see Chapter 5) and calcite cement (fig. 7.4). Direct replacement of the shell by calcite and pyrite is common, but its microstructure was not preserved (fig. 7.4).

The laminated limestone core of these Spittles *Arnioceras* concretions has a variable sediment composition, including irregular – occasionally upward fining – pyritic, peloidal, microsparitic, and organic/clay-rich laminae (fig. 7.4; see Chapter 2). Coupled with an abundance of disarticulated and fragmented shells arranged approximately parallel to bedding (fig. 7.4), this texture points to sediment settling from resuspension following limited post-mortem transport (*sensu* Curtis et al., 2000). The survival of a high proportion of intact spat required a separate stage of quiescent deposition in order to facilitate planktotrophic spatfall or death and settling as a result of temporary seawater anoxia. Despite a possible allochthonous origin, there is no evidence to suggest that redox conditions at the bioclastic source differed from the depositional setting.

Consistent with an inferred dysaerobic/anoxic origin for both lithologies associated with the Spittles *Arnioceras* Bed (e.g. Weedon, 1986, Moghadam and Paul, 2000, Arzani, 2004; see Chapter 2), extensive iron sulphide precipitation indicates that sediment porewaters were anaerobic at the time of deposition or shortly after burial. The lack of infaunal and epifaunal taxa is also characteristic of inhospitable bottom waters. As described by Cherns et al. (2008), the survival of originally aragonitic fauna in this setting was achieved via a limited residency time within the TAZ and/or accumulation below the redox boundary. The preservation of undisturbed microlaminations supports a lack of bioturbational oxidation of the upper sediment column which is known to promote acidity in the TAZ (e.g. Wright et al., 2003, Cherns et al., 2008). Alkalinity generated via processes associated with BSR and iron sulphide precipitation (e.g. Coleman, 1985, Fisher, 1986, Coleman and Raiswell, 1995; see Chapter 5) would have contributed to the prevention of aragonite dissolution during early burial diagenesis, particularly where fragmented shells acted to buffer acidity (see review by Coleman and Raiswell, 1995).

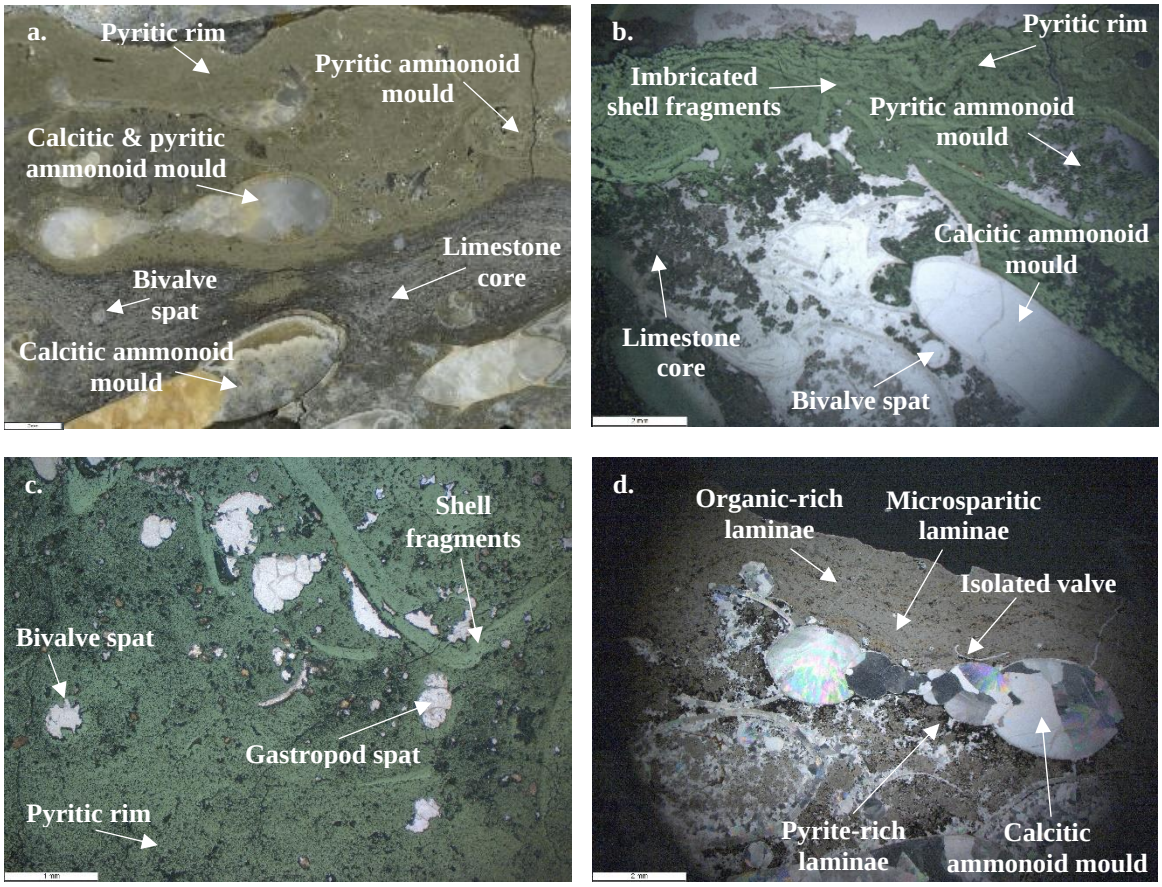

Figure 7.4 – Multiple photographs/photomicrographs of Spittles *Arnioceras* concretions. a. cross-sectioned hand specimen to show the fossiliferous shell bed with abundant *Arnioceras* ammonoids in the limestone core and outer pyrite rim; b. photomicrograph of a concretion under reflected light microscopy showing the composition of the pyritic rim; c. photomicrograph of intact veliger spat within the pyritic rim under reflected light microscopy; d. photomicrograph of the laminated limestone core with sectioned calcitic ammonoid moulds. Scale (a., b., and d.) = 2 mm; (c.) = 1 mm.

Goldstone Bed, BVM. Positioned near to the centre of BVM 9 at the Pinnacle Landslide Section of the Black Ven exposure, the Goldstone Bed is a laterally limited occurrence of pyritiferous limestone concretions contained within a thin layer (20 mm) of paper shales (see Chapter 2). At its centre, and present in both lithologies alike, is a pyritic lens (up to 2 mm in thickness) comprised almost entirely of intact veliger spat from the cardiid bivalve genus *Protocardia* (P. Palmer *pers comms with* M. Foster, 1992) (fig. 7.5; see Chapter 2); there are no adult *Protocardia*. Indeterminate turreted gastropod larvae and ammonoids (e.g. *Asteroceras*, *Promicroceras*, and *Xipheroceras*) are also present (fig. 7.5). Molluscan fauna are exclusive to formerly aragonitic, nektonic and planktonic groups. Fossil preservation is consistent with the Spittles *Arnioceras* Bed and internal moulds are formed

of a combination of pyrite precipitate and calcite cement (fig. 7.5). The original shell was replaced by calcite spar (fig. 7.5).

The fossiliferous Goldstone layer is a product of planktotrophic spatfall (P. Palmer *pers comms with* M. Foster, 1992). The abundance of intact, articulated *Protocardia* indicates a lack of post-mortem transport. Previous authors have described the unsuccessful settling and mortality of veliger larvae as a consequence of oxygen starvation during periods of prolonged anoxia (e.g. Oschmann, 1993, Cherns et al., 2008). In the Goldstone Bed, P. Palmer (*pers comms with* M. Foster, 1992) suggests that a small number of individuals survived the settling stage, albeit for a limited period of time, since there are two distinct size ranges within the assemblage. Whilst this observation necessitates an interval of low oxygen availability, extensive iron sulphide precipitation within the surrounding sediment indicates a predominance of local reducing conditions, possibly contained within micro-environments, or the establishment of anoxic porewaters shortly after burial. The lack of bioturbational disturbance – and thus the preservation of sub-millimetre peloidal, microsparitic, and organic-rich laminae (see Chapter 2) – supports an inferred dysaerobic/anoxic origin (*sensu* Curtis et al., 2000). The survival of originally aragonitic fauna, as discussed previously, is facilitated via a limited residency time within the acidic TAZ (*sensu* Cherns et al., 2008) and alkalinity generated via processes associated with BSR and iron sulphide precipitation (e.g. Coleman, 1985, Fisher, 1986, Coleman and Raiswell, 1995; see Chapter 5).

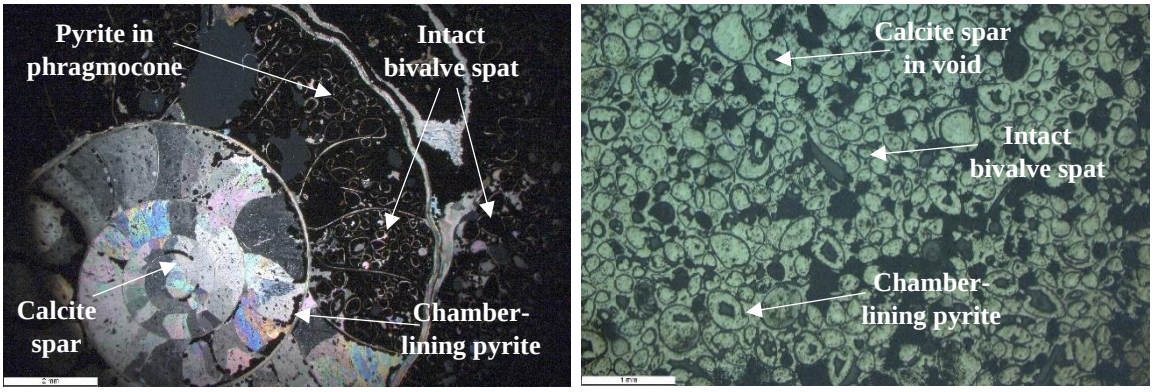

Figure 7.5 – Photomicrographs of the pyritic shell bed preserved in Goldstone concretions. Left: an internal *Promicroceras* ammonoid mould replaced by coarse calcite cement and pyrite precipitate, viewed under cross-polarised light. Right: the pyritiferous, fossiliferous shell bed dominated by articulated bivalve spat (*Protocardia*), viewed under reflected light. Scale = 2 mm and 1 mm respectively.

Syn-sedimentary pyritisation. Pyrite replacement of ammonoid moulds, specifically as it occurs in the upper BVM (BVM 15 and BVM 17; see Chapter 2), is introduced as a new taphonomic window (*sensu* Cherns et al., 2008; see Chapter 5). This type of preservation occurs dispersed throughout the Early Jurassic of Dorset and East Devon, as well as other biogeographical and geological settings, but the BVM contains a particularly fine example (see Chapter 5). BVM 15 and BVM 17, best exposed at East Beach on the Stonebarrow exposure, are predominantly made up of dark marls (Lang and Spath, 1926; see Chapter 2) although local sedimentological variability is not uncommon.

It was not possible to quantify the relative abundance of different faunal groups in these strata owing to the nature of the exposure, but observations based on the number of *ex situ* specimens indicate that the fossil assemblage was dominated by ammonoids (see Chapter 5). In their original description of the equivalent section, Lang and Spath (1926) identified a total of 7 different bivalve genera; this remains an accurate record according to contemporary collectors. Within the bivalve assemblage there was a predominance of calcitic and bimineralic epifaunal genera (*Inoceramus*, *Oxytoma*, *Ostrea*, *Aequipecten* [*Pseudopecten*], and *Plagiostoma*) and a single semi-infaunal genus *Modiolus* (Lang and Spath, 1926). Formerly aragonitic bivalves were limited to the shallow burrower *Nuculana* [*Mesosacella*] (Lang and Spath, 1926). The brachiopod genus *Rhynchonella*, which shares a similar ecological niche and taphonomic survival rate with the aforementioned epifauna, was also recorded by Lang and Spath (1926). The precise replacement context of specimens described by Lang and Spath (1926) could not be determined owing to access restrictions at the Natural History Museum (NHM) during the Covid-19 pandemic. As a result, this preservation model can only be applied to formerly aragonitic ammonoid shells since these were collected in large numbers for this study (see Chapter 5). It is however important to note that there is no *a priori* reason to suggest that pyrite replacement was not capable of preserving shelly groups other than ammonoids, nor that palaeoenvironmental inferences based on previously recorded taxa are unreliable, since pyritic moulds of several bivalve genera have also been identified in private collections (e.g. *Inoceramus*, *Oxytoma*, *Pseudopecten*, and *Plagiostoma*).

The presence of epifaunal and infaunal bivalve genera throughout these strata (e.g. Lang and Spath, 1926, Lord et al., 2010), as well as the poor preservation/mixing of original sediment laminae, indicates that accumulation occurred in oxygenated bottom waters. These conditions would have typically promoted the selective dissolution of formerly

aragonitic shelly fauna (e.g. Wright et al., 2003). In the proposed taphonomic window, the survival of ammonoids was a consequence of processes associated with syn-sedimentary pyritisation that inhibited the acidic influence of the TAZ (see Chapter 5). Since ammonoids were positioned in the upper, oxic sediment column, aerobic decay of retained soft tissues was essential in order to form a reducing micro-environment within the shell (*sensu* Hudson and Palframan, 1968, Hudson, 1982, Fisher, 1986) that enabled these reactions to occur (see Chapter 5). Local buffering effects were imposed by direct pyrite precipitation using *in situ* sources of iron to form S^0 via iron reduction and iron limitation during BSR (*sensu* Coleman, 1985, Fisher, 1986, Coleman and Raiswell, 1995). The transition away from initial pyrite precipitation in the reducing micro-environment occurred once widespread anoxic conditions were established in the surrounding sediment. Assuming *in situ* sources of iron were exhausted, the reaction pathway for subsequent pyrite formation generated acidity (via H^+) that was buffered by dissolution of the aragonitic shell (*sensu* Coleman and Raiswell, 1995; see Chapter 5).

Stratigraphy	Dominant background fauna	Background fauna – shell composition, life habit	Dominant taphonomic window fauna	Taphonomic window fauna – shell composition, life habit	Taphofacies	Palaeoenvironmental setting
1. Storm beds						
1.1. Black *Arnioceras* Bed, SB 12 (*sensu* Gallois, 2008a), SWB	Low faunal abundance, sparse ammonoids	Aragonitic, nektonic	Ammonoids, veliger spat	Aragonitic, nektonic and planktonic	Rapid burial, storm bed in a dysaerobic/anoxic environment	Dysaerobic/anoxic, offshore carbonate ramp, edge of storm wave base
2. Shell plasters and other shell beds of dysaerobic/anoxic environments						
2.1. Ammonite Graveyard, Bed 29, BLF (e.g. Jordan et al., 2015, Jordan, 2016; see Chapter 3)	Low diversity epifaunal bivalves (e.g. *Liostrea*, *Plagiostoma*, *Pseudolimea*), *Calcirhynchia*, ammonoids	Mostly calcitic and bimineralic, epifaunal, aragonitic, nektonic	Ammonoids, rare gastropods, Low diversity epifauna (e.g. *Liostrea*, *Plagiostoma*, *Calcirhynchia*)	Aragonitic, nektonic and epifaunal, calcitic and bimineralic, epifaunal	Anoxic intervals	Fluctuating bottom water redox state, offshore carbonate ramp, below storm wave base
2.2. Spittles *Arnioceras* Bed, BVM 7, BVM	Low faunal abundance, sparse ammonoids	Aragonitic, nektonic	Ammonoids, veliger spat	Aragonitic, nektonic and planktonic	Settling of suspended sediment, deposition in a dysaerobic/anoxic environment, syn-sedimentary pyrite replacement	Dysaerobic/anoxic, offshore carbonate ramp, edge of storm wave base
2.3. Goldstone Bed, BVM 9, BVM	Low faunal abundance, sparse ammonoids	Aragonitic, nektonic	Veliger spat, ammonoids	Aragonitic, planktonic and nektonic	Unsuccessful settling of spat, accumulation in a dysaerobic/anoxic environment, syn-sedimentary pyrite replacement	Dysaerobic/anoxic, offshore carbonate ramp, below storm wave base
3. Syn-sedimentary pyritisation						
3.1. BVM 15 and BVM 17, BVM	Low diversity epifaunal bivalves, ammonoids	Mostly calcitic and bimineralic, epifaunal, aragonitic, nektonic	Ammonoids	Aragonitic, nektonic	Local micro-reducing conditions within the shell, syn-sedimentary pyrite replacement	Oxic, offshore carbonate ramp

Table 7.2 – Summary of taphonomic windows from the Early Jurassic of Dorset and East Devon.

7.4. Discussion

The results presented in this chapter show qualifiable, lithology-specific variance between the typical shelly fossil assemblage – based on taxa that occurred in over 5 % of sampled horizons – and the predicted ecological assemblage. The potential for different taphonomic windows to preserve a truer representation of original, ecological skeletal diversity and abundance was also unequal. These concepts can be expressed by modelling taphonomic distortion – ranging from no discernible effect to a major decrease in the relative abundance and diversity of vulnerable shelly fauna – as a function of different states of bottom water oxygenation.

Oxic environments. The maximum relative abundance and diversity of shelly fauna is predicted to occur in oxygenated bottom waters since palaeoenvironmental factors were conducive to habitation. The predicted faunal assemblage is based on comparisons with an early silicified fauna in Wright et al. (2003) and indicates that the shelly palaeocommunity would have occupied the nektonic, epifaunal, semi-infaunal, and infaunal tiers (fig. 7.6). Diagenetic processes known to strengthen the acidic TAZ, specifically aerobic decay of organic matter (*sensu* Canfield and Raiswell, 1991a) and bioturbational oxidation of hydrogen sulphide (*sensu* Aller, 1982, Canfield and Raiswell, 1991a, Sanders, 2003, Sanders, 2004) are typical of the upper, oxic sediment column (see review by Cherns et al., 2008); as a result, taphonomic distortion via selective dissolution of originally aragonitic groups is predicted to be most significant in this setting. In the Early Jurassic of Dorset and East Devon, the two lithologies that are generally attributed to an oxic depositional environment are bioturbated limestones and light marls (e.g. Weedon, 1986, Moghadam and Paul, 2000, Weedon et al., 2018; see Chapter 2). Since both form under similar pre-diagenetic conditions (Weedon et al., 2018), they offer an opportunity to examine taphonomic distortion associated with diagenetic processes such as carbonate cementation.

The typical fossil assemblage of both oxic lithologies is dominated by low diversity, calcitic and bimineralic epifaunal bivalve genera (*Liostrea*, *Plagiostoma*, and *Pseudolimea*) as well as the calcitic brachiopod *Calcirhynchia* (fig. 7.6; table 7.1); these taxa share a similar ecological niche and taphonomic survival rate. Despite a basic similarity between the key components, the remaining fossil assemblage differs significantly (fig. 7.6; table 7.1). Bioturbated limestones show greater species richness among calcitic and bimineralic epifaunal bivalves (*Gryphaea*, *Pseudopecten*, and *Antiquilima*) and contain bimineralic semi-infauna (*Modiolus* and *Pinna*), originally

aragonitic deep infauna (*Pholadomya* and *Pleuromya*), and ammonoids – none of which were present in the light marl lithology (fig. 7.6; table 7.1). Gastropods were exclusive to the bioturbated limestones but not counted within the typical fossil assemblage owing to their rarity (fig. 7.6; table 7.1). Assuming that original shelly diversity was consistent for the bioturbated limestones and light marls as a result of comparable pre-diagenetic depositional conditions (e.g. Weedon et al., 2018; see Chapter 2), and that this ecological assemblage was similar to the early silicified fauna of Wright et al. (2003), then the preservation of different fossil assemblages within each lithology indicates that the extent of taphonomic distortion was uneven.

In the light marl lithology, selective dissolution within the TAZ appears to have eradicated the aragonitic molluscan component, including deep-burrowing anomalodesmatan bivalves and gastropods (fig. 7.6). This is also the only lithology in which ammonoids were not preserved (fig. 7.6; table 7.1). Consistent with observations by Cherns and Wright (2009), the fossil assemblage was further depleted via the loss of the entire shallow infaunal tier and a reduction in the number of epifaunal bivalve genera (fig. 7.6). Whilst the dissolution of some bimineralic semi-infauna was possible, perhaps owing to a thinner shell and thin outer calcitic layer (e.g. *Modiolus*), the lack of common thick-shelled pteriomorph bivalves (e.g. *Pinna* and *Gryphaea*) is difficult to attribute to taphonomic bias and so the cause of their omission remains unclear. Based on the typical fossil assemblages, taphonomic distortion appears to have had a lesser relative impact on the bioturbated limestone lithology (fig. 7.6). It is however important to note that the extent of taphonomic distortion was not uniform and many individual limestone beds contain differing fossil assemblages, some of which lack formerly aragonitic molluscs (see Chapter 3). The overall diversity of epifaunal bivalves in the bioturbated limestone lithology is similar to that recorded in the early silicified fauna of Wright et al. (2003), albeit with some variation in the specific genera present (fig. 7.6). Consistent with observations by previous authors (e.g. Fürsich et al., 2001, Wright et al., 2003, Cherns and Wright, 2009), deep-burrowing aragonitic anomalodesmatan bivalves (*Pholadomya* and *Pleuromya*) occasionally survived selective dissolution and were preserved *in situ* (fig. 7.6; see Chapter 3). Formerly aragonitic ammonoids were also common (e.g. Paul et al., 2008, Weedon et al., 2018; fig. 7.6; table 7.1). The shallow infaunal tier was poorly represented and only the bimineralic genera *Modiolus* and *Pinna* were present (fig. 7.6; table 7.1). The relative abundance of aragonitic gastropods was also reduced (e.g. Wright et al., 2003).

The differential extent of taphonomic distortion in the bioturbated limestone lithology compared with the light marl lithology is, in part, a consequence of the unequal influence of diagenetic processes associated with carbonate cementation. James et al. (2005) predicted that aragonitic fauna should be well represented in hardgrounds where the shell was locked into the sediment prior to dissolution (see review by Cherns et al., 2008). Cherns et al. (2008) later suggested that mouldic replacement of these groups following early lithification could function as a taphonomic window, even if the original shell was later dissolved by acidity within the TAZ. This was true of the *in situ*, deep-burrowing aragonitic anomalodesmatan bivalves present in bioturbated limestones (see Chapter 3); *Pholadomya* and *Pleuromya* survived taphonomic processes associated with the Missing Molluscs effect because they were positioned at the base of/below the shallow-burial zone of dissolution and preserved where early cementation enabled retention of the mould (e.g. Cherns and Wright, 2009). Weedon et al. (2018) also recognised that preservation of vulnerable shelly groups, particularly ammonoids, was achieved where carbonate cementation occurred prior to aragonite dissolution. However, whilst Weedon et al. (2018) succeeded in demonstrating that the preservation potential of some formerly aragonitic fauna was improved, the frequent predominance of large-bodied ammonoids in homogenised sediments implies that selective dissolution of small-bodied taxa/individuals could have occurred in the period of time between rapid deposition and non-deposition/limestone formation, a transition that Weedon et al. (2018) note was not instantaneous. The authors also state that the relative timing of carbonate cementation varied on a bed-by-bed basis, including post-dating aragonite dissolution, such that the preservation of formerly aragonitic fauna was not consistent (Weedon et al., 2018). As a result, early cementation in this context is not a true taphonomic window, nor can the presence of large-bodied ammonoids found throughout the section be considered indicative of a more complete representation of true ecological molluscan diversity and abundance. There are additional factors that may have potentially affected the extent of taphonomic distortion within the bioturbated limestone lithology – including the scale of rapid burial that preceded non-deposition and the degree to which early dissolution of shell aragonite, particularly of small or thin-shelled taxa, was achieved in order to facilitate cementation – but these need to be considered at a greater resolution than the current study.

Despite extensive evidence for taphonomic distortion, it is important to note that the regularity with which inferred oxic lithologies in the BLF yield anoxic Fe_{HR}/Fe_T ratios –

notwithstanding the potential for false anoxic Fe_{HR}/Fe_T ratios to show in oxic carbonate-rich sediments as a result of increased sensitivity to secondary Fe_{HR} enrichment (*sensu* Clarkson et al., 2014) – indicates that many of these horizons were not constantly oxygenated (fig. 4.9; see Section 4.4.2). If presumed oxic depositional environments were subject to variable dysaerobic/anoxic intervals that remained unresolved in the analyses owing to homogenisation of the sediment package or as a function of the study's resolution (see Section 4.4.2), it is possible that the local faunal assemblage may have been relatively poorly developed compared with the predicted faunal assemblage. This palaeoecological control could account for individual beds that are dominated by single species or low diversity bivalve assemblages (e.g. *Liostrea* and *Plagiostoma*; see Chapter 3), particularly where these taxa represent opportunistic colonisers (see also Weedon et al., 2018), resulting in an overestimation of the extent of taphonomic distortion. The impact of short-lived dysaerobic/anoxic intervals remains uncertain, but it does not appear to have affected ichnotaxomic distribution and/or the degree of bioturbation, nor does it account for the widespread lack of aragonitic nektonic and epifaunal groups (see Chapter 3).

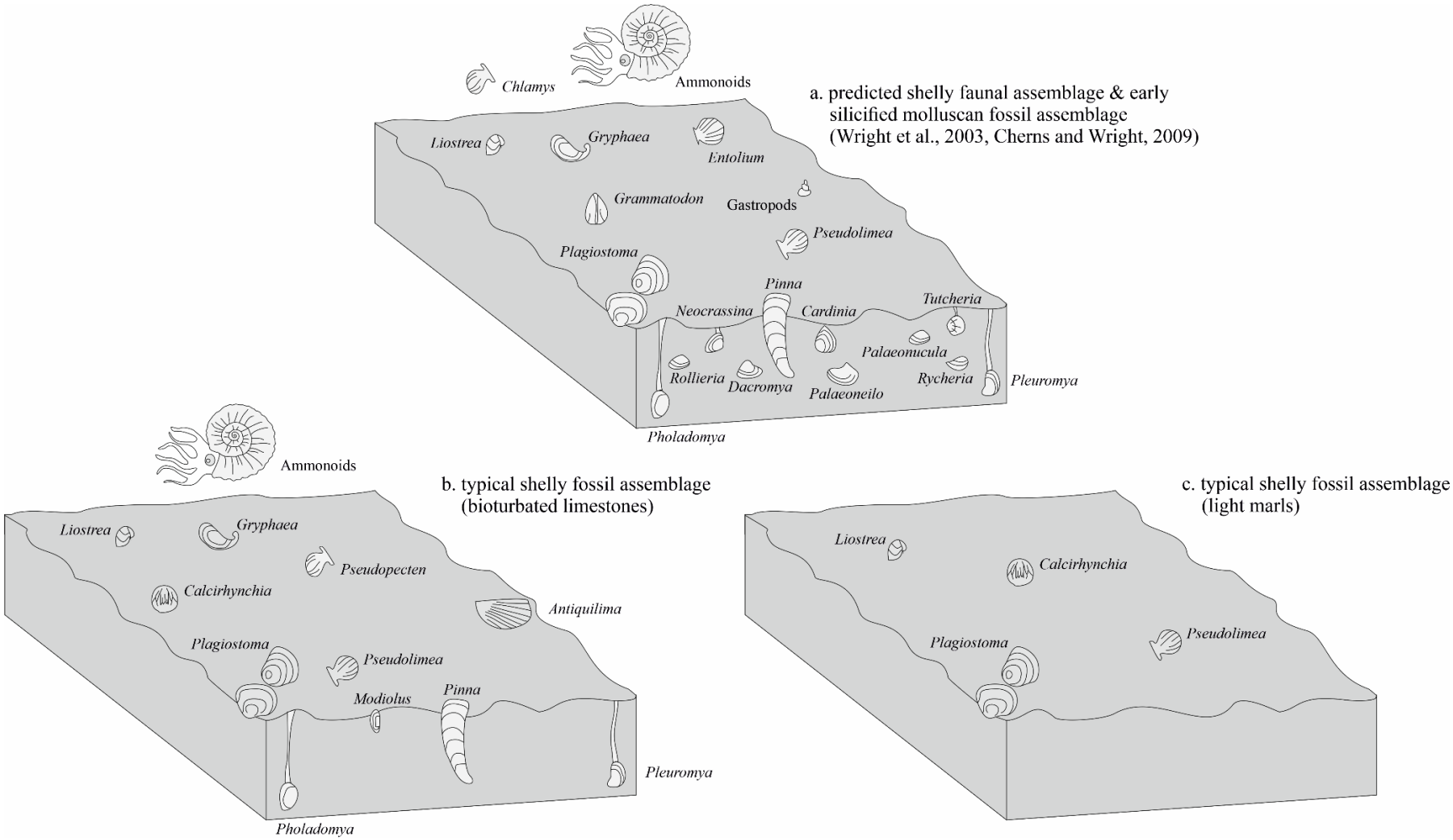

Figure 7.6 – Shelly palaeocommunity reconstructions for oxic lithologies in the Early Jurassic of Dorset and East Devon; a. predicted shelly faunal assemblage based on an early silicified fauna in Wright et al. (2003) and Cherns and Wright (2009), b. typical shelly fossil assemblage in the bioturbated limestone lithology, and c. typical shelly fossil assemblage in the light marl lithology (table 7.1; see Chapter 3).

Restricted environments. Establishing the predicted shelly faunal assemblage for restricted depositional environments is difficult since this setting is taken to represent the range of oxygen conditions between oxic and dysaerobic/anoxic end-members. Differing degrees of bottom water oxygenation, including relatively lower oxygen availability in the shale lithology compared with the dark marl lithology, as well as the unequal duration and frequency of episodic fluctuations in the dominant redox state, would have resulted in an inconstant or varied shelly palaeocommunity. Potential inconsistencies regarding the composition of the predicted faunal assemblage demonstrates the importance of considering supporting sedimentological evidence when qualifying the extent of taphonomic distortion. Despite this variability, it is fair to assume that the original shelly palaeocommunity likely contained similar nektonic, epifaunal and shallow infaunal groups to those identified in the early silicified fauna of Wright et al. (2003), but would have generally lacked deep-burrowers, particularly during shale deposition (fig. 7.7). It is anticipated that the relative diversity and abundance of shallow infaunal – and possibly epifaunal – taxa would have been reduced in the shale lithology owing to greater oxygen restriction when compared with the dark marl lithology.

The typical shelly fossil assemblages of both restricted lithologies are dominated by calcitic and bimineralic pteriomorph bivalves (*Liostrea* and *Plagiostoma;* fig. 7.7; table 7.1). Total epifaunal species richness was greatest in the dark marls (fig. 7.7; table 7.1); the bivalve genera *Pseudolimea* and *Antiquilima* as well as the brachiopod genus *Calcirhynchia* were exclusive to this lithology (fig. 7.7; table 7.1). Whilst semi-infauna (*Modiolus*) are limited to the typical shale fossil assemblage, contrary to presuppositions based on the relative degree of inferred bottom water oxygenation, the omission of similar taxa from the typical dark marl assemblage is, in part, a consequence of differential sampling potential. In the dark marl lithology, *Pinna* were represented by the same number of specimens (n = 1; table 7.1) but, owing to a greater total number of sampled horizons, the criterion to be considered typical of a given fossil assemblage was not met. An isolated occurrence of *Pholadomya* in the dark marls (table 7.1) demonstrates that this lithology accounts for a range of potential oxygen conditions. Ammonoids were present in the dark marls and shales alike (fig. 7.7; table 7.1).

Qualifying the extent of taphonomic distortion within this setting is difficult owing to the potential for differing degrees of bottom water oxygenation to have resulted in an inconstant and varied shelly palaeocommunity that cannot be precisely defined. When

compared with the equivalent tier in the early silicified fauna of Wright et al. (2003), epifauna in the typical dark marl and shale fossil assemblages show progressively poorer species richness that is proportional to the degree of inferred oxygen restriction (fig. 7.7) and therefore likely to be a consequence of palaeoenvironmental factors not differential taphonomic distortion. The near-complete lack of deep-burrowing aragonitic anomalodesmatan bivalves is generally attributed to limited oxygen availability within the sediment column – particularly during shale deposition – as opposed to selective dissolution (fig. 7.7), but it is important to note that the singular *Pholadomya* in the dark marl lithology (table 7.1) demonstrates that local oxygen conditions were not stable and, at their maximum, did support infrequent occupation of the deep infaunal tier. Both fossil assemblages have a depleted shallow infaunal tier (fig. 7.7), but it is unclear whether this reduction in the abundance and diversity of shallow-burrowing bivalves is associated with taphonomic processes, prevailing palaeoenvironmental conditions, or a combination of both. Selective dissolution of originally aragonitic fauna in the TAZ would account for the total lack of gastropods, especially considering that alternative epifauna were abundant, although ammonoids were preserved in both lithologies (fig. 7.7). These observations suggest that whilst taphonomic distortion is widespread in oxic environments and can therefore be qualified with respect to the early silicified fauna in Wright et al. (2003), these comparisons become more ambiguous in restricted settings.

Ammonoids preserved within the syn-sedimentary pyritisation taphonomic window are considered truly representative of the group's ecological abundance. However, until the more comprehensive NHM collections become accessible for study and the precise replacement context of specimens collected by Lang and Spath (1926) can be assessed in order to determine if they form part of the taphonomic window fauna, it is uncertain whether the shelly fossil assemblage is characteristic of overall ecological skeletal diversity and abundance. The fossil assemblage recovered from these strata by Lang and Spath (1926), irrespective of its preservation context, is similar to the typical fossil assemblages of the dark marl and shale lithologies (fig. 7.7).

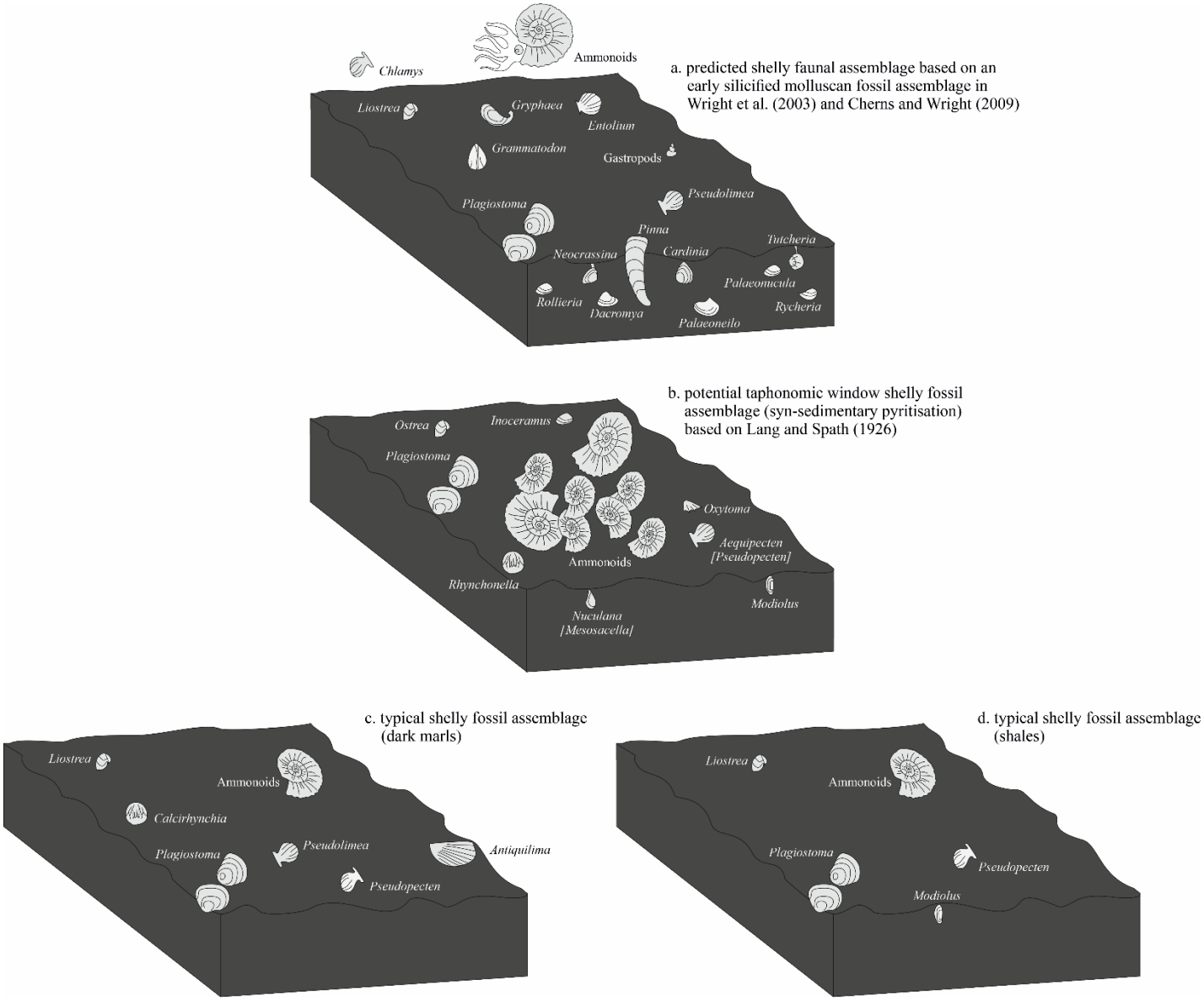
Ammonoids
Chlamys
Liostrea
Gryphaea
Entolium
Grammatodon
Gastropods
Pseudolimea
Plagiostoma
Pinna
Tutcheria
Neocrassina
Cardinia
Palaeonucula
Rollieria
Dacromya
Rycheria
Palaeoneilo
a. predicted shelly faunal assemblage based on an early silicified molluscan fossil assemblage in Wright et al. (2003) and Cherns and Wright (2009)
Ostrea
Inoceramus
Plagiostoma
Oxytoma
Aequipecten [Pseudopecten]
Ammonoids
Rhynchonella
Modiolus
Nuculana [Mesosacella]
b. potential taphonomic window shelly fossil assemblage (syn-sedimentary pyritisation) based on Lang and Spath (1926)
Liostrea
Ammonoids
Calcirhynchia
Plagiostoma
Pseudolimea
Antiquilima
Pseudopecten
c. typical shelly fossil assemblage (dark marls)
Liostrea
Ammonoids
Plagiostoma
Pseudopecten
Modiolus
d. typical shelly fossil assemblage (shales)

Figure 7.7 – Shelly palaeocommunity reconstructions for restricted lithologies in the Early Jurassic of Dorset and East Devon; a. predicted shelly faunal assemblage based on an early silicified fauna in Wright et al. (2003) and Cherns and Wright (2009), b. potential taphonomic window shelly fossil assemblage (syn-sedimentary pyritisation) based on Lang and Spath (1926), c. typical shelly fossil assemblage in the dark marl lithology, and d. typical shelly fossil assemblage in the shale lithology (table 7.1; see Chapter 3). Note that the predicted shelly faunal assemblage is an approximate maximum and that the true shelly palaeocommunity was in fact likely to be inconstant and varied owing to differing degrees of bottom water oxygenation.

Dysaerobic/anoxic environments. In the Early Jurassic of Dorset and East Devon, paper shales and laminated limestones are taken to represent dysaerobic/anoxic depositional environments (e.g. Weedon, 1986, Moghadam and Paul, 2000, Arzani, 2004; see Chapter 2). The predicted shelly faunal assemblage is limited to nektonic groups that were not reliant on hospitable conditions at the sediment surface/seawater interface (fig. 7.8).

The typical shelly fossil assemblages of the paper shale and laminated limestone lithologies are alike (fig. 7.8). As predicted, both contain nektonic ammonoids (fig. 7.8; table 7.1). Although dysaerobic/anoxic environmental conditions generally precluded occupation by epifaunal and infaunal taxa, there is evidence for opportunistic colonisation of the seafloor by *Liostrea* (e.g. Paul et al., 2008) that reflects short-lived intervals of low oxygen availability (Jordan, 2016; see Chapter 3).

A number of the different taphonomic windows identified in the Early Jurassic of Dorset and East Devon occur within this setting – Black *Arnioceras* concretions record storm deposition and shell beds of dysaerobic/anoxic environments include the Spittles *Arnioceras* and Goldstone layers (see Section 7.3.2). Since the taphonomic window fossil assemblages are consistent with the predicted faunal assemblage and preserve formerly aragonitic groups (fig. 7.8), these features are considered to be good representations of original ecological diversity. Occupying a favourable mode of life, planktonic veliger spat were figured in exceptional cases (e.g. the Goldstone Bed; fig. 7.8) despite not being part of the macrofaunal fossil content (see Chapter 3). A high relative bioclastic abundance reflects mass mortality and/or post-mortem transport and is not an artefact of variable taphonomy. Presuppositions regarding the preservation potential of taphonomic windows are supported by the presence of large numbers of formerly aragonitic bivalve and gastropod spat that would have been especially vulnerable to selective dissolution owing to their size and shell composition. The lack of *Liostrea* within the taphonomic window fauna is attributed to stable palaeoenvironmental conditions that were not subject to intervals of

low oxygen availability otherwise required to enable opportunistic colonisation of the seafloor. Despite different causal mechanisms, the survival of originally aragonitic fauna in taphonomic windows associated with dysaerobic/anoxic environments was achieved via limited residency time within the acidic TAZ (Cherns et al., 2008); processes associated with BSR and pyrite replacement may have also prevented localised selective dissolution (see Chapter 5).

Shelly diversity in the predicted faunal assemblage, typical fossil assemblages (of associated lithologies), and taphonomic window fauna of dysaerobic/anoxic environments is limited but consistent (fig. 7.8). Taken to represent good preservation of original ecological diversity, this observation supports the interpretation that taphonomically induced distortion of the shelly palaeocommunity was limited in this setting (e.g. Cherns et al., 2008, Jordan et al., 2015, Jordan, 2016). Whilst previous authors have described the potential for dysaerobic/anoxic environments to preserve formerly aragonitic infaunal and epifaunal bivalves in shell plasters and shell beds with different causal mechanisms (e.g. Cherns et al., 2008) as well as the potential for short-lived anoxic intervals to prevent selective dissolution during accumulation in fluctuating redox conditions (e.g. Jordan et al., 2015, Jordan, 2016), long-lived dysaerobic/anoxic depositional environments persisted throughout parts of the Early Jurassic but which were not associated with concentration lagerstätte. It is possible that the need for taphonomic windows to preserve a true representation of original ecological diversity is largely moot in predominantly dysaerobic/anoxic environments since this setting was not prone to widespread taphonomic distortion.

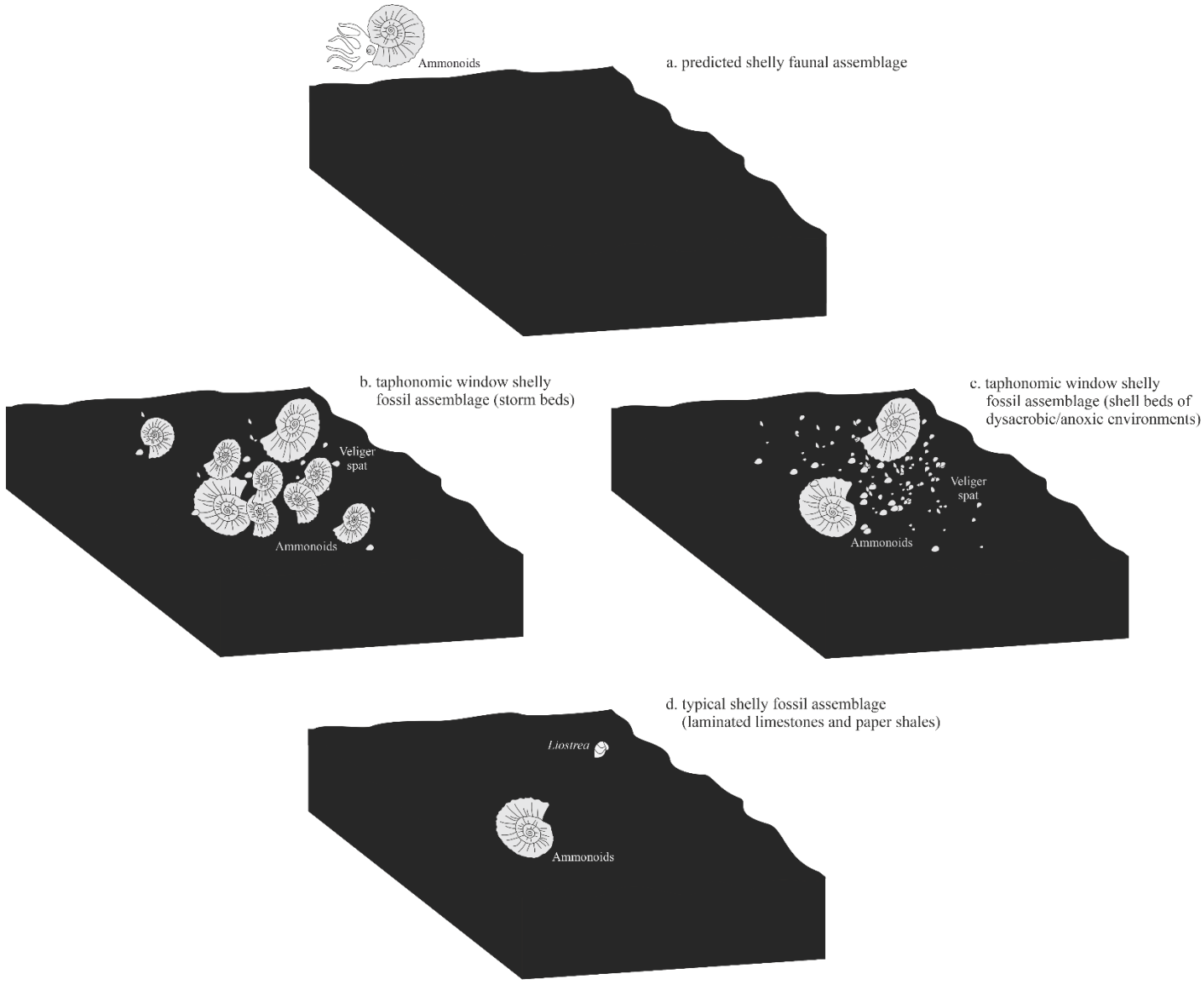
Ammonoids
a. predicted shelly faunal assemblage
b. taphonomic window shelly fossil assemblage (storm beds)
Veliger spat
Ammonoids
c. taphonomic window shelly fossil assemblage (shell beds of dysacrobic/anoxic environments)
Veliger spat
Ammonoids
d. typical shelly fossil assemblage (laminated limestones and paper shales)
Liostrea
Ammonoids

Figure 7.8 – Shelly palaeocommunity reconstructions for dysaerobic/anoxic lithologies in the Early Jurassic of Dorset and East Devon; a. predicted shelly faunal assemblage, b. taphonomic window shelly fossil assemblage (storm beds), c. taphonomic window shelly fossil assemblage (shell beds of dysaerobic/anoxic environments), d. typical shelly fossil assemblage in the laminated limestone and paper shale lithologies (table 7.1; see Chapter 3).

7.5. Conclusions

Based on comparisons with an early silicified fauna in Wright et al. (2003), this study has identified differential taphonomic distortion of the fossil marine shelly community in various lithologies from the Early Jurassic of Dorset and East Devon. In doing so, it has established the parameters for and subsequently qualified the influence of taphonomic bias associated with the Missing Molluscs effect in one of the most intensely studied sections in the world. This work emphasises the importance of considering possible taphonomic distortion as part of any future investigation of the section's palaeoecology, but also the need to consider it a variable bias that was not even throughout the assemblage. This is by no means a complete assessment of taphonomic distortion, even locally, and there is good potential to continue to test the impact of the Missing Molluscs effect in other Jurassic marine mudrocks. The lack of a preserved life assemblage of the skeletal fauna has hampered this study and the assumption has had to be made that the South Wales silicified fauna was close to authentic.

The degree of bottom water oxygenation influenced taphonomic bias associated with the Missing Molluscs effect as it controlled the palaeoecology of a given faunal assemblage as well as the strength and position of the TAZ. Based on data presented in this study, support is given to the inference made by Jordan et al. (2015) that taphonomic distortion was most significant beneath well-oxygenated bottom waters where the shelly palaeocommunity was diverse and least significant within poorly-oxygenated bottom waters where ecological diversity of skeletal biota was low; it is suggested that taphonomic distortion was of little to no consequence in dysaerobic/anoxic environments since this setting was not subject to widespread aragonite dissolution. Consequently, the most diverse faunas we see at outcrop are in fact the most biased, and the least diverse primary faunas are less biased. In open marine settings with a diverse biota, taphonomic bias is greatest because the primary mineralogical composition makes the fauna more susceptible to distortion; the type of bias affects different trophic levels whose presence is in part ecologically controlled.

8. CONCLUSIONS

This work investigates the use of iron sulphide as a marker to decipher taphonomic signals in fossil marine successions. Using a multi-disciplinary approach, different palaeoenvironmental, palaeoecological, and taphonomic factors have been examined in order to understand their influence on skeletal bias associated with the Missing Molluscs effect as well as our ability to predict and account for taphonomic distortion in Jurassic marine successions.

At the beginning of the thesis, three main research questions were introduced:

> *1. To what extent does syn-sedimentary pyritisation contribute to the preservation of true ecological molluscan abundance and diversity, and can this be considered a taphonomic window?*
>
> *2. To what extent are marked variations in the preservation and composition of the shelly fossil assemblage a consequence of taphonomic processes associated with the Missing Molluscs effect and how is this influenced by environmental and diagenetic factors?*
>
> *3. To what extent can iron palaeoredox proxies be used to reconstruct palaeoenvironmental conditions in the Early Jurassic of Dorset and East Devon?*

The following chapter provides an overview of the work undertaken throughout the thesis as well as a summary of the main findings and suggestions regarding the direction of potential future research. Sampling protocols for palaeontological and geochemical analysis were based on a revised lithostratigraphic account of the BLF and basal CMF in Chapter 2. In order to ensure a consistent approach and enable comparative analysis between different formations, lithostratigraphic logs were produced using a modified version of the lithological classification presented by Weedon (1986). Grouping of lithologically similar units – namely, bioturbated limestones (nodular and planar), light

marls, dark marls, shales, paper shales, and laminated limestones (planar and concretionary) – enabled large-scale palaeoenvironmental, palaeoecological, and taphonomic controls to be explored.

8.1. To what extent does syn-sedimentary pyritisation contribute to the preservation of true ecological molluscan abundance and diversity, and can this be considered a taphonomic window?

Iron sulphide is a common replacement mineral in fossil assemblages from Jurassic marine mudrocks (e.g. Hudson, 1982, Fisher and Hudson, 1985, Fisher, 1986, Andrew et al., 2011, Paul, 2011; see chapters 1, 5, and 7). However, despite the range of settings in which pyrite is associated with fossil preservation, its potential to further our understanding of taphonomic bias associated with the Missing Molluscs effect has not been investigated fully. Consequently, this study marks the first qualification of syn-sedimentary pyritisation as a taphonomic window that contributes to the preservation of true ecological skeletal abundance and diversity. In the Early Jurassic of Dorset and East Devon, it is shown that syn-sedimentary pyritisation functioned as a taphonomic window in two different contexts: within the TAZ where aerobic decay of retained organic matter established micro-reducing conditions inside ammonoid shells and enabled pyrite precipitation, or where the TAZ was elevated to within the water column such that molluscan spat and ammonoids were pyritised (see chapters 5 and 7).

Chapter 5 provides the first detailed investigation of pyrite replacement in ammonoid moulds from the CMF of Dorset. Ammonoids were chosen as the focus of this study owing to their high relative abundance when compared with alternative aragonitic molluscs. Based on the examination of 51 newly collected specimens, a complex local paragenetic sequence is presented that shows a range of different replacement minerals, textures, and habits, most of which are consistent with previous descriptions of pyrite replacement from various strata (e.g. Hudson, 1982). This paragenetic sequence was subsequently used to reconstruct the pyrite replacement pathway, including the conditions under which processes associated with BSR and pyrite precipitation functioned as a taphonomic window. Deposition occurred in oxygenated bottom waters, as evidenced by moderate sediment mixing and the presence of macrobenthos (e.g. Lang and Spath, 1926, Lord et al., 2010), and therefore required atypical syn-sedimentary conditions to prevent selective

dissolution of aragonitic groups via microbially induced acidity in the TAZ – a product of the aerobic bacterial decay of organic matter (e.g. Canfield and Raiswell, 1991a) strengthened by oxidation of hydrogen sulphide produced in the sulphate reduction zone (e.g. Aller, 1982, Canfield and Raiswell, 1991a, Sanders, 2003, Sanders, 2004) (see review by Cherns et al., 2008).

Primary pyrite replacement followed post-mortem deposition of the ammonoid shell with soft tissues retained in the body chamber (*sensu* Cope and Sole, 2000, Curtis et al., 2000) (fig. 5.20); accumulation was not as a result of event-based deposition. Soft tissue retention was an important control for the prevention of aragonite dissolution. Aerobic decay of organic matter facilitated the development of localised reducing conditions within the enclosed void of the shell, whilst it was surrounded by non-anoxic sediments in the TAZ, and resultant BSR was initiated within this micro-environment. Local buffering effects were imposed by early direct pyrite precipitation at the apertural margin (fig. 5.20) utilising *in situ* sources of iron – supplied by external sediments within the body chamber – to form S^0 via iron reduction (*sensu* Coleman and Raiswell, 1995); in addition to this, the supply of *in situ* iron was insufficient to react with all available sulphide during BSR and so excess acidic H_2S was lost from the system (*sensu* Coleman, 1985, Fisher, 1986, Coleman and Raiswell, 1995). The potential for such a biological control to prevent aragonite dissolution has not been recognised previously in association with taphonomic window fauna and may have further implications for the Missing Molluscs effect.

Following the establishment of widespread reducing conditions in the surrounding sediment, the main phase of primary pyrite replacement commenced with the formation of pyritic internal precipitate in the body chamber that progressed adapically into the phragmocone (fig. 5.20). By occupying part of the body chamber, retained soft tissues are shown to limit the volume of internal pyrite precipitation, producing infrequent and hitherto unknown relict or ‘ghost’ structures that mimic the shape and position of the ammonoid body (fig. 5.22). Cessation of pyritic internal precipitate formation was followed by chamber-lining pyritisation that coated the inner surfaces of the shell and septal walls as well as the upper surface of pyrite within incompletely filled gas chambers (fig. 5.20). In anoxic sediments, iron reduction and S^0 production occurred outside of the ammonoid shell; both reactants diffused inward where they reacted with H_2S (supplied by BSR) to directly precipitate pyrite (*sensu* Coleman and Raiswell, 1995). The reaction

pathway generated acidity (via H^+) that was buffered by dissolution of the aragonitic shell (*sensu* Coleman and Raiswell, 1995).

Ammonoid moulds were not always completely filled by pyrite prior to the termination of pyrite replacement. Since no subsequent stages of the paragenetic sequence preserved the internal chambered structure of the phragmocone, this point in the replacement pathway (i.e. after the cessation of pyrite formation) is taken to represent the relative timing of total dissolution of the ammonoid shell where it had occurred (fig. 5.20). This observation is noteworthy because although syn-sedimentary pyritisation is shown to contribute to the preservation potential of formerly aragonitic molluscan fauna, their fossils generally lack surviving shell aragonite. Coleman and Raiswell (1995) suggest that consumption of acidity by carbonate dissolution was essential to continued direct pyrite precipitation and so the lack of a carbonate buffer following loss of the shell could terminate pyrite formation via increased acidity and sulphide undersaturation. A number of specimens with secondary replacement habits have retained portions of altered, relict aragonitic shell on the external surface of the mould. It is possible that, in some instances, there was an overabundance of consumable carbonate so that pyrite precipitation was instead limited by reactant availability (iron), especially in association with voluminous outer pyrite growth.

In Chapter 7, two previously unrecorded pyritised faunas that show increased preservation potential of formerly aragonitic molluscan groups were described from the CMF of Dorset. The Spittles *Arnioceras* and Goldstone shell beds reflect different causal mechanisms – distal storm accumulation and unsuccessful planktotrophic spatfall respectively – for deposition in dysaerobic/anoxic environmental conditions. According to Cherns et al. (2008), the survival of originally aragonitic fauna in this setting was achieved via a limited residency time within the TAZ and/or accumulation below the redox boundary which was positioned above the sediment/seawater interface. Given the high proportion of syn-sedimentary pyrite replacement, it is suggested that alkalinity generated via processes associated with BSR and iron sulphide precipitation (e.g. Coleman, 1985, Fisher, 1986, Coleman and Raiswell, 1995; see Chapter 5) also contributed to the prevention of aragonite dissolution during early burial diagenesis. The fossil assemblages contain varying proportions of ammonoids as well as veliger spat of the cardiid bivalve genus *Protocardia* and an indeterminate, turreted gastropod genus (see Chapter 7); spat would have been especially vulnerable to selective dissolution owing to their size and shell composition

(Cherns and Wright, 2011). The Goldstone Bed is currently the only known example of unsuccessful planktotrophic spatfall in the Lower Lias of Dorset.

In summary, this work shows that the replacement context for syn-sedimentary pyritisation broadly functioned as a taphonomic window in two scenarios. Firstly, ammonoids from the pyritic assemblage described in chapters 5 and 7 can be considered truly representative of ecological abundance where aerobic decay of retained organic matter established localised reducing conditions inside of the ammonoid shells and enabled pyrite precipitation whilst they were positioned within the TAZ. This characterisation may be extended to alternative molluscan groups when the more comprehensive NHM collections become accessible for study; there is no *a priori* reason to suggest that pyrite replacement was not capable of preserving shelly fauna other than ammonoids since good preservation of the former was so widely achieved. Secondly, a true representation of original ecological abundance and diversity of skeletal fauna is recorded in shell beds of dysaerobic/anoxic environments where the TAZ was elevated to within the water column such that molluscan spat and ammonoids were pyritised. Fossil content within these taphonomic window fauna mirrors the predicted faunal assemblage – i.e. without benthos – and exhibits preservation of formerly aragonitic groups by syn-sedimentary pyrite (see Chapter 7). The preservation potential of this setting is supported by a high proportion of bivalve and gastropod spat, forms that would have been especially vulnerable to selective dissolution owing to their size and shell composition (Cherns and Wright, 2011).

Although not directly related to syn-sedimentary pyritisation, Chapter 6 documents a similar scenario to that associated with the pyritic ammonoid assemblage (see chapters 5 and 7) whereby soft tissue retention was an important control for the prevention of aragonite dissolution and, as a result, the survival of ammonoid muscle attachment scars. The preservation of muscle attachment scars required that the formerly aragonitic ammonoid shell survived acidic conditions within the TAZ; this was achieved via a limited residency time owing to rapid burial and the establishment of anoxia shortly after deposition (*sensu* Curtis et al., 2000). A comparable model was proposed by Cherns et al. (2008) regarding the potential for shell beds in dysaerobic/anoxic environments to function as a taphonomic window. Since unaltered aragonite is preserved at sites of soft tissue attachment, it was also essential that the inner shell surface associated with these features remained intact following short-lived exposure to acidic porewaters, and that it was subject to the selective prevention of neomorphism. Assuming that the nature and position of the

attachment area made it especially vulnerable to acidity prior to the onset of anoxia, limited aerobic decay of retained soft tissues and the resultant formation of a reducing micro-environment within the body chamber would have acted to prevent selective dissolution. Prolonged connection of the ammonoid musculature to the attachment scar also provided a physical barrier to prevent contact with acidic porewaters. However, exactly how original aragonitic biomineralogy survived at the site of soft tissue attachment, considering the remainder of the shell was neomorphosed to calcite, remains uncertain. Nonetheless, recognition of the potential for physical biological factors to influence or enhance molluscan preservation, specifically through the survival of a known vulnerable biomineralogy, warrants further investigation and has implications for the Missing Molluscs effect.

8.2. To what extent are marked variations in the preservation and composition of the shelly fossil assemblage a consequence of taphonomic processes associated with the Missing Molluscs effect and how is this influenced by environmental and diagenetic factors?

Based on the most complete bed-by-bed account of the macrofaunal fossil assemblage from the BLF in over 200 years of palaeontological study, this work has identified differential taphonomic distortion of the fossil marine shelly community in various lithologies from the Early Jurassic of Dorset and East Devon (figs. 7.6, 7.7, and 7.8; see Chapter 7). In doing so, it has established the parameters for and subsequently qualified the influence of taphonomic biases associated with the Missing Molluscs effect in one of the most intensely studied sections in the world. This work emphasises the importance of considering taphonomic distortion as part of any future investigation of the section's palaeoecology, but also the need to consider it a variable bias that was not even throughout the assemblage. This is by no means a complete assessment of taphonomic distortion, even locally, and there is good potential to continue to test these interpretations in other Jurassic marine mudrocks.

Using the data presented in Chapter 3, it is now possible to more fully investigate the non-uniform fossil content observed throughout the BLF and examine the control that different factors exerted over the shelly palaeocommunity. This high-resolution study indicates that the macrobenthic fossil record was influenced by a combination of changing

palaeoenvironmental conditions at the T-J boundary interval, fluctuations in the dominant redox state, and taphonomic biases associated with the Missing Molluscs effect. The degree of bottom water oxygenation controlled the ecological skeletal palaeocommunity and is a key consideration for fossil assemblages in the BLF where regular lithological alternations can be attributed to fluctuating oxygen conditions (see Chapter 2); even within a single bed, oxygen availability was not necessarily stable, and the fossil content may represent a time-averaged assemblage (see chapters 3 and 4). Within the basal BLF, previous authors have suggested that low oxygen availability or anoxia had a negative palaeoecological impact on the benthic assemblage and were associated with prolonged or staged biotic recovery (e.g. Barras and Twitchett, 2007, Mander et al., 2008, Pugh et al., 2014). This control, although not disputed herein, cannot be reconstructed via a staged recovery model (*sensu* Twitchett, 2006) based on skeletal macrobenthos alone (see Chapter 3). Taphonomic distortion associated with the Missing Molluscs effect and non-uniform depositional processes, including concentration of bioclasts and prolonged exposure to acidic conditions within the TAZ during non-deposition, influenced the fossil assemblage also (see Chapter 3). The results presented in Chapter 7 qualify taphonomic distortion, measured as the difference between the typical fossil assemblage and the predicted ecological assemblage, as a function of different states of bottom water oxygenation (figs. 7.6, 7.7, and 7.8).

Based on comparisons with an early silicified fauna in Wright et al. (2003), maximum taphonomic distortion is attributed to oxic environments where predicted ecological skeletal abundance and diversity was greatest and diagenetic processes known to strengthen the acidic TAZ were most prominent (fig. 7.6; see also Jordan et al., 2015). In open marine settings with a diverse biota, taphonomic bias is greatest because the primary mineralogical composition makes the fauna more susceptible to distortion; the type of bias affects different trophic levels whose presence is in part ecologically controlled.

Assuming that original shelly diversity was consistent in the bioturbated limestone and light marl lithologies as a result of comparable pre-diagenetic, well-oxygenated depositional conditions, although potentially with richer initial faunas in the bioturbated limestones periodically, the preservation of different fossil assemblages indicates that the extent of taphonomic distortion was uneven (fig. 7.6). In the light marls, selective dissolution within the TAZ appears to have eradicated the entire formerly aragonitic molluscan component (fig. 7.6); the fossil assemblage was further depleted via the loss of

the shallow infaunal tier and a reduction in the diversity of epifaunal bivalve genera (fig. 7.6). In the bioturbated limestones, the extent of taphonomic distortion was lesser, although it was non-uniform throughout the succession; many individual limestone beds contain differing fossil content, and some are without formerly aragonitic molluscs (see Chapter 3). Overall, the shallow infaunal tier was poorly represented and aragonitic molluscan abundance was relatively low, notwithstanding that large-bodied ammonoids were common and several horizons preserved *in situ*, deep-burrowing anomalodesmatan bivalves (fig. 7.6; see Chapter 3). Anomalodesmatan bivalves (*Pholadomya* and *Pleuromya*) survived taphonomic processes associated with the Missing Molluscs effect where they were positioned at the base of/below the shallow-burial zone of dissolution and early cementation facilitated retention of the mould (e.g. Cherns and Wright, 2009). In Weedon et al. (2018), carbonate cementation prior to aragonite dissolution was shown to improve the local preservation potential of some shelly groups, particularly ammonoids, although this relative timing was not constant throughout the BLF (Weedon et al., 2018); moreover, the predominance of large-bodied forms and bioturbation of the host sediment suggest that selective dissolution of small-bodied taxa/individuals could have nonetheless occurred in the period of time between deposition and non-deposition/limestone formation, a transition that Weedon et al. (2018) note was not instantaneous. As a result, early cementation in this context is not a true taphonomic window, nor can the presence of large-bodied ammonoids found throughout the section be considered indicative of a more complete representation of original ecological molluscan diversity and abundance.

In dysaerobic/anoxic environments, taphonomically induced distortion of the fossil marine shelly community was limited/without effect (fig. 7.8; Cherns et al., 2008, Jordan et al., 2015, Jordan, 2016). Consistent with Cherns et al. (2008), good preservation of formerly aragonitic groups was a result of limited residency time within the acidic TAZ, although processes associated with BSR and pyrite precipitation may have also prevented localised selective dissolution (see Chapter 5). Taphonomic bias was therefore least significant in poorly-oxygenated settings where ecological skeletal diversity was low (fig. 7.8; see also Jordan et al., 2015), despite the fact that the primary mineralogical composition of the fauna made it particularly vulnerable to dissolution.

In the examined taphonomic window fauna from dysaerobic/anoxic environments, survival of large numbers of formerly aragonitic ammonoids and veliger spat (fig. 7.8) – the latter of which were especially vulnerable to selective dissolution owing to their size and shell

composition – is taken to represent good preservation of ecological skeletal diversity. However, since the molluscan groups found in these fauna are consistent with the typical fossil assemblage, it is suggested that the need for taphonomic windows to preserve a true representation of the original shelly palaeocommunity was moot in this setting as depositional/early burial conditions were not conducive to widespread aragonite dissolution. Previous authors have described the potential for dysaerobic/anoxic environments to preserve formerly aragonitic infaunal and epifaunal bivalves in shell plasters and shell beds with different causal mechanisms (e.g. Cherns et al., 2008) as well as the potential for short-lived anoxic intervals to prevent the loss of vulnerable groups during accumulation in fluctuating redox conditions (e.g. Jordan et al., 2015, Jordan, 2016); however, long-lived dysaerobic/anoxic environments persisted throughout parts of the Early Jurassic, but which were not associated with concentration lagerstätte, and so the possibility that typical fossil content may also represent ecological skeletal diversity and abundance is noteworthy with regards to the influence of taphonomic biases associated with the Missing Molluscs effect.

8.3. To what extent can iron palaeoredox proxies be used to reconstruct palaeoenvironmental conditions in the Early Jurassic of Dorset and East Devon?

Chapter 4 explores the use of iron palaeoredox proxies, specifically the application of Fe_{HR}/Fe_T and Fe_{Py}/Fe_{HR} ratios, to characterise changes in bottom water redox conditions throughout the BLF of Dorset and East Devon. This is the first time that a multi-disciplinary, iron palaeoredox and palaeontological investigation has been conducted at this scale in order to examine whether the method can be used to determine the influence of bottom water redox conditions on ecological skeletal abundance and diversity, as well as its impact on the Missing Molluscs effect.

Whilst there are infrequent samples that reflect inferred oxygen conditions based on palaeontological and sedimentological evidence given elsewhere within the thesis (see chapters 2 and 3), the ranges of lithology specific Fe_{HR}/Fe_T ratios show extensive overlap and the majority of samples from inferred non-anoxic depositional environments plot spuriously above the anoxic 0.38 threshold (fig. 4.9). Conversely, mean Fe_{HR}/Fe_T ratios in non-limestone lithologies correlate well with the relative degree of bottom water

oxygenation and therefore point to significant secondary influences that have masked original redox signals and locally invalidated the established parameters for recognising oxic and anoxic conditions. Excluding oxic samples ($Fe_{HR}/Fe_T < 0.38$), Fe_{Py}/Fe_{HR} ratios show similar overlap between different lithologies (fig. 4.9); in the non-limestone lithologies, mean Fe_{Py}/Fe_{HR} ratios share a weak inverse correlation with the relative degree of bottom water oxygenation. Based on the data presented herein, it is evident that further work is needed before iron speciation can be used to reconstruct the palaeoenvironmental redox state on a bed-by-bed basis in the BLF of Dorset and East Devon; this study would benefit from the application of alternative geochemical analyses including sulphur isotopes, framboid measurements, and the Fe_T/Al ratio.

A major influence on the validity of these data concerns the use of Fe_{HR}/Fe_T ratios in oxic carbonate-rich sediments (*sensu* Clarkson et al., 2014). In this study, application of the $Fe_T > 0.5$ wt. % screening criterion of Clarkson et al. (2014) did not adequately isolate spurious data from bioturbated limestone samples and so the parameter was revised to $Fe_T > 1$ wt. % (fig. 4.10). As a result of these observations, oxic carbonate-rich sediments in the BLF appear inappropriate for the evaluation of water column redox conditions.

Time-averaging – either as a function of sampling resolution or bioturbation and sediment mixing (*sensu* Poulton, 2021) – also impacts the validity of Fe_{HR}/Fe_T ratios locally. Some differences between palaeontological evidence and iron speciation data, specifically the presence of benthic fossil assemblages in association with inferred anoxic sediments showing anoxic Fe_{HR}/Fe_T ratios, are the result of opportunistic colonisation of the seafloor during short-lived oxic intervals that were not resolved owing to a low sampling resolution (*sensu* Poulton, 2021). Whilst this issue could be addressed by increasing the sampling frequency in finely laminated lithologies, the majority of sediments in the BLF are bioturbated and/or homogenised, which limits the preservation potential of small-scale fluctuations. Bioturbation furthered obscuration of original Fe_{HR}/Fe_T ratios (*sensu* Poulton, 2021) since the succession is comprised of alternations that were deposited under regularly fluctuating redox conditions. Variance is a product of physical mixing that either diluted anoxic Fe_{HR}/Fe_T ratios via the addition of oxic sediment or provided a source of secondary Fe_{HR} enrichment to oxic Fe_{HR}/Fe_T ratios by blending earlier anoxic intervals in to the sediment profile (*sensu* Poulton, 2021). The latter scenario indicates that inferred oxic lithologies were not constantly oxygenated. As a result of these controls, interpretations based on the correlation of iron speciation data and fossil content are uncertain since the

palaeocommunity may reflect specific or short-lived depositional conditions within a longer, time-averaged period that was affected by variable or contrasting degrees of bottom water oxygenation. The data presented in Chapter 4 should therefore be considered a time-averaged representation of palaeoenvironmental redox conditions throughout the BLF of Dorset and East Devon rather than a record of true depositional redox state.

8.4. Potential for future research

The work presented in this thesis has established that taphonomic distortion of the fossil marine shelly community was uneven throughout the Early Jurassic of Dorset and East Devon. However, the absence of a preserved life assemblage of the skeletal biota has hampered this study and the assumption has had to be made that the South Wales silicified fauna of Wright et al. (2003) was as close to authentic as we so far know. It is important that future research focuses on establishing a more precise definition of ecological skeletal abundance and diversity for well-oxygenated environments from these strata so that qualifications regarding the extent of taphonomic distortion can be refined. There may be the potential to resolve this issue by expanding the sampled section to include the Belemnite Marl Member of the BVM which has seen an increase in contemporary collecting efforts and appears to contain a diverse assemblage of formerly aragonitic bivalves and gastropods at several horizons. It is also important for future work to provide a more precise definition of the skeletal palaeocommunity from restricted environments, with particular reference to any differences between the dark marl and shale lithologies, for the same reason. A step towards this goal will be the reinvestigation of the syn-sedimentary pyritisation taphonomic window once the more comprehensive NHM collections of alternative molluscan fossils become accessible for study. The continued recognition and quantification of taphonomic window fauna from different environmental and lithological settings in the Early Jurassic of Dorset and East Devon is key to developing a better understanding of the influence of taphonomic biases associated with the Missing Molluscs effect.

The potential for processes associated with BSR and pyrite precipitation to have contributed to the preservation of original ecological skeletal diversity and abundance was almost certainly not unique to the Early Jurassic marine successions of Dorset and East Devon. Pyrite is a common replacement mineral from a range of different geological and

biogeographical settings (see chapters 1 and 5), so it would be well advised to test the syn-sedimentary pyritisation taphonomic window elsewhere. Key Jurassic strata that may provide additional insight regarding variations in the replacement context and biases associated with this type of preservation include the Kimmeridge Clay and Oxford Clay formations. In these sediments, molluscan preservation alternates between pyrite replacement and survival of relict shell aragonite owing to small fluctuations in depositional conditions and diagenetic factors including sulphate availability, organic matter content, and iron availability (e.g. Cherns et al., 2008).

Having recognised that the use of Fe_{HR}/Fe_T and Fe_{Py}/Fe_{HR} ratios to reconstruct palaeoenvironmental redox conditions in the BLF of Dorset and East Devon was complicated by various depositional and diagenetic processes, there is a need to examine how these data can be applied going forward. Future work should attempt to identify samples that represent the original environmental redox state based on supporting palaeontological and sedimentological evidence as well as the application of alternative geochemical analyses including sulphur isotopes, framboid measurements, and the Fe_T/Al ratio. Once this baseline has been established, it may be possible to indicate revised parameters for the method's use locally in order to isolate the influence of secondary controls such as bioturbational mixing.

REFERENCES

ALLER, R. C. 1982. Carbonate dissolution in nearshore terrigenous muds: the role of physical and biological reworking. *The Journal of Geology,* 90**,** 79-95.

ALLISON, P. A. 1988. The role of anoxia in the decay and mineralization of proteinaceous macro-fossils. *Paleobiology,* 14**,** 139-154.

ALLISON, P. A. & BOTTJER, D. J. 2010. *Taphonomy: process and bias through time,* Dordrecht, Springer.

ALLISON, P. A. & BRIGGS, D. E. 1991. *Taphonomy: releasing the data locked in the fossil record,* New York, Plenum Press.

ANDERSON, T. F. & RAISWELL, R. 2004. Sources and mechanisms for the enrichment of highly reactive iron in euxinic Black Sea sediments. *American Journal of Science,* 304**,** 203-233.

ANDREW, C., HOWE, P. & PAUL, C. R. C. 2015. Exceptionally preserved ammonites from the Charmouth Mudstone Formation (Lower Jurassic) and their significance for ammonite taphonomy. *Geoscience in South-West England,* 13**,** 392-400.

ANDREW, C., HOWE, P., PAUL, C. R. C. & DONOVAN, S. K. 2010. Fatally bitten ammonites from the lower Lias Group (Lower Jurassic) of Lyme Regis, Dorset. *Proceedings of the Yorkshire Geological Society,* 58**,** 81-94.

ANDREW, C., HOWE, P., PAUL, C. R. C. & DONOVAN, S. K. 2011. Epifaunal worm tubes on Lower Jurassic (Lower Lias) ammonites from Dorset. *Proceedings of the Geologists' Association,* 122**,** 34-46.

ARZANI, N. 2004. Diagenetic evolution of mudstones: black shales to laminated limestones, an example from the Lower Jurassic of SW Britain. *Journal of Sciences, Islamic Republic of Iran,* 15**,** 257-267.

ARZANI, N. 2006. Primary versus diagenetic bedding in the limestone-marl/shale alternations of the epeiric seas, an example from the Lower Lias (early Jurassic) of SW Britain. *Carbonates and Evaporites,* 21**,** 94-109.

ATKINSON, J. W. & WIGNALL, P. B. 2019. How quick was marine recovery after the end-Triassic mass extinction and what role did anoxia play? *Palaeogeography, Palaeoclimatology, Palaeoecology,* 528**,** 99-119.

BABCOCK, L. E. & SPEYER, S. E. 1987. Enrolled trilobites from the Alden Pyrite Bed, Ledyard Shale (Middle Devonian) of western New York. *Journal of Paleontology,* 61**,** 539-548.

BANDEL, K. 1982. Morphologie und Bildung der frühontogenetischen Gehäuse bei conchiferen Mollusken. *Facies,* 7**,** 1-198.

BARRAS, C. G. & TWITCHETT, R. J. 2007. Response of the marine infauna to Triassic–Jurassic environmental change: Ichnological data from southern England. *Palaeogeography, Palaeoclimatology, Palaeoecology,* 244**,** 223-241.

BAYER, U. 1975. ORGANISCHE TAPETEN IM AMMONITEN-PHRAGMOKON UND IHR EINFLUSS AUF DIE FOSSILISATION.

BENNETT, S. P., BARRETT, P. M., COLLINSON, M. E., MOORE-FAY, S., DAVIS, P. G. & PALMER, C. P. 2012. A new specimen of Ichthyosaurus communis from Dorset, UK, and its bearing on the stratigraphical range of the species. *Proceedings of the Geologists' Association,* 123**,** 146-154.

BENTON, M. J. & SPENCER, P. S. 1995. *Fossil reptiles of great britain,* London, Chapman and Hall.

BERNER, R. A. 1970. Sedimentary pyrite formation. *American journal of science,* 268**,** 1-23.
BERNER, R. A. 1972. Sulfate reduction, pyrite formation, and the oceanic sulfur budget. *In:* DYRSSEN, D. & JAGNER, D. (eds.) *The changing chemistry of the oceans, Nobel Symposium 20.* Stockholm: Almquist and Wiksell.
BERNER, R. A. 1984. Sedimentary pyrite formation: an update. *Geochimica et cosmochimica Acta,* 48**,** 605-615.
BERNER, R. A. 1985. Sulphate reduction, organic matter decomposition and pyrite formation. *Philosophical Transactions of the Royal Society of London. Series A, Mathematical and Physical Sciences,* 315**,** 25-38.
BÖLÜCEK, C. & ILHAN, B. 2006. A survey of pyritised animal, plant, and trace fossils and concretionary pyrites, Germav Formation, southeastern Turkey. *Comptes Rendus Geoscience,* 338**,** 161-171.
BOTTRELL, S. & RAISWELL, R. 1989. Primary versus diagenetic origin of Blue Lias rhythms (Dorset, UK): evidence from sulphur geochemistry. *Terra Nova,* 1**,** 451-456.
BOYER, D. L., OWENS, J. D., LYONS, T. W. & DROSER, M. L. 2011. Joining forces: combined biological and geochemical proxies reveal a complex but refined high-resolution palaeo-oxygen history in Devonian epeiric seas. *Palaeogeography, Palaeoclimatology, Palaeoecology,* 306**,** 134-146.
BRACHERT, T. C. & DULLO, W.-C. 2000. Shallow burial diagenesis of skeletal carbonates: selective loss of aragonite shell material (Miocene to Recent, Queensland Plateau and Queensland Trough, NE Australia)—implications for shallow cool-water carbonates. *Sedimentary Geology,* 136**,** 169-187.
BRETT, C. E. & BAIRD, G. C. 1986. Comparative taphonomy; a key to paleoenvironmental interpretation based on fossil preservation. *Palaios,* 1**,** 207-227.
BRIGGS, D. E. G., BOTTRELL, S. H. & RAISWELL, R. 1991. Pyritization of soft-bodied fossils: Beecher's trilobite bed, Upper Ordovician, New York State. *Geology,* 19**,** 1221-1224.
BRIGGS, D. E. G. & EDGECOMBE, G. D. 1993. Beecher's trilobite bed. *Geology Today,* 9**,** 97-102.
BUSH, A. M. & BAMBACH, R. K. 2004. Did alpha diversity increase during the Phanerozoic? Lifting the veils of taphonomic, latitudinal, and environmental biases. *The Journal of Geology,* 112**,** 625-642.
BUTTERFIELD, N. J. 1990. Organic preservation of non-mineralizing organisms and the taphonomy of the Burgess Shale. *Paleobiology***,** 272-286.
BUTTERFIELD, N. J. 2003. Exceptional fossil preservation and the Cambrian explosion. *Integrative and comparative biology,* 43**,** 166-177.
CANFIELD, D. E. 1989. Reactive iron in marine sediments. *Geochimica et Cosmochimica Acta,* 53**,** 619-632.
CANFIELD, D. E., LYONS, T. W. & RAISWELL, R. 1996. A model for iron deposition to euxinic Black Sea sediments. *American Journal of Science,* 296**,** 818-834.
CANFIELD, D. E., POULTON, S. W., KNOLL, A. H., NARBONNE, G. M., ROSS, G., GOLDBERG, T. & STRAUSS, H. 2008. Ferruginous conditions dominated later Neoproterozoic deep-water chemistry. *Science,* 321**,** 949-952.
CANFIELD, D. E. & RAISWELL, R. 1991a. Carbonate precipitation and dissolution: its revelance to fossil preservation. *Taphonomy: releasing the data locked in the fossil record.* Plenum Press: New York.

CANFIELD, D. E. & RAISWELL, R. 1991b. Pyrite formation and fossil preservation. *In:* ALLISON, P. A. & BRIGGS, D. E. G. (eds.) *Taphonomy: releasing the data locked in the fossil record.* New York: Plenum Press.

CANFIELD, D. E., RAISWELL, R. & BOTTRELL, S. H. 1992. The reactivity of sedimentary iron minerals toward sulfide. *American Journal of Science,* 292**,** 659-683.

CANFIELD, D. E., RAISWELL, R., WESTRICH, J. T., REAVES, C. M. & BERNER, R. A. 1986. The use of chromium reduction in the analysis of reduced inorganic sulfur in sediments and shales. *Chemical geology,* 54**,** 149-155.

CARON, V. & NELSON, C. S. 2009. Diversity of neomorphic fabrics in New Zealand Plio-Pleistocene cool-water limestones: insights into aragonite alteration pathways and controls. *Journal of Sedimentary Research,* 79**,** 226-246.

CHERNS, L., WHEELEY, J. R. & WRIGHT, V. P. 2008. Taphonomic windows and molluscan preservation. *Palaeogeography, Palaeoclimatology, Palaeoecology,* 270**,** 220-229.

CHERNS, L., WHEELEY, J. R. & WRIGHT, V. P. 2011. Taphonomic bias in shelly faunas through time: early aragonitic dissolution and its implications for the fossil record. *In:* ALLISON, P. A. & BOTTJER, D. J. (eds.) *Taphonomy: Process and bias through time.* Dordrecht: Springer.

CHERNS, L. & WRIGHT, V. P. 2000. Missing molluscs as evidence of large-scale, early skeletal aragonite dissolution in a Silurian sea. *Geology,* 28**,** 791-794.

CHERNS, L. & WRIGHT, V. P. 2009. Quantifying the impacts of early diagenetic aragonite dissolution on the fossil record. *Palaios,* 24**,** 756-771.

CHERNS, L. & WRIGHT, V. P. 2011. Skeletal mineralogy and biodiversity of marine invertebrates: size matters more than seawater chemistry. *Geological Society, London, Special Publications,* 358**,** 9-17.

CLARKSON, M. O., POULTON, S. W., GUILBAUD, R. & WOOD, R. A. 2014. Assessing the utility of Fe/Al and Fe-speciation to record water column redox conditions in carbonate-rich sediments. *Chemical Geology,* 382**,** 111-122.

CLÉMENCE, M.-E., BARTOLINI, A., GARDIN, S., PARIS, G., BEAUMONT, V. & PAGE, K. N. 2010. Early Hettangian benthic–planktonic coupling at Doniford (SW England): Palaeoenvironmental implications for the aftermath of the end-Triassic crisis. *Palaeogeography, Palaeoclimatology, Palaeoecology,* 295**,** 102-115.

COLEMAN, M. L. 1985. Geochemistry of diagenetic non-silicate minerals: kinetic considerations. *Philosophical Transactions of the Royal Society of London. Series A, Mathematical and Physical Sciences,* 315**,** 39-56.

COLEMAN, M. L. & RAISWELL, R. 1995. Source of carbonate and origin of zonation in pyritiferous carbonate concretions; evaluation of a dynamic model. *American Journal of Science,* 295**,** 282-308.

COOPER, J. 1977. The Palaeontology of the London Clay (Lower Eocene) of the Herne Bay coastal section, Kent, England. *Proceedings of the Geologists' Association,* 88**,** 163-178.

COOPER, R. A., MAXWELL, P. A., CRAMPTON, J. S., BEU, A. G., JONES, C. M. & MARSHALL, B. A. 2006. Completeness of the fossil record: estimating losses due to small body size. *Geology,* 34**,** 241-244.

COPE, J. C. W., GETTY, T. A., HOWARTH, M. K., MORTON, N. & TORRENS, H. S. 1980. A Correlation of Jurassic Rocks in the British Isles. Part 1: Introduction and Lower Jurassic. *Geological society, London, Special Publications,* 14.

COPE, J. C. W. & SOLE, D. T. C. 2000. Ammonite jaw apparatuses from the Sinemurian (Lower Jurassic) of Dorset and their taphonomic relevance. *Journal of the Geological Society,* 157**,** 201-205.
COX, B. M., SUMBLER, M. G. & IVIMEY-COOK, H. C. 1999. A formational framework for the Lower Jurassic of England and Wales (onshore area). *British Geological Survey Research Report, RR/99/01*.
CRICK, G. C. 1898. IV. On the Muscular Attachment of the Animal to its Shell in some Fossil Cephalopoda (Ammonoidea). *Transactions of the Linnean Society of London. 2nd Series. Zoology,* 7**,** 71-113.
CRUICKSHANK, A. R. I. 1994. A juvenile plesiosaur (Plesiosauria: Reptilia) from the Lower Lias (Hettangian: Lower Jurassic) of Lyme Regis, England: a pliosauroid-plesiosauroid intermediate? *Zoological Journal of the Linnean Society,* 112**,** 151-178.
CURTIS, C. D., COPE, J. C. W., PLANT, D. & MACQUAKER, J. H. S. 2000. 'Instantaneous' sedimentation, early microbial sediment strengthening and a lengthy record of chemical diagenesis preserved in Lower Jurassic ammonitiferous concretions from Dorset. *Journal of the Geological Society,* 157**,** 165-172.
DAGYS, A. S. & KEUPP, H. 1998. Internal ventral keels in Triassic ceratid ammonoids: description and functional interpretation as muscle scars. *Zeitschrift der Deutschen Geologischen Gesellschaft***,** 81-89.
DAHL, T. W., SIGGAARD-ANDERSEN, M.-L., SCHOVSBO, N. H., PERSSON, D. O., HUSTED, S., HOUGÅRD, I. W., DICKSON, A. J., KJÆR, K. & NIELSEN, A. T. 2019. Brief oxygenation events in locally anoxic oceans during the Cambrian solves the animal breathing paradox. *Scientific reports,* 9**,** 1-9.
DAVIES, D. J., POWELL, E. N. & STANTON JR, R. J. 1989. Taphonomic signature as a function of environmental process: shells and shell beds in a hurricane-influenced inlet on the Texas coast. *Palaeogeography, Palaeoclimatology, Palaeoecology,* 72**,** 317-356.
DE LA BECHE, H. 1822. Remarks on the Geology of the South Coast of England, from Bridport Harbour, Dorset, to Babbacombe Bay, Devon. *Transactions of the Geological Society of London,* 2**,** 40-47.
DE LA BECHE, H. 1826. On the Lias of the Coast, in the Vicinity of Lyme Regis, Dorset. *Transactions of the Geological Society of London,* 2**,** 21-30.
DOGUZHAEVA, L. & MUTVEI, H. 1991. Organization of the soft body in Aconeceras (Ammonitina), interpreted on the basis of shell morphology and muscle-scars. *Palaeontographica. Abteilung A, Paläozoologie, Stratigraphie,* 218**,** 17-33.
DOGUZHAEVA, L. & MUTVEI, H. 1996. Attachment of the body to the shell in ammonoids. *In:* LANDMAN, N. H., TANABE, K. & DAVIS, R. A. (eds.) *Ammonoid paleobiology.* Boston, MA: Springer.
DONOVAN, D. T. 2006. Phragmoteuthida (Cephalopoda: Coleoidea) from the Lower Jurassic of Dorset, England. *Palaeontology,* 49**,** 673-684.
DUFFIN, C. J. 1981. The fin spine of a new holocephalan from the Lower Jurassic of Lyme Regis, Dorset, England. *Geobios,* 14**,** 469-475.
EBUKANSON, E. J. & KINGHORN, R. R. F. 1990. Jurassic mudrock formations of southern England: lithology, sedimentation rates and organic carbon content. *Journal of Petroleum Geology,* 13**,** 221-228.
EFREMOV, J. A. 1940. Taphomony: a new branch of geology. *Pan-Am. Geologist,* 74**,** 81-93.
FISHER, I. S. J. 1986. Pyrite replacement of mollusc shells from the Lower Oxford Clay (Jurassic) of England. *Sedimentology,* 33**,** 575-585.

FISHER, I. S. J. & HUDSON, J. D. 1985. Pyrite geochemistry and fossil preservation in shales. *Philosophical Transactions of the Royal Society of London. B, Biological Sciences,* 311**,** 167-169.
FISHER, I. S. J. & HUDSON, J. D. 1987. Pyrite formation in Jurassic shales of contrasting biofacies. *Geological Society, London, Special Publications,* 26**,** 69-78.
FOOTE, M., CRAMPTON, J. S., BEU, A. G. & NELSON, C. S. 2015. Aragonite bias, and lack of bias, in the fossil record: lithological, environmental, and ecological controls. *Paleobiology,* 41**,** 245-265.
FÜRSICH, F. T., BERNDT, R., SCHEUER, T. & GAHR, M. 2001. Comparative ecological analysis of Toarcian (Lower Jurassic) benthic faunas from southern France and east-central Spain. *Lethaia,* 34**,** 169-199.
FÜRSICH, F. T. & PANDEY, D. K. 2003. Sequence stratigraphic significance of sedimentary cycles and shell concentrations in the Upper Jurassic–Lower Cretaceous of Kachchh, western India. *Palaeogeography, Palaeoclimatology, Palaeoecology,* 193**,** 285-309.
GAINES, R. R. 2014. Burgess Shale-type preservation and its distribution in space and time. *The Paleontological Society Papers,* 20**,** 123-146.
GALLOIS, R. W. 2008a. The lithostratigraphy of the shales-with-beef member of the Charmouth mudstone formation, Lower Jurassic. *Geoscience in south-west England: proceedings of the Ussher Society,* 12**,** 32-40.
GALLOIS, R. W. 2008b. The stratigraphy of the Penarth Group (Late Triassic) of the east Devon coast. *Geoscience in south-west England-Proceedings of the Ussher Society,* 11**,** 287-297.
GALLOIS, R. W. & PAUL, C. R. C. 2009. Lateral variations in the topmost part of the Blue Lias and basal Charmouth Mudstone formations (Lower Jurassic) on the Devon and Dorset coast. *Geoscience in Southwest England: Proceedings of the Ussher Society,* 12**,** 125-133.
GEORGE, T., HARLAND, W., AGER, D., BALL, H., BLOW, W., CASEY, R., HOLLAND, C., HUGHES, N., KELLAWAY, G. & KENT, P. 1969. Recommendations on stratigraphical usage. *Proceedings of the Geological Society, London,* 1656**,** 139-166.
GILL, B. C., LYONS, T. W., YOUNG, S. A., KUMP, L. R., KNOLL, A. H. & SALTZMAN, M. R. 2011. Geochemical evidence for widespread euxinia in the Later Cambrian ocean. *Nature,* 469**,** 80-83.
GOLDHABER, M. B. & KAPLAN, I. R. 1974. The sulphur cycle. The sea. *Marine Chemistry,* 5**,** 527-655.
GRIMES, S. T., DAVIES, K. L., BUTLER, I. B., BROCK, F., EDWARDS, D., RICKARD, D., BRIGGS, D. E. G. & PARKES, R. J. 2002. Fossil plants from the Eocene London Clay: the use of pyrite textures to determine the mechanism of pyritization. *Journal of the Geological Society,* 159**,** 493-501.
HALLAM, A. 1964. Origin of the Limestone-Shale Rhythm in the Blue Lias of England: A Composite Theory. *The Journal of Geology,* 72**,** 157-169.
HALLAM, A. 1969. A pyritized limestone hardground in the Lower Jurassic of Dorset (England). *Sedimentology,* 12**,** 231-240.
HALLAM, A. 1990. Correlation of the Triassic-Jurassic boundary in England and Austria. *Journal of the Geological Society,* 147**,** 421-424.
HALLAM, A. 1996. Recovery of the marine fauna in Europe after the end-Triassic and early Toarcian mass extinctions. *Geological Society, London, Special Publications,* 102**,** 231-236.

HALLAM, A. 1999. Evidence of sea-level fall in sequence stratigraphy: examples from the Jurassic. *Geology,* 27**,** 343-346.
HALLAM, A. 2002. How catastrophic was the end-Triassic mass extinction? *Lethaia,* 35**,** 147-157.
HALLAM, A. & LANG, W. D. 1960. A sedimentary and faunal study of the Blue Lias of Dorset and Glamorgan. *Philosophical Transactions of the Royal Society of London. Series B, Biological Sciences,* 242**,** 1-44.
HALLAM, A. & WIGNALL, P. B. 1999. Mass extinctions and sea-level changes. *Earth-Science Reviews,* 48**,** 217-250.
HAMES, W., RENNE, P. & RUPPEL, C. 2000. New evidence for geologically instantaneous emplacement of earliest Jurassic Central Atlantic magmatic province basalts on the North American margin. *Geology,* 28**,** 859-862.
HENDRY, J. P., PEARSON, M. J., TREWIN, N. H. & FALLICK, A. E. 2006. Jurassic septarian concretions from NW Scotland record interdependent bacterial, physical and chemical processes of marine mudrock diagenesis. *Sedimentology,* 53**,** 537-565.
HENDY, A. J. W. 2011. Taphonomic overprints on Phanerozoic trends in biodiversity: lithification and other secular megabiases. *In:* ALLISON, P. A. & BOTTJER, D. J. (eds.) *Taphonomy: Process and bias through time.* Dordrecht: Springer.
HESSELBO, S. & PALMER, T. 1992. Reworked early diagenetic concretions and the bioerosional origin of a regional discontinuity within British Jurassic marine mudstones. *Sedimentology,* 39**,** 1045-1065.
HESSELBO, S. P. & JENKYNS, H. C. 1995. A comparison of the Hettangian to Bajocian successions of Dorset and Yorkshire. *In:* TAYLOR, P. D. (ed.) *Field Geology of the British Jurassic* Geological Society, London.
HESSELBO, S. P., ROBINSON, S. A. & SURLYK, F. 2004. Sea-level change and facies development across potential Triassic–Jurassic boundary horizons, SW Britain. *Journal of the Geological Society,* 161**,** 365-379.
HESSELBO, S. P., ROBINSON, S. A., SURLYK, F. & PIASECKI, S. 2002. Terrestrial and marine extinction at the Triassic-Jurassic boundary synchronized with major carbon-cycle perturbation: A link to initiation of massive volcanism? *Geology,* 30**,** 251-254.
HILLEBRANDT, A. V., KRYSTYN, L. & KUERSCHNER, W. 2007. A candidate GSSP for the base of the Jurassic in the Northern Calcareous Alps (Kuhjoch section, Karwendel Mountains, Tyrol, Austria). *International Subcommission on Jurassic Stratigraphy Newsletter,* 34**,** 2-20.
HILLEBRANDT, A. V., KRYSTYN, L., KÜRSCHNER, W., BONIS, N., RUHL, M., RICHOZ, S., SCHOBBEN, M., URLICHS, M., BOWN, P. & KMENT, K. 2013. The global stratotype sections and point (GSSP) for the base of the Jurassic System at Kuhjoch (Karwendel Mountains, Northern Calcareous Alps, Tyrol, Austria). *Episodes,* 36**,** 162-198.
HODGES, P. 1986. The Lower Lias (Lower Jurassic) of the Bridgend area, South Wales. *Proceedings of the Geologists' Association,* 97**,** 237-242.
HODGES, P. 1991. The relatinship of the mesozoic bivalve Atreta to the Dimyidae. *Palaeontology,* 34**,** 963-970.
HODGES, P. 2000. The Early Jurassic Bivalvia from the Hettangian and lower Sinemurian of southwest Britain. Part 1. *Palaeontographical Society Monograph,* 154**,** 64.
HOUSE, M. R. 1985. A new approach to an absolute timescale from measurements of orbital cycles and sedimentary microrhythms. *Nature,* 315**,** 721-725.

HUDSON, J. D. 1982. Pyrite in ammonite-bearing shales from the Jurassic of England and Germany. *Sedimentology,* 29**,** 639-667.
HUDSON, J. D. & PALFRAMAN, D. F. B. 1968. The ecology and preservation of the Oxford Clay fauna at Woodham, Buckinghamshire. *Quarterly Journal of the Geological Society,* 124**,** 387-418.
JAMES, N. P., BONE, Y. & KYSER, T. K. 2005. Where has all the aragonite gone? Mineralogy of Holocene neritic cool-water carbonates, southern Australia. *Journal of Sedimentary Research,* 75**,** 454-463.
JENKYNS, H. C. & WEEDON, G. P. 2013. Chemostratigraphy (CaCO3, TOC, δ13Corg) of Sinemurian (Lower Jurassic) black shales from the Wessex Basin, Dorset and palaeoenvironmental implications. *Newsletters on Stratigraphy,* 46**,** 1-21.
JONES, D. L. 1961. Muscle attachment impressions in a Cretaceous ammonite. *Journal of Paleontology,* 35**,** 502-504.
JORDAN, N. 2016. *Palaeoenvironmental analysis of British Lower Jurassic epicontinental seas.* Unpublished PhD Thesis, Imperial College London.
JORDAN, N., ALLISON, P. A., HILL, J. & SUTTON, M. D. 2015. Not all aragonitic molluscs are missing: taphonomy and significance of a unique shelly lagerstätte from the Jurassic of SW Britain. *Lethaia,* 48**,** 540-548.
JORDAN, R. 1968. Zur Anatomie mesozoischer Ammoniten nach-den Strukturelementen der Gehäuse-Innenwand. *Beihefte Geologischen Jahrbuch,* 77**,** 1-64.
JØRGENSEN, B. 1977. Bacterial sulfate reduction within reduced microniches of oxidized marine sediments. *Marine Biology,* 41**,** 7-17.
KAPLAN, I. R., EMERY, K. O. & RITTENBEBG, S. C. 1963. The distribution and isotopic abundance of sulphur in recent marine sediments off southern California. *Geochimica et Cosmochimica Acta,* 27**,** 297-331.
KATZ, A. & FRIEDMAN, G. M. 1965. The preparation of stained acetate peels for the study of carbonate rocks. *Journal of Sedimentary Research,* 35**,** 248-249.
KELLY, R. S., ROSS, A. J. & DAVIDSON, P. 2017. Mesozoic Holcoptera (Coleoptera: Coptoclavidae) from England and the United States. *Proceedings of the Geologists' Association,* 128**,** 659-674.
KENT, P. E. 1949. A structure contour map of the surface of the buried pre-Permian rocks of England and Wales. *Proceedings of the Geologists' Association,* 60**,** 87-104.
KIDWELL, S. M. 2005. Shell composition has no net impact on large-scale evolutionary patterns in mollusks. *Science,* 307**,** 914-917.
KIDWELL, S. M. & BOSENCE, D. W. J. 1991. Taphonomy and time-averaging of marine shelly faunas. *In:* ALLISON, P. A. & BRIGGS, D. E. G. (eds.) *Taphonomy: releasing the data locked in the fossil record. Plenum, New York.* New York: Plenum Publishers.
KIDWELL, S. M. & BRENCHLEY, P. J. 1994. Patterns in bioclastic accumulation through the Phanerozoic: changes in input or in destruction? *Geology,* 22**,** 1139-1143.
KIDWELL, S. M., FUERSICH, F. T. & AIGNER, T. 1986. Conceptual framework for the analysis and classification of fossil concentrations. *Palaios,* 1**,** 228-238.
KLOMPMAKER, A. A., WALJAARD, N. A. & FRAAIJE, R. H. 2009. Ventral bite marks in Mesozoic ammonoids. *Palaeogeography, Palaeoclimatology, Palaeoecology,* 280**,** 245-257.
KLUG, C., MONTENARI, M., SCHULZ, H. & URLICHS, M. 2007. Soft-tissue attachment of Middle Triassic Ceratitida from Germany. *In:* LANDMAN, N. H., DAVIS, R. A. & MAPES, R. H. (eds.) *Cephalopods Present and Past: New Insights and Fresh Perspectives.* New York: Springer.

KNOERICH, A. C. & MUTTI, M. 2006. Missing aragonitic biota and the diagenetic evolution of heterozoan carbonates: A case study from the Oligo-Miocene of the central Mediterranean. *Journal of Sedimentary Research,* 76**,** 871-888.
KOLTHOFF, I. M. & SANDELL, E. B. 1963. Textbook of quantitative inorganic analysis. New York, US: Macmillan.
KULICKI, C. 1996. Ammonoid shell microstructure. *In:* LANDMAN, N. H., TANABE, K. & DAVIS, R. A. (eds.) *Ammonoid paleobiology.* Boston, MA: Springer.
KULICKI, C., TANABE, K., LANDMAN, N. H. & KAIM, A. 2015. Ammonoid shell microstructure. *Ammonoid Paleobiology: From anatomy to ecology.* Springer.
LAKE, S. D. & KARNER, G. D. 1987. The structure and evolution of the Wessex Basin, southern England: an example of inversion tectonics. *Tectonophysics,* 137**,** 347-378.
LANDMAN, N. H. & BANDEL, K. 1985. Internal structures in the early whorls of Mesozoic ammonites. 2823**,** 1-21.
LANG, W. 1945. The Coinstone of the Charmouth Lias. *Proceedings of the Dorset Natural History and Archaeological Society,* 67**,** 145-149.
LANG, W. D. 1924. The blue lias of the devon and dorset coasts. *Proceedings of the Geologists' Association,* 35**,** 169-185.
LANG, W. D. & SPATH, L. F. 1926. The black marl of Black Ven and Stonebarrow, in the Lias of the Dorset coast. *Quarterly journal of the Geological Society,* 82**,** 144-165.
LANG, W. D., SPATH, L. F. & RICHARDSON, W. A. 1923. Shales-with-'beef,'a Sequence in the Lower Lias of the Dorset Coast. *Quarterly Journal of the Geological Society,* 79**,** 47-66.
LI, X. & DROSER, M. L. 1999. Lower and Middle Ordovician shell beds from the Basin and Range province of the western United States (California, Nevada, and Utah). *Palaios,* 14**,** 215-233.
LORD, A. R., DAVIS, P. G., DUFFIN, C. J., EDMONDS, R., PAGE, K. N., JOHNSON, B., WHITTAKER, J. E., PAUL, C. R. C., UNDERWOOD, C. J., OWEN, E. F., CLEMENTS, D., PALMER, C. P., TODD, J. A., MUNT, M. C., DOYLE, P., ROSS, A., COLLINS, J. S. H., EWIN, T. A. M., FRASER, N., HUNTER, A. W., LEWIS, D. N., FOREY, P., LONGBOTTOM, A. E., MULLEY, J., MILNER, A. C., WALSH, S. & CHAPMAN, S. D. 2010. *Fossils from the Lower Lias of the Dorset Coast,* London, Palaeontological Association.
LYONS, T. W. & SEVERMANN, S. 2006. A critical look at iron paleoredox proxies: New insights from modern euxinic marine basins. *Geochimica et Cosmochimica Acta,* 70**,** 5698-5722.
MANDER, L., KÜRSCHNER, W. M. & MCELWAIN, J. C. 2013. Palynostratigraphy and vegetation history of the Triassic–Jurassic transition in East Greenland. *Journal of the Geological Society,* 170**,** 37-46.
MANDER, L., TWITCHETT, R. J. & BENTON, M. J. 2008. Palaeoecology of the Late Triassic extinction event in the SW UK. *Journal of the Geological Society,* 165**,** 319-332.
MARSHALL, J. D. 1982. Isotopic composition of displacive fibrous calcite veins; reversals in pore-water composition trends during burial diagenesis. *Journal of Sedimentary Research,* 52**,** 615-630.
MARTILL, D. M., BATTEN, D. J. & LOYDELL, D. K. 2000. A new specimen of the thyreophoran dinosaur cf. Scelidosaurus with soft tissue preservation. *Palaeontology,* 43**,** 549-559.

MARTIN, K. D. 2004. A re-evaluation of the relationship between trace fossils and dysoxia. *Geological Society, London, Special Publications,* 228**,** 141-156.
MARZOLI, A., BERTRAND, H., KNIGHT, K. B., CIRILLI, S., BURATTI, N., VÉRATI, C., NOMADE, S., RENNE, P. R., YOUBI, N. & MARTINI, R. 2004. Synchrony of the Central Atlantic magmatic province and the Triassic-Jurassic boundary climatic and biotic crisis. *Geology,* 32**,** 973-976.
MARZOLI, A., RENNE, P. R., PICCIRILLO, E. M., ERNESTO, M., BELLIENI, G. & DE MIN, A. 1999. Extensive 200-million-year-old continental flood basalts of the Central Atlantic Magmatic Province. *Science,* 284**,** 616-618.
MASSARE, J. A. & LOMAX, D. R. 2018. A taxonomic reassessment of Ichthyosaurus communis and I. intermedius and a revised diagnosis for the genus. *Journal of Systematic Palaeontology,* 16**,** 263-277.
MCELWAIN, J., BEERLING, D. & WOODWARD, F. 1999. Fossil plants and global warming at the Triassic-Jurassic boundary. *Science,* 285**,** 1386-1390.
MCGOWAN, C. 1993. A new species of large, long-snouted ichthyosaur from the English lower Lias. *Canadian Journal of Earth Sciences,* 30**,** 1197-1204.
MCHONE, J. G. 2000. Non-plume magmatism and rifting during the opening of the central Atlantic Ocean. *Tectonophysics,* 316**,** 287-296.
MIRONENKO, A. A. 2014. The soft-tissue attachment scars in Late Jurassic ammonites from Central Russia. *Acta Palaeontologica Polonica,* 60**,** 981-1000.
MOGHADAM, H. V. & PAUL, C. R. C. 2000. Trace fossils of the Jurassic, blue Lias, Lyme Regis, Southern England. *Ichnos,* 7**,** 283-306.
NELSON, C. S. & JAMES, N. P. 2000. Marine cements in mid-Tertiary cool-water shelf limestones of New Zealand and southern Australia. *Sedimentology,* 47**,** 609-629.
NELSON, C. S., WINEFIELD, P. R., HOOD, S. D., CARON, V., PALLENTIN, A. & KAMP, P. J. J. 2003. Pliocene Te Aute limestones, New Zealand: expanding concepts for cool-water shelf carbonates. *New Zealand Journal of geology and geophysics,* 46**,** 407-424.
NEWMAN, B. H. 1968. The Jurassic dinosaur Scelidosaurus harrisoni, Owen. *Palaeontology,* 11**,** 40-43.
NEWTON, R. J., BOTTRELL, S. H., DEAN, S. P., HATFIELD, D. & RAISWELL, R. 1995. An evaluation of the use of the chromous chloride reduction method for isotopic analyses of pyrite in rocks and sediment. *Chemical Geology,* 125**,** 317-320.
NOE-NYGAARD, N., SURLYK, F. & PIASECKI, S. 1987. Bivalve mass mortality caused by toxic dinoflagellate blooms in a Berriasian-Valanginian lagoon, Bornholm, Denmark. *Palaios,* 2**,** 263-273.
NORMAN, D. B. 2001. Scelidosaurus, the earliest complete dinosaur. *The armored dinosaurs***,** 3-24.
ORBELL, G. 1973. Palynology of the British Rhaeto-Liassic. *Bulletin of the Geological Survey of Great Britain,* 44**,** 1-44.
OSCHMANN, W. 1988. Kimmeridge Clay sedimentation—a new cyclic model. *Palaeogeography, Palaeoclimatology, Palaeoecology,* 65**,** 217-251.
OSCHMANN, W. 1991. Distribution, dynamics and palaeoecology of Kimmeridgian (Upper Jurassic) shelf anoxia in western Europe. *Geological Society, London, Special Publications,* 58**,** 381-395.
OSCHMANN, W. 1993. Environmental oxygen fluctuations and the adaptive response of marine benthic organisms. *Journal of the Geological Society,* 150**,** 187-191.
PAGE, K. N. 1994. On the sequence of ammonite correlated chronostratigraphical horizons in the British Sinemurian (Lower Jurassic). *Geobios,* 27**,** 369-379.

PAGE, K. N. 2004. Biostratigraphy of invertebrate macrofossils: macrofossils - ammonites. *In:* SIMMS, M. J., CHIDLAW, N., MORTON, N. & PAGE, K. N. (eds.) *British lower Jurassic stratigraphy.* Peterborough: Joint Nature Conservation Committee.

PÁLFY, J. 2003. Volcanism of the Central Atlantic Magmatic Province as a potential driving force in the end-Triassic mass extinction. *GEOPHYSICAL MONOGRAPH-AMERICAN GEOPHYSICAL UNION,* 136**,** 255-267.

PÁLFY, J., DEMÉNY, A., HAAS, J. N., HETÉNYI, M., ORCHARD, M. J. & VETO, I. 2001. Carbon isotope anomaly and other geochemical changes at the Triassic-Jurassic boundary from a marine section in Hungary. *Geology,* 29**,** 1047-1050.

PÁLFY, J., SMITH, P. L. & MORTENSEN, J. K. 2002. Dating the end-Triassic and Early Jurassic mass extinctions, correlative large igneous provinces, and isotopic events. *SPECIAL PAPERS-GEOLOGICAL SOCIETY OF AMERICA,* 523-532.

PALMER, T. & WILSON, M. 2004. Calcite precipitation and dissolution of biogenic aragonite in shallow Ordovician calcite seas. *Lethaia,* 37**,** 417-427.

PALMER, T. J., HUDSON, J. D. & WILSON, M. A. 1988. Palaeoecological evidence for early aragonite dissolution in ancient calcite seas. *Nature,* 335**,** 809-810.

PAUL, C. R. C. 2011. Dark bands on pyritic internal moulds of the Early Jurassic ammonites Oxynoticeras and Cheltonia from Gloucestershire, England: interpretation and significance to ammonite growth analysis. *Palaeontology,* 54**,** 1213-1221.

PAUL, C. R. C. 2015. Sutural asymmetry in the ammonites Bifericeras and Leptonotoceras from the Lower Jurassic of Bishop's Cleeve, Gloucestershire, England and its significance for ammonite life orientation. *Palaeogeography, Palaeoclimatology, Palaeoecology,* 418**,** 160-175.

PAUL, C. R. C., ALLISON, P. A. & BRETT, C. E. 2008. The occurrence and preservation of ammonites in the Blue Lias Formation (lower Jurassic) of Devon and Dorset, England and their palaeoecological, sedimentological and diagenetic significance. *Palaeogeography, Palaeoclimatology, Palaeoecology,* 270**,** 258-272.

PAUL, C. R. C. & SIMMS, M. J. 2012. Epifauna on ammonites from the Lower Jurassic of the Severn Basin, southern England, and their palaeoenvironmental and taphonomic significance. *Proceedings of the Geologists' Association,* 123**,** 508-519.

POOLE, E. G. 1979. The Triassic-Jurassic boundary in Great Britain. *Geological Magazine,* 116**,** 303-311.

POOLE, E. G. 1980. The Triassic-Jurassic boundary in Great Britain: reply. *Geological Magazine,* 117**,** 619-620.

POOLE, E. G. & COPE, J. C. W. 1991. Further discussion on the correlation of the Triassic-Jurassic boundary in England and Austria. *Journal of the Geological Society, London,* 148**,** 943-944.

POULTON, S. W. 2021. *The Iron Speciation Paleoredox Proxy,* Cambridge University Press.

POULTON, S. W. & CANFIELD, D. E. 2005. Development of a sequential extraction procedure for iron: implications for iron partitioning in continentally derived particulates. *Chemical geology,* 214**,** 209-221.

POULTON, S. W. & CANFIELD, D. E. 2011. Ferruginous conditions: a dominant feature of the ocean through Earth's history. *Elements,* 7**,** 107-112.

POULTON, S. W., FRALICK, P. W. & CANFIELD, D. E. 2004. The transition to a sulphidic ocean~ 1.84 billion years ago. *Nature,* 431**,** 173-177.

POULTON, S. W. & RAISWELL, R. 2002. The low-temperature geochemical cycle of iron: from continental fluxes to marine sediment deposition. *American journal of science,* 302**,** 774-805.
PUGH, A. C., DANISE, S., BROWN, J. R. & TWITCHETT, R. J. 2014. Benthic ecosystem dynamics following the Late Triassic mass extinction event: Palaeoecology of the blue lias formation, Lyme Regis, UK. *Geoscience in South-West England,* 13**,** 255-266.
RADLEY, J. D. 2008. Seafloor erosion and sea-level change: Early Jurassic Blue Lias Formation of central England. *Palaeogeography, Palaeoclimatology, Palaeoecology,* 270**,** 287-294.
RADLEY, J. D. & BARKER, M. J. 2000. Palaeoenvironmental significance of storm coquinas in a Lower Cretaceous coastal lagoonal succession (Vectis Formation, Isle of Wight, southern England). *Geological Magazine,* 137**,** 193-205.
RAISWELL, R. 1971. The growth of Cambrian and Liassic concretions. *Sedimentology,* 17**,** 147-171.
RAISWELL, R. 1988. Chemical model for the origin of minor limestone-shale cycles by anaerobic methane oxidation. *Geology,* 16**,** 641-644.
RAISWELL, R. & BERNER, R. A. 1985. Pyrite formation in euxinic and semi-euxinic sediments. *American Journal of Science,* 285**,** 710-724.
RAISWELL, R., BUCKLEY, F., BERNER, R. A. & ANDERSON, T. F. 1988. Degree of pyritization of iron as a paleoenvironmental indicator of bottom-water oxygenation. *Journal of Sedimentary Research,* 58**,** 812-819.
RAISWELL, R. & CANFIELD, D. E. 1996. Rates of reaction between silicate iron and dissolved sulfide in Peru Margin sediments. *Geochimica et Cosmochimica Acta,* 60**,** 2777-2787.
RAISWELL, R. & CANFIELD, D. E. 1998. Sources of iron for pyrite formation in marine sediments. *American Journal of Science,* 298**,** 219-245.
RAISWELL, R., CANFIELD, D. E. & BERNER, R. A. 1994. A comparison of iron extraction methods for the determination of degree of pyritisation and the recognition of iron-limited pyrite formation. *Chemical geology,* 111**,** 101-110.
RAISWELL, R. & FISHER, Q. 2000. Mudrock-hosted carbonate concretions: a review of growth mechanisms and their influence on chemical and isotopic composition. *Journal of the Geological Society,* 157**,** 239-251.
RAISWELL, R., HARDISTY, D. S., LYONS, T. W., CANFIELD, D. E., OWENS, J. D., PLANAVSKY, N. J., POULTON, S. W. & REINHARD, C. T. 2018. The iron paleoredox proxies: A guide to the pitfalls, problems and proper practice. *American Journal of Science,* 318**,** 491-526.
RAISWELL, R., NEWTON, R., BOTTRELL, S. H., COBURN, P. M., BRIGGS, D. E. G., BOND, D. P. G. & POULTON, S. W. 2008. Turbidite depositional influences on the diagenesis of Beecher's Trilobite Bed and the Hunsrück Slate; sites of soft tissue pyritization. *American Journal of Science,* 308**,** 105-129.
RAISWELL, R., NEWTON, R. & WIGNALL, P. B. 2001. An indicator of water-column anoxia: resolution of biofacies variations in the Kimmeridge Clay (Upper Jurassic, UK). *Journal of Sedimentary Research,* 71**,** 286-294.
RAISWELL, R. & PLANT, J. 1980. The incorporation of trace elements into pyrite during diagenesis of black shales, Yorkshire, England. *Economic Geology,* 75**,** 684-699.
RAKUS, M. 1978. Sur l'existence de deux types distincts d'empreintes de muscles retracteurs chez les ammonites. *Bulletin de la Société vaudoise des sciences naturelles,* 354**,** 139-145.

RICHTER, U. 2002. Gewebeansatz-Strukturen auf pyritisierten Steinkernen von Ammonoideen. *Geologische Beiträge Hannover,* 4**,** 1-113.
RICHTER, U. & FISCHER, R. 2002. Soft tissue attachment structures on pyritized internal moulds of ammonoids. *Abhandlungen der Geologischen Bundesanstalt,* 57**,** 139-149.
RICKARD, D., GRIFFITH, A., OLDROYD, A., BUTLER, I. B., LOPEZ-CAPEL, E., MANNING, D. & APPERLEY, D. 2006. The composition of nanoparticulate mackinawite, tetragonal iron (II) monosulfide. *Chemical Geology,* 235**,** 286-298.
RUHL, M., DEENEN, M., ABELS, H., BONIS, N., KRIJGSMAN, W. & KÜRSCHNER, W. 2010. Astronomical constraints on the duration of the early Jurassic Hettangian stage and recovery rates following the end-Triassic mass extinction (St Audrie's Bay/East Quantoxhead, UK). *Earth and Planetary Science Letters,* 295**,** 262-276.
RUKIN, N. 1990. *The diagenesis of the Shales-with-beef of the Lower Lias, West Dorset.* Unpublished PhD Thesis, University of Liverpool.
SANDERS, D. 2003. Syndepositional dissolution of calcium carbonate in neritic carbonate environments: geological recognition, processes, potential significance. *Journal of African Earth Sciences,* 36**,** 99-134.
SANDERS, D. 2004. Potential significance of syndepositional carbonate dissolution for platform banktop aggradation and sediment texture: a graphic modeling approach. *Austrian Journal of Earth Sciences,* 95**,** 71-79.
SEILACHER, A., REIF, W.-E. & WESTPHAL, F. 1985. Sedimentological, ecological and temporal patterns of fossil Lagerstätten. *Philosophical Transactions of the Royal Society of London. B, Biological Sciences,* 311**,** 5-24.
SELLWOOD, B. W. 1972. Regional environmental changes across a Lower Jurassic stage-boundary in Britain. *Palaeontology,* 15**,** 125-157.
SEVERMANN, S., LYONS, T. W., ANBAR, A., MCMANUS, J. & GORDON, G. 2008. Modern iron isotope perspective on the benthic iron shuttle and the redox evolution of ancient oceans. *Geology,* 36**,** 487-490.
SIMMS, M. J. 2004. The Wessex Basin (Dorset and central Somerset). *Geological Conservation Review Series,* 30**,** 53-107.
SOSZYŃSKA-MAJ, A., KRZEMIŃSKI, W., KOPEĆ, K. & CORAM, R. A. 2016. Phylogenetic relationships within the relict family Eomeropidae (Insecta, Mecoptera) based on the oldest fossil from the Early Jurassic (Sinemurian) of Dorset, southern England. *Journal of Systematic Palaeontology,* 14**,** 1025-1031.
STOOKEY, L. L. 1970. Ferrozine---a new spectrophotometric reagent for iron. *Analytical chemistry,* 42**,** 779-781.
SWEENEY, R. & KAPLAN, I. 1973. Pyrite framboid formation; laboratory synthesis and marine sediments. *Economic Geology,* 68**,** 618-634.
TIHELKA, E. 2019. New Mesozoic earwigs from England, with a catalogue of fossil Dermaptera. *Proceedings of the Geologists' Association,* 130**,** 609-611.
TWITCHETT, R. J. 2006. The palaeoclimatology, palaeoecology and palaeoenvironmental analysis of mass extinction events. *Palaeogeography, Palaeoclimatology, Palaeoecology,* 232**,** 190-213.
TWITCHETT, R. J. & BARRAS, C. G. 2004. Trace fossils in the aftermath of mass extinction events. *Geological Society, London, Special Publications,* 228**,** 397-418.
VINCENT, P. & TAQUET, P. 2010. A Plesiosaur Specimen from the Lias of Lyme Regis: The Second Ever Discovered Plesiosaur by Mary Anning. *Geodiversitas,* 32**,** 377-390.

VIOLLIER, E., INGLETT, P., HUNTER, K., ROYCHOUDHURY, A. & VAN CAPPELLEN, P. 2000. The ferrozine method revisited: Fe (II)/Fe (III) determination in natural waters. *Applied geochemistry,* 15**,** 785-790.
WALTER, L. M. & BURTON, E. A. 1990. Dissolution of recent platform carbonate sediments in marine pore fluids. *American Journal of Science,* 290**,** 601-643.
WARRINGTON, G., AUDLEY-CHARLES, M., ELLIOTT, R., EVANS, W., IVIMEY-COOK, H., KENT, P., ROBINSON, P., SHOTTON, F. & TAYLOR, F. 1980. A Correlation of Triassic Rocks in the British Isles. Special Report of the Geological Society of London, No. 13.
WARRINGTON, G., COPE, J. C. W. & IVIMEY-COOK, H. C. 1994. St Audrie's Bay, Somerset, England: a candidate global stratotype section and point for the base of the Jurassic system. *Geological Magazine,* 131**,** 191-200.
WATERHOUSE, H. K. 1999. Regular terrestrially derived palynofacies cycles in irregular marine sedimentary cycles, Lower Lias, Dorset, UK. *Journal of the Geological Society,* 156**,** 1113-1124.
WEBBY, B. D. & PERCIVAL, I. G. 1983. Ordovician trimerellacean brachiopod shell beds. *Lethaia,* 16**,** 215-232.
WEEDON, G. P. 1986. Hemipelagic shelf sedimentation and climatic cycles: the basal Jurassic (Blue Lias) of South Britain. *Earth and Planetary Science Letters,* 76**,** 321-335.
WEEDON, G. P. 1987. *Palaeoclimatic significance of open marine cyclic sequences.* Unpublished PhD Thesis, University of Oxford.
WEEDON, G. P., JENKYNS, H. C., COE, A. L. & HESSELBO, S. P. 1999. Astronomical calibration of the Jurassic time-scale from cyclostratigraphy in British mudrock formations. *Philosophical Transactions of the Royal Society of London. Series A: Mathematical, Physical and Engineering Sciences,* 357**,** 1787-1813.
WEEDON, G. P., JENKYNS, H. C. & PAGE, K. N. 2018. Combined sea-level and climate controls on limestone formation, hiatuses and ammonite preservation in the Blue Lias Formation, South Britain (uppermost Triassic – Lower Jurassic). *Geological Magazine,* 155**,** 1117-1149.
WEEDON, G. P., PAGE, K. N. & JENKYNS, H. C. 2019. Cyclostratigraphy, stratigraphic gaps and the duration of the Hettangian Stage (Jurassic): insights from the Blue Lias Formation of southern Britain. *Geological Magazine,* 156**,** 1469-1509.
WEITSCHAT, W. & BÄNDEL, K. 1991. Organic components in phragmocones of Boreal Triassic ammonoids: implications for ammonoid biology. *Paläontologische Zeitschrift,* 65**,** 269.
WHEELEY, J. & TWITCHETT, R. 2005. Palaeoecological significance of a new Griesbachian (Early Triassic) gastropod assemblage from Oman. *Lethaia,* 38**,** 37-45.
WIGNALL, P. B. 2001a. Large igneous provinces and mass extinctions. *Earth-science reviews,* 53**,** 1-33.
WIGNALL, P. B. 2001b. Sedimentology of the Triassic-Jurassic boundary beds in Pinhay Bay (Devon, SW England). *Proceedings of the Geologists' Association,* 112**,** 349-360.
WIGNALL, P. B. & BOND, D. P. 2008. The end-Triassic and Early Jurassic mass extinction records in the British Isles. *Proceedings of the Geologists' Association,* 119**,** 73-84.
WIGNALL, P. B. & HALLAM, A. 1991. Biofacies, stratigraphic distribution and depositional models of British onshore Jurassic black shales. *Geological Society, London, Special Publications,* 58**,** 291-309.

WIJSMAN, J. W., MIDDELBURG, J. J. & HEIP, C. H. 2001. Reactive iron in Black Sea sediments: implications for iron cycling. *Marine Geology,* 172**,** 167-180.
WILCOX, C. J. & LOCKLEY, M. G. 1981. A reassessment of facies and faunas in the type Llandeilo (Ordovician), Wales. *Palaeogeography, Palaeoclimatology, Palaeoecology,* 34**,** 285-314.
WOLFF, G. A., RUKIN, N. & MARSHALL, J. D. 1992. Geochemistry of an early diagenetic concretion from the Birchi Bed (L. Lias, W. Dorset, UK). *Organic Geochemistry,* 19**,** 431-444.
WOODWARD, H. B. 1893. *The Lias of England and Wales, Yorkshire Excepted, Memoirs of the Geological Survey of the United Kingdom,* London, HM Stationery Office.
WOODWARD, H. B. & USSHER, W. A. E. 1911. *The geology of the country near Sidmouth and Lyme Regis, Memoirs of the Geological Survey of the United Kingdom (2nd Edition),* London, HM Stationery Office.
WRIGHT, P., CHERNS, L. & HODGES, P. 2003. Missing molluscs: field testing taphonomic loss in the Mesozoic through early large-scale aragonite dissolution. *Geology,* 31**,** 211-214.
WRIGHT, T. 1860. On the zone of Avicula contorta, and the Lower Lias of the south of England. *Quarterly Journal of the Geological Society,* 16**,** 374-411.
WRIGHT, V. P. & CHERNS, L. 2016. How far did feedback between biodiversity and early diagenesis affect the nature of Early Palaeozoic sea floors? *Palaeontology,* 59**,** 753-765.
ZIEGLER, P. A. Geological atlas of western and central Europe. 1990. Geological Society of London.